AD-A044 743 STANFORD UNIV CALIF DEPT OF CIVIL ENGINEERING F/G 8/3
THE STRUCTURE OF MODULATED TURBULENT FLOW OVER PROGRESSIVE WATE--ETC(U)
AUG 77 C HSU, E Y HSU, R L STREET DAAG29-76-G-0125
UNCLASSIFIED TR-221 NL

1 OF 3
AD A044743

Technical Report No. 221

THE STRUCTURE OF MODULATED TURBULENT FLOW OVER PROGRESSIVE WATER WAVES

by

Chin-Tsau Hsu
En Y. Hsu
Robert L. Street

This research was supported by
National Science Foundation
Grant No. ENG 76-15106
Office of Naval Research
Contract No. N00014-76-C-0155
and
U.S. Army Research Office
Grant No. DAAG29-76-G-0125

August 1977

Department of CIVIL ENGINEERING
STANFORD UNIVERSITY

THE STRUCTURE OF MODULATED TURBULENT FLOW OVER PROGRESSIVE WATER WAVES

Interim
Technical Report No. 221

by

Chin-Tsau Hsu

En Y. Hsu

Robert L. Street

August 1977

This research was supported by

National Science Foundation
Grant No. ENG 76-15106

Office of Naval Research
Contract No. N00014-76-C-0155

and

U.S. Army Research Office
Grant No. DAAG29-76-G-0125

Department of Civil Engineering
Stanford University
Stanford, California

THE FINDINGS OF THIS REPORT ARE NOT TO BE CONSTRUED AS AN OFFICIAL DEPARTMENT OF THE ARMY OR DEPARTMENT OF THE NAVY POSITION, UNLESS SO DESIGNATED BY OTHER AUTHORIZED DOCUMENTS.

ERRATA

for

THE STRUCTURE OF MODULATED TURBULENT FLOW
OVER PROGRESSIVE WATER WAVES

by
C.-T. Hsu, E. Y. Hsu and R. L. Street

Technical Report No. 221
Department of Civil Engineering
Stanford University

Page	Line		
14	13	$\overline{<gh'>} = 0$	$\overline{<\tilde{g}h'>} = 0$
31	20	2.61)	(2.61)
39	6	$= <(\tilde{u}_a \tilde{u}_+$	$= <(\tilde{u}_a + \tilde{u}_+$
51	1	$\frac{1}{k} \hat{q}^*_s(Y/k)$	$\frac{1}{k^2} \hat{q}^*_s(Y/k)$
51	3	$k^2 y^{*2}$	$k^2 y^{*2} u_*$
51	3	$(\ln Y - \ln k)^2 Y^2$	$(\ln Y - \ln k)^2 Y^2 u_*$
52	1	$\int_0^Y e^{Y_1} \int_0^{Y_1} \int_0^{Y_2}$	$\int_0^Y e^{Y_1} \int_0^{Y_1} \int_\infty^{Y_2}$
52	2	$\int_0^Y e^{2Y_1} \int_0^{Y_1} e^{-Y_2} \int_\infty^{Y_2}$	$\int_0^Y e^{2Y_1} \int_\infty^{Y_1} e^{-Y_2} \int_\infty^{Y_2}$
53	7	$\frac{(U - c_s)^2}{(1 - c_s)^2}$	$\frac{(U - c_s)}{(1 - c_s)^2}$
57	9,10,16	$(a + b)$	$(a + 2b)$
73	5	$\delta(f - f_\alpha) \cos \theta_\alpha -$	$\delta(f - f_\alpha) \cos \theta_\alpha +$
126	2	$\overline{\tilde{r}^*_{12} \frac{\partial \tilde{v}^*}{\partial x^*}}$	$+ \overline{\tilde{r}^*_{12} \frac{\partial \tilde{v}^*}{\partial x^*}}$
173	Figure 2.3	$u(1 + \frac{\partial f}{\partial y^*} \tilde{\eta}) \Delta y^x$	$u(1 + \frac{\partial f}{\partial y^*} \tilde{\eta}) \Delta y^*$
198	Figure 5.14a	$\frac{\lvert\hat{r}_{11}\rvert}{U_\infty} \times 10^2$	$\frac{\lvert\hat{r}_{11}\rvert}{U^2_\infty} \times 10^4$

ABSTRACT

Theoretical predictions of wave growth by closure modelling have been hindered by the ambiguity about the interface conditions and the lack of knowledge of the dynamics of wave-turbulence interaction. The present experimental program was undertaken in an attempt to clarify the interface flow structure, as well as the closure relations, and to study the dynamic response of wave perturbations to the imposition of air modulations.

The Stanford wind-wave facility was modified to permit generation of an air modulation with a sinusoidal variation. A wave height gauge and an X-array hot-film probe were used to measure simultaneously the wave height and the wind velocity from a wave-follower operating in a transformed coordinate system. Four runs were made, all with a 2.4 m/sec mean free stream velocity and a 1 Hz mechanically-generated water wave of amplitude 2.67 cm, but with modulating frequencies at 0.0, 0.4, 0.7 and 1.5 Hz respectively. Each velocity profile consists of 18 points ranging in mean elevations from 1.604 cm to 39.45 cm above the interface. Theoretical bases were also formed for a better understanding of the flow characteristics in the transformed coordinate system.

The mean velocity profile was found to be basically log-linear with a wake characteristic near the free stream. The friction velocity computed from the profile method agrees with the result obtained from the measured constant shear stress layer near the interface. The lower portion of the mean profiles follows the wave form but the upper portion of the mean profiles seems to be unaware of the existence of the water wave underneath. Thus, describing the flow in the transformed coordinate system is an appropriate approach. Drift current effects on the mean flow were also discussed.

The wave perturbation motion was found to be irrotational near the free stream and to have a strong shear behavior near the interface. All the phases of the wave-induced turbulent Reynolds stresses have a jump of 180^{o} in the middle of the boundary layer, but such jumps do not occur in the phases of the wave perturbation velocities. The relationships between the observed wave perturbation velocities and the induced turbulent Reynolds stresses are basically of an eddy viscosity type.

The energy balance of the wave perturbation field showed that most of the energy transfer occurs in the vicinity of the interface. Energy was drawn from the mean flow to wave perturbation, and then from the wave perturbation to turbulence and to the water wave. The energy transfer from wind to waves is predominantly caused by the wave perturbation pressure. The measured wave growth rate agrees with that observed by Dobson (1971), and is one order in magnitude greater than Miles' prediction. Wave-turbulence interaction is responsible for this higher growth rate.

The response of the wave perturbation to air modulations when the modulating frequencies are lower than the frequency of the water wave is different from that when the modulating frequency is higher than the frequency of the water wave. Air modulations tend to decrease the ripple formation over the mechanically-generated water wave under the same mean flow condition.

ACKNOWLEDGEMENTS

Appreciation is expressed to Prof. I-Dee Chang for reviewing the manuscript. Special thanks are reserved for Mr. Theodor R. Mogel, for his assistance with instrumentation problems, and for Mr. Marion Burzynski, for his skillful work in carrying out mechanical jobs of the experiments. The drafting of the figures by Ms. Andrea Gill is sincerely appreciated.

Financial support for this project was provided by the National Science Foundation Grant No. ENG 76-15106, Office of Naval Research Contract No. N00014-76-C-0155, and U.S. Army Research Office Grant No. DAAG29-76-G-0125.

TABLE OF CONTENTS

LIST OF TABLES

LIST OF FIGURES

NOMENCLATURE

a	wave amplitude of water wave
A	constant of low-pass digital filter
A_1, A_2 and A_{11}	constants used in closure modelling of $\tilde{r}_{ij}$
A_b	blockage area of air flow pulser
B_{11}	constant used in closure modelling of $\tilde{r}_{ij}$
c	phase speed of water wave (wave celerity)
c_1, c_2 and c_3	constant used in closure modelling of $\tilde{r}_{ij}$
C	intercept of mean velocity profile in wall coordinates
C_p	pressure coefficient of wave perturbation pressure
C_f	drag coefficient for turbulent flow over flat plate
C_{hg}	cospectra of h and g
D	derivative with respect to y(= d/dy)
E	energy tranfer from wind to waves; voltage
f	frequency in Hz; decay factor of a transformed coordinate system
F	operator for Fourier transformation
g	arbitrary quantities of interest
$\overline{g}$ and G	time average (or mean) of g
$\langle g \rangle$	phase average of g
$\tilde{g}$	wave component of g
$\hat{g}$	amplitude of $\tilde{g}$ in complex form
$\lvert\hat{g}\rvert$	amplitude of $\tilde{g}$
h	another arbitrary quantities of interest; height
H	height of air portion in a wind-wave channel
$H(f)$	transfer function of a digital filter
k	wave number of water wave
k_o	von Karman constant
K	kinetic energy of the wave perturbation field
L	wave length of water wave

p	pressure
q^2	turbulent kinetic energy
Q_{hg}	quadrature spectra of h and g
(r, θ)	polar coordinates
r_{ij}	turbulent Reynolds stresses
Re	Reynolds number
Re_w	wave Reynolds number
Re_{δ_2}	Reynolds number based on momentum thickness
R_{hg}	correlation function of h and g
S_{ij}	strain rate
t	time
T	period for averaging
u, v, and w	velocity components in the x, y, and z directions respectively
u_i	velocity vector (= (u, v, w))
u_*	friction velocity
U_o	velocity of the drift current
U_d	drift current induced mean air velocity
U_{eff}	effective cooling velocity of hot-film
U_∞	mean free stream velocity
W_c	wake parameter for the mean velocity profile
$\underline{x} = x_i = (x, y, z)$	Cartesian coordinate system; x in flow direction, y in vertical direction and z in lateral direction
y_c	critical height where $U(y_c) = c$
$\overline{y}_c$	effective critical height of turbulently-mixed critical layer
Y	stretched coordinate of y*
z_o	surface roughness produced by ripples

Greek Symbols

β	reciprocal of the thickness of wave Stokes layer
β_p	wave growth rate parameter

δ	turbulent boundary layer thickness
δ_o	diffusion layer thickness of turbulent flow
η	surface displacement about the mean water level
θ_g	phase lag of g with respect to time referred to wave height signal $\tilde{\eta}$
θ_{hg}	phase lag of g to h
$\Lambda_{g'}$	integral scale of g'
ν	kinematic viscosity
ν_d	eddy viscosity due to viscoelastic behavior
ν_t	turbulent eddy viscosity
$\nu_T = \nu_t - \nu_d$	resultant eddy viscosity
ρ	density of air
τ	wave period
ξ	time separation in correlation
ϕ	stream function
Φ_{hg}	cross-spectrum of h and g
$\omega = 2\pi f$	radiant frequency

Subscripts

a	air modulation
d	air-modulation-effected components on wave perturbation
s	interaction-produced waves
T	related to finite time period for averaging

Superscripts

'	turbulent fluctuations; derivative with respect to y
''	fluctuations around a phase averaged quantity
o	for quantities under condition of no drift current
+	wall coordinates, $u^+ = U/u_*$, $y^+ = y^* u_*/\nu$, etc.
*	transformed coordinate system, x*, y*, t*, $\tilde{u}_i^*$ and $\tilde{r}_{ij}^*$, etc.

CHAPTER 1

INTRODUCTION

1.1 General

The generation of surface water waves by wind is a classical problem. To date, although significant advances have been made toward the understanding of the wave generation processes, our knowledge remains incomplete. Recent investigations have suggested that the interaction between the surface water waves and the background turbulence of the wind may strongly enhance the momentum and energy transfer, from the wind to the waves, which ultimately causes the waves' growth. Unfortunately, when the wave-turbulence interaction is considered, the so-called "closure" problem is raised.

The closure problem occurs when an averaging process is applied to the Navier-Stokes equations in describing statistically the wind fields. The averaging process results in the loss of information and introduces new unknown quantities commonly referred to as turbulent Reynolds stresses. In order to solve the problem, closure relations, which relate the Reynolds stresses to other quantities in the averaged equations, should be postulated. In wind-wave generation, the closure problem is associated with the induced turbulent Reynolds stresses that are oscillatorily coherent with the surface water waves. A successful closure modelling for the induced turbulent Reynolds stresses should properly describe the dynamics of wave-turbulence interaction, and the results of its predication should agree with those measured. Hence one realizes immediately that obtaining reliable data associated with the wave perturbation against which the model predictions can be compared is equally important to modelling.

In the past ten years, several closure models have been proposed to predict wave-induced fields (Long 1971; Davis 1970, 1972; Saeger and

Reynolds 1971; Townsend 1972; Norris and Reynolds 1975). Most of the models are based on ad hoc or phenomenological assumptions. Very little effort has been made toward understanding basically how the waves couple with the turbulence in producing the induced turbulent Reynolds stresses. This basic understanding is now considered one of the most important features in the closure modelling. Because the existing turbulence theory is incomplete, direct measurements of the wave perturbation fields, including the induced turbulent Reynolds stresses, should be very instructive, not only to the formation of closure relations in predicting the wind-wave generation but also to the further understanding of the turbulence structure.

Studying the response of the wave perturbations to a calibrated unsteady air motion provides one way of investigating the wave-turbulance interaction. The unsteadiness of air flow can be fixed by generating a controlled air modulation into the interface flow regime. The air modulation possesses a pulsating feature, which varies sinusoidally with time and has a very long wave length when the modulating frequency is low. Although it is hard to visualize that the air modulation serves as one frequency-spectral component of turbulence, it is anticipated that the interaction between the air modulation and the waves does maintain most features of turbulence-wave interaction. The analogy is even more profound when the air modulation frequency is low, because the low-frequency components of turbulence are of large scale and are sometimes regarded as organized waves. By measuring the air flows under the conditions with and without air modulations, the effect of the air modulation on the wave perturbation can be determined.

Aside from the closure problem, there is some ambiguity about the boundary conditions at the interface arising from the oscillatory displacement of the water surface and the possible influence caused by the existence of drift currents. The calculations of closure modelling

are very sensitive to the interface boundary conditions imposed as pointed out by Davis (1970) and Long (1971). The interface boundary conditions should be consistent with the physical process at the interface. Direct measurements of the wave perturbation quantities as close to the interface as possible are urgently needed in resolving this problem. Measurements performed at a fixed elevation are generally believed to be unfruitful since the probe used for data taking can reach only to a distance approximately equal to the maximum wave amplitude from the mean water level. This disadvantage of fixed probe measurements is even more serious at high wind speeds where both the diffusive layer (usually referred to as the momentum thickness) is much thinner than the wave height, and the critical height (the distance from the mean water level to the level where the mean velocity equals the wave speed) is much lower than the wave height.

A coordinate system using the undulating interface as the ordinate and asymptotically matching with the undistorted coordinate system when the ordinates of both systems are away from the interface was first adopted by Benjamin (1959). In Benjamin's analysis the air flow extended to infinite height. For air flow with finite height, a transformed coordinate system which resembled Benjamin's was used successfully by Norris and Reynolds (1975) in predicting the pressure wave perturbations. However, no data of the velocity fields were obtained by Norris and Reynolds for their modelling comparisons, although the velocity field data usually serves as a more sensitive test than the pressures. Measurements of the velocity fields as well as of the turbulent Reynolds stresses in the transformed coordinate systems will not only reveal more information in determining the interface boundary conditions, but also provide basic data for closure model justification.

1.2 Objectives

The objectives of this investigation are as follows:

(1) To design an experiment through which one can

(a). investigate the air-water interface flows in a transformed coordinate system;

(b). investigate the response of the wave perturbations to the pulsating air modulations.

(2) To obtain some reliable data on flows which may possibly resolve some aspects of closure dynamics and lead toward the prediction of wind-wave generation. These experimental data consist of

(a). mean velocity and mean Reynolds stresses to characterize the flow;

(b). induced velocities and induced turbulent Reynolds stresses associated with both the surface water waves and the air modulations;

(c). velocity components produced from the interaction between the surface waves and the air modulations.

(3) To give some thereotical insights to wave-turbulence interactions for better understanding of the interface flows in the transformed coordinate system.

1.3 Previous Work

Interest in the theory of wave generation by winds was reactivated by the works of Eckart (1953) and in particular of Ursell (1956). However, the first significant contribution to the theory should be reserved to those works of Phillips (1957) and Miles (1957).

Phillips' theory can be regarded as a discussion of an ensemble of Kelvin wakes, generated by turbulent pressure fluctuations. Its mechanism is based on resonance and the resulting wave growth rate is linear. But, the later measurements by Snyder and Cox (1966) and by Barnett and Wilkerson (1967) showed that Phillips' theory, although it is valid, can not provide correct estimates of the energy and momentum transfer

from wind to waves, except perhaps in the very initial stages of the wave generation over a smooth water surface.

Miles' theory describes the coupling between surface waves and the mean air flow. The growth mechanism mainly depends on the feedback of the wave-induced air flow perturbations to the surface waves. His mechanism bears a strong resemblance to the classical work on hydrodynamic stability, and the resulting wave growth rate is exponential. Hence, when wave amplitudes are large, Miles' mechanism is more effective than Phillips' mechanism in transferring energy from wind to waves. It was anticipated that Miles' mechanism should provide the major portion of energy transfer; unfortunately, the measurements of Snyder and Cox (1966) and later works of Barnett and Wilkerson (1967), of Shemdin and Hsu (1967), and of Bole and Hsu (1969) showed their measured growth rates to be one order in magnitude greater than those predicted from Miles' theory.

In his 1957 paper, although Miles acknowledged the possible significance of the induced turbulent Reynolds stresses and the ambiguity of the interface boundary conditions caused by using a fixed coordinate system, he based his calculations primarily on the inviscid quasilaminar assumptions where the viscous and the turbulence effects were neglected. The difficulty of the interface boundary conditions was overcome by Miles (1959) and by Benjamin (1959) by using transformed coordinate systems so that the boundary conditions could be evaluated directly at the interface. Hence, the viscous effect could also be included in their calculations. Their main conclusion was that the viscous effect does not significantly contribute to the momentum and energy transfer from wind to waves in the flow regime of practical interest.

The significance of the induced turbulent Reynolds stresses was not only revealed from the failure of the quasilaminar model to predict the major portion of wave growth, but also proven by Longuet-Higgins

(1969) following the concepts given by Stewart (1967). Longuet-Higgins (1969) showed that an oscillating shear stress at the interface could be of equal importance as the wave-induced pressure in transferring the energy to the waves. Kendall (1970) indicated experimentally the strong modulation of turbulent structure caused by the progressive water waves and the significance of direct energy transfer to the waves acted upon by the induced turbulent Reynolds stresses.

When the induced turbulent Reynolds stresses are retained in the linearized perturbation equations, the closure problem impedes any further theoretical predictions. Closure relations were obtained by authors using the existing closure theories in turbulence.

Miles (1967) used the mixing length and the similarity arguments in relating the induced turbulent Reynolds stresses to the induced turbulent vorticity. Although no further calculations were performed in the absence of detailed experimental data at that time, he conjectured that inclusion of induced turbulent Reynolds stresses in the governing equations was necessary to improve the predictions.

Davis (1970) followed Benjamin's (1959) suggestion that "the properties of the flow are dependent on an appropriate measure of the height above the instantaneous wave surface" (Davis 1970, pp. 722) and proposed that the horizontal component of induced turbulent shear stress is directly proportional to the curvature of the mean velocity profile and to the wavy displacement of the vertical ordinate used by Benjamin (1959). Numerical predictions based on this model were inconsistent with Stewart's data (1970) and were inconclusive.

Saeger and Reynolds (1971) adopted an eddy viscosity model to calculate the induced pressures over a flexible wavy surface. The eddy viscosity model was originally proposed by Hussain and Reynolds (1970) to study successfully the behavior of turbulent Tollmein-Schlichting waves in a straight-wall channel. Experimentally-measured pressure data of Saeger and Reynolds disagreed with their predictions.

Details of the closure technique were examined by Davis (1972). Computations following the BFA scheme (Bradshow, Ferriss and Atwell 1967) yielded an exponential wave growth rate one order in magnitude less than the experimental results of Kendall (1970) and of Dobson (1971). Davis also generalized the eddy viscosity model of Hussain and Reynolds to include the elastic behavior of fluid by proposing a "memory" function in characterizing the fluid experience undergoing strain. The eddy viscosity model was subsequently the limiting case of shortest "memory." Results of Davis' calculations showed no apparent difference between the eddy viscosity model and the eddy viscoelasticity model (the generalized model); the predicted wave growth rate agreed reasonably with those of Kendall (1970) and of Dobson (1971).

Townsend (1972) modified the BFA scheme to study the distortion of turbulent boundary layer flow caused by the surface waves running in different directions from the mean velocity. The constitutive relations for the induced turbulent Reynolds stresses were constructed from the concepts of the "relaxation" response, resulting in changes in the intensity and the direction of the mean Reynolds stresses due to the surface waves. The wave growth rate was calculated, but was still considerably less than those measured by Snyder and Cox (1966), by Barnett and Wilkerson (1967), and by Dobson (1971).

Closure models calculated in a transformed coordinate system were first proposed by Norris and Reynolds (1975). Even for the simplest quasilaminar model, their results agreed satisfactorily with their measured induced pressures. The inclusion of non-zero induced turbulent Reynolds stresses did not significantly change the quality of their predictions. They concluded that the quasilaminar transformed coordinate models of Miles (1959) and of Benjamin (1959) are entirely adequate for the induced pressure calculations. This conclusion did not claim that the quasilaminar transformed coordinate model is also adequate in

explaining the major portion of the wave growth. Since the pressure measurements of Norris and Reynolds were taken at the fixed wall of their channel, whether the agreement can also be achieved near the flexible wavy wall is still unknown. No pressure measurements at the wavy wall were reported by Norris and Reynolds. Pressure measurements near the interface in a wave-follower system by Yu et al. (1973) had shown the inconsistency in the wave growth rate between the observed data and the predicted results from Miles' theory. It is believed that the comparison between such observed and predicted quantities as the induced velocity and the induced turbulent Reynolds stresses will provide a direct test of the adequacy of the Norris and Reynolds' model.

Measuring the induced turbulent Reynolds stresses was first attempted by Kendall (1970). His results suggested that the dynamic response of turbulence to the imposed surface waves is significant. Unfortunately, no detailed structure of the induced turbulent Reynolds stresses can be extracted from his measurements.

The induced turbulent Reynolds stresses were also measured by Yu et al. (1973) and by Chao et al. (1976) using a wave-follower system in the Stanford wind-water channel. Data were obtained only in the lower portion (about one third) of the turbulent boundary layer. Although Chao et al. also measured the induced turbulent Reynolds stresses in a fixed frame, these measurements were performed under different flow condition from those of the wave-follower frame, and no direct comparison could be made between the two. Because of the incompleteness of the wave-following data and the disadvantage of the fixed probe data as mentioned in Section 1.1, their data could not clarify the structure of the wave-induced flow fields.

All the closure models cited above were phenomenological. A closure model using a dynamical approach was given by Davis (1974).

The novel aspect of his analysis is that each averaging process is delayed until the dynamical equations have been solved rather than the normal procedure which attempts to find equations for averaged quantities. The constitutive relations hence predicted obey the visco-elastic law in nature but require the detailed turbulent structure, which is still absent, for further model calculations.

In Davis' (1974) formulation, the turbulence was decomposed into two components: one was the original undisturbed turbulent component, and the other was the "active" turbulent component. The active turbulent component is introduced by the wave perturbations and has both the wavy and turbulent behaviors; hence, the active turbulent component is strongly correlated with the turbulence in producing the induced turbulent Reynolds stresses. In the present study, the existence and the relative importance of the active turbulent component were examined.

The controlled air modulations were used in the present experiment to simulate the large scale motions of turbulence in interaction with the surface waves. The modulated air flows in flat rigid wall channels had been studied by Karlsson (1959) and by Acharya and Reynolds (1975). The modulated air flows over wind-generated waves were also investigated by Wu (1973). Details of the air modulation will be discussed in Chapter 3.

1.4 Selection of Flow Conditions

The wind-wave channel at the Stanford Hydraulic Laboratory which will be described in Chapter 4 was modified to produce air modulations resulting in a perturbation velocity with a slug flow character. The mean free stream velocity was set at a low value of 2.4 m/sec to give relatively higher amplitudes of the air modulations. For ease of comparison the frequency of the mechanically-generated water waves was chosen to be 1 Hz, the same as that of Yu et al. (1973) and Chao et al.

(1976), since their experiments were also performed in the Stanford channel. The frequencies of air modulation were selected at 0.4 Hz, 0.7 Hz and 1.5 Hz such that the mechanically-generated water wave frequency was in the range of the modulation frequencies. All the frequencies selected here satisfied the long wave assumption used by Davis (1974). Velocity data were collected in a transformed coordinate system equivalent to that of Norris and Reynolds (1975). The small amplitude assumption of water waves was also satisfied by setting the amplitude a of the mechanically-generated water waves at 2.67 cm to give a value of $ka = 0.1075$ where $k = 0.04026$ (1/cm) is the wave number of the water wave.

1.5 Summary of Primary Conclusions

In this study, measurements of the velocity fields as well as of the Reynolds stresses under the conditions with and without air modulations were taken over most portions of the boundary-layer velocity profile except those in the immediate proximity of the interface. It was found that the mean velocity profile in the transformed coordinate system is basically log-linear with a wake characteristic near the free stream. A constant mean shear stress was observed near the lower portion of the mean shear stress layer. The development of the drift current at the interface affected significantly on the mean velocity profile by releasing partially the shear stress so that the profile in the log-linear plot has a lower slope and a higher intercept than measured for the flow over flat plate.

At the wind speed of this study, the wave perturbation motion was found to be irrotational near the free stream and to have a strong shear behavior near the interface. A continuous shift of the phase angle of approximately 180° across the boundary layer was observed for the horizontal wave perturbation velocity. The phases of the induced turbulent Reynolds stresses have the same jump of 180° at an elevation in

the middle of the boundary layer. The experimental results showed that the relationships between the wave perturbation velocities and the induced turbulent Reynolds stresses are basically of eddy viscosity type.

The energy balance of the wave perturbation field indicated that most of the energy transfer occur near the interface. Kinetic energy was drawn from the mean flow field to the wave perturbation field, and then from the wave perturbation field to the turbulence field and to the water wave field. The energy transfer from wind to waves is predominantly caused by the wave perturbation pressure. The induced turbulent Reynolds stress transfer energy from the waves to the wind, but they are relatively insignificant. The turbulence enhances the energy transfer by the wave perturbation pressure, by changing the structure of the viscous critical layer. The rate of energy transfer from wind to waves in this study agrees with that measured by Dobson (1971), and is one order in magnitude greater than Miles' prediction (1957).

The effect of the air modulation on the wave perturbation was estimated and shown to be important. The air modulation effect consisted of two parts: one produced from the direct coupling between the components of air modulation and wave perturbation, and the other produced from the indirect changes in the behavior of the correlation of the background turbulence and the wave perturbation. Both are of equal importance. An interesting difference in the behavior of the response of wave perturbations to the additional air modulation was observed between the modulating frequencies which lie below and those which lie above the frequency of the mechanically-generated water waves. Further studies are needed to clarify this difference.

Some theories in wave perturbations and in their interactions with the air modulations were developed in both the fixed coordinate system and the transformed coordinate system in this study. The results have greatly clarified the ambiguity of the interface boundary conditions in the classical fixed coordinate analysis to the transformed coordinate

analysis. The concepts and the philosophy of Davis (1974) are reinforced and extended in the present analysis.

CHAPTER 2

THEORETICAL ASPECTS OF WAVE PERTURBATIONS

2.1 Averaging

Since randomness is one of the most important features of turbulence, the discussion of turbulent flows is usually conducted entirely in terms of statistical quantities. The time average $\overline{g}(\underline{x})$ of a flow quantity, $g(\underline{x}, t)$, is defined conventionally as

$$\overline{g}(\underline{x}) = \lim_{T\to\infty} \frac{1}{T} \int_{-T/2}^{T/2} g(\underline{x}, t)\, dt \tag{2.1}$$

Practically, this average is obtained from a very large ensemble of $g(\underline{x}, t_n)$ which are sampled at different times t_n. If $g(\underline{x}, t)$ is stationary, $\overline{g}(\underline{x})$ does not depend on the starting time of averaging and can be obtained by choosing a sufficiently large value of T or by sampling a sufficiently large ensemble such that no change in $\overline{g}(\underline{x})$ is found by a further increase in T or in the size of the ensemble. For a sampling process with a constant sampling interval Δt, $t_n = n\Delta t$ and a digital expression equivalent to (2.1) is

$$\overline{g}(\underline{x}) = \lim_{N\to\infty} \frac{1}{2N+1} \sum_{n=-N}^{N} g(\underline{x}, n\Delta t) \tag{2.2}$$

where $T = (2N+1)\Delta t$ is applied.

When g contains periodic oscillations as are considered in this study, a conditional average of g, called the "phase average" and denoted by $\langle g \rangle$, is defined by

$$\langle g(\underline{x}, t) \rangle = \lim_{N\to\infty} \frac{1}{2N+1} \sum_{n=-N}^{N} g(\underline{x}, t+n\tau) \tag{2.3}$$

where τ is the period of the organized oscillation. The organized wave component of g, denoted by $\tilde{g}$, is defined by

$$\tilde{g} = \langle g \rangle - \bar{g} \tag{2.4}$$

It is then possible to decompose an arbitrary random signal g into three different components, viz.,

$$g(\underline{x}, t) = \bar{g}(\underline{x}) + \tilde{g}(\underline{x}, t) + g'(\underline{x}, t) \tag{2.5}$$

The new component g' in (2.5) is the background fluctuation around the phase average $\langle g \rangle$. Figure 2.1 shows the schematic of the averages. The following relations easily follow:

$$\bar{\tilde{g}} = 0, \quad \langle g' \rangle = 0, \quad \bar{g}' = 0 \tag{2.6a,b,c}$$

$$\overline{\langle g \rangle} = \bar{g}, \quad \langle \bar{g} \rangle = \bar{g} \tag{2.6d,e}$$

$$\overline{\bar{g}h} = \bar{g}\bar{h}, \quad \langle \bar{g}h \rangle = \bar{g}\langle h \rangle, \quad \langle \tilde{g}h \rangle = \tilde{g}\langle h \rangle \tag{2.7a,b,c}$$

$$\overline{\tilde{g}h'} = 0, \quad \overline{\langle gh' \rangle} = 0 \tag{2.7d,e}$$

where h has the same form as g in (2.5).

Comparison of (2.2) and (2.3) shows that during digital processing the time average and the phase average are very similar except for the difference in choosing Δt and τ, the intervals between two consecutive samples. Since in (2.3) every two consecutive samples are separated by an interval equal to the period of the periodic oscillation, the value of t, $0 \leq t < \tau$, represents different phases of the oscillation. If in (2.3) the interval of two sequential samples were $m\tau$ instead of τ, where m is an integer greater than 1, the results of the phase average are not

changed as long as the process is stationary and the size of ensemble is large enough. This property should be clear since the multiplication of τ by m does not change the phase of the sample. On the other hand, this also implies that (2. 3) contains all the information of harmonic oscillations with period equal to τ/m.

The similarity of (2. 2) and (2. 3) also suggests that, in order to yield a meaningful time average, the sampling interval Δt in (2. 2) should be carefully selected not equal to the periods of organized oscillations. This condition is usually fulfilled by using a sufficiently small value of Δt (or low pass filtering the signal) so that there are no significant organized oscillations with period shorter than Δt. (Actually, the frequency band limit of the signal should be $1/(2\Delta t)$, as discussed in Chapter 4, when the alaising problem is considered.)

2. 2 Generalized Definitions of Organized Waves

Because averaging is equivalent to finding the expectation in probability theory, the organized wave defined in (2. 4) can be regarded as the difference of the conditional (phase average) and unconditional (time average) expectations of the first moment. The concepts of an organized wave then can be generalized by the following definitions: A quantity g of interest is said to contain an n^{th} moment organized wave of period τ if there exists a positive integer n such that the n^{th} power of g has different phase and time averages, i. e.,

$$\langle g^n(\underline{x}, t)\rangle \neq \overline{g^n}(\underline{x}) \quad ; \tag{2. 8}$$

the lowest integer n to result in (2. 8) is defined as the degree of content; and g is called as an n-degree wavy quantity associated with period τ. Hence, a quantity g is said to contain no organized wave of period τ if the following relation is satisfied for all positive integer n:

$$\langle g^n \rangle = \overline{g^n} \tag{2.9}$$

The n^{th} moment organized wave component of g, denoted by $\widetilde{g^n}$, can be defined as the difference of the phase and time averages of g^n, i.e.,

$$\widetilde{g^n} = \langle g^n \rangle - \overline{g^n} \ . \tag{2.10}$$

And, similarly for two quantities g and h, the $(m+n)^{th}$ joint moment organized wave $\widetilde{g^m h^n}$ is defined as

$$\widetilde{g^m h^n} = \langle g^m h^n \rangle - \overline{g^m h^n} \tag{2.11}$$

Accordingly, the decomposition of $g^m h^n$ is generalized to

$$g^m h^n = \overline{g^m h^n} + \widetilde{g^m h^n} + (g^m h^n)' \tag{2.12}$$

2.3 Governing Equations

The continuity and momentum equations governing the flowfield, after normalization by the characteristic velocity U_∞ and the characteristic length δ, are

$$\frac{\partial u_i}{\partial x_i} = 0 \tag{2.13}$$

$$\frac{\partial u_i}{\partial t} + u_j \frac{\partial u_i}{\partial x_j} = - \frac{\partial p}{\partial x_i} + \frac{1}{Re} \cdot \frac{\partial^2 u_i}{\partial x_j \partial x_j} \tag{2.14}$$

where the incompressibility and the Newtonian viscous behavior of the fluid are presumed. The value Re in (2.13) is the well-known Reynolds number defined as

$$Re = \frac{U_\infty \delta}{\nu} \tag{2.15}$$

where ν is the kinematic viscosity, U_∞ is generally referred to as mean free stream velocity of boundary layer flow and δ is the boundary layer thickness. In a fully developed channel flow, U_∞ is the channel centerline mean velocity and δ is equal to $\frac{1}{2}H$ where H is height from the mean water level to the roof of the channel. The time scale and the pressure scale used in the normalization are δ/U_∞ and ρU_∞^2 respectively.

Decomposing u_i and p in a way similar to g in (2.5), we have

$$u_i = \bar{u}_i + \tilde{u}_i + u_i' \tag{2.16a}$$

and

$$p = \bar{p} + \tilde{p} + p' \tag{2.16b}$$

Substituting (2.16a,b) into (2.13) and (2.14) and taking time averages, we find that (2.13) and (2.14) reduce to

$$\frac{\partial \bar{u}_i}{\partial x_i} = 0 \tag{2.17}$$

$$\bar{u}_j \frac{\partial \bar{u}_i}{\partial x_j} = -\frac{\partial \bar{p}}{\partial x_i} + \frac{1}{Re} \cdot \frac{\partial^2 \bar{u}_i}{\partial x_j \partial x_j} - \frac{\partial}{\partial x_j} (\overline{\tilde{u}_i \tilde{u}_j} + \overline{u_i' u_j'}) \tag{2.18}$$

If the phase average is taken before the time average and the time averaged equations are substracted from the phase averaged equations, using (2.10) and (2.11) we have

$$\frac{\partial \tilde{u}_i}{\partial x_i} = 0 \tag{2.19}$$

$$\frac{\partial \tilde{u}_i}{\partial t} + \bar{u}_j \frac{\partial \tilde{u}_i}{\partial x_j} + \tilde{u}_j \frac{\partial \bar{u}_i}{\partial x_j}$$

$$= - \frac{\partial \tilde{p}}{\partial x_i} + \frac{1}{Re} \cdot \frac{\partial^2 \tilde{u}_i}{\partial x_j \partial x_j} - \frac{\partial}{\partial x_j} (\widetilde{\tilde{u}_i \tilde{u}_j}) - \frac{\partial}{\partial x_j} (\widetilde{u_i' u_j'}) \qquad (2.20)$$

Now, (2.19) and (2.20) describe the motion of the wave perturbation fields which are of main interest in this study. In (2.20) the quantities

$$\widetilde{\tilde{u}_i \tilde{u}_j} = \langle \tilde{u}_i \tilde{u}_j \rangle - \overline{\tilde{u}_i \tilde{u}_j} = \tilde{u}_i \tilde{u}_j - \overline{\tilde{u}_i \tilde{u}_j} \qquad (2.21a)$$

are quadratic and are usually discarded in the linear analysis (we discarded them here). The term $\widetilde{u_i' u_j'}$, the main stumbling block in the closure problem, is given by

$$\widetilde{u_i' u_j'} = \langle u_i' u_j' \rangle - \overline{u_i' u_j'} \quad , \qquad (2.21b)$$

and is also specially denoted as $\tilde{r}_{ij}$ in the report of Hussain and Reynolds (1970). To avoid confusion, we will also use the same notation; (2.20) then can be read as

$$\frac{\partial \tilde{u}_i}{\partial t} + \bar{u}_j \frac{\partial \tilde{u}_i}{\partial x_j} + \tilde{u}_j \frac{\partial \bar{u}_i}{\partial x_j} = - \frac{\partial \tilde{p}}{\partial x_i} + \frac{1}{Re} \frac{\partial^2 \tilde{u}_i}{\partial x_j \partial x_j} - \frac{\partial \tilde{r}_{ij}}{\partial x_j} \qquad (2.22)$$

The coordinates x_i are $x_1 = x$ in the direction of the wave propagation, $x_2 = y$ in the vertical direction upwards and normal to the mean water level, and $x_3 = z$ in the lateral direction parallel to the wave front. The air flows in the x direction, and the resulting channel flow is assumed fully developed or nearly fully developed so that the mean

flow can be regarded as parallel. The wave perturbations are also assumed two dimensional (x, y). Under these assumptions, the velocity u_i is expressed as

$$u_i = (U(y) + \tilde{u}(x, y, t) + u' , \quad \tilde{v}(x, y, t) + v', w') \tag{2.23}$$

and the pressure perturbation $\tilde{p}$ is a function of x, y, and t only. Equations (2.19) and (2.22) are then reduced to simple forms and are written explicitly as

$$\frac{\partial \tilde{u}}{\partial x} + \frac{\partial \tilde{v}}{\partial y} = 0 \tag{2.24}$$

$$\frac{\partial \tilde{u}}{\partial t} + U\frac{\partial \tilde{u}}{\partial x} + \tilde{v}\frac{\partial U}{\partial y} = -\frac{\partial \tilde{p}}{\partial x} + \frac{1}{Re}\left(\frac{\partial^2 \tilde{u}}{\partial x^2} + \frac{\partial^2 \tilde{u}}{\partial y^2}\right) - \frac{\partial \tilde{r}_{11}}{\partial x} - \frac{\partial \tilde{r}_{12}}{\partial y} \tag{2.25}$$

$$\frac{\partial \tilde{v}}{\partial t} + U\frac{\partial \tilde{v}}{\partial x} = -\frac{\partial \tilde{p}}{\partial y} + \frac{1}{Re}\left(\frac{\partial^2 \tilde{v}}{\partial x^2} + \frac{\partial^2 \tilde{v}}{\partial y^2}\right) - \frac{\partial \tilde{r}_{12}}{\partial x} - \frac{\partial \tilde{r}_{22}}{\partial y} \tag{2.26}$$

Since there are only three equations with six unknowns $\tilde{u}$, $\tilde{v}$, $\tilde{p}$, $\tilde{r}_{11}$, $\tilde{r}_{12}$, and $\tilde{r}_{22}$, proper closure relations for $\tilde{r}_{ij}$ and suitable boundary conditions for $\tilde{u}$, $\tilde{v}$, $\tilde{p}$, and $\tilde{r}_{ij}$ are required in solving the system of equations. The quasilaminar model is obtained by putting $\tilde{r}_{ij} = 0$. Furthermore, neglecting the viscous effect by asumptotically letting $Re \to \infty$ wili yield the well-known inviscid model of Miles (1957). Models with non-zero $\tilde{r}_{ij}$ are generally referred to as turbulent models.

2.4 Expressions for Travelling Waves

The displacement $\tilde{\eta}$ of the water surface from its mean equilibrium position is assumed sinusoidal with a travelling wave property, and is expressed as

$$\tilde{\eta}(x,t) = a \cdot \cos(kx-\omega t) \tag{2.27a}$$

$$= \frac{1}{2} \cdot [a \cdot e^{i(kx-\omega t)} + \text{conjugate}] \tag{2.27b}$$

where a is the wave amplitude,

$$k \text{ is the wave number} = 2\pi/L , \tag{2.28a}$$

$$\omega \text{ is the circular frequency} = 2\pi f = 2\pi/\tau , \tag{2.28b}$$

and L, f, and τ are wave length, wave frequency (Hz) and wave period respectively. When the wave amplitude is finite, the non-linear effect on the water wave usually produces harmonic modes resulting in a non-sinusoidal wave form called "Stokes waves". (Lamb 1932, art. 250). In (2.27a) the small amplitude assumption, $ka << 1$, is invoked so that the Stokesian harmonic modes are neglected.

Since the air flow perturbations are associated with the water surface displacement, $\tilde{\eta}$ is used as a reference signal to estimate the phase lags of other wave quantities. Accordingly, the origins of x and t in (2.27a) are properly selected to give $\tilde{\eta}$ a zero phase. When $\tilde{\eta}$ is given by (2.27a), the velocity perturbations are then represented by

$$\tilde{u}_i(x,y,t) = |\hat{u}_i(y)| \cdot \cos(kx - \omega t + \theta_{\tilde{u}_i}) + \text{harmonics} \tag{2.29}$$

where $|\hat{u}_i|$ and $\theta_{\tilde{u}_i}$ are the amplitude and the phase lag angle with respect to time of the fundamental mode of $\tilde{u}_i$. The harmonics in (2.29) are now primarily produced from the non-linear effect described by the convective terms in the Navier-Stokes equations. We have assumed that the wave perturbations are small such that $|\hat{u}_i|/U << 1$; hence, the harmonics in (2.29) are again negligible because they are of higher order in $|\hat{u}_i|/U$. This negligibility of harmonics also applies to other wave perturbation quantities, such as $\tilde{p}$ and $\tilde{r}_{ij}$, so that the linear analysis is feasible. The wave perturbations are then generally denoted by

$$\tilde{g}(x, y, t) = |\hat{g}(y)| \cdot \cos(kx - \omega t + \theta_{\tilde{g}}) \tag{2.30}$$

$$= \frac{1}{2}[\hat{g}(y) \cdot e^{i(kx-\omega t)} + \text{conjugate}] \tag{2.31}$$

where $\hat{g}(y)$ is regarded as a complex number, $A_{\tilde{g}} + iB_{\tilde{g}}$,

$$|\hat{g}(y)| \text{ is the amplitude } = (A_{\tilde{g}}^2 + B_{\tilde{g}}^2)^{1/2}, \tag{2.32}$$

and $\theta_{\tilde{g}}$ is the phase lag of $\tilde{g}$ with respect to $\tilde{\eta}$, $\theta_{\tilde{g}} = \tan^{-1}\left(\frac{B_{\tilde{g}}}{A_{\tilde{g}}}\right)$ (2.33)

Substituting (2.31) into (2.24), (2.25) and (2.26) and denoting $\frac{d}{dy}$ by D and $\frac{\omega}{k}$ by c, the wave celerity, we have

$$ik\hat{u} + D\hat{v} = 0, \tag{2.34}$$

$$ik(U-c)\hat{u} + (DU)\hat{v} = -ik\hat{p} + \frac{1}{Re}(D^2-k^2)\hat{u} - ik\hat{r}_{11} - D\hat{r}_{12}, \tag{2.35}$$

$$ik(U-c)\hat{v} = -D\hat{p} + \frac{1}{Re}(D^2-k^2)\hat{v} - ik\hat{r}_{12} - D\hat{r}_{22}. \tag{2.36}$$

The wave stream function $\tilde{\phi}(x, y, t)$ is defined as

$$\tilde{u} = \frac{\partial\tilde{\phi}}{\partial y}, \quad \tilde{v} = -\frac{\partial\tilde{\phi}}{\partial x} \tag{2.37a,b}$$

so that the continuity equation (2.24) is automatically satisfied. In terms of the wave expression, (2.37a,b) change to

$$\hat{u} = D\hat{\phi}, \quad \hat{v} = -ik\hat{\phi} \quad . \tag{2.38a,b}$$

Introducing (2.38a,b) into (2.35) and (2.36) and eliminating $\hat{p}$ from the resulting equations, we obtain

$$k[(U-c)\cdot(D^2-k^2) - D^2U]\hat{\phi} = -\frac{i}{Re}(D^2-k^2)^2\hat{\phi} - kD(\hat{r}_{11}-\hat{r}_{22}) + i(D^2+k^2)\hat{r}_{12} \qquad (2.39)$$

When $\hat{r}_{ij} = 0$, (2.39) reduces to the Orr-Sommerfeld equation usually encountered in the theory of hydrodynamic stability.

2.5 Boundary Conditions

For channel flow the no slip condition at the roof gives $\tilde{u} = \tilde{v} = 0$. Hence,

$$\left.\begin{aligned}\hat{\phi} &= 0\\ D\hat{\phi} &= 0\end{aligned}\right\} \quad \text{at} \quad y = H \qquad (2.40a,b)$$

When the channel height H of the air flow portion is sufficiently large, the no slip condition at the roof is automatically replaced by the exponentially decaying property of the wave perturbations which also results in $\tilde{u} = \tilde{v} = 0$ as $y \to \infty$. The value H in (2.40a,b) is now normalized by the boundary layer thickness δ so that (2.40a,b) can describe the upper boundary conditions for flows with either finite or infinite heights. Thus, $H = 2$ when the channel flow is fully developed.

At the interface, the high ratio of water density to air density and the surface tension effect prevent mixing between the air and the water when the air velocity is not too high, as considered in the present investigation. The no slip condition also applies, i.e., the air molecules adhere to those of interface water, which is moving with a circular-orbit due to the deep water wave motion and with a velocity in the downstream direction due to the drift current. The drift current consists of the wave-associated drift current and the wind-induced drift current which usually is predominant. The interaction between the water wave

and the drift current is assumed to be weak so that the linear and orbital motions are regarded as independent and superposable. Accordingly, the interface boundary conditions are given by

$$\left.\begin{aligned} \tilde{v} &= \frac{\partial \tilde{\eta}}{\partial t} + U \frac{\partial \tilde{\eta}}{\partial x} \\ \tilde{u} &= kc\,\tilde{\eta} \end{aligned}\right\} \quad \text{at } y = \tilde{\eta} \qquad (2.41a,b)$$

In terms of the wave expression, (2.41a,b) are

$$\left.\begin{aligned} \hat{\phi} &= (c-U)a \\ D\hat{\phi} &= cka \end{aligned}\right\} \quad \text{at } y = \tilde{\eta} \qquad (2.42a,b)$$

The dependence of the interface boundary conditions on $\tilde{\eta}$ has profoundly handicapped the theoretical treatment of the problem. To circumvent this handicap, either of the following procedures is necessary:

(1) Transformation of the boundary conditions from $y = \tilde{\eta}$ to the mean water level $y = 0$. (Miles 1957; Davis 1970, 1972; Townsend 1972)

(2) Transformation of the entire problem into a new coordinate system such that both the upper and the lower boundaries are fixed relative to the new coordinates. (Miles 1959, Benjamin 1959, Norris and Reynolds 1975, Gent and Taylor 1976)

The second procedure is chosen in the present study because it leads to less ambiguity.

2.6 Transformation into Moving Coordinates

The difficulty of the interface boundary conditions is overcome by using the following coordinate transformation,

$$\begin{cases} t^* = t \\ x^* = x \\ y^* = y - f(y^*) \cdot \tilde{\eta} \end{cases} \qquad (2.43a,b,c)$$

The function $f(y^*)$ is defined such that

$$f(0) = 1 \qquad \text{and} \qquad f(H) = 0 \qquad (2.44a,b)$$

The expression,

$$f(y^*) = \frac{\sinh(kH - ky^*)}{\sinh(kH)} \qquad (2.45)$$

satisfies the requirements (2.44a,b) and results in an exponentially-decaying form which resembles that used by Benjamin (1959) when $H \to \infty$. The coordinate transformation given above is one to one but is not orthogonal. Figure 2.2 shows the lines of constant y^* in physical space.

For some quantity g of interest, we have, from the chain rule for partial derivatives,

$$\frac{\partial g}{\partial s} = \frac{\partial g}{\partial t^*}\frac{\partial t^*}{\partial s} + \frac{\partial g}{\partial x^*}\cdot\frac{\partial x^*}{\partial s} + \frac{\partial g}{\partial y^*}\cdot\frac{\partial y^*}{\partial s} \qquad (2.46)$$

where s can be t, x, or y. The values of $\frac{\partial t^*}{\partial s}$, $\frac{\partial x^*}{\partial s}$, and $\frac{\partial y^*}{\partial s}$ are found from the transformation relations (2.43a,b,c). The result expressions are

$$\frac{\partial g}{\partial t} = \frac{\partial g}{\partial t^*} - f\cdot\frac{\partial \tilde{\eta}}{\partial t}\cdot\frac{\partial g}{\partial y^*} \qquad (2.47a)$$

$$\frac{\partial g}{\partial x} = \frac{\partial g}{\partial x^*} - f\cdot\frac{\partial \tilde{\eta}}{\partial x}\cdot\frac{\partial g}{\partial y^*} \qquad (2.47b)$$

$$\frac{\partial g}{\partial y} = \frac{\partial g}{\partial y^*} \Big/ \left(1 + \frac{\partial f}{\partial y^*} \cdot \tilde{\eta}\right) \tag{2.47c}$$

$$\frac{\partial^2 g}{\partial x^2} = \frac{\partial^2 g}{\partial x^{*2}} - f \cdot \frac{\partial^2 \tilde{\eta}}{\partial x^2} \cdot \frac{\partial g}{\partial y^*} - 2f \cdot \frac{\partial \tilde{\eta}}{\partial x} \cdot \frac{\partial^2 g}{\partial x^* \partial y^*}$$

$$+ f \cdot \left(\frac{\partial \tilde{\eta}}{\partial x}\right)^2 \frac{\partial}{\partial y^*}\left(f \frac{\partial g}{\partial y^*}\right) \tag{2.47d}$$

$$\frac{\partial^2 g}{\partial y^2} = \frac{\partial^2 g}{\partial y^{*2}} \Big/ \left(1 + \frac{\partial f}{\partial y^*} \cdot \tilde{\eta}\right)^2 - \frac{\partial g}{\partial y^*} \cdot \frac{\partial^2 f}{\partial y^{*2}} \cdot \tilde{\eta} \Big/ \left(1 + \frac{\partial^2 f}{\partial y^{*2}} \cdot \tilde{\eta}\right)^3 \tag{2.47e}$$

Before transforming the governing equations of flow motions, it is now assumed that, in the new (x*, y*, t*) coordinate system, the mean flow follows lines of constant y*, the wave perturbations are two dimensional and function of x*, y*, and t* only, and the linear analysis is still valid. Applying (2.47a, b, c, d, e) to the Navier-Stokes equations (2.13) and (2.14), substituting the three-component decompositions generally given by $g = G + \tilde{g} + g'$ into the resulting equations (G is the time average), taking the time averages, and discarding the terms with $O(\tilde{\eta}^2)$ or higher yields the mean flow equations, in the (x*, y*, t*) system,

$$-\frac{\partial P}{\partial x^*} + \frac{\partial}{\partial y^*}\left(\frac{1}{Re} \cdot \frac{\partial U}{\partial y^*} - \overline{u'v'}\right) = 0 \tag{2.48}$$

$$-\frac{\partial P}{\partial y^*} = \frac{\partial}{\partial y^*}\left(\overline{v'v'}\right) \tag{2.49}$$

Equations (2.48) and (2.49) are identical to the mean flow equations in the (x, y, t) system; however, the physical interpretations are different because of the different assumptions made and the different physical (geometrical) positions where the mean quantities are evaluated. Equation (2.49) suggests that the mean-pressure gradient in the x* direction is constant, i.e., $\frac{\partial P}{\partial x^*}$ = constant. (See similar discussion in Section 3.3b.)

If the phase averages are taken before the time averages, the difference between the phase averaged and the time averaged equations gives the wave perturbation equations:

Continuity Equation:

$$\frac{\partial \tilde{u}}{\partial x^*} - f \cdot \frac{\partial \tilde{\eta}}{\partial x} \cdot \frac{\partial U}{\partial y^*} + \frac{\partial \tilde{v}}{\partial y^*} = 0 \,. \tag{2.50}$$

x-Momentum Equation:

$$\begin{aligned} &\frac{\partial \tilde{u}}{\partial t^*} - f \cdot \frac{\partial \tilde{\eta}}{\partial t} \cdot \frac{\partial U}{\partial y^*} + U \cdot \left(\frac{\partial \tilde{u}}{\partial x^*} - f \cdot \frac{\partial \tilde{\eta}}{\partial x} \cdot \frac{\partial U}{\partial y^*} \right) + \tilde{v} \cdot \frac{\partial U}{\partial y^*} \\ &+ \frac{\partial}{\partial x^*} \tilde{r}_{11} - f \cdot \frac{\partial \tilde{\eta}}{\partial x} \cdot \frac{\partial}{\partial y^*} (\overline{u'u'}) + \frac{\partial}{\partial y^*} \tilde{r}_{12} - \frac{\partial f}{\partial y^*} \cdot \tilde{\eta} \cdot \frac{\partial}{\partial y^*} (\overline{u'v'}) \\ &= - \frac{\partial \tilde{p}}{\partial x^*} + f \cdot \frac{\partial \tilde{\eta}}{\partial x} \cdot \frac{\partial P}{\partial y^*} + \frac{1}{Re} \left[\frac{\partial^2 \tilde{u}}{\partial x^{*2}} - f \cdot \frac{\partial^2 \tilde{\eta}}{\partial x^2} \cdot \frac{\partial U}{\partial y^*} + \frac{\partial^2 \tilde{u}}{\partial y^{*2}} \right. \\ &\qquad \left. - 2 \cdot \frac{\partial f}{\partial y^*} \cdot \tilde{\eta} \cdot \frac{\partial^2 U}{\partial y^{*2}} - \frac{\partial^2 f}{\partial y^{*2}} \cdot \tilde{\eta} \cdot \frac{\partial U}{\partial y^*} \right] \end{aligned} \tag{2.51}$$

y-Momentum Equation:

$$\begin{aligned} &\frac{\partial \tilde{v}}{\partial t^*} + U \cdot \frac{\partial \tilde{v}}{\partial x^*} + \frac{\partial \tilde{r}_{12}}{\partial x^*} - f \cdot \frac{\partial \tilde{\eta}}{\partial x} \cdot \frac{\partial}{\partial y^*} (\overline{u'v'}) + \frac{\partial \tilde{r}_{22}}{\partial y^*} - \frac{\partial f}{\partial y^*} \cdot \tilde{\eta} \cdot \frac{\partial}{\partial y^*} (\overline{v'v'}) \\ &= - \frac{\partial \tilde{p}}{\partial y^*} + \frac{\partial f}{\partial y^*} \cdot \tilde{\eta} \cdot \frac{\partial P}{\partial y^*} + \frac{1}{Re} \cdot \left[\frac{\partial^2 \tilde{v}}{\partial x^{*2}} + \frac{\partial^2 \tilde{v}}{\partial y^{*2}} \right] \end{aligned} \tag{2.52}$$

In (2.50), (2.51) and (2.52), the terms with $\tilde{\eta}$ are inhomogeneous terms because they are known quantities when the mean flow and the water wave are predescribed. Equations (2.50), (2.51), and (2.52) are essentially equivalent to those used by Norris and Reynolds (1975). The

appearance of the inhomogeneous terms in these equations has complicated computations employing them. To simplify these equations, the physics of the flow in the transformed coordinate system was reexamined.

When the control volume shown in Fig. 2.3 was considered, the continuity equation obtained by balancing the inflow and outflow is

$$(1 + \frac{\partial f}{\partial y^*} \cdot \tilde{\eta}) \cdot \frac{\partial u}{\partial x^*} + \frac{\partial v}{\partial y^*} - \frac{\partial u}{\partial y^*} \cdot f \cdot \frac{\partial \tilde{\eta}}{\partial x^*} + \frac{\partial w}{\partial z} = 0 . \qquad (2.53)$$

The term $\frac{\partial w}{\partial z}$ in (2.53) is the net flow rate in z-direction and was not shown in Fig. 2.3. The negative term in (2.53) is produced by the horizontal flow crossing the upper and lower boundaries of the control volume. If the decompositions given in (2.23) are substituted into (2.53) and the components of organized oscillations are extracted, we have an equation which is identical to (2.50). This control volume analysis shows that the negative inhomogeneous term in (2.50) comes from the negative term in (2.53). This inhomogeneous term is consequently the result of the non-orthogonality of the (x*, y*, t*) system which does not align with the orthogonal u, v components. However, if the inhomogeneous term is combined with the homogeneous term to result in the following transformations,

$$\tilde{u}^* = \tilde{u} - f \cdot \tilde{\eta} \cdot \frac{\partial U}{\partial y^*} , \qquad \tilde{v}^* = \tilde{v} \qquad (2.54a,b)$$

then (2.50) reduces to

$$\frac{\partial \tilde{u}^*}{\partial x^*} + \frac{\partial \tilde{v}^*}{\partial y^*} = 0 . \qquad (2.55)$$

Equation (2.55) indicates that the transformed velocities $\tilde{u}^*$, $\tilde{v}^*$ in the x*, y* coordinate system satisfy the identical continuity equation as $\tilde{u}$, $\tilde{v}$ in a Cartesian coordinate system. Transformations similar to

(2.54a,b) for $\tilde{p}$ and $\tilde{r}_{ij}$ are found to be

$$\tilde{p}^* = \tilde{p} - f \cdot \tilde{\eta} \cdot \frac{\partial P}{\partial y^*} \tag{2.56}$$

$$\tilde{r}^*_{ij} = \tilde{r}_{ij} - f \cdot \tilde{\eta} \cdot \frac{\partial}{\partial y^*}(\overline{u'_i u'_j}) \tag{2.57}$$

Using (2.48) and (2.49) and applying the transformations (2.54), (2.56) and (2.57), equations (2.51) and (2.52) then reduce to

$$\frac{\partial \tilde{u}^*}{\partial t^*} + U \cdot \frac{\partial \tilde{u}^*}{\partial x^*} + \tilde{v}^* \frac{\partial U}{\partial y^*} = - \frac{\partial \tilde{p}^*}{\partial x^*} + \frac{1}{Re}\left(\frac{\partial^2 \tilde{u}^*}{\partial x^{*2}} + \frac{\partial^2 \tilde{u}^*}{\partial y^{*2}}\right) - \frac{\partial \tilde{r}^*_{11}}{\partial x^*} - \frac{\partial \tilde{r}^*_{12}}{\partial y^*} \tag{2.58}$$

$$\frac{\partial \tilde{v}^*}{\partial t^*} + U \cdot \frac{\partial \tilde{v}^*}{\partial x^*} = - \frac{\partial \tilde{p}^*}{\partial y^*} + \frac{1}{Re}\left(\frac{\partial^2 \tilde{v}^*}{\partial x^{*2}} + \frac{\partial^2 \tilde{v}^*}{\partial y^{*2}}\right) - \frac{\partial \tilde{r}^*_{12}}{\partial x^*} - \frac{\partial \tilde{r}^*_{22}}{\partial y^*} \tag{2.59}$$

A transformed stream function $\tilde{\phi}^*$ can be similarly defined (cf., (2.37a,b)) to combine (2.58) and (2.59) into an equation which is identical to (2.39) except D is replaced by $D^* = \frac{d}{dy^*}$, i.e., the transformed stream function is defined as

$$\tilde{u}^* = \frac{\partial \tilde{\phi}^*}{\partial y^*}, \qquad \tilde{v}^* = - \frac{\partial \tilde{\phi}^*}{\partial x^*} \tag{2.60a,b}$$

and the combined equation in terms of the wave expression is

$$k \cdot [(U-c) \cdot (D^{*2} - k^2) - D^{*2} U] \hat{\phi}^* = - \frac{i}{Re}(D^{*2} - k^2)^2 \hat{\phi}^* - kD^*(\hat{r}^*_{11} - \hat{r}^*_{22}) + i(D^{*2} + k^2)\hat{r}^*_{12} \tag{2.61}$$

Equations (2.55), (2.58), (2.59) and (2.61) have the identical forms as equations (2.24), (2.25), (2.26) and (2.39), respectively. So, $\tilde{u}^*$, $\tilde{v}^*$, $\tilde{p}^*$ and $\tilde{r}^*_{ij}$ in the x*, y* coordinate system are equivalent to $\tilde{u}$, $\tilde{v}$, $\tilde{p}$ and $\tilde{r}_{ij}$ in the rectangular Cartesian coordinate system. Details of this are presented in Chapter 6.

The transformation of the wave perturbation fields implies, at the same time, the transformation of the interface boundary conditions. Using (2.54a,b) and (2.60a,b), the boundary conditions are now transformed into

$$\left.\begin{aligned} \hat{\phi}^* &= 0 \\ D^*\hat{\phi}^* &= 0 \end{aligned}\right\} \quad \text{at } y^* = H \qquad (2.62a,b)$$

and

$$\left.\begin{aligned} \hat{\phi}^* &= (c-U)a \\ D^*\hat{\phi}^* &= cka - aD^*U \end{aligned}\right\} \quad \text{at } y^* = 0\,. \qquad (2.63a,b)$$

Equations (2.62a,b) and (2.63a,b) are the same forms as those boundary conditions obtained by the transformation of the boundary conditions using procedure 1 mentioned in Section 2.5 for the untransformed coordinate system. (See Saeger and Reynolds 1971, p. 13.)

Because $\hat{\phi}^*(y^*)$ in the (x*, y*, t*) system has the identical forms of governing equation and boundary conditions as those for $\hat{\phi}(y)$ in the (x, y, t) system, the same results should be obtained for $\hat{\phi}^*(y^*)$ and $\hat{\phi}(y)$ if the same mean velocity profile and the same closure relations are used in the model calculations. Consequently, the numerical results of $\tilde{u}^*$, $\tilde{v}^*$, $\tilde{p}^*$, and $\tilde{r}^*_{ij}$ in the (x*, y*, t*) system will be identical to those of $\tilde{u}$, $\tilde{v}$, $\tilde{p}$, and $\tilde{r}_{ij}$ in the (x, y, t) system. However, the physical interpretations of these two sets of predicted quantities are different. First, when the same mean velocity profile is used, U is assumed to be parallel to x in the (x, y, t) system so that the mean velocity is

constant along a horizontal line of constant y; but, in the (x^*, y^*, t^*) system, U is still the Cartesian horizontal mean velocity but is constant along an undulating curve where y^* is constant. Similarly, when the same forms of closure relations are used, the flow properties associated with the closure relations in the (x^*, y^*, t^*) system are regarded to be dependent on the measuring height y^* above the instantaneous wave surface; however, in the (x, y, t) system, those flow properties are regarded to be dependent on the height y above the mean water level.

Secondly, in the (x, y, t) system, the velocities $\tilde{u}(x, y, t)$ and $\tilde{v}(x, y, t)$ are Cartesian velocities which describe the actual oscillations of air particles around the mean velocity U(y) and are evaluated at fixed elevation y; but, in the (x^*, y^*, t^*) system, although $\tilde{u}(x^*, y^*, t^*)$ and $\tilde{v}(x^*, y^*, t^*)$ are also Cartesian velocities, they describe the actual air particle oscillations around the mean velocity $U(y^*)$ and are evaluated at constant y^*. The velocities $\tilde{u}^*(x^*, y^*, t^*)$ and $\tilde{v}^*(x^*, y^*, t^*)$ are related to $\tilde{u}(x^*, y^*, t^*)$ and $\tilde{v}(x^*, y^*, t^*)$ through the transformation defined in (2.54a,b). Little physical interpretations can be made from $\tilde{u}^*$ and $\tilde{v}^*$ because $\tilde{u}^*$ and $\tilde{v}^*$ do not describe the actual oscillations of air particles. These arguments also apply to other wave perturbation quantities such as the induced pressure wave and the induced turbulent Reynolds stresses.

Thirdly, the interface boundary conditions for the (x, y, t) system are obtained by transforming the boundary conditions from $y = \tilde{\eta}$ to $y = 0$ using the Taylor series expansion. This extrapolation from $y = \tilde{\eta}$ to $y = 0$ is very ambiguous when $\tilde{\eta} > 0$ such that $y = 0$ is below the water surface where no air flow exists. (See more insights to this point in Section 6.2.) On the other hand, the interface boundary conditions (2.63a,b) are obtained by transforming the wave perturbation velocities $\tilde{u}(x^*, y^*, t^*)$ and $\tilde{v}(x^*, y^*, t^*)$ to $\tilde{u}^*(x^*, y^*, t^*)$ and $\tilde{v}^*(x^*, y^*, t^*)$ so that the boundary conditions are still described exactly at the interface by (2.63a,b). It should be emphasized that the transformation of

boundary conditions by Taylor series expansion is only valid for infinitesimal waves. For small amplitude waves, the series expansion method is usually not valid when the wind speed is high, because the wave amplitude is not small relative to the thickness of the air flow diffusion layer where the mean velocity varies drastically within a distance much less than the wave amplitude. This is a substantial limitation to the application of the extrapolation scheme which employs the series expansion. In the (x^*, y^*, t^*) system, the boundary conditions obtained by the wave perturbation field transformation do not have this limitation and apply more generally to small amplitude waves. It is seen that the ambiguity about the physical meanings of flow quantities near the interface (below the wave crests) is the common disadvantage in using the fixed coordinate system. (See the detailed discussion in Section 6.2.)

In the (x^*, y^*, t^*) system, once the closure relations for $\tilde{r}_{ij}$ (x^*, y^*, t^*) are specified, (2.57) can be used to obtain the closure relations for $\tilde{r}^*_{ij}$. The boundary conditions for $\tilde{r}^*_{ij}$ can be obtained in the same way after describing the boundary conditions for $\tilde{r}_{ij}(x^*, y^*, t^*)$. The quantities $\tilde{u}^*$, $\tilde{v}^*$, $\tilde{p}^*$, $\tilde{r}^*_{ij}$, and $\tilde{\phi}^*$ then can be calculated from the equations (2.59), (2.60a,b) and 2.61), closure relations, and their boundary conditions. Consequently, $\tilde{u}$, $\tilde{v}$, $\tilde{p}$, and $\tilde{r}_{ij}$ in (x^*, y^*, t^*) can be evaluated from (2.54a,b), (2.56) and (2.57). It should be emphasized that the wave perturbation data measured in the fixed coordinate system are not comparable to the quantities so predicted because of the differences in the physical interpretations between flow quantities in the (x^*, y^*, t^*) and the (x, y, t) systems as mentioned above. (Actually the measured and predicted results at the fixed wall of the channel are still comparable because there the wave perturbation quantities are independent of the coordinate systems used.)

According to (2.57), a homogeneous closure model for $\tilde{r}_{ij}$ in (x^*, y^*, t^*) will result in an inhomogeneous closure model for $\tilde{r}^*_{ij}$. A

quasilaminar model with $\tilde{r}_{ij}(x^*, y^*, t^*) = 0$ in the (x^*, y^*, t^*) system should predict $\tilde{u}^*$, $\tilde{v}^*$, and $\tilde{p}^*$ to have the same values as $\tilde{u}$, $\tilde{v}$, and $\tilde{p}$ predicted by the model using the inhomogeneous closure relations given by $\tilde{r}_{ij}(x, y, t) = f \cdot \tilde{\eta} \cdot \frac{\partial}{\partial y} \overline{u_i' u_j'}$ in the (x, y, t) system. The transformed coordinate quasilaminar model of Norris and Reynolds (1975), which predicted satisfactorily the pressure wave perturbations, implied the use of the closure relations

$$\tilde{r}^*_{11} = 0 \,, \quad \frac{\partial \tilde{r}^*_{12}}{\partial y^*} = - f \cdot \tilde{\eta} \cdot \frac{1}{Re} \cdot \frac{\partial^3 U}{\partial y^{*3}} \,, \quad \tilde{r}^*_{22} = 0 \qquad (2.64a,b,c)$$

Hence, if one uses (2.64a,b,c) with *'s dropped for the (x, y, t) system the satisfactory prediction of the pressure wave perturbations should be obtained, because Norris and Reynolds compared their predicted and measured pressure waves at the fixed wall of their channel. The closure model in the fixed (x, y, t) system proposed by Norris and Reynolds (1975), which yielded poor predictions of the induced pressure waves, did not have the inhomogeneous feature. One may anticipate that the model predictions in the fixed coordinate system can be improved by including some inhomogeneous terms in the closure relations; however, the limitation of the boundary condition transformation by Taylor series expansion still exists and tends to disconnect the predicted results from the data measured in the fixed coordinate system. Hence, one may conclude that the transformation of the coordinate system and of the wave perturbation fields instead of just the simple extrapolation of the interface boundary conditions is essential in resolving the air flow structure of interface flows.

Because there has been no data available in the transformed coordinate system, the present investigation is largely devoted to collecting reliable data of wave perturbation fields in the (x^*, y^*, t^*) system rather than attempting to calculate a closure model. Since $\tilde{r}^*_{ij}$

does not possess too much physical meaning as mentioned above, the closure model should be directly addressed to $\widetilde{r}_{ij}(x^*, y^*, t^*)$. Measurements of $\widetilde{u}$, $\widetilde{v}$, and $\widetilde{r}_{ij}$ in (x^*, y^*, t^*) may not only provide the details of the air interface flow structure but also reveal some clues for closure modelling by subsequent investigators. The details of the experiments are presented in Chapter 4, and the results of the experiments in Chapter 5.

CHAPTER 3

DYNAMICS OF MODULATED AIR FLOW OVER WATER SURFACE WAVES

3.1 General

In order to characterize the response of wave perturbations due to the unsteadiness of the air flow, air modulations were introduced into the wind-wave channel by changing the flow exit area of the channel periodically. The channel and the air modulation generation technique will be described in Chapter 4. However, some basic characteristics of the air modulation are discussed in this chapter, together with its interaction with the water surface waves. In general, the air modulation has a pulsating and a non-dispersive behavior and has a very long wave length so that its wave number can be regarded as zero when its frequency is low.

Characteristics of air modulation in a two dimensional channel with flat-plate walls were studied in detail by Acharya and Reynolds (1975). The frequencies of the air modulations in their study were 24 and 40 Hz. The interesting phenomena of air modulation in a channel flow is the existence of a viscous layer called a "Stokes layer" near the channel boundary. For turbulent channel flow, the experimental results of Acharya and Reynolds (1975) showed that the behavior of the Stokes layer is very different from that in a laminar flow due to the strong mixing effect of the background turbulence. In their study, the turbulent Reynolds stresses perturbed by air modulation were found to be out of phase with the strain-rates, indicating a viscoelastic type of response. Air modulations in a wind-wave channel at low frequencies (0.21, 0.44, and 0.77 Hz) were also studied by Wu (1973) to resolve the air modulation effect on the wind-generated waves. The results of Wu's study were: (a) the air modulations were important to wind and wave structure, when the regime of the air boundary layer was affected, and (b),

when the air boundary layer was aerodynamically rough, the air modulation effects on the wind structure were secondary but more capillary water waves were produced. In Wu's study, the air modulation effect on the wind fields was inferred from wind-stress coefficient calculations based on mean flow measurements; no details of air modulation structure were reported.

Studying flows with air modulation over mechanically-generated water waves has been one of the most important tasks in the present study. Results of this study not only provide the detailed structure of the air modulation in the interface flow, but also reveal dynamic features of the interaction between the air modulations and the water surface waves. The effects of air modulation on the wave perturbation fields can also be resolved. The theoretical aspects of the air modulation and of its interaction with the water waves are presented in this chapter. Experimental procedures, data reduction schemes and the experimental results are presented in the subsequent chapters.

3.2 Description of the Flow

When an air modulation is imposed in the flow regime, the flow fields are generally expressed as

$$g = \bar{g} + \tilde{g} + \tilde{g}_a + \tilde{g}_+ + \tilde{g}_- + g' \qquad (3.1)$$

where $\tilde{g}_a$ represents the air modulation component and $\tilde{g}_+$ and $\tilde{g}_-$ are the wave components produced from the interaction between the air modulation $\tilde{g}_a$ and the wave perturbation $\tilde{g}$. The wave representations for $\tilde{g}_a$, $\tilde{g}_+$ and $\tilde{g}_-$ are very similar to that for $\tilde{g}$ as in (2.31), and can be expressed as

$$\tilde{g}_a = \frac{1}{2} \cdot [\hat{g}_a(y)\, e^{-i\omega_a t} + \text{conjugate}] \qquad (3.2)$$

$$\tilde{g}_s = \frac{1}{2} \cdot [\hat{g}_s(y)\, e^{i(kx-\omega_s t)} + \text{conjugate}] \qquad (3.3)$$

where $\omega_s = \omega + s\omega_a$ with $s = \pm$ and ω and ω_a are the frequencies of water wave and air modulation respectively. The phase average of g is denoted by $\langle g \rangle_\alpha$ where the subscript α can be null, a, or s to indicate the wave perturbations, the air modulations, or the interaction-produced waves respectively. The period used in the phase average of the corresponding waves is $\tau_\alpha = 2\pi / |\omega_\alpha|$. The wave component $\tilde{g}_\alpha$ is defined as

$$\tilde{g}_\alpha = \langle g \rangle_\alpha - \bar{g} \qquad (3.4)$$

When the phase average $\langle g \rangle_\alpha$ is subtracted from the total flow quantity g as expressed in (3.1), the remaining flow component may be regarded as a background oscillation g''_α around $\langle g \rangle_\alpha$ and is expressed as

$$g''_\alpha = g - \langle g \rangle_\alpha \qquad (3.5)$$

Consequently, the decomposition expression

$$g = \bar{g} + \tilde{g}_\alpha + g''_\alpha \qquad (3.6)$$

is feasible. If $\tilde{g}$ is of order ϵ and $\tilde{g}_a$ is of order ϵ_a, $\tilde{g}_s$ is of order $\epsilon\epsilon_a$ because $\tilde{g}_s$ is produced from the coupling between $\tilde{g}$ and $\tilde{g}_a$.

3.3 Governing Equations

Decomposing u, v, and p in the Navier-Stokes equations into the form of (3.6), taking the phase average $\langle\ \rangle_\alpha$ and the time average separately, subtracting the time averaged equations from the phase averaged equations and neglecting non-linear terms in the resulting equations, we have the continuity equation,

$$\frac{\partial \tilde{u}_\alpha}{\partial x} + \frac{\partial \tilde{v}_\alpha}{\partial y} = 0 , \tag{3.7}$$

the x-momentum equation,

$$\frac{\partial \tilde{u}_\alpha}{\partial t} + U \frac{\partial \tilde{u}_\alpha}{\partial x} + \tilde{v}_\alpha \frac{\partial U}{\partial y} + \frac{\partial}{\partial x} \widetilde{u''_\alpha u''_\alpha} + \frac{\partial}{\partial y} \widetilde{u''_\alpha v''_\alpha}$$

$$= - \frac{\partial \tilde{p}_\alpha}{\partial x} + \frac{1}{Re} \left(\frac{\partial^2 \tilde{u}_\alpha}{\partial x^2} + \frac{\partial^2 \tilde{u}_\alpha}{\partial y^2} \right) \tag{3.8}$$

and the y-momentum equation,

$$\frac{\partial \tilde{v}_\alpha}{\partial t} + U \frac{\partial \tilde{v}_\alpha}{\partial x} + \frac{\partial}{\partial x} \widetilde{u''_\alpha v''_\alpha} + \frac{\partial}{\partial y} \widetilde{v''_\alpha v''_\alpha}$$

$$= - \frac{\partial \tilde{p}_\alpha}{\partial y} + \frac{1}{Re} \left(\frac{\partial^2 \tilde{v}_\alpha}{\partial x^2} + \frac{\partial^2 \tilde{v}_\alpha}{\partial y^2} \right) \tag{3.9}$$

where

$$\widetilde{u''_{i\alpha} u''_{j\alpha}} = \tilde{r}_{ij\alpha} = \langle u''_{i\alpha} u''_{j\alpha} \rangle_\alpha - \overline{u''_{i\alpha} u''_{j\alpha}} . \tag{3.10}$$

Equations (3.7), (3.8) and (3.9) are the general expressions for the wave perturbation field, the air modulation field or the interaction-produced wave field, when α is assigned to be null, a, or s respectively. The differences in the order of magnitude and in the flow characteristics among these three fields lead ultimately to equation systems of different forms.

3.3a Wave perturbation field

If α refers to the wave perturbation, equations (3.7), (3.8) and (3.9) reduce to (2.24), (2.25) and (2.26) except that the induced

turbulent Reynolds stresses are now given by

$$\tilde{r}_{11} = \langle u''u'' \rangle - \overline{u''u''}$$

$$= \langle (\tilde{u}_a + \tilde{u}_+ + \tilde{u}_- + u')^2 \rangle - \overline{(\tilde{u}_a + \tilde{u}_+ + \tilde{u}_- + u')^2}$$

$$\simeq \langle u'u' \rangle - \overline{u'u'} + 2\langle \tilde{u}_a \tilde{u}_+ \rangle + 2\langle \tilde{u}_a \tilde{u}_- \rangle \qquad (3.11a)$$

$$\tilde{r}_{12} = \langle u''v'' \rangle - \overline{u''v''}$$

$$= \langle (\tilde{u}_a \tilde{u}_+ + \tilde{u}_- + u')(\tilde{v}_a + \tilde{v}_+ + \tilde{v}_- + v') \rangle - \overline{(\tilde{u}_a + \tilde{u}_+ + \tilde{u}_- + u')(\tilde{v}_a + \tilde{v}_+ + \tilde{v}_- + v')}$$

$$\simeq \langle u'v' \rangle - \overline{u'v'} + \langle \tilde{u}_a (\tilde{v}_+ + \tilde{v}_-) \rangle + \langle \tilde{v}_a (\tilde{u}_+ + \tilde{u}_-) \rangle \qquad (3.11b)$$

$$\tilde{r}_{22} = \langle v''v'' \rangle - \overline{v''v''}$$

$$= \langle (\tilde{v}_a + \tilde{v}_+ + \tilde{v}_- + v')^2 \rangle - \overline{(\tilde{v}_a + \tilde{v}_+ + \tilde{v}_- + v')^2}$$

$$\simeq \langle v'v' \rangle - \overline{v'v'} + 2\langle \tilde{v}_a \tilde{v}_+ \rangle + 2\langle \tilde{v}_a \tilde{v}_- \rangle \qquad (3.11c)$$

In reaching (3.11a,b,c), we have assumed that the frequency of the air modulation is carefully selected to satisfy $2\omega_a \neq \omega$ so that $\langle \tilde{u}_{ia} \tilde{u}_{ja} \rangle$ does not contain any organized waves of order ϵ_a^2 at frequency ω, i.e., $\langle \tilde{u}_{ia} \tilde{u}_{ja} \rangle - \overline{\tilde{u}_{ia} \tilde{u}_{ja}}$ is of higher order than ϵ_a^2 and is neglected. The terms $\langle \tilde{u}_{i+} \tilde{u}_{j+} \rangle$, $\langle \tilde{u}_{i+} \tilde{u}_{j-} \rangle$ and $\langle \tilde{u}_{i-} \tilde{u}_{j-} \rangle$ are also of higher order and are neglected in (3.11a,b,c). The differences between $\tilde{r}_{ij}$ in (3.11a,b,c) and in (2.21b) are attributed to air modulation and can be identified as two types. One is that produced by the direct coupling between the air modulation and the wave perturbation, such as terms $\langle \tilde{u}_a \tilde{u}_s \rangle$ in (3.11a,b,c). The other is that produced indirectly by the distortion of the background turbulence due to the existence of air modulation. This distortion can be regarded as the changes in the

intensity and the correlation behavior of the turbulence. This implies that there may possibly be some differences in $\langle u_i' u_j' \rangle - \overline{u_i' u_j'}$ for those flows with and without air modulations.

The boundary conditions here for the wave perturbations are the same as those given by $\tilde{u} = \tilde{v} = 0$ at $y = H$ and by (2.41a, b) at $y = \tilde{\eta}$ in Chapter 2.

3.3b Air modulation field

The independence of air modulation with respect to x as shown in (3.2) reduces the continuity equation (3.7) to

$$\frac{\partial \tilde{v}_a}{\partial y} = 0 \tag{3.12}$$

The boundary condition $\tilde{v}_a = 0$ at $y = H$ gives $\tilde{v}_a(y,t) \equiv 0$ for all y. Hence the continuity equation is satisfied automatically. The momentum equations are then

$$\frac{\partial \tilde{u}_a}{\partial t} + \frac{\partial}{\partial y} \tilde{r}_{12a} = - \frac{\partial \tilde{p}_a}{\partial x} + \frac{1}{Re} \cdot \frac{\partial^2 \tilde{u}_a}{\partial y^2} \tag{3.13}$$

$$\frac{\partial}{\partial y} \tilde{r}_{22a} = - \frac{\partial \tilde{p}_a}{\partial y} \tag{3.14}$$

As will be seen in (3.16a, b), the pressure gradient $\frac{\partial \tilde{p}_a}{\partial x}$ is independent of x, but the pressure $\tilde{p}_a$ is not. The existence of the pressure gradient is necessary to drive the flow system. Because

$$\frac{\partial \tilde{u}_a}{\partial x} = \frac{\partial \tilde{r}_{12a}}{\partial x} = \frac{\partial \tilde{r}_{22a}}{\partial x} = 0$$

for fully developed flows, taking derivatives with respect to x to (3.13) and (3.14) results in

$$\frac{\partial}{\partial x}\left(\frac{\partial \tilde{p}_a}{\partial x}\right) = 0 , \quad \frac{\partial}{\partial y}\left(\frac{\partial \tilde{p}_a}{\partial x}\right) = 0 \qquad (3.15a,b)$$

Introducing the wave representation,

$$\frac{\partial \tilde{p}_a}{\partial x} = \frac{1}{2} \cdot \left[\frac{\partial \hat{p}_a}{\partial x} \cdot e^{-i\omega_a t} + \text{conjugate} \right] ,$$

into (3.15a,b), we obtain

$$\frac{\partial \hat{p}_a}{\partial x} = \hat{g}_c = \text{constant} \qquad (3.16a)$$

Hence, integration of (3.16a) and (3.14) gives

$$\hat{p}_a = \hat{p}_{1a}(y) + \hat{g}_c x \qquad (3.16b)$$

and

$$\hat{r}_{22a} = \hat{p}_{1a}(H) - \hat{p}_{1a}(y) \qquad (3.16c)$$

where the upper boundary condition for $\tilde{r}_{22a}$ is assumed to be zero, i.e., $\hat{r}_{22a}(H) = 0$. Equation (3.13) is inhomogeneous and the modulation flow system behaves like a visco-elastic oscillator driven by a constant external periodic force, $\frac{\partial \tilde{p}_a}{\partial x}$. Note in (3.13) the system is independent of the mean flow.

The turbulent Reynolds stress modulations are given by

$$\tilde{r}_{11a} = \langle u''_a u''_a \rangle_a - \overline{u''_a u''_a}$$

$$\simeq \langle u'u' \rangle_a - \overline{u'u'} + 2\langle \tilde{u}\tilde{u}_+ \rangle_a + 2\langle \tilde{u}\tilde{u}_- \rangle_a \qquad (3.17a)$$

$$\tilde{r}_{12a} = \langle u''v'' \rangle_a - \overline{u''v''}_a$$

$$\simeq \langle u'v' \rangle_a - \overline{u'v'} + \langle \tilde{u}(\tilde{v}_+ + \tilde{v}_-) \rangle_a + \langle \tilde{v}(\tilde{u}_+ + \tilde{u}_-) \rangle_a \qquad (3.17b)$$

$$\tilde{r}_{22a} = \langle v''v'' \rangle_a - \overline{v''v''}_a$$

$$\simeq \langle v'v' \rangle_a - \overline{v'v'} + 2\langle \tilde{v}\tilde{v}_+ \rangle_a + 2\langle \tilde{v}\tilde{v}_- \rangle_a \qquad (3.17c)$$

In (3.17a,b,c), we have assumed that $2\omega \neq \omega_a$ so that $\langle \tilde{u}_i \tilde{u}_j \rangle_a$ does not contain organized oscillations at frequency ω_a. Terms with order higher than $\epsilon^2 \epsilon_a$ are also neglected in (3.17a,b,c). Although all the components $\tilde{r}_{11a}$, $\tilde{r}_{12a}$ and $\tilde{r}_{22a}$ exist in the real flow, the turbulent shear stress modulation $\tilde{r}_{12a}$ is the only force that requires closure modelling for the prediction of velocity $\tilde{u}_a$ as indicated by (3.13).

The modulated air flow in a channel without surface waves was studied in detail by Acharya and Reynolds (1975). Because $\tilde{u}_i = \tilde{u}_{is} = 0$, the $\tilde{r}_{ija}$ in their study was then simplified to $\tilde{r}_{ija} = \langle u'_i u'_j \rangle_a - \overline{u'_i u'_j}$. Several closures were considered by Acharya and Reynolds (including the quasilaminar model $\tilde{r}_{ija} = 0$ which yields an exact analytical solution). Their predictions were inconsistent with their experiment data. Although they suggested that the pressure strain effect is important and that a turbulent Reynolds stress closure model or a model using an integral-differential closure relation for pressure strain should be constructed, the dynamics that describes the interaction between the wave and the turbulence was still missing.

From the wave-turbulence interaction point of view, the closure models for $\tilde{r}_{ij}$ and $\tilde{r}_{ija}$ are similar. Since we are more interested in the interaction of water waves with the turbulent flow, the subject of air modulation was not pursued further. For those who desire a better understanding of the air modulation, the report of Acharya and Reynolds (1975) is recommended.

The boundary conditions for $\tilde{u}_a$ are

$$\tilde{u}_a = 0 \qquad \text{at } y = H \tag{3.18a}$$

and

$$\tilde{u}_a = 0 \qquad \text{at } y = \tilde{\eta} \tag{3.18b}$$

The lower boundary condition is determined by assuming that there is no oscillating mode corresponding to the frequency ω_a at the interface. This assumption can be justified by the high ratio of water density to air density. In air modulation flow, the oscillation $\tilde{u}_a$ at the interface is regarded as the oscillating drift current induced by air modulation. Because (3.13) and (3.14) for air modulation are very similar to (2.48) and (2.49) for mean flow except for the appearance of the time varying term $\frac{\partial \tilde{u}_a}{\partial t}$ in (3.13), the magnitude of the induced oscillating drift current can only be about 2-3% of $\tilde{u}_a$ at the free stream, which is roughly the same percentage as the mean drift current is of the mean free stream velocity as reported by Wu (1968). So practically (3.18b) is a good approximation to the lower boundary condition.

3.3c Interaction-produced wave field

If the subscript α refers to s in (3.7), (3.8) and (3.9), the governing equations describing the interaction-produced wave fields are obtained. The interaction Reynolds stress $\tilde{r}_{ijs}$ are then expressed as

$$\begin{aligned} \tilde{r}_{11s} &= \langle u''_s u''_s \rangle_s - \overline{u''_s u''_s} \\ &\simeq \langle u'u' \rangle_s - \overline{u'u'} + 2\langle \tilde{u}_a \tilde{u} \rangle_s \end{aligned} \tag{3.19a}$$

$$\begin{aligned} \tilde{r}_{12s} &= \langle u''_s v''_s \rangle_s - \overline{u''_s v''_s} \\ &\simeq \langle u'v' \rangle_s - \overline{u'v'} + \langle \tilde{u}_a \tilde{v} \rangle_s + \langle \tilde{u}\tilde{v}_a \rangle_s \end{aligned} \tag{3.19b}$$

$$\tilde{r}_{22s} = \langle v''_s v''_s \rangle_s - \overline{v''_s v''_s}$$

$$\simeq \langle v'v' \rangle_s - \overline{v'v'} + 2\langle \tilde{v}_a \tilde{v} \rangle_s \qquad (3.19c)$$

The terms with $\langle \tilde{u}_{ia} \tilde{u}_j \rangle_s$ serve as the source terms that drive the interaction-produced wave system. These source terms are assumed dominant in governing the behavior of the interaction-produced wave components.

The boundary conditions for $\tilde{u}_s$ and $\tilde{v}_s$ are identified as

$$\tilde{u}_s = \tilde{v}_s = 0 \qquad \text{at } y = H \qquad (3.20a)$$

and

$$\tilde{u}_s = \tilde{v}_s = 0 \qquad \text{at } y = \tilde{\eta} \qquad (3.20b)$$

Similar to that for air modulation, the lower boundary conditions are justified from the negligibility of the oscillation mode with frequency ω_s at the interface.

3.4 Systems in the Transformed-Coordinate System

The flow described in the transformed coordinate system given by (2.43a, b, c) can be obtained in a similar way as in Chapter 2. When equations (2.47a, b, c, d, e) and (3.1) are applied to the Navier-Stokes equations and the non-linear terms are neglected after averaging, equation systems that govern the mean field, the wave perturbation field, the air modulation field and the interaction-produced wave field are found as follows.

3.4a Mean field

In the transformed coordinate system, the mean flow equations (2.48) and (2.49) remain unchanged. However, the mean Reynolds

stresses may be subjected to minor changes due to the effect of air modulation.

3.4b Wave perturbation field

The equations, (2.50) to (2.61), and the boundary conditions, (2.62a,b) and (2.63a,b), are still applicable to the wave perturbation field in the modulated air flow except that the $\tilde{r}_{ij}$ are now described by (3.11a,b,c).

3.4c Air modulation field

The effect of the coordinate transformation to the air modulation field is only of $O(\tilde{\eta}^2)$. In determining the basic characteristics of the air modulation, it can be ignored. The equations for the air modulation are then

$$\frac{\partial \tilde{u}_a}{\partial t^*} + \frac{\partial}{\partial y^*} \tilde{r}_{12a} = - \frac{\partial \tilde{p}_a}{\partial x^*} + \frac{1}{Re} \cdot \frac{\partial^2}{\partial y^{*2}} \tilde{u}_a \qquad (3.21)$$

$$\frac{\partial}{\partial y^*} \tilde{r}_{22a} = - \frac{\partial \tilde{p}_a}{\partial y^*} \qquad (3.22)$$

with boundary conditions,

$$\tilde{u}_a = 0 \qquad \text{at both } y^* = H \text{ and } y^* = 0 \qquad (3.23a,b)$$

The turbulent Reynolds stresses $\tilde{r}_{ija}$ are still given by (3.17a,b,c) but remember that all of them are now evaluated in the transformed coordinate system. Note that the same arguments can be made on $\tilde{p}_a$ and $\tilde{r}_{22a}$ as in Section 3.3b.

3.4d Interaction-produced wave field

In the transformed coordinate system (x^*, y^*, t^*), the equations for the interaction-produced wave components are changed considerably

due to the coupling between the oscillating transformed coordinate system and the air modulation. These changes in the equations are very similar to those changes in the equations for wave perturbations caused by the coupling between the oscillating transformed coordinate system and the mean flow. In order to simplify the transformed equations, transformations of the interaction-produced wave field similar to those given in (2.54a,b), (2.56) and (2.57) are very helpful. These transformations can be expressed as:

$$\tilde{u}^*_s = \tilde{u}_s - f \cdot \frac{\partial}{\partial y^*} \langle \tilde{\eta} \tilde{u}_a \rangle_s \tag{3.24a}$$

$$\tilde{v}^*_s = \tilde{v}_s \tag{3.24b}$$

$$\tilde{p}^*_s = \tilde{p}_s - f \cdot \frac{\partial}{\partial y^*} \langle \tilde{\eta} \tilde{p}_a \rangle_s \tag{3.24c}$$

$$\tilde{r}^*_{ijs} = \tilde{r}_{ijs} - f \cdot \frac{\partial}{\partial y^*} \langle \tilde{\eta} \tilde{r}_{ija} \rangle_s \tag{3.24d}$$

Then, the governing equations are

$$\frac{\partial \tilde{u}^*_s}{\partial x^*} + \frac{\partial \tilde{v}^*_s}{\partial y^*} = 0 \tag{3.25}$$

$$\frac{\partial \tilde{u}^*_s}{\partial t^*} + U \frac{\partial \tilde{u}^*_s}{\partial x^*} + \tilde{v}^*_s \frac{\partial U}{\partial y^*} + \frac{\partial}{\partial x^*} \tilde{r}^*_{11s} + \frac{\partial}{\partial y^*} \tilde{r}^*_{12s}$$
$$= - \frac{\partial \tilde{p}^*_s}{\partial x^*} + \frac{1}{Re} \left(\frac{\partial^2 \tilde{u}^*_s}{\partial x^{*2}} + \frac{\partial^2 \tilde{u}^*_s}{\partial y^{*2}} \right) \tag{3.26}$$

$$\frac{\partial \tilde{v}^*_s}{\partial t^*} + U \cdot \frac{\partial \tilde{v}^*_s}{\partial x^*} + \frac{\partial}{\partial x^*} \tilde{r}^*_{12s} + \frac{\partial}{\partial y^*} \tilde{r}^*_{22s}$$
$$= - \frac{\partial \tilde{p}^*_s}{\partial y^*} + \frac{1}{Re} \left(\frac{\partial^2 \tilde{v}^*_s}{\partial x^{*2}} + \frac{\partial^2 \tilde{v}^*_s}{\partial y^{*2}} \right) \tag{3.27}$$

Equations (3.25), (3.26) and (3.27) were obtained in a similar way as (2.54), (2.58) and (2.59) except that the role of (2.48) and (2.49) was taken by (3.21) and (3.22). The boundary conditions (3.20a,b) are then evaluated in a time independent way and are

$$\tilde{u}_s^* = \tilde{v}_s^* = 0 \qquad \text{at} \quad y^* = H \tag{3.28a}$$

and

$$\tilde{u}_s^* = \tilde{v}_s^* = 0 \qquad \text{at} \quad y^* = 0 \tag{3.28b}$$

The interaction-produced wave stream function $\tilde{\phi}_s^*$ is defined by

$$\tilde{u}_s^* = \frac{\partial \tilde{\phi}_s^*}{\partial y^*} \quad , \qquad \tilde{v}_s^* = - \frac{\partial \tilde{\phi}_s^*}{\partial x^*} \tag{3.29a,b}$$

Eliminating $\tilde{p}_s^*$ from (3.26) and (3.27), substituting (3.29a,b) into the resulting equation, and applying the wave representation,

$$\tilde{\phi}_s^* = \frac{1}{2} \cdot [\hat{\phi}_s^*(y^*)\, e^{i(kx^* - \omega_s t^*)} + \text{conjugate}] \tag{3.30}$$

we have

$$[(U-c_s)\cdot(D^{*2}-k^2) - D^{*2}U]\hat{\phi}_s^* + \frac{i}{kRe}(D^{*2}-k^2)^2\hat{\phi}_s^* = \hat{q}_s^* \tag{3.31}$$

where

$$\hat{q}_s^* = - D^*(\hat{r}_{11s}^* - \hat{r}_{22s}^*) + \frac{i}{k}(D^{*2} + k^2)\hat{r}_{12s}^* \tag{3.31}$$

and $c_s = \omega_s/k$ is the wave speed of the interaction-produced waves.

The boundary conditions in terms of wave expressions are

$$\hat{\phi}_s^* = D^*\hat{\phi}_s^* = 0 \qquad \text{at} \quad y^* = H \tag{3.33a,b}$$

and

$$\hat{\phi}_s^* = D^*\hat{\phi}_s^* = 0 \qquad \text{at} \quad y^* = 0 \tag{3.34a,b}$$

3.5 Inviscid Quasilaminar Model of Interaction-produced Waves

We will examine the limiting case of $Re \to \infty$ so that the viscous effect is important only in the viscous wall layer and in the critical layer where $U = c_s$. As shown by Lin (1955), the solution of (3.31) as $Re \to \infty$ can be approximated by the solution of inviscid equation obtained by setting $\frac{1}{Re} = 0$ and taking the frequency ω_s to be a complex number with a vanishingly-small positive, imaginary part.

For the present analysis, we will also neglect the turbulent effect terms $\langle u_i' u_j' \rangle_s - \overline{u_i' u_j'}$ in the source function $\hat{q}^*_s$. One may argue that $\langle u_i' u_j' \rangle_s - \overline{u_i' u_j'}$ might play a similar significant role in determining the interaction-produced wave field as that role of $\langle u_i' u_j' \rangle - \overline{u_i' u_j'}$ in effecting the wave-perturbation field. Our postulation is that, unlike $\langle u_i' u_j' \rangle - \overline{u_i' u_j'}$ which are the only source terms in determining the turbulence effect on the wave velocity, the source terms $\langle \tilde{u}_i \tilde{u}_{ja} \rangle_s$ and $\langle \tilde{\eta} \tilde{\omega}_{ia} \rangle_s$ have dominantly influenced the interaction-produced wave field so as to overshadow the significance of $\langle u_i' u_j' \rangle_s - \overline{u_i' u_j'}$. Thus, the inviscid quasi-laminar assumption is imposed a priori in the following analysis.

Under these assumptions, (3.31) reduces to

$$[(U - c_s) \cdot (D^{*2} - k^2) - D^{*2} U] \hat{\phi}^*_s = \hat{q}^*_s \tag{3.35}$$

and the explicit expression for $\hat{q}^*_s$ is

$$\hat{q}^*_s = D^*\left(\frac{1}{2} \cdot f \cdot a \cdot D^* \hat{f}^s_{11a} - \hat{u} \cdot \hat{u}^s_a - \frac{1}{2} \cdot f \cdot a \cdot D^* \hat{f}^s_{22a}\right)$$

$$+ \frac{i}{k}(D^{*2} + k^2)\left(\frac{1}{2} \cdot \hat{v} \cdot \hat{u}^s_a - \frac{1}{2} f \cdot a \cdot D^* \hat{f}^s_{12a}\right) \tag{3.36}$$

where the notations $\hat{u}^s_a$, $\hat{f}^s_{11a}$, $\hat{f}^s_{12a}$ and $\hat{f}^s_{22a}$ with $s = \pm$ are generally expressed as

$$\hat{g}_a^+ = \hat{g}_a \tag{3.37}$$

and $\hat{g}_a^-$ is the complex conjugate of $\hat{g}_a^+$. The no slip conditions that restricted the horizontal oscillation at the boundaries of the flow are relaxed. When $H \to \infty$, the boundary conditions are

$$\hat{\phi}_s^* = 0 \qquad \text{as} \quad y^* \to \infty \tag{3.38}$$

$$\hat{\phi}_s^* = 0 \qquad \text{at} \quad y^* = 0 \tag{3.39}$$

The lower boundary condition is actually evaluated outside the viscous layer which becomes very thin as $Re \to \infty$. The viscous layer near the interface presumably brings $D^*\hat{\phi}_s^*$ to zero, but consideration of this is outside of the range of the present study.

3.6 Asymptotic Solution under Long Wave Approximation.

The long wave approximation was constructed under the condition that the diffusive layer in the air flow was very thin in comparison to the wave length of the water surface waves. The flow then can be divided into two regions. The first is the region near the interface in the boundary layer of the mean flow where the boundary layer thickness is a proper length scale, the second is the region far from the interface in the free stream where the curvature of the mean velocity profile (vorticity gradient) is small. Here the wave decaying phenomena dominantly characterizes the interaction-produced wave field so that the wave length is a proper length scale.

The mean velocity profile normalized by U_∞ is given by

$$U = 1 + \frac{1}{2} \cdot \frac{u_*}{k_o} \cdot \ln y^* - \left[\left(\frac{1}{2} \cdot \frac{u_*}{k_o} \cdot \ln y^* \right)^2 + 10^{-4} \right]^{1/2} \tag{3.40}$$

where u_* is the normalized shear velocity and k_o is the von Karman

constant which is 0.4 in this study. The term 10^{-4} in (3.40) is introduced because we set $U = 0.99$ at $y^* = 1$; recall that y^* is normalized by the boundary layer thickness δ. This velocity profile corresponds to the log-profile in the wall region and asymptotically approaches unity when one is far from the interface. Although, in Chapter 5, a more sophisticated log-wake profile is used in the curve fitting procedure in the mean flow study, the wake effect does not profoundly change the analysis procedure or the results, and is minor in this discussion.

Under the long wave approximation, $k << 1$ when $y^* = O(1)$ and equation (3.35) is simplified to

$$(U - c_s)D^{*2}\hat{\phi}_s^* - (D^{*2}U)\hat{\phi}_s^* = \hat{q}_s^* \tag{3.41}$$

and the lower boundary condition is

$$\hat{\phi}_s^*(0) = 0 \tag{3.42}$$

The solution to (3.41) and (3.42) is

$$\hat{\phi}_s^*(y^*) = (U-c_s) \int_0^{y^*} \frac{1}{(U-c_s)^2} \cdot \left[C_1 + \int_\infty^{y_1^*} \hat{q}_s^* dy_2^* \right] dy_1^* \tag{3.43}$$

Equation (3.43) is regarded as the inner solution and the constant C_1 will be determined by matching (3.43) to an outer solution.

To obtain the outer solution, the coordinate y^* is stretched by a factor k, say $Y = ky^*$, and in terms of the stretched coordinate (3.35) is

$$(U - c_s)\left(\frac{d^2\Phi_s}{dY^2} - \Phi_s \right) - \frac{d^2U}{dY^2} \cdot \Phi_s = Q_s \tag{3.44}$$

where $Q_s(Y) = \frac{1}{k}\hat{q}_s^*(Y/k)$ is of O(1) in the outer region and Φ_s is the outer function defined by $\Phi_s(Y) = \hat{\phi}_s^*(Y/k)$. Equation (3.40) gives

$$\frac{d^2U}{dY^2} = \frac{1}{k^2} \cdot \frac{d^2U}{dy^{*2}} \simeq -\frac{k_o}{(\ln y^*)^2} \cdot \frac{10^{-4}}{k^2 y^{*2}} = -\frac{k_o \cdot 10^{-4}}{(\ln Y - \ln k)^2 Y^2}$$

As $k \to 0$, $\frac{d^2U}{dY^2} \to 0$, $U \to 1$, and the first order approximation to (3.44) is

$$(1 - c_s)\left(\frac{d^2\Phi_s}{dY^2} - \Phi_s\right) = Q_s \tag{3.45}$$

The outer boundary condition is then

$$\Phi_s = 0 \quad \text{as} \quad Y \to \infty \tag{3.46}$$

The solution to (3.45) and (3.46) is

$$\Phi_s(Y) = e^{-Y} \int_0^Y e^{2Y_1} \cdot \int_\infty^{Y_1} \frac{Q_s}{(1-c_s)} \cdot e^{-Y_2} dY_2 \cdot dY_1 + A_1 e^{-Y} \tag{3.47}$$

To insure the convergence of the integral term in (3.47), the quantity $\int_0^\infty Q_s(Y)\,dY$ should be bounded. This is true since physically only finite sources can be supplied by wave perturbations and air modulation. The result that $Q_s \to 0$ exponentially as $Y \to \infty$ guarantees that $\Phi_s \to 0$ as $Y \to \infty$.

After it is integrated by parts, the integral term in (3.47) can be expressed as

$$\int_0^Y \int_\infty^{Y_1} \frac{Q_s}{(1-c_s)}\, dY_2\, dY_1 - e^{-Y} \int_0^Y e^{Y_1} \int_0^{Y_1} \int_0^{Y_2} \frac{Q_s}{(1-c_s)}\, dY_3 dY_2 dY_1$$

$$+ e^{-Y} \int_0^Y e^{2Y_1} \int_0^{Y_1} e^{-Y_2} \int_\infty^{Y_2} \frac{Q_s}{(1-c_s)}\, dY_3 dY_2 dY_1$$

Hence, as $Y \to 0$, equation (3.47) can be expanded into

$$\Phi_s = A_1 - A_1 Y + \int_0^Y \int_\infty^{Y_1} \frac{Q_s}{(1-c_s)}\, dY_2 dY_1 + \text{triple integral terms.}$$

Rewriting this into the inner variable y^*, we have

$$\Phi_s(ky^*) = \hat{\phi}_s^*(y^*) = A_1 + \int_0^{y^*} \int_\infty^{y_1^*} \frac{\hat{q}_s^*}{(1-c_s)}\, dy_2^* dy_1^* + O(k) \tag{3.48}$$

The asymptotic form as $y^* \to \infty$ for the inner solution (3.43) is

$$\hat{\phi}_s^*(y^*) = (1-c_s) \cdot \int_0^\infty G_s \cdot \left[\int_\infty^{y_1^*} \hat{q}_s^{*\prime}\, dy_2^* + C_1 \right] dy_1^*$$

$$+ \frac{1}{(1-c_s)} \int_0^{y^*} \int_\infty^{y_1^*} \hat{q}_s^*\, dy_2^*\, dy_1^* + \frac{C_1}{(1-c_s)}\, y^* \tag{3.49}$$

where

$$G_s(y^*) = \frac{1}{(U(y^*)-c_s)^2} - \frac{1}{(1-c_s)^2} \tag{3.50}$$

So, (3.49) matches (3.48) if $C_1 = 0$ and

$$A_1 = (1-c_s) \int_0^\infty G_s \cdot \int_\infty^{y_1^*} \hat{q}_s^* \, dy_2^* dy_1^* \tag{3.51}$$

In summary, we have the inner solution,

$$\hat{\phi}_s^*(y^*) = (U-c_s) \int_0^{y^*} \frac{1}{(U-c_s)^2} \cdot \int_\infty^{y_1^*} \hat{q}_s^* \, dy_2^* \, dy_1^* \tag{3.52}$$

and the outer solution given by (3.47) with constant A_1 given by (3.51). The composite solution can be written as

$$\hat{\phi}_s^*(y^*) = (U-c_s) \, e^{-ky^*} \int_0^{y^*} G_s \int_\infty^{y^*} \hat{q}_s^* \, dy_2^* \, dy_1^*$$

$$+ \frac{(U-c_s)^2}{(1-c_s)^2} \, e^{-ky^*} \int_0^{y^*} e^{2ky_1^*} \int_\infty^{y_1^*} \hat{q}_s^* \, e^{-ky_2^*} \, dy_2^* dy_1^* \tag{3.53}$$

This long wave approximation approach is fundamentally similar to that of Davis (1974) except that his applications of the log-profile mean velocity to the entire flow region and of long wave approximation to the Fourier components of turbulent fluctuations have raised some ambiguity in his analysis. Another difference is that the present analysis is performed over a wavy boundary surface in a transformed coordinate system, but that of Davis was still restricted to the flat boundary wall.

As pointed out in the first chapter, the present study emphasizes experimental studies of the dynamical aspect of the interaction between wave perturbation and air modulation. Accordingly, numerical calculations of interaction-produced wave fields will be reserved for subsequent investigations and are not attempted in this study.

CHAPTER 4

THE APPARATUS, INSTRUMENTATION AND DATA REDUCTION SCHEMES

4.1 The Air-Water Channel

The channel used for the experiments was described in detail by Hsu (1965) and subsequent investigators at Stanford. It was designed to generate water waves by wind and/or by a mechanical wave generator to facilitate the experimental study of the wave generation problem. For the present experiment, modifications were made at the flow exit of the channel by adding a control unit to generate an oscillating air modulation. Figure 4.1 shows a schematic of the channel. It is 38 m long, 1 m wide and 1.9 m high. The glass-walled test section is approximately 24 m from the air entrance to the down-stream beach. The data taking station was located at 13 m from the air entrance.

Wind was produced by drawing air through the test section with a suction fan at the downstream end of the channel. At the entrance to the air inlet, fiberglass furnace filters were mounted to prevent large particles of dust from getting into the channel; a thick honeycomb and a group of fine-meshed screens were also installed at the exit of the air inlet to produce a uniform turbulent velocity profile in the test section. A second honeycomb was located just in front of the fan at the down-stream end to prevent the vortex motion caused by the fan from extending upstream into the test section. The maximum possible wind speed in the test section was 15 m/sec; this was reduced to 8 m/sec when the air modulator was installed. A mean free stream velocity of 2.4 m/sec was selected for this study.

The water wave generator is a horizontal-displacement oscillating plate driven by a hydraulic cylinder and subjected to a closed-loop servo-control system. The input signal for the wave plate displacements

was provided by an electronic function generator. The wave plate was situated well upstream from the entrance of test section to form a forebay, which acted as a transition region for the development of mechanically-generated water waves. A sloping beach, formed by a series of rectangular baskets filled with stainless steel turnings, was located at the downstream end to reduce the wave reflection. This water wave generator can produce sinusoidal waves with frequencies ranging from 0.2 to 2.0 Hz. The frequency used in this experiment was 1 Hz ($\omega = 2\pi$ rad/sec). The wave length L determined from the dispersion relation of deep water waves is

$$L = \frac{2\pi}{k} = \frac{2\pi g}{\omega^2} = 1.561 \text{ m} \qquad (4.1)$$

where k is the wave number and g is the gravitational acceleration (9.807 m/sec^2).

4.2 The Air Flow Pulser

Controlled air modulations were produced in the channel by periodically regulating the channel-to-flow resistance by means of an air pulser unit mounted at the flow exit. Figure 4.2 shows the details of the unit, which consists of a rotating blade, a fixed blade, a variable speed motor, amplitude control plates and a supporting frame. The rotating blade was shaped in a form described by

$$r = \sqrt{a + b(1 + \cos 2\theta)} \qquad (4.2)$$

where (r, θ) represent the polar coordinates. The configuration of the blade with $a = 171 \text{ cm}^2$ and $b = 1621 \text{ cm}^2$ is given in Figure 4.3. The blade was made of half inch thick Douglas fir marine plywood to give a high ratio of tensile strength to density, and to prevent its distortion due to absorbtion of moisture in the passing air flow and/or surroundings

Plywood was used to reduce the weight of the blade for easier handling and to decrease the inertia force for easier motor starting. The thickness of a half inch was chosen to minimize structural deflection of the blade during rotation.

The fixed blade is also shown in Figure 4. 3 with the angular cut of inclined angle $\alpha = 120^{o}$, symmetric on both sides. When the rotating blade moved at a constant angular speed, a sinusoidal blockage area A_b was produced according to the following equation,

$$A_b = \pi(a+b) - \alpha b + b\sin\alpha \cdot \cos(2\omega_o t) \qquad (4.3)$$

where ω_o is the frequency of the blade rotation. In (4. 3), $\pi(a+b) - \alpha b$ is the mean blockage area for opening angle α during rotations and is regarded as wasted area; on the other hand, $2b \cdot \sin\alpha$ represents the maximum variable area which is usable for regulating the blockage. Hence, an optimum opening angle α should result in larger usable area with smaller wasted area. As a result, we need to maximize the ratio $\gamma = b\sin\alpha/(\pi(a+b) - \alpha b)$ to determine the optimal angle α. Although theoretically, when $\alpha = 130^{o}$, the fixed blade would operate most efficiently to give γ a maximum value of 0. 637, the angle $\alpha = 120^{o}$ which gives $\gamma = 0.628$ was used for practical construction. The frequency of the air modulation is twice the frequency of the blade rotation, i. e., $\omega_a = 2\omega_o$.

A $\frac{1}{2}$ H. P. d. c. motor, connected to the rotating blade shaft by a flexible coupling, was operated through a control unit. The motor and the control unit were manufactured by Electro-Craft Co. The control unit enables the motor to operate at a constant speed over a range from 0 Hz up to 20 Hz by means of a feedback control system. The frequency of the blade rotation was determined within 0. 5% by inputting the pulse signal from the control unit into a frequency counter. Although the frequency counter readings of two sequential data files were quite constant, a systematical change in reading caused by drift in the

control unit circuity was visible in the long term. In order to keep the air modulation frequency constant during a run, the frequency knob of the control unit was adjusted approximately every half hour to retain the frequency reading set at the beginning.

The blade shaft is supported by two self-aligned bearings which were mounted on an angle-iron structural frame. The frame has a pyramid shape with a rectangular base. The blade shaft serves as the ridge of the pyramid. The vertical angle of the frame is 46^{o}. This angle is less than the angle of the fixed blade (60^{o}) to insure that the frame is hidden behind the fixed blade to avoid possible influence of the frame on the air flow.

The amplitude of the air modulation is controlled by the amplitude control plates which regulate the ratio of the total blockage area to the total net open area at the flow exit as shown in Figure 4.3. This ratio in turn determines the ratio γ_a, the velocity amplitude of air modulation to the mean free stream velocity. In order to maintain constant mean flow, no adjustment of the amplitude control plates was made during each run.

The frequencies of air modulation selected in this experiment were 0.4 Hz, 0.7 Hz and 1.5 Hz with ratio γ_a approximately equal to 3.5%, 2.7% and 1.5% respectively.

4.3 Wave Follower System

The wave-follower system developed by Yu and Hsu (1971) was modified and used as the primary instrument for the measurements. It consists of mechanical and electrical systems. The mechanical portion contains a low-inertia motor and a vertical motion mechanism that has an aluminum-channel holding a stainless-steel tube guided by nylon bushings. The tube is driven by the motor through a pulley-and-cable assembly. The electrical portion is a control panel that

implements the wave-follower motion and provides the input and output signal jacks. Figure 4.4 shows the wave-follower system.

The vertical motion mechanism has a range of about 15 cm. Hence for a 2.67 cm amplitude wave, only about 9 cm is left as the traverse range of the mean elevation, which is about four tenths of the boundary layer thickness. In order to extend the range of the wave-follower system to cover the whole boundary layer, an elevator for the wave-follower was constructed as shown in Figures 4.4 and 4.5. The elevator consists of an aluminum box which is 60 cm high and has 30 cm x 30 cm horizontal dimensions, a movable horizontal aluminum plate running on three threaded vertical steel rods, a chain and sprocket assembly and a turning handle. The handle was mounted to one threaded rod which is connected to the other two threaded rods by the chain and sprocket assembly. The rods are supported on the top and the bottom plates of the box with ball bearings. When the handle was turned, the three rods were turned synchronously and the moving plate with the wave-follower assembly on it moved up and down. Change of elevation was 2.309 mm for 1 turn (eleven turns per inch). A scale was fixed to the box to indicate the position of the moving plate.

The elevator was seated on top of the roof of the wind-wave channel. The wave follower was mounted on the moving plate of the elevator with the aluminum channel and the stainless-steel tube intruding into the tunnel through the channel roof. The hot film and the pitot tube probes were then attached to the lower end of the moving stainless-steel tube. Figure 4.5 shows the arrangement of measuring probes.

The details for operating the wave-follower system were reported by Yu and Hsu (1971). Briefly, the system is controlled by two sets of dials on the control panel. One is the OFFSET dial that pre-sets the distance from the mean water level to the probes. The other is the INPUT dial that determines the amplitude of the oscillation of the

stainless-steel tube and the attached sensors. The readings of the OFFSET dial and of the position indicator on the elevator give the y^* values. The accuracy of the y^* values is ±0.25 mm.

Unlike the wave-following system measurements made at Stanford in the past, the amplitude of the wave-follower oscillation in our investigation decreases according to Eq. (2.43c). Consequently, the INPUT dial setting must be calculated for each y^* value based on the calibration constants of the system components. Because the wave height signal was used as input for the wave-follower system and because a 10 Hz lowpass RC filter was used before inputting the wave height signal to the wave-follower to eliminate the effect of ripples, the INPUT dial setting (D_{wf} scale) was calculated from the calibration constant of wave height gauge (C_w volt/cm), the gain of the RC filter (G_f), the calibration constant of the wave-follower system (C_{wf} cm/volt-scale) and the factor f given by Eq. (2.45), from knowledge of y^*, H, and k. The following equation gives the concepts for the calculation:

$$\underset{(1)}{\tilde{\eta}} \cdot \underset{(2)}{C_w} \cdot \underset{(3)}{G_f} \cdot \underset{(4)}{C_{wf}} \cdot \underset{(5)}{D_{wf}} \cdot \quad = f \cdot \tilde{\eta}$$

where

(1). wave height (cm)

(2). wave height signal (volt)

(3). RC filtered wave follower input signal (volt)

(4). specific displacements of the wave-follower (cm/scale)

(5). resulting displacements of the wave-follower (cm)

Hence,

$$D_{wf} = \frac{f}{C_w \cdot G_f \cdot C_{wf}}$$

$$= \frac{\sinh(kH - ky^*)}{C_w \cdot G_f \cdot C_{wf} \cdot \sinh(kH)} \qquad (4.4)$$

The values used for C_w, G_f, C_{wf}, k and H were 0.2610 (volt/cm), 0.97 (volt/volt) at 1 Hz, 2.540 (cm/volt-scale), 0.04026 (1/cm) for 1 Hz water waves, and 97.03 (cm) respectively.

For the 1 Hz wave, there is a phase lag of 9.28° between the wave-follower displacements and the surface wave displacements due to the accumulation of the phase lags from the RC filter (6.58°) and from the wave-follower system (2.7°). In order to make the velocity sensors follow the mechanically-generated water waves as synchronously as possible, the sensing wire of the wave height gauge was placed upstream from the velocity sensors a distance of

$$156.1 \times \frac{9.28}{360} = 4.02 \text{ cm}$$

or approximately 4.0 cm.

4.4 Instrumentation and Calibration

The sensors used in this experiment included a wave height gauge, an X-array hot-film probe and a Pitot-static tube. The hot-film probe and the Pitot-static tube were mounted on a plexi-glas frame that was attached to the stainless-steel tube of the wave-follower. An optical transit was used to align the arms of the hot-film probe and the Pitot-static tube to be parallel each other to the flow direction and to align the tips of the sensors to be at the same fetch. The sensor tips were separated approximately by 5 cm to avoid interference.

The wave height gauge was mounted on an aluminum-angle support fixed to the channel roof. The wave height gauge was placed at

one side to the other sensors with a distance separation of about 10 cm. The sensing wire of the wave height gauge was approximately 4.0 cm upstream of the other sensors to correct for the phase lag as previously stated.

In order to determine the sensor elevation accurately, a point gauge was used. The gauge is a stainless-steel pin mounted vertically along with the hot-film sensors. The lower tip of the pin was adjusted to a known distance below the sensors (2.62 cm in this experiment). The upper end of the pin was connected to an electrical circuit. When the tip of the pin contacted the water surface, the light indicator in the circuit was turned on.

The probe arrangements are shown in Figure 4.5.

4.4a Wave height gauge

The capacitance wave height gauge is a No. 32 Nylclad insulated copper wire stretched between the arms of a U-shaped frame. The wire was aligned normal to the mean water surface with half its length immersed in the water. The upper end of the wire was connected to a Sanborn 958-1100 capacitance bridge amplifier.

For calibration, the wave height gauge was mounted vertically on a vertical traversing mechanism. The traverse was used to change the depths of the wire immersion. For each immersion, the corresponding voltage output of the Sanborn was recorded on an HP2100A computer. The data sets consisting of depths and voltage readings were then linearly least square curve-fitted in the computer at the end of calibration to obtain the slope (volt/cm) as the calibration constant. Figure 4.6 shows the calibration curve of the wave height gauge. After the calibration, the wave height gauge was installed on the aluminum-angle support and aligned for data taking. Preliminary experiment showed that the calibration slope is very steady and changed less than 0.5%. Hence, no additional calibrations were required during the data taking.

4.4b Pitot-static tube

There were two purposes for using a Pitot-static tube. One was to cross check the mean velocity obtained from the hot-film output and the other was to serve as a reference against which the hot-film probe could be calibrated.

The outer diameter of the Pitot-static tube is 2.34 mm. The leads of the total pressure and the static pressure were connected to a Pace differential pressure transducer (Model P90D), which was then connected to a Sanborn 656-1100 carrier amplifier. The pressure difference of the two leads (dynamic pressure of the flow) was converted to voltage in the Pace transducer and then amplified by the Sanborn amplifier.

The Pace transducer was calibrated against a Combust micromanometer with the aid of the HP2100A computer. The micromanometer contained a fluid of specific gravity 0.82 and has a resolution of pressure head difference of ±0.0006 cm of the fluid. For each attenuation of the Sanborn, different readings of micromanometer input to the computer resulted in corresponding outputs of voltage and then slope of calibration (volt/cm of 0.82 fluid) was found by linear least square curve-fit. Figure 4.7 shows the calibration curves.

Preliminary data of mean velocity showed that the result of Pitot-static tube checked very well with that of hot-film. It also showed that the Pitot-static tube data usually had higher uncertainty. Hence, based on this preliminary cross check, the signal of Pitot-static tube was not recorded in the final data taking.

4.4c Hot-film probe

The velocity fields were measured with a hot-film probe. The hot-film probe selected was TSI Model 1241-20. It is an X-array hot-film probe for both the U- and V-components velocity measurement and is specially quartz-coated to protect the films from possible water

spray ejected from the interface. As specified by the manufacturer, the films are 0.0508 mm in diameter and 1.016 mm long and have a frequency response up to 40,000 Hz. The orientation angles of the films relative to the probe centerline were measured with the aid of an optical comparator. The values for the angle are shown in Figure 4.5.

Each hot-film was connected to a TSI model 1010A constant temperature anemometer where the film acted as one leg of a Wheatstone bridge. The anemometer drives the film at some pre-set over-heat ratio. The over-heat ratios used in this experiment were 1.563 and 1.561 for the two hot-films. The air flow passing the film will cause a cooling effect and change the film resistance. The corresponding voltage output due to the resistance change is amplified and used as a feedback in maintaining the bridge in balance. Higher air flow velocity results in higher voltage output and the following experimental relation holds,

$$E^2 = A + B \cdot U_{eff}^n \tag{4.5}$$

where E is the voltage output of the anemometer, U_{eff} is the effective cooling velocity normal to the film direction, and A, B and n are constants to be determined from calibration.

The hot-film probe was calibrated against the Pitot-static tube in the core flow region of the wind-wave channel at a height of 45 cm from the mean water level, immediately before the data taking. Although the misalignment of the probe centerline to the mean flow direction was greatly reduced by using the optical transit, the angle of misalignment was determined by re-calibrating the hot-film probe after it was rotated 180° about the probe axis. The misalignment angle so obtained was then used to correct the hot-film orientation to the mean flow direction in the data-reduction process. Since calibration constants obtained from two sequential data taking days were within 1% of each other no

correction of the calibration constants was made during the data taking. Figure 4.8 shows typical calibration results of the hot-film probe.

4.5 Data-Acquisition-Reduction System

The data-acquisition-reduction system consists of an HP2100A digital computer and its peripheral devices. The computer is the central processor which can execute basic instructions in 1.96 microseconds. It is a multilevel priority interrupt system that allows input/output to take place simultaneously with program execution. It has 32k core storage providing a user area of about 25k after all the FORTRAN support subroutines are loaded into core.

The peripheral devices consisted of: CRT terminal, photo reader, paper tape punch, scope display, main disc drive, floppy disc drive, line printer, digital magnetic tape drive and Analog-to-Digital (A/D) converter. The CRT terminal is an input-output device which supplies the basic communication with the computer. The photo reader can read programs and/or data into core at a rate of 500 characters per second and the paper tape punch can punch programs and/or numerical data out of core at a rate of 120 characters per second. The scope display plots curves for data using a 256 x 256 dot matrix. The line printer output rate is 300 lines of 136 characters per minute. The digital magnetic tape drive is an HP7970B 9-track magnetic tape drive. Its recording rate is 18,000 words per second. The start and stop time of the unit is 8.66 msec. Hence the average data transfer rate is dependent on the length of the data blocks. The A/D converter is an HP2313 A/D subsystem. The sampling rate of the A/D subsystem is from 0.0004 samples/sec to 45,000 samples/sec with a 5 mV resolution and a full scale of ±10.23 volts. The subsystem can sample simultaneously up to 32 channels of data line. The main disc drive is an HP7901A disc drive. The disc used in the unit can store 1.2 million words of data. The unit has an average access time of 35 milliseconds

and an average data transfer rate of 125,000 words per second. All the system and user programs are stored on the disc and are loaded into core as needed. The floppy disc drive has basically the features similar to those of the main disc drive but with a smaller capacity and a slower speed. It provides an easier way to classify and to store programs and/or files.

The data-acquisition-reduction system was a disc operating system (DOS). The programs used to instruct the system can be written in FORTRAN, ALGOL, BASIC and assembly languages. A symbolic editor is available to aid the user in correcting or modifying programs. The operations of compiling or assembling programs, of modifying programs, and of running the resulting programs are also greatly simplified by the DOS. Calibration programs, data taking programs and data reduction programs in this experiment were written in FORTRAN.

4.6 Data Taking Procedures

The output signals of velocity from hot-film anemometers as well as that of wave height from Sanborn capacitance bridge amplifier were first conditioned before entering the data acquisition system. The purpose of the signal conditioning is to minimize the errors in digitizing caused by the A/D converter. Two types of errors are identified. One is the error due to the 5 mV resolution of the A/D converter and the other is the error due to the aliasing in the sampling. In order to minimize the resolution error, the signals must have their d.c. components suppressed and the remainder amplified to the levels as close to the peak of the dynamic range (±10.23 volts) of the A/D converter as possible, but without any overshoot. The aliasing problem only occurs when the sampling frequency is lower than the frequency bandwidth of the signals, and can be eliminated by using low pass filters. The signals after conditioning were input into the data acquisition

system that sampled the signals simultaneously at a rate of 1,000 samples/sec for 184.32 sec. Figure 4.9 shows the signal processing procedures of data taking. Since the wave height gauge was well balanced, the wave height signal had a very low d.c. level and a very narrow bandwidth; hence, only amplification was needed for the wave height signal conditioning. For 1,000 samples/sec sampling rate, the filters for hot-film signals were set at 500 Hz lowpass to satisfy the Nyquist sampling criterion.

The data taking procedures can be summarized as follows:

(1). After hot-film calibration, set the wind velocity and the frequency and the amplitude of the mechanically-generated water wave.

(2). Adjust d.c. offsets and amplifiers to obtain maximum dynamic range.

(3). Initiate the data taking program and input the parameters such as C_w, G_f, C_{wf}, k, H and sampling rate, etc.

(4). Input y* to the computer to obtain D_{wf} from Eq. (4.4).

(5). Adjust the offset and the amplitude on wave-follower control panel according to y* and D_{wf}.

(6). Instruct the computer to start sampling and to store data on digital magnetic tape.

(7). Change to new y* and repeat (4), (5), (6) to cover the whole velocity profile.

Four velocity profiles with the same mean free stream velocity (2.4 m/sec) were measured for the cases without air modulation and with air modulations at 0.4, 0.7 and 1.5 Hz respectively. A mechanically-generated water wave at 1 Hz with amplifule 2.67 cm was set throughout the experiments. Each velocity profile consisted of 18 velocities measured at different elevations ranging from 1.604 cm to 39.45 cm above the interface.

4.7 Data Reduction Scheme

The purposes of data reduction were mainly to obtain the mean field, the wave perturbation field, the air modulation field and the interaction-produced wave field. Three computer programs were developed for these purposes.

The first program (program A) is to calculate the mean velocities and the mean water level. The main components and the steps of calculation are as follows:

(A1). Call the data stored in the magnetic tape and convert them into u, v and η in cm/sec, cm/sec and cm, respectively, by using the calibration constants.

(A2). Take time average to obtain U, V and $\bar{\eta}$.

(A3). Punch U, V and $\bar{\eta}$ for later use and print U, V and $\bar{\eta}$ for record.

The second program (program B) is mainly designed for calculations of $\tilde{u}$, $\tilde{v}$ and $\tilde{r}_{ij}$ and mean values, $\overline{u_i' u_j'}$ and $\overline{\tilde{u}_i \tilde{u}_j}$. The key features and steps of the reduction precedures are:

(B1). Wave period counting from wave height signal,

(B2). Mean velocity and mean water level subtraction,

(B3). Squaring and multiplication,

(B4). Phase averaging,

(B5). Phase correction for wave height and probe oscillation correction for vertical velocity,

(B6). Mean Reynolds stresses calculation and subtraction to give $\tilde{r}_{ij}$, ($\tilde{u}$, $\tilde{v}$, $\tilde{r}_{ij}$ and the reference $\tilde{\eta}$ are obtained)

(B7). Low-pass digital filtering and re-sampling $\tilde{u}$, $\tilde{v}$, $\tilde{r}_{ij}$ and $\tilde{\eta}$ at $\Delta t_r = 23\ \Delta t$ by cyclically repeating the periodic data.

(B8). Fast Fourier transform to obtain auto-spectrum and cross-spectrum to give amplitudes of $\tilde{u}$, $\tilde{v}$, $\tilde{r}_{ij}$ and $\tilde{\eta}$, and phase lags of $\tilde{u}$, $\tilde{v}$, $\tilde{r}_{ij}$ relative to $\tilde{\eta}$.

Because there has no reference signals being recorded for the air modulation and for the interaction-produced waves the second program can not perform proper data reduction of these two fields. Consequently, a third program (program C) was constructed based on cross-correlation scheme. The main functions and steps of program C are as follows:

(C1). Mean velocity subtraction

(C2). Multiplication and squaring

(C3). Low pass digital filtering and re-sampling at $\Delta t_r = 10\ \Delta t$ to reduce computation time in step (C4).

(C4). Cross-correlation with $\cos(2\pi f_\alpha t)$ for 40 seconds

(C5). Curve fitting the correlation result to give the power $\frac{1}{2}\left|\hat{g}_\alpha\right|^2$ of the signal

(C6). Calculating the amplitude from the averaged power of several correlation results

The main component of the third program is cross-correlations of the interesting signals to an artificial cosine signal. As we will see in Section 4. 10, the correlation of a signal to a cosine signal is just equivalent to the application of a band pass digital filter. The time length of correlation must be carefully selected. Longer time of correlation implies narrower band pass, but may result in loss of information due to the frequency "jitter" in the air modulation and the possible mismatch between the frequencies of the air modulation and the artificial cosine signal. On the other hand, too short a time for the correlation usually produces results with large background noise due to turbulence, which gives more uncertainty. In view of this, a period of 40 sec was chosen in step (C4).

It is seen that time averaging, phase averaging, cross-spectral analysis and correlation are the four main techniques used in the data reduction scheme. A close look at these techniques is given in the next sections. In Section 4. 10, we show that the averaging processes and

and the Fourier transform applied in the data reduction program are also equivalent to band-pass digital filters. The fundamental properties of these processes are thus revealed. The low-pass digital filter used in steps (B7) and (C3) before the re-sampling process is of a different kind and is discussed first.

4.8 Low-Pass Digital Filter

Although the signals before entering the A/D subsystem had been analogly low pass filtered at 500 Hz for the sampling interval 0.001 sec to prevent alaising error, the alaising problem was again developed if one re-sampled the digitalized data at a longer time increments, say $m\Delta t$. The re-sampling process will change the Nyquist folding frequency to $\frac{1}{2m\Delta t}$.

A recursive digital filter used in the present data reduction scheme is one adopted from Bendat and Piersol (1971). The filter executes according to the following relation,

$$y_n = (1 - A)x_n + A \cdot y_{n-1} \tag{4.6}$$

where $x_n = x(n\Delta t)$ is the input signal and $y_n = y(n\Delta t)$ is the filtered signal. In the frequency domain, the linear transfer function of the digital filter is

$$H(f) = \frac{1 - A}{1 - A \cdot e^{-i2\pi f\Delta t}} \tag{4.7}$$

Hence

$$\left|H(f)\right|^2 = \frac{(1 - A)^2}{(1+A^2) - 2A \cdot \cos(2\pi f\Delta t)} \tag{4.8}$$

represents the filter gain of the power spectrum of signal.

Figure 4.10 shows the sketch of the characteristics of the low pass digital filter for $A = 0.98$ and $\Delta t = 0.001$ seconds, which were used in the present data analysis programs. The power spectrum of the digitally-filtered data was then restored by the frequency dependent gain factor given by (4.8) and the restoration results in a numerical error less than 0.1%.

4.9 Cross-Correlation and Cross-Spectral Analysis

In this and the next sections, all the time varying functions are regarded as real unless specified otherwise. The cross-correlation of a signal g(t) to a reference signal h(t) is defined by

$$R_{hg}(\xi) = \overline{h(t)g(t+\xi)} = \lim_{T\to\infty} \frac{1}{T} \cdot \int_{-T/2}^{T/2} h(t)g(t+\xi)dt \qquad (4.9)$$

The cross-spectral density of h and g is defined as the Fourier transform of the cross-correlation, i.e., as

$$\Phi_{hg}(f) = \int_{-\infty}^{\infty} R_{hg}(\xi) \cdot e^{-i2\pi f\xi} d\xi \qquad (4.10)$$

$$= C_{hg}(f) - iQ_{hg}(f) \qquad (4.11)$$

where C_{hg} is the co-spectra and Q_{hg} is the quadrature spectra. The phase lag of g to h is then given by

$$\theta_{hg}(f) = \tan^{-1}\left[\frac{Q_{hg}(f)}{C_{hg}(f)}\right]^{o} + He(-C_{hg})\,180^{o} \qquad (4.12)$$

where He(x) is the Heaviside unit step function defined by

$$He(x) = \begin{cases} 1 , & x > 0 \\ 0 , & x \leq 0 \end{cases} \tag{4.13}$$

Fourier transformation of (4.9) also gives

$$\Phi_{hg}(f) = G(f) \cdot H^*(f) \cdot df \tag{4.14}$$

where G and H are the Fourier transforms of g and h and * denotes the complex conjugate. Hence the cross-spectral density can be obtained by direct transformation of g and h. The auto-spectral density is obtained by letting h = g, i.e.,

$$\Phi_{gg}(f) = G(f) \cdot G^*(f) \cdot df = C_{gg}(f) \tag{4.15}$$

because, when h = g, $R_{gg}(\xi)$ is symmetric and $Q_{gg}(f) = \int_{-\infty}^{\infty} R_{gg}(\xi) \sin 2\pi f \xi \, d\xi = 0$ from (4.10).

For two sinusoidal functions h(t) and g(t), which are of main interest in this study and are given by

$$h(t) = \left| \hat{h}_\alpha \right| \cdot \cos(2\pi f_\alpha t) \tag{4.16}$$

and

$$g(t) = \left| \hat{g}_\alpha \right| \cdot \cos(2\pi f_\alpha t - \theta_\alpha) , \tag{4.17}$$

The cross-correlation of g to h is

$$R_{hg}(\xi) = \frac{\left| \hat{h}_\alpha \right| \cdot \left| \hat{g}_\alpha \right|}{2} \cos(2\pi f_\alpha \xi - \theta_\alpha) \tag{4.18}$$

and the cross-spectrum is

$$\Phi_{hg}(f) = \frac{|\hat{h}_\alpha| \cdot |\hat{g}_\alpha|}{4} \left[e^{-i\theta_\alpha} \delta(f-f_\alpha) + e^{i\theta_\alpha} \delta(f+f_\alpha) \right] \tag{4.19}$$

where $\delta(f)$ is the Dirac delta function. The phase lag at $f = f_\alpha$ is then equal to

$$\theta_{hg}(f_\alpha) = \tan^{-1} \left\{ \frac{\frac{|\hat{h}_\alpha| \cdot |\hat{g}_\alpha|}{4} \cdot \left[\delta(f-f_\alpha)\sin\theta_\alpha - \delta(f+f_\alpha)\sin\theta_\alpha \right]}{\frac{|\hat{h}_\alpha| \cdot |\hat{g}_\alpha|}{4} \cdot \left[\delta(f-f_\alpha)\cos\theta_\alpha - \delta(f+f_\alpha)\cos\theta_\alpha \right]} \right\}_{f=f_\alpha}$$

$$= \tan^{-1}(\tan\theta_\alpha)$$

$$= \theta_\alpha \tag{4.20}$$

The amplitude of g is calculated from integrating the auto-spectrum of g over a neighborhood of $f = f_\alpha$, i.e.,

$$\frac{|\hat{g}_\alpha|^2}{4} = \int_{f_\alpha - \Delta_1}^{f_\alpha + \Delta_1} \Phi_{gg}(f)df$$

$$|\hat{g}_\alpha| = 2 \left[\int_{f_\alpha - \Delta_1}^{f_\alpha + \Delta_1} \Phi_{gg}(f)df \right]^{1/2} \tag{4.21}$$

where Δ_1 is a finite value which depends on the length of the data used in the Fourier transformation. Theoretically, if an infinitely long record was used in the Fourier transformation, Δ_1 can be chosen as small as one wishes; but, when the finite length T_f of record is used the delta function distribution of the auto-spectrum is spread into a

finite narrow band which is proportional to $\frac{1}{T_f}$, as we will see in the next section. Hence, a finite Δ_1 is required during the practical calculation. The value Δ_1 used in this study was $\frac{5}{T_f}$.

4.10 Band-Pass Digital Filters

In digital processing, the correlation given by (4.9) is written as

$$R_{hg}(\xi) = \lim_{M\to\infty} \frac{1}{2M+1} \sum_{m=-M}^{M} h(m\Delta t_1)g(m\Delta t_1+\xi) \tag{4.22}$$

by letting $T = (2M+1)\Delta t_1$. In (4.22), as long as M is large enough, Δt_1 need not be equal to the sampling interval of data taking Δt since we have assumed the processes are stationary. The actual computation of (4.22) is only possible for finite T, and (4.22) is changed to

$$\overline{[h(t)g(t+\xi)]}_T = \frac{1}{2M+1} \sum_{m=-M}^{M} h(m\Delta t_1)g(m\Delta t_1+\xi) \tag{4.23}$$

where the subscript T indicates the finite time calculation. The selection of the time interval Δt_1 depends on the frequency range of interest. When M is fixed, a larger Δt_1 was usually required for the lower frequency range to provide better resolution.

It is of interest that, when $h(t) = 1$ and $\Delta t_1 = \Delta t$, (4.23) reduces to

$$\bar{g}_T(\xi) = \frac{1}{2M+1} \sum_{m=-M}^{M} g(m\Delta t + \xi) , \tag{4.24}$$

which is the familiar finite time average. The similarity between the phase average and the time average stated in Chapter 2 suggests that,

when $h(t) = 1$ and $\Delta t_1 = \tau$ (the wave period of the water wave), (4.23) then describes the phase average,

$$\langle g_T \rangle = \frac{1}{2M+1} \sum_{m=-M}^{M} g(m\tau + \xi) \tag{4.25}$$

Other interesting digital processes such as correlation to cosine waves can be obtained by replacing $h(t)$ by $\cos(2\pi f_\alpha t)$. Before we discuss the individual processes, the general behavior of the digital filter corresponding to the correlation described by (4.23) and the uncertainty inherent due to the finite T are examined.

By introducing the symbolic functions $\Pi(t)$ and $\text{Ш}(t)$ (see Bracewell 1966), i.e.,

$$\Pi(t) = \begin{cases} 1 \ , & -\frac{1}{2} < t < \frac{1}{2} \\ 0 \ , & \text{otherwise} \end{cases} \tag{4.26}$$

and

$$\text{Ш}(t) = \sum_{n=-\infty}^{\infty} \delta(t-n) \ , \tag{4.27}$$

we can rewrite (4.23) as

$$\overline{[h(t)g(t+\xi)]}_T = \int_{-\infty}^{\infty} \frac{1}{T} \cdot \Pi\left(\frac{t}{T}\right) \text{Ш}\left(\frac{t}{\Delta t_1}\right) h(t)g(t+\xi) \cdot dt \tag{4.28}$$

If we let $t + \xi = \lambda$, (4.28) is changed to

$$\overline{[h(t)g(t+\xi)]}_T = \int_{-\infty}^{\infty} \frac{1}{T} \cdot \Pi\left(\frac{\lambda-\xi}{T}\right) \cdot \text{Ш}\left(\frac{\lambda-\xi}{\Delta t_1}\right) h(\lambda-\xi)g(\lambda)d\lambda \tag{4.29}$$

Since Π and Ш are even functions, equation (4.29) may be written as

$$\overline{[h(t)g(t+\xi)]}_T = \int_{-\infty}^{\infty} \frac{1}{T}\,\Pi\left(\frac{\xi-t}{T}\right)\,\text{Ш}\left(\frac{\xi-t}{\Delta t_1}\right)h(t-\xi)g(t)dt$$

$$= h_T(t) \;@\; g(t) \tag{4.30}$$

where

$$h_T(t) = \frac{1}{T}\,\Pi\left(\frac{t}{T}\right)\,\text{Ш}\left(\frac{t}{\Delta t_1}\right)h(-t) \tag{4.31}$$

and @ denotes the convolution operator.

Denoting the Fourier transform of $\overline{[h(t)g(t+\xi)]}_T$ by $F\left\{\overline{[h(t)g(t+\xi)]}_T\right\}$, using the convolution theorem and taking the Fourier transformation of (4.30), we have

$$F\left\{\overline{[h(t)g(t+\xi)]}_T\right\} = H_T(f)G(f) \tag{4.32}$$

The similarity theorem given by

$$F\{x(at)\} = \frac{1}{a}\,X\left(\frac{f}{a}\right) \tag{4.33}$$

and the convolution theorem of the inverse transform given by

$$F^{-1}\{X(f) \;@\; Y(f)\} = x(t)y(t) \tag{4.34}$$

suggest that Fourier transformation of (4.31) gives

$$H_T(f) = \frac{1}{T}\left[F\left\{\Pi\left(\frac{t}{T}\right)\right\} \;@\; F\left\{\text{Ш}\left(\frac{t}{\Delta t_1}\right)\right\}\right] \;@\; F\left\{h(-t)\right\}$$

$$= [\,\mathrm{sinc}(Tf) \circledast \Delta t_1 \amalg(\Delta t_1 f)\,] \circledast H(-f) \tag{4.35a}$$

$$= [\,\mathrm{sinc}(Tf) \circledast H(-f)\,] \circledast \Delta t_1 \amalg(\Delta t_1 f) \tag{4.35b}$$

where

$$F\{\Pi(t)\} = \mathrm{sinc}(f) = \frac{\sin \pi f}{\pi f} \tag{4.36}$$

and

$$F\{\amalg(t)\} = \amalg(f) \tag{4.37}$$

were used. The plot of $\mathrm{sinc}(Tf) \circledast H(-f)$ and $H_T(f)$ when $H(f)$ particularly has a narrow bandwidth is shown in Figure 4.11(a), (b).

The uncertainty introduced by the finite time T during the data processing is expressed by calculating the standard deviation of $\overline{[h(t)g(t+\xi)]}_T$, namely,

$$\sigma = \left\{ \overline{\left(\overline{[h(t)g(t+\xi)]}_T - \overline{h(t)g(t+\xi)} \right)^2} \right\}^{1/2} \tag{4.38}$$

Let the error of the correlation at time ξ be represented by $e_T(\xi)$; then

$$\overline{[h(t)g(t+\xi)]}_T = \overline{h(t)g(t+\xi)} + e_T(\xi) \tag{4.39}$$

The limiting case as $T \to \infty$ yields

$$\lim_{T\to\infty} \overline{[h(t)g(t+\xi)]}_T = \overline{h(t)g(t+\xi)} \tag{4.40}$$

and

$$\lim_{T\to\infty} e_T(\xi) = 0 \tag{4.41}$$

Hence, (4.38) can be expressed as

$$\sigma = \left\{ \overline{e_T^2(\xi)} \right\}^{1/2} \tag{4.42}$$

$$= \left\{ \int_{-\infty}^{\infty} \Phi_{e_T e_T}(f)df \right\}^{1/2} \tag{4.43}$$

where $\Phi_{e_T e_T}$ is auto-spectral density of $e_T(\xi)$ defined by

$$\Phi_{e_T e_T}(f) = \int_{-\infty}^{\infty} \overline{e_T(\xi)e_T(\xi+s)} \cdot e^{-i2\pi fs} ds \tag{4.44}$$

Evaluating the inverse transform of (4.44) at $s = 0$ leads to

$$\overline{e_T(\xi)e_T(\xi+s)} \Big|_{s=0} = \int_{-\infty}^{\infty} \Phi_{e_T e_T} e^{i2\pi fs} df \Big|_{s=0}$$

i.e.

$$\overline{e_T^2(\xi)} = \int_{-\infty}^{\infty} \Phi_{e_T e_T}(f) \cdot df \tag{4.45}$$

which also gives (4.43).

When h(t) and g(t) are band limited in the frequency band $-f_N < f < f_N$, where $f_N = \frac{1}{2\Delta t}$ is the Nyquist frequency, the spectral density $\Phi_{e_T e_T}(f)$ is also limited in this frequency band. Equation (4.43) can be reduced to

$$\sigma = \left\{ \int_{-f_N}^{f_N} \Phi_{e_T e_T}(f) \cdot df \right\}^{1/2} \tag{4.46}$$

The relative uncertainty is given by

$$\epsilon_r = \frac{\sigma}{\left\{ \left[\overline{h(t)g(t+\xi)} \right]^2 \right\}^{1/2}} \cdot 100\% \tag{4.47}$$

4.11 Digital Filters of Specific Data Reduction Processes

Application of the theory described in Section 4.10 to some particular processes is discussed in the following:

A. Time average ($h(t) = 1$, $\Delta t_1 = \Delta t$)

When $h(t) = 1$ and $\Delta t_1 = \Delta t$, $\overline{[h(t)g(t+\xi)]}_T = \overline{g}_T(\xi)$ reduces to the time average. For a quantity g decomposed into

$$g = \overline{g} + \tilde{g} + g' = \overline{g} + g'' \ , \tag{4.48}$$

the time average over period T gives

$$\overline{g}_T = \overline{g} + \overline{g}''_T \tag{4.49}$$

Since $H(f) = F\{1\} = \delta(f)$, from (4.35) we have

$$H_T(f) = \text{sinc}(Tf) \circledast \Delta t \, \text{Ш}(\Delta t f) \tag{4.50}$$

Figure 4.11(c) shows the sketch of (4.50).

The linear relationship given by $G_T(f) = H_T(f) \cdot G(f)$ also suggests that

$$\bar{G}''_T(f) = H_T(f)G''(f)$$

Hence, the spectrum density for $\bar{g}''_T(t)$ is

$$\Phi_{\bar{g}''_T\bar{g}''_T}(f) = \left| H_T(f) \right|^2 \cdot \Phi_{g''g''}(f) \tag{4.51}$$

Since $\tilde{g}$ and g' are uncorrelated, transformation of $g'' = \tilde{g} + g'$ will ultimately lead to

$$\Phi_{g''g''}(f) = \Phi_{\tilde{g}\tilde{g}}(f) + \Phi_{g'g'}(f) \tag{4.52}$$

When

$$\tilde{g}(t) = \sum_{\alpha=1}^{n} \left|\hat{g}_\alpha\right| \cos(2\pi f_\alpha t - \theta_\alpha) ,$$

the spectrum $\Phi_{\tilde{g}\tilde{g}}$ is

$$\Phi_{\tilde{g}\tilde{g}}(f) = \sum_{\alpha=1}^{n} \frac{\left|\hat{g}_\alpha\right|^2}{4} \cdot \left[\delta(f-f_\alpha) + \delta(f+f_\alpha)\right] . \tag{4.53}$$

If T is sufficiently large,

$$\left|H_T(f)\right|^2 \approx \text{sinc}^2(Tf) \sim \frac{1}{T}\delta(f) \quad , \quad -f_N < f < f_N \tag{4.54}$$

Substituting equations (4.52), (4.53) and (4.54) into (4.51) and identifying that $e_T = \bar{g}''_T$ for time average, we have the standard deviation calculated from (4.46), i.e.,

$$\sigma = \left\{ \int_{-f_N}^{f_N} \Phi_{\bar{g}''_T\bar{g}''_T}(f)\,df \right\}^{1/2}$$

$$= \left\{ \int_{-f_N}^{f_N} \mathrm{sinc}^2(Tf) \left[\Phi_{g'g'}(f) + \Phi_{\tilde{g}\tilde{g}}(f) \right] \cdot df \right\}^{1/2}$$

$$\sim \left\{ \frac{1}{T} \Phi_{g'g'}(0) + \sum_{\alpha=1}^{n} \mathrm{sinc}^2(Tf_\alpha) \frac{\left|\hat{g}_\alpha\right|^2}{2} \right\}^{1/2}$$

$$= \left\{ \frac{2\,\overline{g'^2}\,\Lambda_{g'}}{T} + \sum_{\alpha=1}^{n} \mathrm{sinc}^2(Tf_\alpha) \frac{\left|\hat{g}_\alpha\right|^2}{2} \right\}^{1/2} \qquad (4.55)$$

where $\overline{g'^2}$ is the power of g' and $\Lambda_{g'}$ is the integral time scale of g' defined by

$$\Lambda_{g'} = \int_0^\infty \frac{R_{g'g'}(\xi)}{R_{g'g'}(0)} d\xi \qquad (4.56)$$

In (4.55), the summation term is usually small compared to the first term when T is large. Then

$$\sigma \sim \left\{ \frac{2\,\overline{g'^2}\,\Lambda_{g'}}{T} \right\}^{1/2} \qquad (4.57)$$

The relative error is now given by

$$\epsilon_r = \frac{\sigma}{\overline{g}} \cdot 100\% \qquad (4.58)$$

B. Phase average ($h(t) = 1$, $\Delta t_1 = \tau$)

The function $H_T(f)$ is now changed to

$$H_T(f) = \mathrm{sinc}(Tf) \circledast \tau \amalg(\tau f) \qquad (4.59)$$

which is shown in Figure 4.11(d). For a signal with mean subtracted, $g = \tilde{g} + g'$, the standard deviation σ can be similarly obtained by the procedure used above, and the result is

$$\sigma = \left\{ 2\,\overline{g'^2}\,\Lambda_{g'}\gamma \cdot \frac{1}{T} \right\}^{1/2} \tag{4.60}$$

where

$$\gamma = 1 + 2 \sum_{m=1}^{\tau f_N} \frac{\Phi_{g'g'}(\frac{m}{\tau})}{\Phi_{g'g'}(0)} \tag{4.61}$$

The relative error ϵ_r is

$$\epsilon_r = \frac{\sigma}{\left(\overline{\tilde{g}^2}\right)^{1/2}} \; 100\% \tag{4.62}$$

C. Fourier transform $(h(t) = T \cdot e^{-i2\pi f_\alpha t},\ \Delta t_l = \Delta t_r)$

Since the Fourier transform of $e^{-i2\pi f_\alpha t}$ is $\delta(f+f_\alpha)$, it is easy to show that, for this case,

$$H_T(f) = T \cdot \mathrm{sinc}(Tf - Tf_\alpha) \circledast \Delta t_r \text{Ш}(\Delta t_r f) \tag{4.63}$$

Hence, the Fourier transform itself works like a band-pass digital filter with a gain factor T and a band width $\frac{2}{T}$. Plot of $\frac{1}{T} H_T(f)$ is shown in Figure 4.11(e).

The standard deviation calculation previously mentioned is not applicable here because h(t) is a complex quantity. But fortunately this is not significant to the present study. Since the Fourier transform used in the data reduction is mainly to obtain the autospectrum and the cross-spectrum in determining the amplitude and the phase

AD-A044 743 STANFORD UNIV CALIF DEPT OF CIVIL ENGINEERING F/G 8/3
THE STRUCTURE OF MODULATED TURBULENT FLOW OVER PROGRESSIVE WATE--ETC(U)
AUG 77 C HSU, E Y HSU, R L STREET DAAG29-76-G-0125
UNCLASSIFIED TR-221 NL

2 OF 3
AD
A044743

relationship of wave perturbations, the error produced can only be obtained by directly examining the spectral structure.

The digital form of Fourier transform in finite time T can be written as

$$F_T\{g(t+\xi)\} = \int_{-T/2}^{T/2} g(t+\xi)\cdot e^{-i2\pi f_\alpha t}\,dt$$

$$= \frac{1}{2N+1}\sum_{n=-N}^{N} Tg(n\Delta t+\xi)\,e^{-i2\pi f_\alpha n\Delta t}$$

$$= \int_{-\infty}^{\infty} \Pi\left(\frac{t}{T}\right)\text{Ш}\left(\frac{t}{\Delta t_r}\right) g(t+\xi)\; e^{-i2\pi f_\alpha t}\,dt \qquad (4.64)$$

$$= \left[T\,\mathrm{sinc}(Tf_\alpha) \circledast \Delta t_r\,\text{Ш}(\Delta t_r f_\alpha)\right] \circledast \left[G(f_\alpha)e^{i2\pi f_\alpha \xi}\right] \qquad (4.65)$$

Taking the complex conjugate of (4.65) and using the relationship denoted by (4.15), we have

$$(\Phi_{gg})_T(f_\alpha) = \int_{-\infty}^{\infty} |A(f)|^2\,\Phi_{gg}(f_\alpha - f)\,df \qquad (4.66)$$

where $(\Phi_{gg})_T(f)$ and $\Phi_{gg}(f)$ are the auto-spectra of g corresponding to the finite time and the infinite time Fourier transforms respectively, and

$$A(f) = T\cdot\mathrm{sinc}(Tf) \circledast \Delta t_r\,\text{Ш}(\Delta t_r f) \qquad (4.67)$$

It is easy to show that the cross-spectra have the following relation,

$$(\Phi_{hg})_T(f_\alpha) = \int_{-\infty}^{\infty} |A(f)|^2 \cdot \Phi_{hg}(f_\alpha - f)\,df \tag{4.68}$$

When $g = \tilde{g} + g'$, the amplitude calculation of wave perturbation quantities according to (4.21) will develop an approximate relative error,

$$\epsilon_a = \frac{4\,\Delta_1 \Phi_{g'g'}(f_\alpha)}{|\hat{g}_\alpha|^2} \cdot 100\% \tag{4.69}$$

The uncertainty in phase calculation from the cross-spectrum by using (4.12) will produce an approximate relative error,

$$\epsilon_{\theta_\alpha} = \frac{4\,|\Phi_{h'g'}(f_\alpha)|}{T\,|\hat{h}_\alpha|\,|\hat{g}_\alpha|} \cdot \frac{180^\circ}{3.1416} \tag{4.70}$$

D. Correlation to cosine ($h(t) = \cos(2\pi f_\alpha t)$, $\Delta t_1 = \Delta t_r$)

Since $H(f)$ is now

$$H(f) = \frac{1}{2}[\delta(f - f_\alpha) + \delta(f + f_\alpha)]\ ,$$

the filter characteristic is then

$$H_T(f) = [\,\frac{1}{2}\,\mathrm{sinc}(Tf - Tf_\alpha) + \frac{1}{2}\,\mathrm{sinc}(Tf + Tf_\alpha)\,] \;@\; \Delta t_r \text{Ш}(\Delta t_r f) \tag{4.71}$$

Plot of (4.71) is given in Figure 4.11(f).

For a signal represented as

$$g = |\hat{g}_\alpha| \cos(2\pi f_\alpha t - \theta_\alpha) + g'\ ,$$

we have

$$\sigma = \left\{ \frac{2}{T} \cdot \overline{g'^2} \cdot \Lambda_{g'} \cdot \gamma_c \right\}^{1/2} \tag{4.72}$$

where

$$\gamma_c = \frac{\Phi_{g'g'}(f_\alpha) + \Phi_{g'g'}(-f_\alpha)}{\Phi_{g'g'}(0)} \tag{4.73}$$

and the relative error ϵ_r is

$$\epsilon_r = \frac{\sqrt{2} \cdot \sigma}{|\hat{g}_\alpha|} \ 100\% \tag{4.74}$$

CHAPTER 5

EXPERIMENTAL RESULTS

5.1 General

In Chapters 2 and 3, physical quantities such as velocities and Reynolds stresses that govern the interface flows have been described, and in Chapter 4, reliable schemes to obtain data associated with such flow quantities have also been given. The data obtained are presented in this chapter, together with a discussion of their features. Comparisons of our data to that of other studies are also made when appropriate.

As described in the previous chapters, the data were obtained in the Stanford wind-wave channel at a station 13 m from the test section entrance. The mean free stream velocity was 2.4 m/sec with air modulations at f_a = 0.0, 0.4, 0.7, or 1.5 Hz where the flow without air modulation is regarded as f_a = 0.0 Hz. The air flows were over a 1 Hz mechanically-generated, sinusoidal water wave with an amplitude of 2.67 cm. The reduced data consist of those associated with the mean flow, the wave perturbation, the air modulation, and the interaction-produced wave. The effects of the air modulations on the wave perturbations are also presented.

The flow quantities are generally presented in profile distributions as a function of y* ordinates. The profiles are usually in non-dimensional forms; the mean free stream velocity U_∞ and its square U_∞^2 are used to normalize the velocities and the Reynolds stresses respectively. The ordinates y* are generally normalized by 1/k, where k is the wave number. As shown in Section 5.3 the boundary layer thickness is 23.16 cm. Accordingly, a factor of

$$\frac{y^*/\delta}{y^* \cdot k} = \frac{1}{k \cdot \delta} = \frac{1}{(.04026) \cdot (23.16)} = 1.072$$

should be applied to ky* if one wishes to interpret the data in y^*/δ coordinates.

Since we have denoted that the wave perturbation quantity

$$\tilde{g}_\alpha = |\hat{g}_\alpha| \cos(\omega_\alpha t - \theta_{\tilde{g}_\alpha}) + \text{harmonics} ,$$

$\tilde{g}_\alpha$ includes all harmonics, while $|\hat{g}_\alpha|$ and $\theta_{\tilde{g}_\alpha}$ are the amplitude and the phase of the fundamental mode. The phase $\theta_{\tilde{g}_\alpha}$ is the phase lag with respect to time using the water wave as a reference. In this study, the harmonic modes are generally weak compared to the fundamental mode; hence, the wave perturbation quantity can be approximated by its fundamental mode without changing the overall conclusion.

The ambient temperature during the period of data taking was quite steady to within $\pm 1^{\circ}C$. The ambient pressure variation was also less than 0.5 mm of mercury. Thus, the effects of ambient temperature and pressure are negligible. The data uncertainty is estimated and is presented in Appendix I.

5.2 Water Wave Field and Surface Condition

Before presenting the air flow fields, the water wave field and the surface condition should be identified. A typical result of the phase average of the mechanically-generated water wave is shown in Figure 5.1(a), (b), together with the phase average results of $\tilde{u}$, $\tilde{v}$, and $\tilde{r}_{ij}$ for $y^* = 1.604$ cm. The position $y^* = 1.604$ cm is the elevation closest to the interface in our data. The phase average result is used to obtain the amplitude and the phase lag for each mode by Fast Fourier Transform (FFT) and cross-spectral analysis. When 1024 data points with sampling interval 0.001 sec were used, the resolution of the spectrum was 0.976 Hz. The resolution is improved to 0.0424 Hz by artificially repeating the phase average results, low-pass digital

filtering and re-sampling at an interval 0.023 sec as described in Chapter 4. The result of auto-spectral analysis for $\tilde{\eta}$ shows that the harmonic modes produced by the Stokes non-linear phenomena are less than 5% of the fundamental mode and are negligible. The parameter ka is 0.1075 corresponding to a = 2.67 cm.

For U_∞ = 2.4 m/sec, the ripples riding on the mechanically-generated water waves are small but visible. If we denote the ripples by η', the randomness of the ripples results in $\overline{\eta}' = \langle \eta' \rangle = 0$. However, the mean square $\overline{\eta'^2}$ is non-zero and represents the square of mean roughness of the water surface on the mechanically-generated water waves. It is anticipated that η'^2 is perturbed by the mechanically-generated water waves in a way similar to that by which the turbulent Reynolds stresses are perturbed. Hence

$$\eta'^2 = \overline{\eta'^2} + \widetilde{\eta'^2} + (\eta'^2)' \tag{5.1a}$$

and

$$\langle \eta'^2 \rangle = \overline{\eta'^2} + \widetilde{\eta'^2} \tag{5.1b}$$

Figure 5.2 shows the results of $\widetilde{\eta'^2}$ with $\overline{\eta'^2}$ given in the legend. The values $\overline{\eta'^2} \cdot 10^2$ are 0.9778, 0.7805, 0.7374 and 0.7469 cm^2 for the air modulations at 0., 0.4, 0.7, and 1.5 Hz respectively. The root mean square $\sqrt{\overline{\eta'^2}}$ is approximately 0.09 cm which is roughly 3% of the amplitude of the mechanically-generated water wave.

Wu (1973) observed that the effect of the air modulations was to produce more capillary waves in a wind-generated wave field. In the presence of the mechanically-generated water wave, the decrease in the mean square values of the ripples in the present experiment shows that the air modulations tend to impede ripple production. This difference suggests that the mechanism of wind-wave generation over swell (long water wave) is different from that over a flat water surface. The

distortion of the wind field due to swell and the interaction between the ripples and the swell may contribute to this inconsistency. For future investigation, experiments with modulated air flows over wind-generated waves, performed at the Stanford wind-wave channel, are needed in resolving the ripple structure.

The mean square values of the ripples also show that the effect of the air modulations is prominent when the frequency of the air modulation is close to the frequency of the mechanically-generated water wave as shown in Figure 5.2. Figure 5.2 shows also that (a) the ripples are high at both windward and leeward of the mechanically-generated water wave, (b) they are moderate in the trough, and (c) they are almost zero on the crest. The recovery of the ripple roughness for f_a = 1.5 Hz is expected because the ripple structure should return to that of the no air modulation situation when f_a is sufficiently high. (At very high f_a, the channel flow does not respond to the air flow pulser, hence the flow is equivalent to that without air modulation.)

With the aid of $\tilde{r}_{12}$ shown in Figure 5.1(b) at the lowest elevation y^* = 1.604 cm in our data (Details of $\tilde{r}_{12}$ will be discussed in Section 5.4(c).), it is now possible to determine the surface condition over the mechanically-generated water waves. If the surface is fully rough, we expect that $\tilde{r}_{12}$ near the interface should strongly correlate with $\widetilde{\eta'^2}$. However, the data of $\tilde{r}_{12}$ shown in Figure 5.1(b) indicate that $\tilde{r}_{12}$ strongly correlates to $\tilde{\eta}$ instead of to $\widetilde{\eta'^2}$. This implies that $\tilde{r}_{12}$ is mainly induced by the mechanically-generated water wave. As shown in the next section the friction velocity u_* in this study is 8.578 cm/sec, for $z_o = \sqrt{\overline{\eta'^2}} \simeq 0.09$ cm the roughness parameter $z_o^+ = \frac{z_o u_*}{\nu}$ is 4.95; hence, the surface condition is aerodynamically smooth.

5.3 Mean Flow Fields

The mean flow fields presented are those for velocities and turbulent Reynolds stresses. These two fields determine the basic mean turbulent flow upon which the wave perturbations and the air modulations were imposed. This basic mean flow should be identified before examining the wave perturbation and the air modulation fields because different mean flows result in different wave perturbations and air modulations.

(a). Mean velocity profiles

The mean horizontal velocity behaves like a typical turbulent boundary layer flow. To obtain a better understanding, the traditional log-linear plot (U versus logarithmic y*) was used and the results are shown in Figure 5.3. When the linear portion of the profiles in Figure 5.3 was used to curve-fit

$$U = \frac{u_*}{k_o} \cdot \ln y^* + D \qquad (5.2)$$

the friction velocity u_* found by assuming $k_o = 0.40$ is approximately 30% greater than that calculated from the direct measurement, i.e., $u_*^2 = -\overline{u''v''}$ (the value of $-\overline{u''v''}$ will be discussed later). We also found that the results of u_* depend on the number of points in the linear portion of the profiles used for curve-fitting, the variation being as large as 15%. In addition, when the wall coordinates

$$u^+ = \frac{U}{u_*} \qquad \text{and} \qquad y^+ = \frac{y^* u_*}{\nu} \qquad (5.3a, b)$$

are used, all the y^+ values corresponding to the data points are greater than 100, which is in contrary to the argument that the log-linear profile exists only in the region where $30 < y^+ < 70$. Hence, we conclude that the simple log-linear curve-fitting procedure is not adequate.

A better representation of the mean velocity U was achieved by identifying the wake characteristics near the outer edge of the boundary layer. The wake behavior was also observed in the Stanford wind-wave channel by Young et al. (1973) for both the flat-plate and the interface flows. In the outer region, the profile is the "law of the wake" (Coles 1956), which can be written as

$$\frac{U_\infty - U}{u_*} = -\frac{1}{k_o} \ln \frac{y^*}{\delta} + \frac{W_c}{k_o} \left[2 - W\left(\frac{y^*}{\delta}\right) \right] \tag{5.4}$$

where W is the wake function and W_c is the wake parameter. The wake function W can be approximated by (Hinze 1975)

$$W\left(\frac{y^*}{\delta}\right) = 1 - \cos\left(\frac{\pi y^*}{\delta}\right) \tag{5.5}$$

The wake parameter W_c can only vary with x^* when the outer layer profile of the flow is not self-similar. Substituting (5.5) into (5.4) and rewriting (5.4) into the wall variables, we find

$$u^+ = \frac{1}{k_o} \ln y^+ + \left(u_\infty^+ - \frac{1}{k_o} \ln \delta^+ - 2\frac{W_c}{k_o} \right) + \frac{W_c}{k_o} \left[1 - \cos\left(\frac{\pi y^+}{\delta^+}\right) \right] \tag{5.6}$$

where

$$u_\infty^+ = \frac{U_\infty}{u_*} \quad \text{and} \quad \delta^+ = \frac{\delta u_*}{\nu}$$

Equation (5.2) is the asymptotic form of the inner profile governed by the "law of the wall", and can be written as

$$u^+ = \frac{1}{k_o} \ln y^+ + C \tag{5.7}$$

As $y^* \to 0$, (5.6) asymptotically matches (5.7) with the matching condition

$$C = u_{\infty}^{+} - \frac{1}{k_o} \ln \delta^{+} - 2 \frac{W_c}{k_o} \tag{5.8}$$

So, the outer profile

$$u^{+} = \frac{1}{k_o} \ln y^{+} + C + \frac{W_c}{k_o} \left[1 - \cos\left(\frac{\pi y^{+}}{\delta^{+}} \right) \right] \tag{5.9}$$

applies also in the log-linear region.

The experimental data for the mean velocity were curve-fitted to the wake log-linear profile to determine U_{∞}, u_* and δ by the least-square method. The profile parameters C, W_c and δ^{+} and then the profiles described by (5.9) were calculated. The comparisons between the data and the curve-fit results are shown in Figures 5.4(a), (b). The agreements are excellent. Table 5.1 shows the velocity-profile parameters and the comparison of u_* between the results of curve-fitting and of direct measurement. The comparison of u_* results in an average difference of 1.23%. The measured u_* given in Table 5.1 was computed from the lowest point of the $\overline{-u''v''}$ profiles. From Table 5.1, the parameters U_{∞}/c, u_*/U_{∞} and $U_{\infty}\delta/\nu$ (Reynolds number) which characterize the mean flow were determined and were 1.541, 0.03589, and 35,700 respectively.

The vertical mean velocity V is shown in Figure 5.5. The negative value of V indicates that the vertical mean velocity is downward toward the interface. The magnitude of V decreases to zero when it approaches to the interface where the boundary condition for V is zero. The downward vertical mean velocity is regarded as the result of the drift current at the interface. At the interface, the developing drift current results in $\frac{\partial U}{\partial x^*} > 0$; hence from the continuity equation,

$$\frac{\partial U}{\partial x^*} + \frac{\partial V}{\partial y^*} = 0 ,$$

we have $\frac{\partial V}{\partial y^*} < 0$. So, with $V = 0$ at the interface, V should be negative in the boundary layer. The change of V is large near the interface and decays to zero at the free stream as shown in Figure 5.5.

(b). Mean Reynolds stresses and turbulent intensity

Since as described in Chapter 4, the subtraction of the air modulation velocity from the total velocity is not feasible, the mean Reynolds stresses $\overline{u_i'' u_j''}$ contain the contribution from the air modulation. For a fully-developed flow, $\overline{-u''v''}$ and $\overline{v''v''}$ are not affected by the air modulation because $\tilde{v}_a$ equals to zero and $\tilde{u}_a$ is not correlated with v'. This was the case in the study of Acharya and Reynolds (1975) since their flow was fully-developed and there was no water waves; however, this is not the case in this study because there exists the interaction-produced wave component $\tilde{u}_{is}$ and the component $\tilde{v}_a$ may exist. (The existence of $\tilde{v}_a$ may be due to the weak development of the boundary layer.) As shown in Figure 5.6, the values of $\overline{-u''v''}$ and $\overline{v''v''}$ for modulated air flows are systematically, but not largely different from those without air modulation. However, the difference is small.

In Figure 5.6, an almost constant shear layer is observed in the lower portion of the $\overline{-u''v''}$ profiles. The slight decrease of the shear stress at the lowest portion of the constant shear layer is regarded as the release of the shear stress caused by the developing drift current. It can not be regarded as the influence of viscous effects because all the y^+ values corresponding to the data obtained are greater than 87 so the viscous effect can be ignored.

The magnitude of $\overline{u''u''}$ shown in Figure 5.6 is approximately one order larger than those of $\overline{-u''v''}$ and $\overline{v''v''}$; this is as expected. (Note the different scales used for $\overline{-u''v''}$ and $\overline{v''v''}$ in the plots.) The

greater values of $\overline{u''u''}$ for the air flows with air modulation compared to those without air modulation mainly result from the contribution of the component $\overline{\tilde{u}_a \tilde{u}_a}$. Hence,

$$\frac{1}{2} \left|\hat{u}_a\right|^2 \simeq \Delta(\overline{u''u''})$$

i.e.,

$$\left|\hat{u}_a\right| \simeq [(2\Delta(\overline{u''u''})]^{1/2} \tag{5.10}$$

where Δ denotes the change of a quantity due to imposing the air modulation. An estimate of $\left|\hat{u}_a\right|$ from (5.10) roughly agrees with those obtained from the cross-correlation technique, thus justifying the usage of the cross-correlation scheme.

When $f_a = 0$, there is no air modulation, so $\overline{u_i''u_j''} = \overline{u_i'u_j'}$. Then, the two-dimensional turbulent intensity is represented by $\overline{q^2} = \overline{u'u'} + \overline{v'v'}$. Figure 5.7 shows the plot of $Q^{+2} = \overline{q^2}/u_*^2$ versus y^+, together with the data obtained by Laufer (1951) and Klebanoff (1954). Remember that their data were obtained for flows in two-dimensional solid boundary channels, not for interface flows.

5.4 Wave Perturbation Fields

The wave perturbation fields consist of the wave-induced velocities $\tilde{u}_i$, the wave-associated mean Reynolds stresses $\overline{\tilde{u}_i \tilde{u}_j}$, and the wave-induced turbulent Reynolds stresses $\tilde{r}_{ij}$. The stresses $\overline{\tilde{u}_i \tilde{u}_j}$ play a very significant role in the energy transfer between the mean flow and the wave perturbation field; on the other hand, the stresses $\tilde{r}_{ij}$ are coupled with $\tilde{u}_i$ in transferring the energy between the wave perturbation field and the background turbulence. (Ref. Hussain and Reynolds 1970). When the air modulation is imposed, the effect of the air modulation is to change the wave perturbation fields. A close examination of the air modulation effect will be made in Section 5.6.

Experimental results for the wave perturbation fields are discussed in the following three subsections:

(a). Wave perturbation velocities

A typical result for $\tilde{u}$ and $\tilde{v}$ obtained by phase averaging is shown in Figure 5.1(a) for $y^* = 1.604$ cm and $f_a = 0.0$ Hz, and the result deviates from the nearly sinusoidal $\tilde{\eta}$ as indicated. Spectral analysis of $\tilde{u}$ and $\tilde{v}$ indicates that the magnitude of the harmonic modes contained in the velocity components are about 10% of those of the fundamental modes. The higher percentage in harmonic modes than in $\tilde{\eta}$ indicates the relative importance of the non-linear effect of the wave-perturbed air flow field rather than the non-linearity of the water wave. This non-linear perturbation may result from the non-linear convection of the air flow.

The phase average results of $\tilde{u}$ and $\tilde{v}$ are used to find the amplitudes $|\hat{u}|$ and $|\hat{v}|$ and the phase lags $\theta_{\tilde{u}}$ and $\theta_{\tilde{v}}$ by FFT and spectral analysis as described in Chapter 4. The plots of the amplitude $|\hat{u}|$ and the phase lag $\theta_{\tilde{u}}$ versus ky^* are given in Figures 5.8(a) and (b) and the plots for $|\hat{v}|$ and $\theta_{\tilde{v}}$ in Figures 5.9(a) and (b). In the proximity of the interface, the magnitude of $|\hat{u}|$ is clearly one order greater than that of $|\hat{v}|$, but their amplitudes tend to be of the same order when they are away from the interface. This suggests that, close to the interface where the mean flow vorticity and the turbulent intensity are large, the wave perturbation field strongly depends on the shear flow behavior and the turbulent mixing. Away from the interface, the wave perturbation field behaves similar to that in an inviscid flow with almost uniform velocity profile. Hence the exponential decay character is predominant in the free stream. As shown in Figures 5.8(b) and 5.9(b), the phase difference between $\theta_{\tilde{u}}$ and $\theta_{\tilde{v}}$ of about 90^o provides a strong evidence for the inviscid potential wave motion of the fluid particles near the free stream.

Since $\overline{\tilde{u}_i \tilde{u}_j}$ describes the coupling between the wave perturbation field and the mean flow, the 90^o phase difference between $\theta_{\tilde{u}}$ and $\theta_{\tilde{v}}$ which results in an almost zero value of $-\overline{\tilde{u}\tilde{v}}$ indicates that the mean flow and the wave perturbation field are almost decoupled in the free stream. On the other hand, an almost 180^o phase difference between $\theta_{\tilde{u}}$ and $\theta_{\tilde{v}}$ near the interface shows the strong coupling between the mean flow and the wave perturbation field. This coupling effect in the boundary layer results in the different orders in magnitude of $|\hat{u}|$ and $|\hat{v}|$ and in the phase shifts of $\theta_{\tilde{u}}$ and $\theta_{\tilde{v}}$, as shown in Figures 5.8(a), (b) and 5.9(a), (b).

Because the wave perturbation field is also dependent on the turbulent mixing effect characterized by $\tilde{r}_{ij}$, it is not now feasible to give an overall structure of the wave perturbation velocities. Details of $\overline{\tilde{u}_i \tilde{u}_j}$ and $\tilde{r}_{ij}$ are given in part (b) and (c) of this section. However, a discussion on the structure of the wave perturbation field is given in Chapter 6.

If we assume that the drift current at the interface is 3% of U_∞, the interface boundary condition (2.41a) indicates that $\frac{|\hat{v}|}{U_\infty} \cdot 10^2 = 6.67$ and $\theta_{\tilde{v}} = 270^o$ when $y^* = 0$. The sharp increase in $|\hat{v}|$ at the lower portion of the $|\hat{v}|$ profile given in Figure 5.9(a) and the phase $\theta_{\tilde{v}}$ approaching 270^o as $y^* \to 0$ in Figure 5.9(b) show that the interface boundary condition for $\tilde{v}$ seems to be verified by the present data. The interface boundary condition for $\tilde{u}$ can not be checked by the results inferred from the data trend of the $|\hat{u}|$ and $\theta_{\tilde{u}}$ profiles shown in Figures 5.8(a) and (b) because the inferred results are based on inviscid analysis and the viscous effect is significant for $\tilde{u}$ near the interface.

A systematic change in the wave perturbation velocities due to the imposition of the air modulation is seen in Figures 5.8(a), (b) and 5.9(a), (b). The change in amplitude caused by the air modulation is not large but still visible. An interesting difference in change in the phase

lags is observed between those with the air modulation frequency larger than and smaller than the frequency of the mechanically-generated water wave. The air modulations at 0.4 and 0.7 Hz tend to increase the phase lags of the wave perturbation velocities, but the air modulation at 1.5 Hz just behaves in an opposite way. Details of the air modulation effect are given in Section 5.6.

(b). Wave-associated Reynolds stresses

Figures 5.10, 5.11, and 5.12 show the distributions of the wave-associated Reynolds stresses $\overline{\tilde{u}_i \tilde{u}_j}$. When the harmonic modes are relatively weak compared to the fundamental mode, they can be approximated by

$$\overline{\tilde{u}_i \tilde{u}_j} \simeq \frac{1}{2} |\hat{u}_i| \cdot |\hat{u}_j| \cdot \cos(\theta_{\tilde{u}_i} - \theta_{\tilde{u}_j}) \tag{5.11}$$

The data of $|\hat{u}_i|$ and $\theta_{\tilde{u}_i}$ were used to estimate $\overline{\tilde{u}_i \tilde{u}_j}$ based on (5.11). The results agree with those shown in Figures 5.10, 5.11, and 5.12 to within 5%. Hence, the harmonic modes are negligible and the linear analysis described in Chapters 2 and 3 is feasible.

According to Miles' theory (1957), the wave-associated shear stress is equal to the average of the wave perturbation pressure supported by the water wave form, i.e., $\overline{\tilde{p} \frac{\partial \tilde{\eta}}{\partial x}} = -\rho \overline{\tilde{u} \tilde{v}}$ (Phillips 1966, p. 94). The energy transfer from the wind to the wave is then given by (see the more detailed discussion in Chapter 6)

$$-\overline{\tilde{p}\tilde{v}}\Big|_{y=\tilde{\eta}} = -\overline{\tilde{p}\left(\frac{\partial \tilde{\eta}}{\partial t} + u \frac{\partial \tilde{\eta}}{\partial x}\right)}\Bigg|_{y^*=0} = (c - U_o)\, \overline{\tilde{p} \frac{\partial \tilde{\eta}}{\partial x}}\Bigg|_{y^*=0}$$

$$= -(c - U_o)\, \rho\, \overline{\tilde{u}\tilde{v}}\Big|_{y^*=0} \tag{5.12}$$

When (5.12) is normalized by ρU_∞^3, we find

$$E_p = \frac{-\overline{\tilde{p}\tilde{v}}\big|_{y^*=0}}{\rho U_\infty^3} = \left(\frac{c}{U_\infty} - \frac{U_o}{U_\infty}\right) \frac{-\overline{\tilde{u}\tilde{v}}\big|_{y^*=0}}{U_\infty^2} \qquad (5.13)$$

To find an estimate of E_p, the value of $-\overline{\tilde{u}\tilde{v}}/U_\infty^2$ at $y^* = 0$ is obtained by extrapolation of the data plotted in Figure 5.11 with the result being approximately $11.0 \cdot 10^{-4}$. With $c/U_\infty = 0.649$ and $U_o/U_\infty = 0.03$, the value of E_p is $6.81 \cdot 10^{-4}$. An alternative but direct estimate of E_p can be obtained by correlating $\tilde{p}$ to $\tilde{v}$, i.e., $\overline{\tilde{p}\tilde{v}} = \frac{1}{2}|\hat{p}||\hat{v}| \cdot \cos(\theta_{\tilde{p}} - \theta_{\tilde{v}})$. The wave perturbation pressure was measured by Yu et al. (1973). The values of C_p $(=|\hat{p}|/\frac{1}{2}\rho U_\infty^2)$ and $\theta_{\tilde{p}}$ corresponding to $U_\infty/c = 1.541$ are now found from Figure 44 in their report to be 0.048 and 60^o respectively. The variation of $\tilde{p}$ in the boundary layer is small so these values can be regarded as those at the interface. The interface boundary condition for $\tilde{v}$ gives $|\hat{v}|/U_\infty = 0.0667$ and $\theta_{\tilde{v}} = 270^o$. So the direct calculation of E_p based on the correlation of $\tilde{p}$ and $\tilde{v}$ results in

$$E_p = -\frac{1}{4} \cdot C_p \cdot \frac{|\hat{v}|}{U_\infty} \cdot \cos(\theta_{\tilde{p}} - \theta_{\tilde{v}}) = 6.93 \cdot 10^{-4}$$

which agrees with the calculation based on $-\overline{\tilde{u}\tilde{v}}$. This agreement suggests that the Miles' inviscid theory may describe adequately the energy transfer from the wind to the wave due to the wave perturbation pressure even there is turbulence in the wind. A detailed investigation of this aspect is needed. Because additional energy transfer from wind to waves may be produced by the wave-induced turbulent Reynolds stresses, the total budget of the energy transfer can only be evaluated when these turbulent effects are known. This is given in Chapter 6.

The wave-associated Reynolds stresses are significant not only in transferring the energy across the interface to cause the growth of water wave, but also in transferring the energy from the mean flow to the wave perturbation field. The rate of energy transfer per unit volume from the mean flow to the wave perturbation field is given by $-\overline{\tilde{u}\tilde{v}} \cdot \frac{\partial U}{\partial y^*}$. Because $\frac{\partial U}{\partial y^*} > 0$ in the boundary layer as shown in Figure 5.3, Figure 5.13 shows that the energy transfer rate is negative (from the wave perturbation field to the mean flow) in the upper portion of the boundary layer ($0.18 < ky^*$) and is positive (from the mean flow to the wave perturbation field) in the lower portion ($0 < ky^* < 0.18$). The distribution of $-\overline{\tilde{u}\tilde{v}} \cdot \frac{\partial U}{\partial y^*}$ was obtained from the averages of the $|\hat{u}_i|$ and $\theta_{\tilde{u}_i}$ profiles using (5.11) to calculate $\overline{\tilde{u}\tilde{v}}$ and from the curve fitted mean velocity profile. The energy production is confined to the boundary layer and is concentrated near the interface.

(c). Wave-induced turbulent Reynolds stresses

The phase average results for $\tilde{r}_{ij}$ for $y^* = 1.604$ cm are also shown in Figure 5.1(b). Near the interface, $\tilde{r}_{11}$ and $\tilde{r}_{22}$ are coherent and oscillate in phase. Thus, the oscillatory turbulent intensity $\tilde{q}^2 = \tilde{r}_{11} + \tilde{r}_{22}$ is also in phase with $\tilde{r}_{11}$ and $\tilde{r}_{22}$. The turbulence is enhanced by the presence of the mechanically-generated water wave on the lee-ward side of it with a peak occurring about 15° ahead of the wave crest. Turbulence is reduced on the wind-ward side. When ky^* is large, we will see that this structure is changed. The oscillatory shear stress $\tilde{r}_{12}$ shown in Figure 5.1(b) indicates that, for $y^* = 1.604$ cm, the turbulent Reynolds stress $-\langle u''v'' \rangle = -\overline{u''v''} - \tilde{r}_{12}$ is relatively high on the lee-ward side and relatively low on the wind-ward side of the water wave ($-\overline{u''v''}$ is shown in Figure 5.6). This is consistent with the turbulent intensity $\overline{q^2} + \tilde{q}^2$ because higher turbulent intensity usually results in higher turbulent shear stress, although their peaks are not necessarily matched. This consistency between the turbulent

intensity and the turbulent shear stress holds uniformly through the turbulent boundary layer, as shown later in profile distributions. The distribution of $\tilde{r}_{12}$ along the wavy surface for small y* is contrary to what expected from the form drags caused by flow separation over the wave crests. If the flow separation occurs, the maximum turbulent shear should be positioned on the wind-ward side of the waves. Thus, we conclude that there has no flow separation and that the sheltering effect of Jeffrey's hypothesis (1925, 1926) is insignificant for the flow of this study.

The phase average results were used to calculate $|\hat{r}_{ij}|$ and $\theta_{\tilde{r}_{ij}}$ by FFT and cross-spectral analysis. The distributions of $|\hat{r}_{ij}|$ and $\theta_{\tilde{r}_{ij}}$ are shown in Figures 5.14, 5.15, and 5.16. The amplitudes $|\hat{r}_{ij}|$ are large near the interface; they decrease as ky* increases. They all decrease to a "*minimum*" at ky* = 0.6 and regain their amplitudes when further away from the interface. Finally they decrease again and tend to zero in the free stream. Physically, the "minimum" should be zero because there is a phase jump of 180° at ky* = 0.6 in the $\theta_{\tilde{r}_{ij}}$ profiles. The non-zero values of $|\hat{r}_{ij}|$ at ky* = 0.6 are caused perhaps by misalignment between the oscillatory probe positions and the positions where the flow has a constant value for $\langle u_i' u_j' \rangle$. If the amplitudes $|\hat{r}_{ij}|$ are considered as positive near the interface and the phase shifts of $\theta_{\tilde{r}_{ij}}$ are considered as continuous across the boundary layer, the amplitudes of $\tilde{r}_{ij}$ for ky* > 0.6 can be taken as negative. This means that the oscillatory turbulent stresses just above ky* = 0.6 act in the opposite direction to those stresses just below. The continuous phase shift across the boundary layer is approximately 270°. However, $\tilde{r}_{11}$ and $\tilde{r}_{22}$ have almost the same phase distribution as a function of ky*, while $\tilde{r}_{12}$ has an approximately constant phase difference of 90° compared to those of $\tilde{r}_{11}$ and $\tilde{r}_{22}$ throughout the boundary layer.

The dip-down to a "minimum" behavior resulting in the double peaks in the profiles of $|\hat{r}_{ij}|$ and in the phase jump of 180^{o} at ky* = 0.6 were not observed by Yu et al. (1973) and by Chao et al. (1976). The experimental data obtained by Yu et al. were in the wave-follower mode operated with a constant amplitude oscillation instead of the present y* coordinate. In addition, their measurements only extended to ky = 0.4 which is about one third of the thickness of the boundary layer. Therefore, they were unable to give a clear structure of the wave perturbation flow. In the measurements of Chao et al. (1976), although they used probes in both the fixed and the wave-following frames to obtain the velocities, their wave-follower measurement had the same disadvantage as that of Yu et al. It was expected that the fixed probe measurement which covered the whole boundary layer should provide a usable picture of the structure of the wave perturbation flow, despite its inferiority in describing the interface flow. Unfortunately, the correlation scheme used by Chao et al. (also by Yu et al.) to reduce $|\hat{r}_{ij}|$ and $\theta_{\tilde{r}_{ij}}$ contained the contribution of $\widetilde{\tilde{u}_i \tilde{u}_j}$ which may mask the real behavior of $|\hat{r}_{ij}|$ and $\theta_{\tilde{r}_{ij}}$ in the upper portion of the boundary layer where the signals of $\tilde{r}_{ij}$ are weak.

Gent and Taylor (1976) used an isotropic eddy viscosity model to calculate the interface flow in a curvilinear coordinate system under finite-amplitude wave conditions. They predicted that the amplitudes of the induced turbulent Reynolds stresses would have double-peak profiles and that the phase distributions of the induced turbulent Reynolds stresses shift 180^{o} in the downstream direction through the boundary layer. However, their model also predicted that near the interface the maximum turbulent intensity and the maximum turbulent shear stress occur windward of the water wave. This is contrary to our observation. The phase jump of 180^{o} at ky* = 0.6 in $\theta_{\tilde{r}_{ij}}$ again was not predicted by their model. To improve the prediction, perhaps an eddy viscosity model with an anisotropic behavior should be considered.

The changes in the induced turbulent Reynolds stresses due to the effect of the air modulations are clearly seen in Figures 5.14, 5.15, and 5.16. The changes of both the $|\hat{r}_{ij}|$ and $\theta_{\tilde{r}_{ij}}$ distributions due to air modulations depend on whether the air modulation frequency is larger than or less than the frequency of water waves. The difference is shown more clearly in the phase distributions of $\theta_{\tilde{r}_{ij}}$. More refined results and discussions on the air modulation effect are presented later in this chapter.

Consideration is now given to the wave-turbulence interaction. The energy drain from the wave perturbation field to the background turbulent field is given by $\overline{-\tilde{r}_{ij}\partial\tilde{u}_i/\partial x_j^*}$. The profiles of $|\hat{u}_i|$, $\theta_{\tilde{u}_i}$, $|\hat{r}_{ij}|$ and $\theta_{\tilde{r}_{ij}}$ shown in Figures 5.8, 5.9, 5.14, 5.15 and 5.16 were averaged and then used for calculating the energy drain. The results of the calculation are shown in Figure 5.17. The horizontal stress-strain correlation contributes dominantly to the energy drain near the interface. The net energy drain indicated by the line segments in Figure 5.17 shows that for $ky^* < 0.68$ the wave-induced turbulent Reynolds stresses convert the kinetic energy of the wave perturbation into background turbulence. For $ky^* > 0.68$ the energy is transferred from the turbulence to the wave perturbation. The amount of the energy drawn from the wave perturbation field to the turbulence in the lower portion of the boundary layer is much larger than the amount of the energy given to the wave perturbation field from the turbulence near the free stream.

Liu and Merkine (1976) studied the interactions between the wave-like large-scale structure and the fine-grained turbulence in a free shear flow. Their prediction on the wave-turbulence energy transfer (Figure 3 in their paper) resembles our observations. They showed that the horizontal stress-strain correlation is predominant. However, their predicted total transfer is uniformly from the wave field (large-scale) to the turbulent field (fine-grained turbulence). Since our

results are related to a boundary layer flow where there are interactions between the large-scale turbulence and a wave, this may cause the difference between our results and their predictions. In general, our observations and their predictions seem to be consistent.

5.5 Air Modulation Fields

In Chapter 3, we denoted a quantity g in the air-modulated flow by

$$g = G + \tilde{g}_a + g''_a$$

where $\tilde{g}_a$ is the air modulation component given by

$$\tilde{g}_a = \left|\hat{g}_a\right| \cdot \cos(\omega_a t - \theta_{\tilde{g}_a})$$

and g''_a is the background oscillation with respect to $\tilde{g}_a$. When g is correlated to $\cos(\omega_a t)$ for a time period T, we find

$$\overline{[\cos(\omega_a t) g(t+\xi)]}_T = \frac{1}{2}\left|\hat{g}_a\right| \cos(\omega_a \xi - \theta_{\tilde{g}_a}) + \frac{1}{2}\left|\hat{g}''_a\right| \cos(\omega_a \xi - \theta_{g''_a}) \tag{5.14}$$

The second term on the right hand side of (5.14) is the residual error produced by the background oscillation. This error can be reduced to a negligible level if T is sufficiently large. Unfortunately, the "jitter" and the drift in the frequency of the air modulator, as described in Chapter 4, has prevented us from making such a long time correlation. Because no reference signal for $\tilde{g}_a$ was registered, the phase $\theta_{\tilde{g}_a}$ was not reducible. The amplitude $\left|\hat{g}_a\right|$ can be calculated based on the averaged power of the correlated signal, i.e.,

$$P_{\tilde{g}_a} = \frac{1}{2}\left|\hat{g}_a\right|^2 + \frac{1}{2}\left|\hat{g}''_a\right|^2 \tag{5.15}$$

To eliminate $\frac{1}{2}\left|\hat{g}''_a\right|^2$ from $P_{\tilde{g}_a}$, the same data reduction precedure (Program C in Chapter 4) was performed over the data record without the air modulation, which gives

$$(P_{\tilde{g}_a})_o = \frac{1}{2}\left|\hat{g}''_a\right|^2_o \tag{5.16}$$

where the subscript "o" refers to the case of $f_a = 0$. Taking the difference between (5.15) and (5.16) gives

$$\Delta(P_{\tilde{g}_a}) = \frac{1}{2}\left|\hat{g}_a\right|^2 + \frac{1}{2}\Delta(\left|\hat{g}''_a\right|^2) \tag{5.17}$$

The second term on the right hand side of (5.17) now includes the residual error due to the background turbulence and the distortion of the turbulence at the frequency ω_a due to the air modulation. This term represents the uncertainty of the air modulation signal. The distortion of the background turbulent spectrum is considered significant so $\Delta(P_{\tilde{g}_a})$ can be negative if the air modulation effect results in a decrease of the power spectrum of the turbulence at ω_a and if the signal of $\tilde{g}_a$ is also relatively weak. Hence, we define a quantity $\|\tilde{g}_a\|$ as

$$\|\tilde{g}_a\| = \begin{cases} \left|2\Delta(P_{\tilde{g}_a})\right|^{1/2} & \text{if } \Delta(P_{\tilde{g}_a}) \geq 0 \\ -\left|2\Delta(P_{\tilde{g}_a})\right|^{1/2} & \text{if } \Delta(P_{\tilde{g}_a}) < 0 \end{cases} \tag{5.18}$$

which characterizes both the amplitude $\left|\hat{g}_a\right|$ and the distortion of the background turbulence. When the distortion is relative weak, we have $\|\tilde{g}_a\| = \left|\hat{g}_a\right|$. The arguments given above apply not only to the air modulation field but also to the interaction-produced wave field, because the same data reduction precedure was used. The data presented in this section are those of $\|\tilde{u}_{ia}\|$ and $\|\tilde{r}_{ija}\|$. The best

interpretation curves accompanying the data were obtained by locally smoothing the $P_{\tilde{g}_a}$ and $(P_{\tilde{g}_a})_o$ profiles before the subtraction and then using Chebyshev polynomials to fit the subtracted results.

(a). Air modulation velocities

The profiles of $\|\tilde{u}_a\|$ are shown in Figure 5.18. For $\tilde{u}_a$, the background distortion of the turbulence is relatively weak so $\|\tilde{u}_a\|$ is approximately equal to $|\hat{u}_a|$. From Figure 5.18, the amplitude of the air modulation decreases as the frequency of the air modulation increases. Because the amplitude control plates of the air flow pulser were not adjusted during each run, the decreasing amplitude reflects the dynamic response of the air flow to the flow pulser; a higher frequency results in a lower amplitude response.

For each f_a, the $\|\tilde{u}_a\|$ profile remains almost constant except near the interface where the role of the Stokes layer becomes predominant. The present results for $\|\tilde{u}_a\|$ agree with those measured by Acharya and Reynolds (1975). For each profile, there is a peak near the interface followed by a dip-down as ky* increases. The position of the peak shifts to higher elevation as the frequency of the air modulation increases. This is not consistent with results predicted in a laminar flow; the laminar flow prediction gives a peak closer to the boundary for a higher frequency. This peak and dip-down feature was also observed by Acharya and Reynolds (1975) in their 40 Hz modulation, but not in their 24 Hz modulation. According to their data trend, it is conjectured that there might exist a similar feature for their 24 Hz modulation in the vicinity of their channel wall where they could not measure.

Figure 5.19 shows the profiles of $\|\tilde{v}_a\|$. Since $\tilde{v}_a$ is primarily due to the developing boundary layer, it is estimated that

$$\frac{|\hat{v}_a|}{U_\infty} \simeq \frac{V}{U} \cdot \frac{|\hat{u}_a|}{U_\infty} \simeq 0.0008$$

Because $\tilde{v}_a$ is so weak, the data for $\|\tilde{v}_a\|$ shown in Figure 5.19 contain mainly the background turbulence distortion, which gives a large uncertainty. Near the free stream where the turbulence intensity is weak, we have $\|\tilde{v}_a\| \simeq |\hat{v}_a|$. The order of magnitude of $\|\tilde{v}_a\| / U_\infty$ near the free stream agrees with our estimation.

(b). Modulated turbulent Reynolds stresses

The profiles of $\|\tilde{r}_{ija}\|$ are shown in Figures 5.20, 5.21, and 5.22. Three components are responsible for $\|\tilde{r}_{ija}\|$: the first component is produced from the direct interaction of the air modulation with the background turbulence, the second component is produced from the interaction between the air modulation and the wave perturbation, and the third component results from the distortion of the turbulence due to the imposition of the air modulation. The first two components contribute to $\tilde{r}_{ija}$; the third component is picked up by the data reduction precedure and is not the desired. The negative value in $\|\tilde{r}_{ija}\|$ results mainly from this third component.

The relative orders of magnitude among $\|\tilde{r}_{11a}\|$, $\|\tilde{r}_{12a}\|$ and $\|\tilde{r}_{22a}\|$ are basically consistent with those measured by Acharya and Reynolds (1975). The general features of $\|\tilde{r}_{ija}\|$ are as follows: highly peaked near the interface; dipped down at the middle portion of the boundary layer; and relatively flat near the free stream. This structure is similar to that of the induced turbulent Reynolds stresses given in Section 5.4(c). This similarity suggests that the response of the turbulence to the organized oscillations is principally by the same mechanism. The locations of the dip-down for $\|\tilde{r}_{ija}\|$ are relatively higher than those of $\|\tilde{u}_a\|$; this was also observed by Acharya and Reynolds (1975). However, with the differences in the data reduction scheme (they used the correlation to a registrated reference signal), in the flow condition (their flow is a solid-boundary channel flow), and in the range of the air modulation frequency, no further comparison can be made. With the relatively high uncertainty in $\tilde{r}_{ija}$, we will not examine further the data results for the air modulation field.

5.6 Effects of Air Modulation on Wave Perturbation

When air modulation was imposed on a wave perturbed flow, the wave perturbation field was changed. If $(\tilde{g})_A$ and $(\tilde{g})_o$ denote the wave perturbation quantities with and without the air modulation, respectively, the effect of the air modulation on the wave perturbation is given by

$$\tilde{g}_d = \Delta\tilde{g} = (\tilde{g})_A - (\tilde{g})_o \tag{5.19}$$

Introducing the wave expression (2.31), we find

$$\hat{g}_d = (\hat{g})_A - (\hat{g})_o \tag{5.20}$$

Since $\hat{g}_d$, $(\hat{g})_A$ and $(\hat{g})_o$ are complex numbers, Equation (5.20) may be expressed as

$$|\hat{g}_d| = \left\{(|\hat{g}|)_A^2 + (|\hat{g}|)_o^2 - 2(|\hat{g}|)_A(|\hat{g}|)_o\cos[(\theta_{\tilde{g}})_A - (\theta_{\tilde{g}})_o]\right\}^{1/2} \tag{5.21}$$

and

$$\theta_{\tilde{g}_d} = \tan^{-1}\left\{\frac{(|\hat{g}|)_A\sin(\theta_{\tilde{g}})_A - (|\hat{g}|)_o\sin(\theta_{\tilde{g}})_o}{(|\hat{g}|)_A\cos(\theta_{\tilde{g}})_A - (|\hat{g}|)_o\cos(\theta_{\tilde{g}})_o}\right\} \tag{5.22}$$

Equations (5.21) and (5.22) were used to calculate the amplitude and the phase of $\tilde{g}_d$, which may represent $\tilde{u}_{id}$ or $\tilde{r}_{ijd}$. The results of the calculation are shown in Figures 5.23-5.27. The profiles of $(\tilde{g})_A$ and $(\tilde{g})_o$ were locally smoothed before these calculations.

From these figures, we see that the response of the wave perturbation to the air modulation near the interface is different from the response near the free stream. Near the free stream, the response is strongly dependent on the frequency of the air modulation compared to the frequency of the water waves. The cases of $f_a = 0.4$ and 0.7 Hz have similar features and belong to the lower frequency range where the air modulation frequencies are smaller than the water wave frequency. The case of $f_a = 1.5$ Hz belongs to the upper frequency range

where the air modulation frequency is larger than the water wave frequency. Near the free stream, the phases of $\tilde{u}_{id}$ and $\tilde{r}_{ijd}$ for these two frequency ranges are almost 180^{o} different as shown in the figures. The difference between these two frequency ranges is also shown in the amplitude distributions of $\tilde{u}_{id}$, but not for $\tilde{r}_{ijd}$.

Near the interface, the response of the wave perturbation seems to be relatively insensitive to the frequency of the air modulation, compared to the response near the free stream. In the proximity of the interface ($ky^* < 0.2$), the profiles of $|\hat{u}_{id}|$, $\theta_{\tilde{u}_{id}}$, $|\hat{r}_{ijd}|$, and $\theta_{\tilde{r}_{ijd}}$ have similar characteristics for all the three air modulation frequencies. (Note that a 360^{o} different in phase is of the same phase.) Although $\theta_{\tilde{u}_{id}}$ and $\theta_{\tilde{r}_{ijd}}$ show some different trends between the two frequency ranges, for the intermediate values of ky^*, their structure is regarded as different from that near the free stream because there is no persistent 180^{o} phase difference near the interface between these two ranges. The elevation where the free stream and the interface regions are divided is located approximately at $ky^* = 0.6$. The apparent existence of these two regions occurs both in the profiles of $\tilde{u}_{id}$ and $\tilde{r}_{ijd}$; on the other hand, we have shown in Section 5.4 that similar behavior was observed for $\tilde{r}_{ij}$ at $ky^* = 0.6$, but not for $\tilde{u}_{i}$.

The effect of air modulation on the wave perturbation is of two types. The first is the direct interaction between the air modulation and the water wave, and the second is the indirect changes in the coupling structure between the basic flow (the mean flow and the turbulence) and the wave due to the air modulation. The first process is demonstrated by the production of the interaction-produced waves. When the interaction-produced waves couple further with the air modulation, the wave-induced turbulent Reynolds stresses are increased and the velocity perturbation field is modified. This type of process was first suggested by Hasselmann (1967, 1968) in describing the wave-turbulence interaction, which was one of the original motivations of our present study. As shown by Hasselmann (1968), this type of coupling process is

parametric and the coupling parameter is dependent on the intensity (power) of the air modulation and on the air modulation frequency f_a relative to the water wave frequency f. It is reasonable to assume that Hasselmann's interaction process may be responsible for the observed behavior in both $\tilde{u}_{id}$ and $\tilde{r}_{ijd}$ depending on whether $f_a < f$ or $f_a > f$. Because this process is described by the interaction-produced waves with frequencies $f_a \pm f$, a more intuitive insight to this process can be obtained by examining the propagation directions of the interaction-produced waves. When $f_a < f$, both components of the interaction-produced wave propagate downstream in the same direction as the water wave. When $f_a > f$, the component with frequency $f + f_a$ still propagates downstream, but the other component with frequency $f_a - f$ propagates upstream. Hence, the direct interaction between the air modulation and the water wave should be different for these two frequency ranges.

The second process results mainly from the perturbation of the basic flow structure due to the air modulation, i.e., the coupling of the basic flow to the water wave is changed by the imposition of the air modulation. It was shown by Hall (1975) and Seminara and Hall (1975) that laminar flows were destabilized by the air modulation without regard to the frequency range of the air modulation. No analysis similar to Hall's has been performed for a turbulent flow; however, the air modulation must have an effect on its stability. Since the turbulence is usually considered to be the consequence of flow instability, the turbulence characteristics may be more strongly affected by the air modulation than the mean flow characteristics. Consequently, the change in the turbulent structure due to the air modulation is assumed to be the dominant mechanism which governs the second process. As inferred from Hasselmann's interaction theory (1968), the second process is characterized by the intensities of the air modulation and the turbulence and is due to higher order interactions. Hence, the second process is relatively weak in comparison to the first process if the air modulation

and the turbulence are of the same order of magnitude in their intensities; this is the case near the free stream. However, near the interface, the turbulence is considerably stronger than the air modulation so the second process may be of equal importance to or even dominant over the first process. The second process is also governed by the relative location of the air modulation frequency to the frequency band with high turbulent energy. All the air modulations in the present study are located on the lower side of the energetic frequency band of turbulence, so their effects on the wave perturbation based on the second process are presumably similar.

The characteristics discussed above are consistent with the data of $\tilde{u}_{id}$ and $\tilde{r}_{ijd}$. It is surprising that the data of $\tilde{u}_i$ and $\tilde{r}_{ij}$ have similar trends on the phase distributions to the data of $\tilde{u}_{id}$ and $\tilde{r}_{ijd}$ for f_a = 1.5 Hz; the similar trends include the direction and the range of phase shift across the boundary layer. This similarity supports our arguments given above, because the energetic frequency band of the turbulence in this study and the frequency of the air modulation (f_a = 1.5 Hz) are both located above the frequency of the water wave.

5.7 Interaction-Produced Wave Fields

The data reduction scheme used for the interaction-produced wave is the same as that used for the air modulation. So the results for $\tilde{u}_{is}$ are presented as $\|\tilde{u}_{is}\|$ as given by equation (5.18) where the subscript "a" is replaced by "s". As mentioned previously, because no reference signal for $\tilde{g}_a$ was recorded, no phase information of $\tilde{u}_{is}$ is available. The profiles of $\|\tilde{r}_{ijs}\|$ are not presented because they are basically equal to the amplitudes of $\langle \tilde{u}_i \tilde{u}_{ja} \rangle_s$. Figures 5.28 and 5.29 show the distributions of $\|\tilde{u}_s\|$ and $\|\tilde{v}_s\|$. Again the best interpretation curves in these figures are obtained by locally smoothing and curve-fitting with Chebyshev polynomials as described in Section 5.5.

The magnitudes of $\|\tilde{u}_s\|$ are relatively higher than those of $\|\tilde{v}_s\|$ as expected; the ratio of $\|\tilde{u}_s\| / \|\tilde{v}_s\|$ is approximately of the order of the ratio $|\hat{u}| / |\hat{v}|$. According to the inviscid linear analysis given in Chapter 3, the order of $|\hat{u}_s| / U_\infty$ is approximately of 10^{-3}; this is found in the present data. However, the consistency should be regarded as only qualitative because of the uncertainty in the data. The data suggest the existence of the interaction-produced waves, i.e., the existence of the direct interaction between the air modulation and the water wave. Unfortunately, no conclusive or quantitative results could be found due to unfavorable data quality.

CHAPTER 6

DISCUSSION

6.1 Preview

Because specific discussions of the experimental results were given in Chapter 5, the discussions presented in this chapter are concentrated on the general aspects of turbulent flow over a wave-perturbed air-water interface. The topics include: a close look at the quantities measured in the coordinate systems (x, y, t) and (x*, y*, t*), a discussion of the mean flow structure, an energy consideration of the wave perturbation field, an insight to the interaction between the wind and the waves, a general picture of the interface flow structure, and finally an overview at the closure modelling of $\tilde{r}_{ij}$. Because the data were collected in the (x*, y*, t*) coordinate system and because there exist different physical meanings for quantities expressed in the (x, y, t) and (x*, y*, t*) coordinate systems, a realistic understanding of the flow structure can be obtained only when the difference in these two coordinate systems is recognized.

6.2 Quantities in (x, y, t) and in (x*, y*, t*) Coordinates

It is seen from equation (2.4) that the wave-induced quantity $\tilde{g}$ is only defined when the mean of g, now denoted by G, exists. In the fixed frame the mean quantity G does not exist for $y < a$ because it is impossible to perform any time average process for fixed (x, y) if $y < a$. Hence, the wave quantity $\tilde{g}(x, y, t)$ can not be determined experimentally from equation (2.4) for $y < a$. However, in the transformed coordinate system, G(x*, y*) is experimentally obtainable for $y^* < a$ since G(x*, y*) represents the time average performed along curves where (x*, y*) is constantly in the air regime. So the quantity $\tilde{g}(x^*, y^*, t^*)$ is defined. Despite of the difference in $\tilde{g}$ in (x, y, t) and in (x*, y*, t*) systems,

the phase average result $\langle g \rangle$ is well behaved in both the (x, y, t) and (x*, y*, t*) coordinate systems; $\langle g \rangle(x, y, t)$ and $\langle g \rangle(x^*, y^*, t^*)$ are identical only if (x, y) and (x*, y*) represent the same physical position. As a result, equations given in the previous chapters that describe the wave perturbation field in the fixed frame are not valid for $y < a$ unless we can give a proper description for $\tilde{g}(x, y, t)$ in this region. On the other hand, equations for $\tilde{g}(x^*, y^*, t^*)$ in the transformed coordinate system do not have this difficulty because they are derived from the equations for $\langle g \rangle$ and because $\tilde{g}(x^*, y^*, t^*)$ exists for $y^* \geq 0$.

When $x^* = x$, equations (2.43a, b, c) indicate that $(x^*, y^*=h)$ and $(x, y=h+f\tilde{\eta})$ represent the same physical position, so we have

$$\langle g \rangle(x^*, y^*, t^*)\Big|_{y^*=h} = \langle g \rangle(x, y, t)\Big|_{y=h+f\tilde{\eta}} \tag{6.1}$$

Taylor series expansion yields

$$\begin{aligned}
&\langle g \rangle(x, y, t)\Big|_{y=h} \\
&= \langle g \rangle(x, h+f\tilde{\eta} - f\tilde{\eta}, t) \\
&= \langle g \rangle(x, h+f\tilde{\eta}, t) - \frac{\partial \langle g \rangle}{\partial y}(x, h+f\tilde{\eta}, t) f\tilde{\eta} \\
&\quad + \frac{\partial^2 \langle g \rangle}{\partial y^2}(x, h+f\tilde{\eta}, t) \frac{f^2\tilde{\eta}^2}{2} + O(\tilde{\eta}^3)
\end{aligned} \tag{6.2}$$

Equation (6.2) is only valid when $\tilde{\eta}$ is sufficiently small. Criterion for its validity will be discussed later. Applying the relations (2.47c) and (2.47e) and substituting (6.1) into (6.2) we find

$$\langle g\rangle(x, y, t)\Big|_{y=h} = \langle g\rangle(x^*, y^*, t^*)\Big|_{y^*=h} - f\tilde{\eta}\frac{\partial\langle g\rangle}{\partial y^*}\Big|_{y^*=h}$$

$$+ \tilde{\eta}^2\frac{\partial}{\partial y^*}\left(\frac{f^2}{2}\cdot\frac{\partial\langle g\rangle}{\partial y^*}\right)\Big|_{y^*=h} + O(\tilde{\eta}^3) \qquad (6.3)$$

For $h > a$, the time averages can be obtained both in (x, y, t) and (x^*, y^*, t^*). So the decomposition of $\langle g\rangle$ into $G + \tilde{g}$ is feasible. Thus, by equating the mean and oscillatory portions of (6.3), we obtain

$$G(x, y)\Big|_{y=h} = \left[G(x^*, y^*) - \overline{f\tilde{\eta}\frac{\partial\tilde{g}}{\partial y^*}} + \frac{\partial}{\partial y^*}\left(\frac{f^2}{2}\cdot\frac{\partial G}{\partial y^*}\right)\overline{\tilde{\eta}^2}\right]_{y^*=h}$$

$$+ O(\tilde{\eta}^3) \qquad (6.4)$$

and

$$\tilde{g}(x, y, t)\Big|_{y=h} = \tilde{g}(x^*, y^*, t^*)\Big|_{y^*=h} - \frac{\partial G}{\partial y^*}\cdot f\cdot\tilde{\eta}\Big|_{y^*=h} + O(\tilde{\eta}^2) \qquad (6.5)$$

Equations (6.4) and (6.5) show the relationships between quantities measured for the same physical variable in the two coordinate systems at the same mean elevation. The difference between $G(x, y)$ and $G(x^*, y^*)$ is of second order in $\tilde{\eta}$ so that they can be taken as the same unless the curvature of the mean profile is too large. The difference in $\tilde{g}(x, y, t)$ and $\tilde{g}(x^*, y^*, t^*)$ is of first order and can not be neglected unless $\frac{\partial G}{\partial y^*}$ is relatively small.

Let us consider the case where g is the horizontal velocity u. If the mean velocity profile follows the wave form and has a sharp velocity gradient, $\frac{\partial U}{\partial y^*}\cdot f\cdot\tilde{\eta}$ is large because it represents the oscillatory velocity picked up by a fixed probe due to periodically upwards and downwards translation of the mean velocity profile. For low wind speeds we also expect $\tilde{u}(x^*, y^*, t^*)$ to be relatively weak so $\tilde{u}(x, y, t)$ is mainly caused by $-\frac{\partial U}{\partial y^*}\cdot f\cdot\tilde{\eta}$. On the other hand, if the mean velocity profile does not follow the wave form, the roles of $\tilde{u}(x, y, t)$ and

$\tilde{u}(x^*, y^*, t^*)$ are interchanged. At high wind speeds, $\tilde{u}(x, y, t)$ and $\tilde{u}(x^*, y^*, t^*)$ are usually large. So $\frac{\partial U}{\partial y^*} \cdot f \cdot \tilde{\eta}$ cannot be used as a sensitive test to determine whether the mean velocity profile follows the wave form.

For $h < a$, the decomposition of $\langle g \rangle$ into $G+\tilde{g}$ is only feasible in the transformed coordinate system. To obtain an interpretation of $G(x, y)$ and $\tilde{g}(x, y, t)$, it is reasonable to extend the relations (6.4) and (6.5) from the region $h > a$ to the region $h < a$ by continuation. In this manner, $G(x, y)$ and $\tilde{g}(x, y, t)$ at $y < a$ are calculated from $G(x^*, y^*)$ and $\tilde{g}(x^*, y^*, t^*)$ according to (6.4) and (6.5), not by taking the time and phase averages of g at fixed (x, y). With this extention, $G(x, y)$ and $\tilde{g}(x, y, t)$ have a physical meaning for $y < a$ which is consistent with the result of a traditional perturbation scheme. The boundary conditions (2.41a, b) at the interface now should be described as those for $\tilde{u}(x^*, y^*, t^*)$ and $\tilde{v}(x^*, y^*, t^*)$, not for $\tilde{u}(x, y, t)$ and $\tilde{v}(x, y, t)$. The difficulty of using a fixed coordinate system is that the interface boundary conditions for $\tilde{u}(x, y, t)$ and $\tilde{v}(x, y, t)$ must be obtained by extrapolation using the Taylor series expansion and the series expansion is not in general valid. The advantage of using a transformed coordinate system is immediately seen because it does not require the validity of the Taylor series expansion.

To insure the validity of the Taylor series expansion, the following condition must hold, viz.,

$$\langle g \rangle (x^*, y^*, t^*) >> f\tilde{\eta} \cdot \frac{\partial \langle g \rangle}{\partial y^*} \tag{6.6}$$

As an example, let $\langle g \rangle$ as $\langle u \rangle$. For typical turbulent boundary layer flows,

$$\frac{\partial \langle u \rangle}{\partial y^*} \simeq \frac{\partial U}{\partial y^*}$$

under the small amplitude wave assumption. The greatest rate of change in U occurs near the interface where the laminar sublayer gives a linear mean velocity profile. We have

$$\left(\frac{\partial U}{\partial y^*}\right)_o = \frac{u_*^2}{\nu}$$

The length scale of $\partial U/\partial y^*$ at the interface is

$$\delta_o = \frac{U_\infty}{\left(\frac{\partial U}{\partial y^*}\right)_o} = \frac{U_\infty \nu}{u_*^2} \tag{6.7}$$

The most stingent condition for (6.6) is at the interface where $f(0) = 1$; this results in

$$\frac{a}{\delta_o} << 1 \tag{6.8}$$

In terms of the wall coordinate, (6.7) can be written as

$$\delta_o^+ = \frac{\delta_o u_*}{\nu} = \frac{U_\infty}{u_*}$$

Note that δ_o^+ is also the reciprocal of the root square of the drag coefficient. The wall-coordinate parameter for a is given by

$$a^+ = \frac{a u_*}{\nu}$$

and is the non-dimensional roughness of the water wave. Condition (6.8) is now

$$\frac{a^+}{\delta_o^+} << 1 \tag{6.9}$$

For typical turbulent boundary layer flows, $\delta_o^+ = \frac{U_\infty}{u_*} \simeq 25 \sim 30$ which corresponds approximately to the lower edge of the log-linear profile. To insure the validity of the linear analysis in the fixed coordinate system, the amplitude of the water waves must be less than thickness of the viscous sublayer, i.e., the roughness produced by the water waves should be small enough to guarantee that the surface condition is still aerodynamically smooth. Condition (6.9) is not satisfied in a laboratory in general, because the wave amplitude has to be maintained large enough to give a reasonable signal-to-noise ratio. For instance, $\delta_o = 0.51$ cm and $a = 2.67$ cm in this study, so $\delta_o^+ = 28$, $a^+ = 146$, and $a^+/\delta_o^+ = 5.24 > 1$.

We now compare the differences among $\tilde{g}(x, y, t)$, $\tilde{g}(x^*, y^*, t^*)$ and $\tilde{g}^*(x^*, y^*, t^*)$. Equation (6.5) shows that $\tilde{g}(x, y, t)\big|_{y=h}$ and $\tilde{g}(x^*, y^*, t^*)\big|_{y^*=h}$ are always different by the amount $f\tilde{\eta}\,\frac{\partial G}{\partial y^*}\Big|_{y^*=h}$ no matter how small the wave amplitude is (unless $a = 0$ such that $\tilde{g}(x, y, t) = \tilde{g}(x^*, y^*, t^*) = 0$.) When $\tilde{g}(x, y, t)$ is evaluated at the time varying position $y = h + f\tilde{\eta}$, we have

$$\tilde{g}(x, y, t)\Big|_{y=h+f\tilde{\eta}} = \tilde{g}(x, y, t)\Big|_{y=h} + O(\tilde{\eta}^2) \tag{6.10}$$

Hence, $\tilde{g}(x, y, t)\big|_{y=\tilde{\eta}}$ can be approximated by $\tilde{g}(x, y, t)\big|_{y=0}$ but not by $\tilde{g}(x^*, y^*, t^*)\big|_{y^*=0}$, as we have remarked for the interface boundary conditions. Equation (2.56) provides us

$$\tilde{g}^*(x^*, y^*, t^*) = \tilde{g}(x^*, y^*, t^*) - f\tilde{\eta}\,\frac{\partial G}{\partial y^*} \tag{6.11}$$

Recall that (6.11) is exact (no higher order terms were neglected) and that $\tilde{g}^*(x^*, y^*, t^*)$ is evaluated at $y^* =$ constant. If condition (6.9) is satisfied, from (6.5), (6.10) and (6.11) we have

$$\tilde{g}^*(x^*, y^*, t^*)\Big|_{y^*=h} = \tilde{g}(x, y, t)\Big|_{y=h} + O(\tilde{\eta}^2) \tag{6.12}$$

$$= \tilde{g}(x, y, t)\Big|_{y=h+f\tilde{\eta}} + O(\tilde{\eta}^2) \tag{6.13}$$

The value of $\tilde{g}^*(x^*, y^*, t^*)$ evaluated at $y^* = h$ can be regarded as the value of $\tilde{g}(x, y, t)$ evaluated at $y = h$ in (x, y, t) coordinate system. It may be visualized that the coordinate transformation can be achieved by stretching the undulating curve of $y^* =$ constant into a horizontal line, if $ka << 1$. When condition (6.9) is satisfied, the stretching process and the extrapolation by Taylor series expansion have little difference, so $\tilde{g}(x, y, t)$ and $\tilde{g}^*(x^*, y^*, t^*)$ can be taken as the same. However, when condition (6.9) is not satisfied such that $\tilde{g}(x, y, t)$ can not be obtained, the transformed quantity $\tilde{g}^*(x^*, y^*, t^*)$ still has meaning and we assume that $\tilde{g}^*(x^*, y^*, t^*)$ will take an equivalent role to $\tilde{g}(x, y, t)$ under this condition.

6.3 Mean Flow Structure

As shown in Chapter 5, the mean velocity has a wake log-linear profile. This profile holds to the vicinity of the interface below the crests of the mechanically-generated water wave. The mean Reynolds stresses measured in the transformed coordinate system as shown in Figure 5.6 also have a structure similar to that observed by others in flat, solid boundary channels. This suggests that the interface flow characteristics are dependent on the instantaneous height above the water surface as first proposed by Benjamin (1959), and not on the height above the mean water level.

In Section 6.2, we showed that, when the wind speed is low, comparing $\tilde{u}(x, y, t)$ and $\tilde{u}(x^*, y^*, t^*)$ should give a direct test to whether the mean profiles follow the wave form. Chao et al. (1976) measured $\tilde{u}$ in a fixed frame and in a wave-following frame ($y_f = y - \tilde{\eta}$). The

present measurement in the transformed coordinate system is equivalent to the wave-following measurement near the interface and matches the fixed frame measurement in the free stream. The results of Chao et al. showed that $\tilde{u}(x, y, t)$ is substantially larger than $\tilde{u}(x, y_f, t)$ near the interface when U_∞/c is low. The order of magnitude of $\tilde{u}(x, y, t)$ is also consistent with that of $\tilde{\eta}\frac{\partial U}{\partial y}$. Unfortunately, their data in the two frames measurement was obtained at different elevations under different mean flow conditions so that no direct check could be made of the relation between $\tilde{u}(x, y, t)$ and $\tilde{u}(x, y_f, t)$. In order to fulfill this specific objective, a separate experiment has been performed, in which we measured the interface flow in the three coordinate systems ($y = y$, $y_f = y - \tilde{\eta}$, and $y^* = y - f\tilde{\eta}$) at the same mean elevation and under the same flow condition. The results of that experiment show a clearer picture of this wind-following-wave character. Detailed results of this separate experiment will be presented in a later report.

We conclude that the mean flow follows the wave form if the mean wind speed is not too high. This is true for the flow in this study because no flow separation is observed and because the mean profiles are similar to the well-behaved turbulent flows in solid wall channel. Hence, describing the interface flow in the transformed coordinate system is an appropriate approach.

Let us now give attention to the velocity profile parameter C given in equation (5.9). The average value of C is found to be 8.26 (Table 5.1) in this study. Stewart (1970) measured the velocity profiles over smooth water surfaces and over a 1.96 Hz mechanically-generated water wave under a low wind condition (similar to this study). He found C = 7.2 for smooth flat water surface and C = 3.7 for generated water waves. He stated that the lower value of C = 3.7 resulted from the roughness created by the mechanically-generated water waves. We disagree. If the generated water waves are considered as portions of the boundary roughness, the form drag exhibited by the wave-associated

Reynolds stress $-\rho\overline{\tilde{u}\tilde{v}}$ should be incorporated with the mean turbulent Reynolds stress $-\rho\overline{u'v'}$ to give the total resistance of the water surface. Our measurement and the measurement of Kendall (1970) showed that $-\rho\overline{\tilde{u}\tilde{v}}$ varies drastically near the interface. When $-\rho\overline{\tilde{u}\tilde{v}}$ and $-\rho\overline{u'v'}$ are combined, the structure of the constant stress layer is totally distorted.

The lower value of C = 3.7 in Stewart's results was a consequence of his fixed probe measurements. If he had measured the flow in the transformed coordinate system, we expect that the value of C would be relatively high (near 7.2) because the mean profiles were following the waves and the water surface was relatively smooth with respect to the water waves. All the second-order correction terms appearing in the right-hand side of (6.4) are negative, so the mean velocity measured in the fixed frame is smaller than that measured in the transformed frame. The difference between these two frames of measurement is small near the free stream and generally increases as one approaches to the interface. As the result, the value of u_* determined from the profile method should give a higher value for fixed frame data than for transformed frame data. The value of C for fixed frame measurement is then considerably lower than that for transformed frame measurement. The argument stated above is confirmed by our measured results in the three coordinate systems, where we found that u_* and C were about 10.8 cm/sec and 7.5 for transformed frame data and 18.3 cm/sec and -2.7 for fixed frame data at $U_\infty/c = 1.88$. Chao et al. (1976) observed that $u_* = 9.3$ cm/sec and C = 0.9 for fixed frame data at $U_\infty/c = 1.12$. The u_* values reported by Stewart (1970) also showed 10 to 25% higher values for the generated wave cases than for the smooth flat water surface cases. If the generated water waves are regarded as surface roughness, we also expect that the C value should continuously decrease as the wind speed is increased when the wave amplitude is kept

constant because the relative roughness given by $a^+ = au_*/\nu$ is larger at higher wind speed. This was not observed by Stewart.

For flows over smooth flat plate, measurements of Young et al. (1973), of Hussain and Reynolds (1970), and of Acharya and Reynolds (1975) showed that C is approximately 5.0, and Coles' (1954) data showed that C is about 6.2. These values are considerably smaller than our 8.26 and Stewart's 7.2 values of C. Agreement is obtained if we account for the effects of the drift current. The effects of the drift current release a portion of the turbulent shear stress to give a lower value of u_* for interface flows than that for smooth wall (flat or wavy) flows. Accordingly, the curve-fitting by profile method results in a lower slope u_*/k_o and a higher intercept C. Let the mean velocity for a no drift flow be given by

$$U^o = \frac{u_*^o}{k_o} \ln \frac{y^* u_*^o}{\nu} + C^o u_*^o \qquad (6.14)$$

where C^o is 5.0 or 6.2 as described. When a drift current U_o exists on the interface, the velocity excess is transported across the boundary layer by the existing turbulence due to mixing and the turbulent shear stress is partially released. The transport of the excess momentum is similar to the transport of an excess temperature or humidity appearing at the interface. So the current-induced velocity is also given by a log-linear profile, i.e.,

$$U_o - U_d = \frac{u_{*d}}{k_o} \ln \frac{y^* u_{*d}}{\nu} + C^o u_{*d} \qquad (6.15)$$

where U_d is the current-induced velocity and u_{*d} is the characteristic friction velocity of the drift current. Since $U = U^o + U_d$, combining (6.14) and (6.15) and comparing the combined result to (5.2) and (5.7) yields

$$u_* = u_*^o - u_{*_d} \tag{6.16}$$

and

$$C = C^o + \frac{U_o}{u_*} + \frac{1}{k_o} \cdot \left(\frac{u_*^o}{u_*} \cdot \ln \frac{u_*^o}{u_*} + \frac{u_{*_d}}{u_*} \cdot \ln \frac{u_*}{u_{*_d}} \right) \tag{6.17}$$

Because $U_o > 0$ and $u_*^o > u_* > u_{*_d}$, all the correction terms on the right-hand side of (6.17) are positive. So, $C > C^o$. To give a quantitative estimate of C, let us assume the drift current to be 3% of U_∞, i.e., $U_o = 7.2$ cm/sec for $U_\infty = 2.4$ m/sec. The value of u_*^o can be obtained from the empirical formula given by Moffat et al. (1967), i.e.,

$$\left(\frac{u_*^o}{U_\infty} \right)^2 = C_f = 0.013 (Re_{\delta_2})^{-1/4} \tag{6.18}$$

where C_f is the shear stress coefficient for smooth plate and Re_{δ_2} is the Reynolds number based on the momentum thickness. For Re = 35700 (Table 5.1), $Re_{\delta_2} = 3470$ from the 1/7-th-power law (Schlichting 1968, p. 599). So we have $u_*^o = 9.89$ cm/sec from (6.18) and $u_{*_d} = 1.31$ cm/sec from (6.16) when $u_* = 8.58$ cm/sec (Table 5.1). When u_*^o, u_{*_d}, u_*, U_o, and k_o (=0.40) are substituted into (6.17), we find $C = 6.92$ if $C^o = 5.0$ and $C = 8.12$ if $C^o = 6.2$. Considering the scatter in C^o, our result for C is not inconsistent with Stewart's.

6.4 Energy Budget of Wave Perturbation Field

In a turbulent shear flow, there is continuous dissipation of turbulent kinetic energy into internal thermal energy due to viscous stress and an accompanying transfer of energy from the mean field by turbulent Reynolds stresses acting against the mean velocity gradient for replenishment of the turbulent kinetic energy. There is also continuous diffusion of turbulent kinetic energy by fluctuating motions. With the addition of wave perturbation, the interaction between the mean flow

and the turbulence is subjected to modifications. There are additional interactions between the mean flow and the wave perturbation and between the turbulence and the wave perturbation; these interactions presumably establish the evolution of the wave perturbation field. Consequently, the energy budget among these three fields is re-adjusted. In this study, we consider only the energy budget of the wave perturbation field. Because $\tilde{g}^*(x^*, y^*, t^*)$ is equivalent to $\tilde{g}(x, y, t)$ when (6.9) is satisfied, the energy consideration is focused on $\tilde{g}^*(x^*, y^*, t^*)$ for generalization.

The kinetic energy K of the wave perturbation field is

$$K = \frac{1}{2}\left(\overline{\tilde{u}^*\tilde{u}^*} + \overline{\tilde{v}^*\tilde{v}^*}\right) \tag{6.18a}$$

Energy balance equations for the horizontal kinetic energy $\frac{1}{2}\overline{\tilde{u}^*\tilde{u}^*}$ and the vertical kinetic energy $\frac{1}{2}\overline{\tilde{v}^*\tilde{v}^*}$ can be obtained by multiplying the momentum equations (2.58) and (2.59) by $\tilde{u}^*$ and $\tilde{v}^*$, respectively, and then taking time averages. The results are

$$\frac{d}{dt^*}\left(\frac{1}{2}\overline{\tilde{u}^*\tilde{u}^*}\right) = -\frac{\partial}{\partial x^*}\overline{\tilde{p}^*\tilde{u}^*} - \overline{\tilde{u}^*\tilde{v}^*}\frac{\partial U}{\partial y^*} + \overline{\tilde{p}^*\frac{\partial \tilde{u}^*}{\partial x^*}} + \frac{1}{Re}\left(\frac{\partial^2}{\partial x^{*2}} + \frac{\partial^2}{\partial y^{*2}}\right)\frac{\overline{\tilde{u}^*\tilde{u}^*}}{2}$$

$$- \frac{1}{Re}\left[\overline{\left(\frac{\partial \tilde{u}^*}{\partial x^*}\right)^2} + \overline{\left(\frac{\partial \tilde{u}^*}{\partial y^*}\right)^2}\right] - \frac{\partial}{\partial x^*}\overline{\tilde{u}^*\tilde{r}^*_{11}}$$

$$+ \overline{\tilde{r}^*_{11}\frac{\partial \tilde{u}^*}{\partial x^*}} - \frac{\partial}{\partial y^*}\overline{\tilde{u}^*\tilde{r}^*_{12}} + \overline{\tilde{r}^*_{12}\frac{\partial \tilde{u}^*}{\partial y^*}} \tag{6.19}$$

$$\frac{d}{dt^*}\left(\frac{1}{2}\overline{\tilde{v}^*\tilde{v}^*}\right) = -\frac{\partial}{\partial y^*}\overline{\tilde{p}^*\tilde{v}^*} + \overline{\tilde{p}^*\frac{\partial \tilde{v}^*}{\partial y^*}} + \frac{1}{Re}\left(\frac{\partial^2}{\partial x^{*2}} + \frac{\partial^2}{\partial y^{*2}}\right)\frac{\overline{\tilde{v}^*\tilde{v}^*}}{2}$$

$$- \frac{1}{Re}\left[\overline{\left(\frac{\partial \tilde{v}^*}{\partial x^*}\right)^2} + \overline{\left(\frac{\partial \tilde{v}^*}{\partial y^*}\right)^2}\right] - \frac{\partial}{\partial x^*}\overline{\tilde{v}^*\tilde{r}^*_{12}} + \overline{\tilde{r}^*_{12}\frac{\partial \tilde{v}^*}{\partial x^*}}$$

(continued)

$$- \frac{\partial}{\partial y^*} \overline{\tilde{v}^* \tilde{r}^*_{22}} + \overline{\tilde{r}^*_{22} \frac{\partial \tilde{v}^*}{\partial y^*}} \qquad (6.20)$$

where

$$\frac{d}{dt^*} = \frac{\partial}{\partial t^*} + U \frac{\partial}{\partial x^*}$$

On the right-hand side of (6.19), the first term is the energy transport due to pressure work; the second term is the energy production from the mean field by the wave-associated Reynolds stress; the third term is the energy transfer to the vertical wave motion due to the pressure-strain; the fourth term (with $\frac{1}{Re}$) is the diffusion by viscosity; the fifth term (with $\frac{1}{Re}$) is the viscous dissipation; and the last four terms are the energy transport and the stress-strain work due to the wave-induced turbulent Reynolds stresses. Their overall effect results in the change in the horizontal kinetic energy. Similar interpretations can also be given to the vertical kinetic energy balance equation (6.20). Note that the energy production only appears in (6.19) for parallel shear flows. The pressure-strain terms in (6.19) and (6.20) form a compensatory pair as the result of continuity, i.e., when $\overline{\tilde{p}^* \frac{\partial \tilde{u}^*}{\partial x^*}}$ is a source term in (6.19), $\overline{\tilde{p}^* \frac{\partial \tilde{v}^*}{\partial y^*}}$ is a drain term in (6.20) so that the energy is transferred from vertical oscillation to horizontal oscillation, and vice versa.

If the flow is fully or almost fully developed, the change of averaged quantities with respect to x^* is relatively small. Accordingly, the terms with $\frac{\partial}{\partial x^*}$ in front of averaged quantities can be dropped from (6.19) and (6.20). We find, after taking the flow to be stationary,

$$\underset{(1)}{-\overline{\tilde{u}^* \tilde{v}^*} \frac{\partial U}{\partial y^*}} + \overline{\tilde{p}^* \frac{\partial \tilde{u}^*}{\partial x^*}} + \underset{(2)}{\frac{1}{Re} \frac{\partial^2}{\partial y^{*2}} \left(\frac{1}{2} \overline{\tilde{u}^* \tilde{u}^*} \right)} - \underset{(3)}{\frac{1}{Re} \left[\overline{\left(\frac{\partial \tilde{u}^*}{\partial x^*} \right)^2} + \overline{\left(\frac{\partial \tilde{u}^*}{\partial y^*} \right)^2} \right]}$$

$$+ \underset{(5)}{\overline{\tilde{r}^*_{11} \frac{\partial \tilde{u}^*}{\partial x^*}}} - \underset{(4)}{\frac{\partial}{\partial y^*} \overline{\tilde{u}^* \tilde{r}^*_{12}}} + \underset{(6)}{\overline{\tilde{r}^*_{12} \frac{\partial \tilde{u}^*}{\partial y^*}}} = 0 \qquad (6.21)$$

$$- \frac{\partial}{\partial y^*} \overline{\tilde{p}^* \tilde{v}^*} + \overline{\tilde{p}^* \frac{\partial \tilde{v}^*}{\partial y^*}} + \frac{1}{Re} \frac{\partial^2}{\partial y^{*2}} \left(\frac{1}{2} \overline{\tilde{v}^* \tilde{v}^*} \right) - \frac{1}{Re} \left[\overline{\left(\frac{\partial \tilde{v}^*}{\partial x^*} \right)^2} + \overline{\left(\frac{\partial \tilde{v}^*}{\partial y^*} \right)^2} \right]$$

(1) (2)

$$\overline{\tilde{r}^*_{12} \frac{\partial \tilde{v}^*}{\partial x^*}} - \frac{\partial}{\partial y^*} \overline{\tilde{v}^* \tilde{r}^*_{22}} + \overline{\tilde{r}^*_{22} \frac{\partial \tilde{v}^*}{\partial y^*}} = 0 \qquad (6.22)$$

(4) (3) (5)

Our measured data were used to calculate each term in (6.21) and (6.22) except those with $\tilde{p}^*$. Because no pressure data were obtained, $\overline{\tilde{p}^* \frac{\partial \tilde{u}^*}{\partial x^*}}$ was calculated by balancing (6.21) by summation of all other terms. $\overline{\tilde{p}^* \frac{\partial \tilde{v}^*}{\partial y^*}}$ equals $-\overline{\tilde{p}^* \frac{\partial \tilde{u}^*}{\partial x^*}}$ by continuity. Then, $\frac{\partial}{\partial y^*} \overline{\tilde{p}^* \tilde{v}^*}$ was obtained by balancing (6.22). The calculation results are given in Table 6.1. The horizontal energy balance is plotted in Figure 6.1 and the vertical energy balance in Figure 6.2. It is seen that the transfer processes are concentrated in a region very near the interface. The lines on each graph represent the sum of the terms shown there. Thus, if one adds the values at any point on these two lines, one obtains the pressure transport value $-\frac{\partial}{\partial y^*} \overline{\tilde{p}^* \tilde{v}^*}$. (Note the different scales used in Figures 6.1 and 6.2.) In Table 6.1, it is interesting to see that near the interface, $\overline{\left(\frac{\partial \tilde{u}^*}{\partial y^*} \right)^2} >> \overline{\left(\frac{\partial \tilde{u}^*}{\partial x^*} \right)^2} \simeq \overline{\left(\frac{\partial \tilde{v}^*}{\partial y^*} \right)^2} >> \overline{\left(\frac{\partial \tilde{v}^*}{\partial x^*} \right)^2}$; the energy dissipation is, therefore, mostly due to $\frac{1}{Re} \overline{\left(\frac{\partial \tilde{u}^*}{\partial y^*} \right)^2}$. As $\overline{\left(\frac{\partial \tilde{u}^*}{\partial x^*} \right)^2} \simeq \overline{\left(\frac{\partial \tilde{v}^*}{\partial y^*} \right)^2}$, the continuity equation is apparently satisfied by the measured data. Near the free stream, all these four dissipation terms are of the same order so the motion of the wave perturbation is irrotational as we have argued in Section 5.4. Table 6.1 shows that the viscous effects are of higher order (in magnitude) and are negligible. The turbulent energy transport and the energy drain to turbulence of the horizontal kinetic energy are one order in magnitude greater than those of turbulent energy transport and energy drain of the vertical kinetic energy.

A general structure of the energy flux in the region near the interface is as follows. The energy source of horizontal kinetic energy in a control volume is mainly provided by the turbulent energy transport from the control volume lying below and the energy production from the mean field. This energy source is partially balanced by dissipation into internal thermal energy and energy drain into background turbulence; however, the largest portion is converted into the vertical kinetic energy by the pressure perturbation. This vertical kinetic energy source is then balanced partially by the dissipation and the energy drain of the vertical kinetic energy, the remaining and largest portion of the energy source, combined with the additional energy source caused by turbulent transport from the control volume below, is balanced by the downward transport due to the pressure perturbation.

The equation for the total kinetic energy K given by equation (6.18a) is obtained by adding (6.21) and (6.22), which gives

$$- \frac{\partial}{\partial y^*} \overline{\tilde{p}^* \tilde{v}^*} - \overline{\tilde{u}^* \tilde{v}^*} \frac{\partial U}{\partial y^*} + \frac{1}{Re} \frac{\partial^2 K}{\partial y^{*2}} - \frac{1}{Re} \cdot \left[\overline{\left(\frac{\partial \tilde{u}^*}{\partial x^*} \right)^2 + \left(\frac{\partial \tilde{u}^*}{\partial y^*} \right)^2} + \overline{\left(\frac{\partial \tilde{v}^*}{\partial x^*} \right)^2 + \left(\frac{\partial \tilde{v}^*}{\partial y^*} \right)^2} \right]$$

$$- \frac{\partial}{\partial y^*} \left(\overline{\tilde{u}^* \tilde{r}^*_{12}} + \overline{\tilde{v}^* \tilde{r}^*_{22}} \right) + \overline{\tilde{r}^*_{11} \frac{\partial \tilde{u}^*}{\partial x^*}}$$

$$+ \overline{\tilde{r}^*_{12} \frac{\partial \tilde{u}^*}{\partial y^*}} + \overline{\tilde{r}^*_{12} \frac{\partial \tilde{v}^*}{\partial x^*}} + \overline{\tilde{r}^*_{22} \frac{\partial \tilde{v}^*}{\partial y^*}} = 0 \qquad (6.23)$$

Integrating (6.23) from y^* to the free stream yields

$$\int_{y^*}^{\infty} -\overline{\tilde{u}^* \tilde{v}^*} \cdot \frac{\partial U}{\partial y^*} \, dy^* - \frac{1}{Re} \int_{y^*}^{\infty} \left[\overline{\left(\frac{\partial \tilde{u}^*}{\partial x^*} \right)^2 + \left(\frac{\partial \tilde{u}^*}{\partial y^*} \right)^2 + \left(\frac{\partial \tilde{v}^*}{\partial x^*} \right)^2 + \left(\frac{\partial \tilde{v}^*}{\partial y^*} \right)^2} \right] dy^*$$

(continued)

$$+\int_{y^*}^{\infty} \overline{\left(\tilde{r}^*_{11}\frac{\partial\tilde{u}^*}{\partial x^*} + \tilde{r}^*_{12}\frac{\partial\tilde{u}^*}{\partial y^*} + \tilde{r}^*_{12}\frac{\partial\tilde{v}^*}{\partial x^*} + \tilde{r}^*_{22}\frac{\partial\tilde{v}^*}{\partial y^*}\right)} dy^*$$

$$= -\overline{\tilde{p}^*\tilde{v}^*} + \frac{1}{Re}\frac{\partial K}{\partial y^*} - \overline{\tilde{u}^*\tilde{r}^*_{12}} - \overline{\tilde{v}^*\tilde{r}^*_{22}} \qquad (6.24)$$

Now the control volume is a slice of width dx^* with the lower boundary at y^* and the upper boundary at the free stream. When (6.24) is evaluated at $y^* = 0$, the right-hand side of (6.24) represents the energy transfer across interface by the wave-induced forces $\tilde{p}^*$, $\tilde{r}^*_{ij}$ and $\frac{1}{Re}\cdot\frac{\partial\tilde{u}^*_i}{\partial y^*}$. The left-hand side of (6.24) is then the power supply from the wind field. Because our measurement closest to the interface was at $y^* = 1.604$ cm, the energy balance of (6.24) was calculated down to that point; the result is shown in Table 6.2.

It must be pointed out that $-\overline{\tilde{r}^*_{12}\tilde{u}^*}\Big|_{y^*=0}$ does not represent the energy transfer to the water wave by the wave-induced turbulent shear stress, because $\tilde{u}^*\big|_{y^*=0}$ does not describe the wave motion of the water particles. The horizontal oscillation of the water particles at the interface is described by $\tilde{u}(x^*, y^*, t^*)\Big|_{y^*=0}$ as shown in Section 6.2. When the flow is described in the fixed or in the stretched transformed coordinate systems, the mean turbulent shear stress $-\overline{u'v'}$ over the undulating water surface produces an oscillatory force $-f\tilde{\eta}\frac{\partial}{\partial y^*}\overline{u'v'}$, which combines with $-\tilde{r}^*_{12}$ to give the energy transfer when they acted on the oscillatory surface-water particles. The energy transfer from wind to waves by horizontal turbulent shear stresses is given then by

$$(-\overline{\tilde{r}^*_{12}\tilde{u}})_{y^*=0} + \left(-\overline{f\tilde{\eta}\frac{\partial}{\partial y^*}\overline{u'v'}\cdot\tilde{u}}\right)_{y^*=0} = -\overline{\tilde{r}_{12}\tilde{u}}\Big|_{y^*=0}$$

This argument was proven by the authors in the report of Wu et al. (1977) where the derivation for the energy transfer was based on the

phase average results and the derived results were not affected by which coordinate system was used. An additional argument can also be obtained by considering a flow over a solid wavy wall. There is no energy transfer across the solid wavy wall because the wall is stationary; however, there is non-zero value of $-\overline{\tilde{r}^*_{12}\tilde{u}^*}\Big|_{y^*=0}$. The argument shown above applies also to the other oscillatory forces such as $\tilde{p}^*$, $\tilde{r}^*_{22}$ and $\frac{1}{Re}\cdot\frac{\partial\tilde{u}^*_i}{\partial y^*}$, so the energy transfer to the water wave is given by

$$E = \left\{ -\overline{\tilde{p}\tilde{v}} - \overline{\tilde{r}_{12}\tilde{u}} - \overline{\tilde{r}_{22}\tilde{v}} + \frac{1}{Re}\cdot\frac{\partial}{\partial y^*}\left(\frac{1}{2}\overline{\tilde{u}\tilde{u}} + \frac{1}{2}\overline{\tilde{v}\tilde{v}} \right) \right\}_{y^*=0} \tag{6.25}$$

Table 6.3 shows the energy transfer calculated for each terms of (6.25) using our measured data. As in Section 5.4(b), the information of the pressure perturbation was inferred from the measurement of Yu et al. (1973). Note that Table 6.3 is obtained for $y^* = 1.604$ cm, not for $y^* = 0$. Because the energy production and the wave perturbation velocities change drastically near the interface, the value given in Table 6.3 are not an exact representation of the surface values. However, Table 6.3 does show that $-\overline{\tilde{p}\tilde{v}}$ is dominant over other transfer terms. The domination of the $-\overline{\tilde{p}\tilde{v}}$ term should remain valid at the interface. A better interpretation for $-\overline{\tilde{p}\tilde{v}}$ at the interface was given in Section 5.4(b).

Regarding the energy transfer by the induced turbulent Reynolds stresses, Table 6.3 shows that $-\overline{\tilde{r}_{12}\tilde{u}}$ is one order in magnitude greater than $-\overline{\tilde{r}_{22}\tilde{v}}$, but is one order in magnitude smaller than $-\overline{\tilde{p}\tilde{v}}$. Both $-\overline{\tilde{r}_{12}\tilde{u}}$ and $-\overline{\tilde{r}_{22}\tilde{v}}$ are negative, i.e., the energy is transferred from the water wave to the wind. The negative transfer in $-\overline{\tilde{r}_{12}\tilde{u}}$ and $-\overline{\tilde{r}_{22}\tilde{v}}$ and the relative orders of magnitude among $-\overline{\tilde{p}\tilde{v}}$, $-\overline{\tilde{r}_{12}\tilde{u}}$, and $-\overline{\tilde{r}_{22}\tilde{v}}$

were also observed by Wu et al. (1977) for wind-waves. Because the turbulent oscillations are presumably damped at the interface by viscosity, the role of the induced turbulent Reynolds stresses is gradually taken by the viscous oscillatory stresses when one approaches the interface. It is known that the viscous effect at the interface tends to attenuate the water wave and results in the energy transfer from the water wave to the wind. So $-\overline{\tilde{r}_{12}\tilde{u}}$ and $-\overline{\tilde{r}_{22}\tilde{v}}$ are expected to be negative.

Based on the integral energy balance (Table 6.2) and the discussion on the energy transfer from the wind to the water wave, the energy budget for the wave perturbation field is illustrated graphically in Figure 6.3. The arrows in Figure 6.3 indicate the directions of the energy transfer.

6.5 Interaction between Wind and Waves

We now attempt to discuss the physics that describes the interaction between the wind and the waves. In order to do this, we need to start with the case of zero wind to show the basic behavior of the wave perturbation field and the phase shift of $\tilde{u}$ due to the existence of a Stokes layer near the interface. Then the wind is introduced, but the wind speed is still within the range of $U_\infty < c$, to show the first-step effect of the wind on the wave perturbation field and how the Stokes layer is affected by turbulence. Finally, the wind speed is further increased to the range of $U_\infty > c$ to produce a critical layer. The critical layer mechanism which describes the energy transfer from wind to waves, the changes in the structure of the critical layer due to the influence of the turbulent wind, and the interaction between the critical layer and the Stokes layer are examined. The discussions given in this section are for an infinitely extended air flow, i.e., $H \to \infty$. Results for air flows with finite height are expected to be similar to those for $H \to \infty$.

The wave-induced velocities for the no wind condition are described by irrotational motion so that

$$\tilde{u} = -kac\, e^{-ky} \cos(kx - \omega t) \tag{6.26a}$$

$$\tilde{v} = kac\, e^{-ky} \sin(kx - \omega t) \tag{6.26b}$$

Equation (6.26a) does not satisfy the interface boundary condition (2.41b), so the viscous effect should be considered. The viscous effect results in a Stokes layer near the interface, and there

$$\tilde{u} = -kac\, e^{-ky} \cos(kx - \omega t) + 2kac\, e^{-\beta y} \cos(kx - \omega t + \beta y) \tag{6.27a}$$

$$\tilde{v} = kac\, e^{-ky} \sin(kx - \omega t) - kac \cdot \left(\frac{k}{\beta}\right) \cdot \left[e^{-\beta y} \cos\left(kx - \omega t + \beta y - \frac{\pi}{4}\right) - \cos\left(kx - \omega t - \frac{\pi}{4}\right)\right] \tag{6.27b}$$

where $\beta = \left(\frac{\omega}{2\nu}\right)^{1/2}$ is the reciprocal of the Stokes layer thickness (Phillips 1966, p. 34). $\tilde{u}$ is changed drastically by the viscous effect near the interface. The phase lag of $\tilde{u}$ increases from 0^{o} to 180^{o} when one moves from the interface across the Stokes layer; $\tilde{v}$ is only slightly modified because $\frac{k}{\beta} = \left(\frac{2}{Re_w}\right)^{1/2}$ is small, where $Re_w = \frac{\omega}{\nu k^2}$ is the wave-Reynolds number.

When a wind with $U_\infty < c$ is introduced into the flow field, the wave perturbation is affected by the mean velocity and the turbulence of the wind. The mean velocity causes the wave perturbation to decay more rapidly. This is represented by multiplying $\tilde{v}$ by an approximate decay factor $\left(1 - \frac{U}{c}\right)$, as suggested by Miles (1957) and Lighthill (1957). The turbulence introduces turbulent mixing as described by eddy viscosity, so the wave perturbation motion is no longer irrotational in the boundary layer. The range of turbulent mixing depends on the diffusion

layer thickness δ_o of the mean flow (local scale) and the thickness of the boundary layer δ (global scale). When the Stokes layer thickness of the wave perturbation is thicker than δ_o, i.e., $\delta_o\beta \ll 1$, the upper portion of the Stokes layer is dominated by turbulent mixing. Turbulent mixing outside the Stokes layer usually results in a more uniform profile of the wave perturbation near the free stream and a steeper profile near the interface. This can be justified by comparing the mean velocity profiles in a turbulent flow and in a laminar flow. The phase of $\tilde{u}$ and $\tilde{v}$ in the boundary layer is not so strongly affected by turbulence when $U_\infty < c$. Outside the turbulent boundary layer, the wave perturbation motion is still irrotational. An additional effect of the turbulence is the production of the induced turbulent Reynolds stresses. Details of the induced turbulent Reynolds stresses are discussed in Section 6.7.

When one observes the flow with $U_\infty < c$ in a travelling-wave coordinate system given by $x_t = x - ct$, the wave form is stationary. The mean wind flows from right to left with a velocity c-U if the water wave propagates from left to right. The flow confined in the boundary layer can be regarded as flowing over a series of convergent and divergent regions. Above the wave crest, $c - (U+\tilde{u})$ is a maximum because that is the narrowest passage of the flow. Therefore, $\tilde{u}$ must be a minimum and negative above the crest. Similarly, $\tilde{u}$ must be a maximum and positive above the wave trough. Hence the phase lag of $\tilde{u}$ is 180^o with respect to $\tilde{\eta}$.

If the wind speed is increased such that $U_\infty > c$, the interaction between the mean flow and the wave is complicated due to the introduction of an interaction scale, called the "critical height" y_c. The critical height is measured from the mean water level to the elevation where $U(y_c) = c$. Above the critical height, the mean wind flows from left to right with a velocity U-c when one observes the flow field in x_t. Above the wave crest, $U+\tilde{u}-c$ is a maximum, so $\tilde{u}$ is positive; above

the wave trough, $U+\tilde{u}-c$ is a minimum, so $\tilde{u}$ is negative. Flow below the critical height is similar to that for the case of $U_\infty < c$. Hence there is a phase change of 180^o for $\tilde{u}$ below and above the critical height. The classical hydrodynamic stability theory showed a discontinuity in $\tilde{u}$ at y_c. The viscous effect is significant near y_c in smoothing the discontinuity, if there has no turbulent mixing. As a result, the viscous effect produces a critical layer near y_c. The thickness of the critical layer is given by

$$\delta_c = \left[\frac{\nu}{kU'} \right]^{1/3}_{y=y_c} \tag{6.28}$$

where the primes denote the derivative with respect to y. δ_c is usually very thin for a log-linear mean velocity profile. The viscous effect leads to a continuous phase shift of $\tilde{u}$ across the critical layer. The phase of $\tilde{u}$ shifts in the wave propagating direction; this is different from that produced by the Stokes layer at the interface.

We now consider the situation where y_c is high enough that the critical layer and the Stokes layer are well-separated. Outside the critical layer, but above the Stokes layer, the wave perturbation motion is inviscid. A good approximation to $\tilde{v}$ is given by (Phillips 1966, p. 99)

$$\tilde{v} = \Gamma ka \cdot (U-c) \cdot e^{-ky} \sin(kx - \omega t) \tag{6.29}$$

where $\Gamma = -1$ for $y < y_c$ and $\Gamma^2 \simeq \frac{1}{3}$ for $y > y_c$. Equation (6.29) shows that the amplitude $|\hat{v}|$ decreases as $y \to y_c$ from both sides of the critical layer. As a result, there is a minimum value of $|\hat{v}|$ in the critical layer.

The most significant result of the quasilaminar (or inviscid) analysis is the production of the wave-associated Reynolds stress $-\overline{\tilde{u}\tilde{v}}$

in the critical layer; this provides the energy transfer mechanism for the wave's growth. According to Miles theory (1957), $-\overline{\tilde{u}\tilde{v}}$ has the form

$$-\overline{\tilde{u}\tilde{v}} = \begin{cases} 0 & \text{for } y > y_c \\ \pi \left[\left(\frac{-U''}{kU'} \right) \cdot \overline{\tilde{v}^2} \right]_{y=y_c} & \text{for } y < y_c \end{cases} \tag{6.30}$$

From equation (5.13), the energy transfer due to the pressure perturbation is given by

$$E_p = \frac{\pi}{2} \left(\frac{c}{U_\infty} - \frac{U_o}{U_\infty} \right) \cdot \left[\left(\frac{-U''}{kU'} \right) \left(\frac{|\hat{v}|}{U_\infty} \right)^2 \right]_{y=y_c} \tag{6.31}$$

According to the curve-fitted mean velocity profile given in Figure 5.4, the critical layer occurs at $y_c^+ = 46.7$ where $u^+ = 18.2$. We have then $y_c = 0.849$ cm and $ky_c = 0.0342$ for the present experiment. We also have $|\hat{v}|/U_\infty = 2.1 \cdot 10^{-2}$ at y_c from Figure 5.9(a). Hence, the value of E_p found from (6.31) is $1.26 \cdot 10^{-2}$, which is almost 20 times greater than those estimated in Section 5.4(b). The main reason for this discrepancy is that (6.31) is based on the viscous critical layer mechanism, but here is applied to a turbulent flow. In (6.31), it is seen that the location of the critical height is the key to this mechanism. In a turbulent flow, the critical layer structure is distorted by turbulent mixing and the critical height in the turbulently-mixed critical layer is not clearly defined. Hence, (6.31) is not adequate for a turbulent flow unless we can locate the critical height in the turbulently-mixed critical layer. We will come back to this point after the turbulent effect on the wave perturbation is discussed.

Before we examine the turbulent effect, let us take a quick look at the case where $y_c < (\delta_c + 1/\beta)$. In this situation, the critical layer and the Stokes layer overlap. Since the upper portion of the Stokes

layer is affected by the critical layer, the 180^{o} phase shift of $\tilde{u}$ in the Stokes layer is usually not completed before the critical layer becomes predominant. The effect of the critical layer pushes the phase shift back into the downstream direction. As a result, one will not observe the 180^{o} phase lag of $\tilde{u}$ near the interface but outside the Stokes layer.

Let us now examine the role of the turbulence. In a turbulent flow, the smoothing by viscous effects of the discontinuity in the wave perturbation is replaced by turbulent mixing. Hence, the critical layer structure is greatly distorted by the turbulence. One may visualize that the location of the critical height is shifted up and down by turbulent fluctuations according to $U + u' - c = 0$. Although $\tilde{u}$ can also shift the critical height, it was shown by Davis (1969) that this is a result of nonlinear effects and is not responsible for the wave's growth because no energy transfer was found; hence, it is not considered here. The instantaneous, local viscous critical layer is further thinned or thickened by the turbulent fluctuations; this can easily be seen from (6.28) where the velocity gradient is changed when the mean profile U is replaced by the instantaneous profile $U + u'$. The structure of the instantaneous critical layer is also subjected to changes due to vertical convection by v', which was not considered in Miles (1957) analysis where $V = v' = 0$ due to parallel flow and inviscid quasilaminar assumptions. The statistically averaged result of this turbulent mixing is a turbulently mixed critical layer.

The turbulently mixed critical layer is thick and may extend over most of the boundary layer. The thickness of the turbulently mixed critical layer should depend on the intensity and the statistical properties of u', instead of being given by (6.28). When y_c is low, the turbulent critical layer overlaps the upper portion of the Stokes layer. Thus, the phase lag of $\tilde{u}$ near the interface is not 180^{o}; we observed $\theta_{\tilde{u}}$ approximately 85^{o} (see Figure 5.8(b)). The phase lag of 85^{o} in $\tilde{u}$

is expected to decrease at higher wind speed because more of the Stokes layer is affected by the turbulent critical layer. This is confirmed by our three coordinate-systems measurement where we observed that $\theta_{\tilde{u}} \simeq 55^{o}$ for $U_{\infty}/c = 1.88$. Contrary to the prediction of (6.30), the distribution of $-\overline{\tilde{u}\tilde{v}}$ is expected to be continuous and smoothly varying over the whole boundary layer; this behavior was observed in this study.

Suppose now we let $\bar{y}_c$ represent the averaged effective critical height and assume that it depends on the magnitude as well as the distribution of the u'-component in the boundary layer. Then, $\bar{y}_c$ can only be determined experimentally. However, it can be argued that since the magnitude of the u'-component increases drastically at the interface as y increases and then decreases when near the free stream, $\bar{y}_c$ tends to be located at higher elevation than $y_c [U(y_c) = c]$ for small y_c and at lower elevation than y_c for large y_c near the free stream. As inferred from the quasilaminar result, it is reasonable to assume that $\bar{y}_c$ is located at a position where $|\hat{v}|$ has a minimum. Details of the turbulent effect on the critical layer structure are now being experimentally determined by the authors and will be reported in the near future.

From Figure 5.9(a), we found the minimum value of $|\hat{v}|/U_{\infty}$ is approximately $1.3 \cdot 10^{-2}$ at $k\bar{y}_c = 0.26$. E_p calculated by (6.31) is then equal to $6.3 \cdot 10^{-4}$ which is consistent with those values obtained in Section 5.4(b). We now conclude that the estimate of E_p based on (6.31) from the viscous critical layer mechanism is entirely inadequate for a turbulent flow. A better estimate can be obtained by replacing the viscous critical layer by the turbulently mixed critical layer. Because the energy transfer rate given by (6.31) is independent of ν, replacing ν by eddy viscosity ν_t for the closure modelling of $\tilde{r}_{ij}$ will not significantly change the energy transfer rate. Our present experimental results indicate that the turbulence produces major effects only

on the wave perturbation by distorting the critical layer structure and has only minor effects on the direct transfer of the energy from the wind to the wave by $\tilde{\tau}_{ij}$. It is still possible that Miles inviscid theory may properly predict the energy transfer rate because $\overline{\tilde{p}\frac{\partial\tilde{\eta}}{\partial x^*}} = -\rho\overline{\tilde{u}\tilde{v}}$ as shown in Section 5.4(b) and because $\overline{\tilde{v}^2}\Big|_{y=y_c}$ predicted by Miles theory might be comparably smaller than what we had measured. Unfortunately, this is not the case. In Miles theory (1957), the wave perturbation pressure is expressed as

$$\hat{p}(y) = (\alpha_p + i\beta_p)\rho U_1^2 ka$$

where $U_1 = 2.5u_*$. Since $C_p = |\hat{p}|/\frac{1}{2}\rho U_\infty^2$, the wave growth parameter is

$$\beta_p\Big|_{y=\tilde{\eta}} = \left(\frac{U_\infty}{U_1}\right)^2 \frac{C_p \cdot \sin\theta_{\tilde{p}}}{2 \cdot ka}\Bigg|_{y^*=0} = 24.3$$

for the flow of this study. The corresponding value of β_p based on the inviscid theory (using equation (6.31) but with $\overline{\tilde{v}^2}\Big|_{y=y_c}$ calculated numerically) was found to be 2.9 for $ky_c = 0.0342$ (Figure 1 in Bole and Hsu 1967). Our value of 24.3 is consistent with Dobson's (1971) field data (run 4b in their measurements) where he found $\beta_p = 19$ for $c/u_* = 17$, and is 8 times larger than the 2.9 value predicted by Miles' theory. This indicates that the distortion of the critical layer by turbulence is responsible for the higher measured growth rate. Turbulence produces little direct energy transfer, but works like a "catalyst" in producing $-\overline{\tilde{u}\tilde{v}}$ as pointed out by Stewart (1967).

6.6 The Structure of Interface Flow

Based on the discussions given in the previous sections, a general structure of the interface flow is now described in three categories by

the consideration of flow scales. When there is no air flow, the wave perturbation field is characterized by three scales, i.e., wave amplitude a, wave length $1/k$, and thickness of the viscous Stokes layer $1/\beta$. a and $1/\beta$ are local scales and $1/k$ is a global scale. For a turbulent flow, the boundary layer thickness δ is a global scale and the viscous sub-layer thickness δ_o is a local scale. Another scale is H which measures the extent of the air flow. Our present discussion is restricted to small amplitude waves where $ka << 1$, and infinitely extended air flow where $kH >> 1$. The global scales form a nondimensional parameter $k\delta$. If $k\delta << 1$, the long wave approximation described in Chapter 3 applies. We do not consider the situation where the wave length is short and comparable to the local scales.

The local scales form the non-dimensional parameters a/δ_o and βa. The condition $a/\delta_o << 1$ is required for the validity of using a fixed coordinate system as described in Section 6.2 when there is a turbulent wind. The parameter βa interprets the relative scale between the water wave and the Stokes layer of the wave perturbed flow; hence it is a parameter for non-linear behavior. Under no wind condition, condition (6.6) does not reduce to $a/\delta_o << 1$; instead, it reduces to $\beta a << 1$ which is required for the validity of using a linear analysis in a fixed frame. Hence, when $\beta a >> 1$, a transformed coordinate system must be used to improve the linear analysis. However, $a/\delta_o << 1$ usually insures $\beta a << 1$ in a typical turbulent interface flow.

There are also the velocity scales of the wind and of the wave, which form the parameter c/U_∞. This parameter determines the position of the critical height y_c. When $c/U_\infty \geq 1$, the turbulent shear flow travels behind the travelling water wave. We call this interface flow "sub-critical". Almost no energy transfer from the wind to the wave is produced by the wave perturbation pressure for this case. There may be some energy transfers by viscous force and $\tilde{r}_{ij}$, but they are insignificant. When $0 < c/U_\infty < 1$, the upper portion of air flow travels faster than the water wave but the lower portion still lags behind.

There is a critical layer. We call this interface flow "critical". The energy transfer by the perturbation pressure is small when the critical height is large. The transfer increases as y_c decreases. However, when y_c is submerged into the viscous sublayer, the transfer rate decreases as y_c decreases. (Here we consider decreasing y_c by decreasing c.) When $c = 0$, there has no energy transfer because there is no wave motion at the boundary wall (the case of wavy solid wall). When $c/U_\infty < 0$, the wave propagates against the wind. We call this interface flow "super-critical". In this situation, energy is transferred in the opposite direction, i.e., from wave to wind by the pressure perturbation.

The situation of $c/U_\infty \simeq 0$ can not be obtained in an air-water interface flow because the minimum wave speed is 23 cm/sec at a wave length of 1.7 cm. Wave lengths shorter than 1.7 cm are for capillary waves, which are not in the range of the present study. To give a complete and systematic examination of the interface flow structure, an experiment performed at $c/U_\infty \simeq 0$ is required. Studying the flow over a stationary or flexible wavy wall, as accomplished by Kendall (1970) and Saeger and Reynolds (1971), provided the complementary portion of the interface flow study. It is even more instructive to measure the air flows over water surface waves and over a stationary wavy wall in the same wind-waves channel. A current experimental program is being undertaken at Stanford toward this end.

6.7 Closure Modelling of $\tilde{r}_{ij}$

A satisfactory closure model of $\tilde{r}_{ij}$ should not only result in good predictions, but also describe the physics of the flow. Here we examine the forms of closure model which are most realistic in comparison to our experimental results. A new closure model of $\tilde{r}_{ij}$ is proposed. Calculation of the proposed closure model will be made in a subsequent investigation and is not attempted in this study.

It has been pointed out in Chapter 2 that the closure modelling of the induced turbulent Reynolds stresses should be addressed to $\tilde{r}_{ij}(x^*, y^*, t^*)$ not to $\tilde{r}^*_{ij}(x^*, y^*, t^*)$. The equivalence between $\tilde{r}_{ij}(x, y, t)$ and $\tilde{r}^*_{ij}(x^*, y^*, t^*)$ as described in Section 6.2 indicates that $\tilde{r}_{ij}(x, y, t)$ is not a suitable quantity for closure modelling. This can also be inferred from the physical result that the mean profiles follow the wave forms. Therefore, the flow properties such as the mixing length, the eddy viscosity, etc., must be measured from the instantaneous distance above the interface.

Let us re-examine the experimental results of $\tilde{r}_{ij}$. Figures 5.14, 5.15 and 5.16 showed that the phases of $\tilde{r}_{11}$ and $\tilde{r}_{22}$ are almost the same and are approximately 90^o in the lead of the phase of $\tilde{u}$, while the phase of $\tilde{r}_{12}$ is about 90^o out of phase with those of $\tilde{r}_{11}$ and $\tilde{r}_{22}$ for $ky^* < 0.6$. This indicates that $\tilde{r}_{11}$ and $\tilde{r}_{22}$ are linearly related to $\frac{\partial \tilde{u}}{\partial t^*}$ and $\frac{\partial \tilde{u}}{\partial x^*}$. There is a possibility then that an eddy viscosity model may be adequate for the flow. We consider now only $\tilde{r}_{11}$. Closure models for $\tilde{r}_{12}$ and $\tilde{r}_{22}$ can be easily found after the model for $\tilde{r}_{11}$ is completed. Since only $\frac{\partial \tilde{u}}{\partial t^*}$ and $\frac{\partial \tilde{u}}{\partial x^*}$ produce 90^o phase differences, the following relation is proposed,

$$\tilde{r}_{11} = A_{11} \frac{\partial \tilde{u}}{\partial t^*} + B_{11} \frac{\partial \tilde{u}}{\partial x^*} \tag{6.32}$$

To characterize A_{11} and B_{11}, let us consider the flow over a stationary wavy wall. In this case, $\frac{\partial \tilde{u}}{\partial t^*} = 0$ and we have

$$\tilde{r}_{11} = B_{11} \frac{\partial \tilde{u}}{\partial x^*}$$

The flow over a stationary wall is similar to that over a flat plate if the curvature of the wavy surface is small. The phase averaged results for the mean velocity and the turbulent Reynolds stresses are to be

related by the familiar rule of eddy viscosity. So we find

$$B_{11} = -2\nu_t$$

where ν_t is the eddy viscosity. Another limit case to be considered is the situation where $k \to 0$. This corresponds to the flow with air modulation. Equation (6.32) becomes

$$\tilde{r}_{11} = A_{11} \frac{\partial \tilde{u}}{\partial t^*}$$

It is well known that the turbulent intensity is decreased in an accelerating mean flow. Since higher turbulent intensity is associated with deceleration, the value of A_{11} should be negative. A consequent result is that the air modulation velocity leads the modulated turbulent Reynolds stress $\tilde{r}_{11a}$ by 90^o. The 90^o phase lead of $\tilde{u}_a$ to $\tilde{r}_{11a}$ in the flow region outside the viscous Stokes layer was observed by Acharya and Reynolds (1975) for both $f_a = 24$ and 40 Hz. Unfortunately, no phase relation was available in this study for confirmation. Although it is realized that the air modulation in an interface flow is similar to that in a solid wall channel, a re-check of this phase relation by measuring the phases of $\tilde{u}_a$ and $\tilde{r}_{11a}$ in a wind-waves channel is required.

If we let $A_{11} = -2\nu_d/c$, equation (6.32) can be expressed as

$$\tilde{r}_{11} = -\frac{2\nu_d}{c} \frac{\partial \tilde{u}}{\partial t^*} - 2\nu_t \frac{\partial \tilde{u}}{\partial x^*}$$

$$= -2(\nu_t - \nu_d) \frac{\partial \tilde{u}}{\partial x^*} \qquad (6.33)$$

Equation (6.33) is apparently an eddy viscosity model but the eddy viscosity is now given by $\nu_t - \nu_d$. This eddy viscosity is different from the

mean flow eddy viscosity ν_t by an amount of ν_d. The data shown in Figure 5.14 requires that $\nu_t > \nu_d$ when $ky^* < 0.6$ and $\nu_t < \nu_d$ when $ky^* > 0.6$ to produce a phase jump of 180^o at $ky^* = 0.6$. Closure relations for $\tilde{r}_{12}$ and $\tilde{r}_{22}$ can be found from the eddy viscosity law as

$$\tilde{r}_{12} = -(\nu_t - \nu_d)\left(\frac{\partial \tilde{u}}{\partial y^*} + \frac{\partial \tilde{v}}{\partial x^*}\right) \tag{6.34}$$

$$\tilde{r}_{22} = -2(\nu_t - \nu_d)\frac{\partial \tilde{v}}{\partial y^*} \tag{6.35}$$

Because $\frac{\partial \tilde{u}}{\partial y^*} >> \frac{\partial \tilde{v}}{\partial x^*}$, (6.34) shows that $\tilde{r}_{12}$ is almost in phase with $\tilde{u}$ as indicated in Figure 5.15. There are two inconsistencies between the eddy viscosity model and our experimental data: (a) equation (6.35) predicts that $\tilde{r}_{22}$ is 180^o out of phase to $\tilde{r}_{11}$, and (b) the amplitude of $\tilde{r}_{22}$ predicted by (6.35) is of the same order of the amplitude of $\tilde{r}_{11}$ according to continuity. To correct these discrepencies, the following model is considered.

It is well known that the eddy viscosity model is a simplified form of the constitutive relation which describes the turbulent stresses by the analog of molecular viscous stresses. The constitutive relation attributed to Prandtl in 1925 and Von Karman in 1930 is expressed as

$$\bar{R}_{ij} = \frac{\overline{q^2}}{3}\delta_{ij} - 2\nu_T \bar{S}_{ij} \tag{6.36}$$

where

$$\bar{S}_{ij} = \frac{1}{2}\left(\frac{\partial \bar{u}_i}{\partial x_j} + \frac{\partial \bar{u}_j}{\partial x_i}\right) \tag{6.37}$$

and ν_T is the eddy viscosity. For the interface flow with a water wave, $\bar{R}_{ij}$, $\overline{q^2}$, and $\bar{S}_{ij}$ should be replaced by the phase averaged quantities, i.e.,

$$\langle R_{ij} \rangle = \overline{R}_{ij} + \tilde{r}_{ij} \tag{6.38a}$$

$$\langle q^2 \rangle = \overline{q^2} + \tilde{q^2} \tag{6.38b}$$

$$\langle S_{ij} \rangle = \overline{S}_{ij} + \tilde{S}_{ij} = \frac{1}{2}\left(\frac{\partial \langle u_i \rangle}{\partial x_j} + \frac{\partial \langle u_j \rangle}{\partial x_i}\right) \tag{6.38c}$$

And, the coordinate should be one which moves with the wave speed to eliminate time dependence. Since (6.33) is also regarded as observed in the coordinate system moving with the wave speed, we have $\nu_T = \nu_t - \nu_d$. The constitutive relation for the wave perturbation quantities is now found as

$$\tilde{r}_{ij} = \frac{\tilde{q^2}}{3}\delta_{ij} - 2\nu_T \tilde{S}_{ij} \tag{6.39}$$

where

$$\tilde{S}_{ij} = \frac{1}{2}\left(\frac{\partial \tilde{u}_i}{\partial x_j} + \frac{\partial \tilde{u}_j}{\partial x_i}\right) \tag{6.40}$$

If (6.39) is taken to be in the transformed coordinate system, $\tilde{q^2} = 0$ will result in (6.33), (6.34) and (6.35). Our measurement of $\tilde{r}_{11}$ and $\tilde{r}_{22}$ showed that $\tilde{q^2}$ has the same phase distribution as $\tilde{r}_{11}$ and $\tilde{r}_{22}$. So we propose that

$$\tilde{q^2} = -6A(\nu_t - \nu_d)\frac{\partial \tilde{u}}{\partial x^*} \tag{6.41}$$

The relation (6.39) is based on homogeneous isotropic turbulence. To characterize anisotropic behavior of the shear flow, the value of A in (6.41) can be taken as different for $\tilde{r}_{11}$ and $\tilde{r}_{22}$. So the final results for $\tilde{r}_{11}$ and $\tilde{r}_{22}$ are

$$\tilde{r}_{11} = -2(1+A_1)(\nu_t - \nu_d)\frac{\partial \tilde{u}}{\partial x^*} \tag{6.42}$$

$$\tilde{r}_{22} = -2(\nu_t - \nu_d)(A_2 \frac{\partial \tilde{u}}{\partial x^*} + \frac{\partial \tilde{v}}{\partial y^*}) \tag{6.43}$$

and (6.34),

$$\tilde{r}_{12} = -(\nu_t - \nu_d)\left(\frac{\partial \tilde{u}}{\partial y^*} + \frac{\partial \tilde{v}}{\partial x^*}\right)$$

remains unchanged.

The closure model given above is basically an eddy viscosity model, but with features distinct from that proposed by Norris and Reynolds (1975). In the model of Norris and Reynolds, the eddy viscosity was regarded as due to an organized wave with the mean eddy viscosity equal to the one corresponding to the flow without the surface waves. The wave component of the eddy viscosity $\tilde{\nu}_t$ is combined with the mean strain $\partial U/\partial y^*$ to produce an additional wave-induced turbulent shear stress $\tilde{\nu}_t \partial U/\partial y^*$. Thus their model is

$$\tilde{r}_{12} = -\tilde{\nu}_t \frac{\partial U}{\partial y^*} - \nu_t\left(\frac{\partial \tilde{u}}{\partial y^*} + \frac{\partial \tilde{v}}{\partial x^*}\right)$$

In our model, we postulate that the change of the mean eddy viscosity from ν_t to $\nu_t - \nu_d$ due to the propagating property of the surface wave is of significance in describing the induced turbulent Reynolds stresses. This model does not contradict to Norris and Reynolds' but is complementary. When $c = 0$, $\nu_d = 0$ according to our model but $\tilde{\nu}_t$ need not equal zero. Combination of these two modelling schemes should give a better description of the wave perturbation flow. However, we will not investigate this combination untill we have tested our present model. Detailed calculation of the wave perturbation field based on these models is reserved for subsequent investigations.

From our present data for $\tilde{r}_{ij}$, it is also seen that $\tilde{u}$ and $\tilde{r}_{11}$ are of the same phase near the free stream; this is not consistent with the closure relation (6.42). In the free stream, the turbulent mixing is

weak and the turbulent fluctuation is intermittent and of large scale. Hence, the fluid motion is shear free and irrotational. According to the Bernoulli equation, we have

$$\frac{p}{\rho} + \frac{1}{2}\{(u-c)^2 + v^2 + w^2\} = \frac{\partial \Theta}{\partial t} \tag{6.44}$$

where Θ is the potential function. Substituting equation (2.23) into (6.44) and extracting the wave component, we obtain

$$\frac{\tilde{p}}{\rho} + \frac{1}{2}(U-c)\tilde{u} + \frac{1}{2}(\tilde{r}_{11} + \tilde{r}_{22} + \tilde{r}_{33}) = 0 \tag{6.45}$$

In (6.45), both $(U-c)\tilde{u}$ and $(\tilde{r}_{11} + \tilde{r}_{22} + \tilde{r}_{33})$ are the responses of velocity to the pressure perturbation $\tilde{p}$, so they are of the same phase. Hence,

$$\tilde{r}_{11} = c_1(U-c)\tilde{u}$$

$$\tilde{r}_{12} = -c_2(U-c)\tilde{u}$$

$$\tilde{r}_{22} = c_3(U-c)\tilde{u}$$

where the relation for $\tilde{r}_{12}$ is proposed based on the fact that higher turbulent intensity results in higher turbulent shear stress. With the adjustment of the closure relation near the free stream, the more complete expressions for $\tilde{r}_{ij}$ are now given as

$$\tilde{r}_{11} = -2(1+A_1)(\nu_t - \nu_d)\frac{\partial \tilde{u}}{\partial x^*} + c_1(U-c)\tilde{u} \tag{6.46}$$

$$\tilde{r}_{12} = -(\nu_t - \nu_d)\left(\frac{\partial \tilde{u}}{\partial y^*} + \frac{\partial \tilde{v}}{\partial x^*}\right) - c_2(U-c)\tilde{u} \tag{6.47}$$

$$\tilde{r}_{22} = -2(\nu_t - \nu_d)\left(A_2\frac{\partial \tilde{u}}{\partial x^*} + \frac{\partial \tilde{v}}{\partial y^*}\right) + c_2(U-c)\tilde{u} \tag{6.48}$$

Thus, our proposed model for $\tilde{r}_{ij}$ combines the features of the mean eddy viscosity characterized by ν_t, the time-dependent viscoelastic response characterized by ν_d due to propagating waves, the anisotropy of the turbulence characterized by A_1 and A_2, and the potential flow behavior characterized by c_1, c_2, and c_3 near the free stream. ν_t can be determined by relating the measured U and $-\overline{u'v'}$ by mean eddy viscosity model, ν_d and c_2 by curve-fitting the measured $\tilde{r}_{12}$ to (6.47), and A_1 and c_1 and A_2 and c_3 by curve-fitting the measured values of $\tilde{r}_{11}$ and $\tilde{r}_{22}$ to (6.46) and (6.48) respectively.

CHAPTER 7

CONCLUSIONS AND RECOMMENDATIONS

7.1 Conclusions

The overall objectives of this study were largely accomplished. Based on the results and the discussions presented in Chapters 5 and 6, the following conclusions can be drawn:

(1) The mean flow basically follows the water wave form in the vicinity of the interface. However, the flow in the free stream tends to be unaware of the existence of the water wave underneath. This conclusion is supported not only by the measured mean velocity which persists as a log-linear profile to the region below the wave crests, but also by the observed eddy viscosity type of the induced turbulent Reynolds stresses as described in the transformed coordinate system. The constant stress layer of $-\rho \overline{u'v'}$ near the interface provided another evidence of this wave-form following property of the mean flow. Describing the interface flow in the transformed coordinate system given by (2.43a, b, c) is clearly an appropriate approach.

(2) The drift current affects significantly the mean velocity profile parameters by partially releasing the mean shear stress. As a result, the value of C is higher than and the value of u_* is lower than those measured for turbulent air flows over a flat plate. The mean flow in a wind-wave channel possesses a slightly Couette turbulent flow behavior.

(3) The ripples are strongly modulated by the mechanically-generated water wave. However, at the wind speed of this study, the roughness produced by the ripples is not large enough to interfere with the wind field. Hence, with respect to the wavy surface of the generated water wave, the surface condition is still regarded as aerodynamically smooth. At high wind speeds, the ripple effect must be taken into account.

(4) The mechanically-generated water wave produces an additional form drag to the wind field as described by $\overline{\tilde{p}\,\frac{\partial\tilde{\eta}}{\partial x^*}}\Big|_{y^*=0}$. We found that $\overline{\tilde{p}\,\frac{\partial\tilde{\eta}}{\partial x^*}}\Big|_{y^*=0} = -\rho\,\overline{\tilde{u}\tilde{v}}\Big|_{y^*=0}$. The value of $-\rho\,\overline{\tilde{u}\tilde{v}}$ decreases rapidly as the distance from the interface increases, so the total Reynolds shear stress $-\rho(\overline{u'v'} + \overline{\tilde{u}\tilde{v}})$ does not have a constant stress layer. Measuring the total shear stress at any distance above the interface usually results in a value much lower than that at the interface. The ratio γ_m of the momentum flux supported by the wave to the total momentum flux supported by the interface is given by $\gamma_m = \overline{\tilde{u}\tilde{v}}/(\overline{u'v'} + \overline{\tilde{u}\tilde{v}})$. Hence, if the wave supported momentum flux $-\rho\,\overline{\tilde{u}\tilde{v}}$ is determined by measuring $\tilde{p}$ and $\tilde{\eta}$ (correct value) and the total momentum flux is inferred from the concept of a constant stress layer by measuring the velocity fluctuations (including turbulence and wave perturbation velocities) somewhere above the interface (too low a value), the ratio γ_m then is too high (and indeed may be found to be in excess of unity.) The high value of the momentum transfer ratio reported by Dobson (1971) is the consequence of using this evaluating scheme. It is now concluded that estimating the portion of momentum transfer across the interface based on the constant total shear stress layer assumption, as made by Stewart (1961), is entirely inadequate when the wave field is highly peaked near the dominant frequency.

(5) Because $-\rho\,\overline{\tilde{u}\tilde{v}}\Big|_{y^*=0}$ is dependent on the square of the wave amplitude under the same wind condition where $-\rho\,\overline{u'v'}$ is constant, the ratio of the momentum supported by the waves to the total momentum across the interface can vary from zero when there is no mechanically-generated water wave to approximately 0.83 when the generated water wave is saturated ($ka \simeq 0.29$) at the wind condition of this study. (The measured ratio is 0.42 for $ka = 0.1075$.) It is concluded that the momentum transfer ratio depends on the wave field, on the wind field, and on the fetch; it can not be regarded as a fixed value.

(6) At the wind speed of this study, the wave perturbation motion is irrotational in the free stream, so there is no wave-associated Reynolds stress $-\rho\,\overline{\tilde{u}\tilde{v}}$ produced. But, in the turbulent boundary layer, the wave perturbation motion is rotational due to the turbulent mixing. Across the boundary layer, a phase shift of approximately 180° in $\tilde{u}$ was observed. The phase shift is continuous over the entire boundary layer, not sharp as predicted by Miles' theory (1957) which gives a 180° phase jump at the critical height. We observed a phase jump of 180° for $\tilde{r}_{ij}$ approximately at $ky^{*} = 0.6$. This phase jump is not related to Miles' theory, but can be interpreted as the result from the time-dependent viscoelastic response of the turbulent air flow to the propagating wave. The relationships between $\tilde{u}_i$ and $\tilde{r}_{ij}$ according to our measurement are basically of an eddy viscosity type. However, the effects of the propagating wave and of the potential flow behavior near the free stream have to be counted of if one looks for better relationships between $\tilde{u}_i$ and $\tilde{r}_{ij}$.

(7) Estimating the energy budget for the wave perturbation field showed that the kinetic energy transferred to the wave motion is mainly drawn from the mean flow field to the wave perturbation field by the wave-associated Reynolds stress $-\rho\,\overline{\tilde{u}\tilde{v}}$, from the wave perturbation field to the background turbulence field by $\tilde{r}_{ij}$ and from the wave perturbation field to the water wave field by the wave-induced pressure $\tilde{p}$. The result of the energy balance also showed that most of the energy transfer processes occur in a close proximity to the interface. Therefore, in evaluating the energy transfer from wind to waves either by using the energy balance scheme or the extrapolation from the measured profiles, data information near the interface is important. For the data obtained in this study, the extrapolation produces not only an excellent agreement between $\overline{\tilde{p}\,\frac{\partial \tilde{\eta}}{\partial x^{*}}}\Big|_{y^{*}=0}$ and $-\rho\,\overline{\tilde{u}\tilde{v}}\Big|_{y^{*}=0}$ but also between our wave growth rate and that measured in the field by Dobson

(1971). Hence, we conclude that the measurement in the transformed coordinate system using a wave-follower system, as performed in this study, seems to be essential in resolving the physical processes of the interface flow, especially for the flow over a mechanically-generated water wave. Interpreting the flow fields in the transformed coordinate system and formulating a realistic closure model for $\tilde{r}_{ij}$ are crucial to the ultimate theoretical prediction of the wave generation processes. To measure the air flow in closer proximity of the interface than in this study could provide additional information, but is not critical to the theoretical modelling of the interface flow; such data may, however, be useful to the final confirmation of theoretical predictions.

(8) The energy transfer from wind to water waves is predominantly caused by the wave perturbation pressure $\tilde{p}$. The induced turbulent Reynolds stresses transfer relatively small amounts of energy directly to the waves. However, the turbulence plays an important role in changing the structure of the viscous critical layer into a turbulently-mixed critical layer which greatly affects the rate of the energy transfer through the pressure $\tilde{p}$. It is found that Miles' theory is entirely inadequate in describing the energy transfer from wind to waves. Substituting the measured values of $|\hat{v}|$, U' and U'' at y_c into Miles' formula (6.31) results in a transfer rate 20 times higher than the measured transfer rate caused by $\tilde{p}$. On the other hand, using the measured log-linear mean velocity profile, one predicts theoretically an energy transfer rate 8 times too small.

From our measured energy transfer rate and the consistant resultant transfer rate observed by Dobson (1971), it is clear that the direct input of wind energy by pressure perturbation provides a main energy source for wave generation. This direct energy source from wind is of significance in explaining the high wave growth rate observed by Snyder and Cox (1966), by Barnett and Wilkerson (1967),

and by Bole and Hsu (1969). It was also found by Wu et al. (1977) that the energy transfer from wind by pressure perturbation is strongly correlated with the wave height for a wind-wave spectrum. The evolution of the wave spectrum is determined by the air energy input, the non-linear wave-wave interaction within the wave spectrum, and the white-cap dissipation of wave energy to current (including turbulence). This was observed by JONSWAP (Hasselmann et al., 1973) in the field and by Wu et al. (1977) in the laboratory. The net energy transfer in the wave spectrum can be divided into three frequency ranges. In the low frequency range, the air input and the transfer of non-linear wave-wave interaction are positive and the dissipation is weak so the positive transfer results in the waves' growth and the continuous shifting of the dominant wave to lower frequency. The intermediate frequency range lies between the dominant wave frequency and approximately twice the dominant wave frequency. In the intermediate frequency range, the net energy transfer is negative because the wave-wave interaction transfer and the dissipation are negative and their sum is larger than the positive transfer from wind. This indicates the recovery from the overshoot phenomena. In the high frequency range (or the equilibrium range), the positive transfer of wind and of wave-wave interaction are balanced by dissipation.

The ratio of the positive energy transfer by wind to that by wave-wave interaction at the low frequency range depends on the wind and the wave conditions. Measurement of Wu et al. (1977) showed that a larger ratio corresponds to higher wind speed and longer fetch (well-developed wave field). Hence, both the air input and the wave-wave interaction are responsible for the waves' growth. Barnett (1971) concluded that from 30% to 90% of the waves' growth is accounted for by the wave-wave interaction. However, for an unsaturated mechanically-generated water wave such as that in this study (or for a swell in the ocean), the air input is the unique energy source for waves' growth because no non-linear wave-wave interaction occurs.

(9) The wave perturbation field is definitely affected by the air modulation. Air modulation with a modulating frequency lower than the frequency of the water wave has a different effect on the wave perturbation from that with a modulating frequency higher than that of the water waves. The overall effect of turbulence on the wave perturbation is similar to that of air modulation with a modulating frequency higher than the frequency of the water wave, because most of the energetic components of the turbulence are of higher frequency than that of the water wave.

(10) The effect of air modulation on the ripples is a lower surface roughness (with respect to the mechanically-generated water wave) than that without air modulation. Wu (1973) observed a different result when there was no mechanically-generated water wave. Further examinations of the air modulation effect are required.

7.2 Recommendations

For a better understanding of the air-sea interaction, the following recommendations are made:

(1) For a complete measurement of a wave perturbation flow, the measurement of the pressure field should be incorporated with the measurements of the velocity and the wave-height fields.

(2) To obtain a clearer picture of the interface flow in the transformed coordinate system, the flow at other wind speeds should be studied. However, the special case of $c = 0$ can only be investigated for a flow over wavy solid wall. These basic studies and the study of the air modulation are crucial to the closure modelling of the wave-induced turbulent Reynolds stresses.

(3) As the viscous critical layer is strongly influenced by the background turbulence, to obtain direct insight to the energy transfer mechanism from wind to waves the detailed structure of the turbulently-mixed critical layer must be examined.

(4) For a better understanding of the turbulent effect on the wave perturbation flow, a refined measurement of the air modulation field is required. This includes a registration of a reference signal for the air modulation to permit education of the phase relationship between the modulated quantities. The air modulation can be incorporated with studies under suggestions (1), (2) and (3), or with the flows over wind-generated waves.

REFERENCES

Acharya, M. and Reynolds, W. C. (1975), "Measurements and Predictions of a Fully Developed Turbulent Channel Flow with Imposed Controlled Oscillations", Dept. of Mechanical Engrg., Tech. Report No. TF-8, Stanford University.

Barnett, T. P. and J. C. Wilkerson (1967), "On the Generation of Ocean Wind Waves as Inferred from Airborne Radar Measurements of Fetch-Limited Spectra," J. Mar. Res., 25(3),pp. 292-321.

Barnett, T. P. (1971), "An International Attempt to Understand Wind Generated Ocean Waves," Part 2: Some Results. Res. Lab., Westinghouse Elec. Corp., Pittsburgh, Penn., 15 June.

Bendat, J. S. and A. G. Piersol (1971), Random Data: Analysis and Measurement Procedures, Wiley-Interscience, New York.

Benjamin, T. B. (1959), "Shearing Flow over a Wavy Boundary", J. Fluid Mech., Vol. 6, pp. 161-205.

Bole, J. B. and E. Y. Hsu (1967), "Response of Gravity Water Waves to Wind Excitation," Dept. of Civil Engr., Tech. Rept. No. 79, Stanford University, Stanford, California.

Bole, J. B. and E. Y. Hsu (1969), "Response of Gravity Water Waves to Wind Excitation," J. Fluid Mech., 35, pp. 657-675.

Bracewell, R. (1966), The Fourier Transform and Its Applications, McGraw-Hill, Inc., New York.

Bradshaw, P., Ferriss, D. H. and Atwell, N. P. (1967), "Calculation of Boundary Layer Development Using the Turbulent Energy Equation", J. Fluid Mech., Vol. 28, Part 3, pp. 593-616.

Chao, S. P., E. Y. Hsu and R. L. Street (1976), "The Interaction between Turbulent Wind and Progressive Water Waves," Tech. Rept. No. 204, Dept. of Civil Engr., Stanford Univ., Stanford, Calif.

Coles, D. E. (1954), "The Problem of the Turbulent Boundary Layer," Z. angew. Math. Phys. 5, pp. 181-203.

Coles, D. E. (1956), "The Law of the Wake in the Turbulent Boundary Layer", J. Fluid Mech., Vol. 1, pp. 191-226.

Davis, R. E. (1969), "On the High Reynolds Number Flow Over a Wavy Boundary", J. Fluid Mech., Vol. 36, pp. 337.

Davis, R. E. (1970), "On the Turbulent Flow over a Wavy Boundary," J. Fluid Mech., 42(5), pp. 721-731.

Davis, R. E. (1972), "On Prediction of the Turbulent Flow over a Wavy Boundary," J. Fluid Mech., 52(2), pp. 287-306.

Davis, R. E. (1974), "Perturbed Turbulent Flow, Eddy Viscosity and the Generation of Turbulent Stresses", J. Fluid Mech., Vol. 63, Part 4, pp. 673-693.

Dobson, F. W. (1971), "Measurements of Atmospheric Pressure on Wind-Generated Sea Waves", J. Fluid Mech., Vol. 48, Part 1, pp. 91-127.

Eckart, C. (1953), "The Generation of Wind Waves over a Water Surface," J. Appl. Phys., 24, pp. 1485-1494.

Gent, P. R. and P. A. Taylor (1976), "A Numerical Model of the Air Flow above Water Waves," J. Fluid Mech., Vol. 77, pp. 105-128.

Hall, P. (1975), "The Stability of Poiseuille Flow Modulated at High Frequencies". Proc. Roy. Soc. Lond., A. 344, pp. 453-464.

Hasselmann, K. (1967), "Non-Linear Interactions Treated by the Methods of Theoretical Physics (with Application to the Generation of Wave by Wind)," Proc. Roy. Soc., A 299, pp. 77-100.

Hasselmann, K. (1968), "Weak Interaction Theory of Ocean Waves," Basic Developments in Fluid Dynamics, Vol. 2, Ed. by M. Holt. Academic Press, New York.

Hasselmann, K., T. P. Barnett, E. Bouws, H. Carlson, D. E. Cartwright, K. Enke, J. A. Ewing, H. Gienapp, D. E. Hasselmann, P. Kruseman, A. Meerburg, P. Müller, D. J. Olbers, K. Richter, W. Sell, H. Walden (1973), "Measurements of Wind-wave Growth and Swell Decay during the Joint North Sea Wave Project," Deutsches Hydrographisches Institut, Hamburg.

Hinze, J. O. (1975), Turbulence--An Introduction to Its Mechanism and Theory, McGraw-Hill, New York.

Hsu, E. Y. (1965), "A Wind, Water-Wave Research Facility," Dept. of Civil Engr. Tech. Rept. No. 57, Stanford Univ., Stanford, Calif.

Hussain, A. K. M. F. and W. C. Reynolds (1970), "The Mechanics of a Perturbation Wave in a Turbulent Shear Flow," Dept. of Mech. Engr. Tech. Rept. FM-6, Stanford Univ., Stanford, Calif.

Jeffreys, Sir H. (1925), "On the Formation of Water Waves by Wind," Proc. Roy. Soc., A. 107, pp. 189-206.

Jeffreys, H. (1926), "On the Formation of Waves by Wind. II," Proc. Roy. Soc., A. 110, pp. 241-247.

Karlsson, S. K. F. (1959), "An Unsteady Turbulent Boundary Layer," J. Fluid Mech., Vol. 5, pp. 662.

Kendall, J. J., Jr. (1970), "The Turbulent Boundary Layer over a Wall with Progressive Surface Waves", J. Fluid Mech., Vol. 41, pp. 159-281.

Klebanoff, P. S. (1954), "Characteristics of Turbulence in a Boundary Layer with Zero Pressure Gradients," NACA Tech. Note No. 3178.

Kline, S. J. and F. A. McClintock (1953), "Describing Uncertainties in Single Sample Experiments," Mechanical Engineering, ASME, pp. 3-8.

Lamb, H. (1932), Hydrodynamics, Cambridge University Press.

Laufer, J. (1951), "Investigation of Turbulent Flow in a Two-Dimensional Channel", NACA Report No. 1053.

Lighthill, M. J. (1957), "The Fundamental Solution for Small Steady Three-Dimensional Disturbances to a Two-Dimensional Parallel Shear Flow," J. Fluid Mech., Vol. 3, pp. 113.

Lin, C. C. (1955), The Theory of Hydrodynamic Stability. Cambridge University Press.

Liu, J. T. C. and L. Merkine (1976), "On the Interactions between Large-Scale Structure and Fine-Grained Turbulence in a Free Shear Flow. I. The Development of Temporal Interactions in the Mean," Proc. Roy. Soc. Lond., A. 352, pp. 213-247.

Long, R. B. (1971), "On Generation of Ocean Waves by a Turbulent Wind", Ph. D. Dissertation, University of Miami, Coral Gables, Florida.

Longuet-Higgins, M. S. (1969), "Action of a Variable Stress at the Surface of Water Waves," Phys. Fluids, 12, pp. 737-740.

Miles, J. W. (1957), "On the Generation of Surface Waves by Shear Flows", J. Fluid Mech., Vol. 3, pp. 185.

Miles, J. W. (1959), "On the Generation of Surface Waves by Shear Flows. Part 2," J. Fluid Mech., Vol. 6, Part 4, pp. 568-582.

Miles, J. W. (1967), "On the Generation of Surface Waves by Shear Flows. Part 5," J. Fluid Mech., Vol. 30, pp. 163-175.

Moffat, R. J. and W. M. Kays (1967), "The Turbulent Boundary Layer on a Porous Plate: Experimental Heat Transfer with Uniform Blowing and Suction," Report No. HMT-1, Thermosciences Division, Department of Mechanical Engineering, Stanford University, Stanford, California.

Norris, H. L. and Reynolds, W. C. (1975), "Turbulent Channel Flow with a Moving Wavy Boundary", Mech. Engrg. Dept., Report TF-7, Stanford University.

Phillips, O. M. (1957), "On the Generation of Surface Waves by Turbulent Wind", J. Fluid Mech., Vol. 2, pp. 417-445.

Phillips, O. M. (1966), The Dynamics of the Upper Ocean, Cambridge University Press, Cambridge.

Saeger, J. C. and Reynolds, W. C. (1971), "Perturbation Pressures over Travelling Sinusoidal Waves with Fully Developed Turbulent Shear Flow", Mech. Engrg. Dept., Report No. FM-9, Stanford University.

Schlichting, H. (1968), Boundary Layer Theory, McGraw-Hill Book Company.

Seminara, G. and P. Hall (1975). "Linear Stability of Slowly Varying Unsteady Flows in a Curved Channel," Proc. Roy. Soc. Lond., A 346, pp. 279-303.

Shemdin, O. H. and Hsu, E. Y. (1967), "Direct Measurements of Aerodynamic Pressure above a Simple Progressive Gravity Wave", J. Fluid Mech., Vol. 30, pp. 403-416.

Snyder, R. L. and Cox, C. S. (1966), "A Field Study of the Wind Generation of Ocean Waves", J. Mar. Res., Vol. 24 (2), pp. 141-178.

Stewart, R. H. (1970), "Laboratory Studies of the Velocity Field Over Deep-Water Waves", J. Fluid Mech., Vol. 42, Part 4, pp. 733-754.

Stewart, R. W. (1961), "The Wave Drag of Wind Over Water," J. Fluid Mech., 10, pp. 189-194.

Stewart, R. W. (1967), "Mechanics of Air-Sea Interface," Phys. Fluids Suppl., 10, pp. S47-55.

Townsend, A. A. (1972), "Flow in a Deep Turbulent Boundary Layer Over a Surface Distorted by Water Waves", J. Fluid Mech., 55, pp. 719-753.

Ursell, F. (1956), "Wave Generation by Wind," Surveys in Mechanics (ed. G. K. Batchelor), pp. 216-249, Cambridge Univ. Press.

Wu, H. Y., E. Y. Hsu and R. L. Street (1977), "The Energy Transfer Due to Air-Input, Non-Linear Wave-Wave Interaction and White-Cap Dissipation Associated with Wind-Generated Waves," Dept. of Civil Engr. Tech. Rept. No. 207, Stanford Univ., Stanford, Calif.

Wu, Jin (1968), "Laboratory Studies of Wind-wave Interactions," J. Fluid Mech., 34, pp. 91-111.

Wu, Jin (1973), "Microscopic Structure of Disturbed Water Surface Under Fluctuating Winds," Hydronautics, Incorporated Technical Report 7211-5.

Young, M. B. O., E. Y. Hsu and R. L. Street (1973), "Air-Water Interaction: the Nature of Turbulent Heat, Mass and Momentum Transfer Mechanisms in the Air Boundary Layer," Dept. of Civil Engr. Tech. Rept. No. 163, Stanford Univ., Stanford, Calif.

Yu, H. Y., Hsu, E. Y. and Street, R. L. (1971), "A Refined Measurement of Aerodynamic Pressure Over Progressive Water Waves", Civil Engrg. Dept., Report No. 146, Stanford University.

Yu, H. Y., Hsu, E. Y. and Street, R. L. (1973), "Wave-Induced Perturbations in a Turbulent Boundary Layer Over Progressive Water Waves," Civil Engrg. Dept., Report No. 172, Stanford University.

APPENDIX I

UNCERTAINTY ANALYSIS

Measurement uncertainty generally occurs during data acquisition and reduction. Uncertainty in data acquisition usually results from improper performance of instruments, limitations in probe sensitivity and frequency response, and inaccuracy of instruments. Because the same probes and instruments were used for both calibrations and data taking, uncertainties of this type propagate and enter into a final result as calibration uncertainty.

The uncertainty due to data reduction results mainly from the use of a finite data record in calculating a statistical mean. This type of uncertainty also depends on which of the data reduction schemes used. Formulas used to estimate the data reduction uncertainty are given in Section 4.11.

Kline and McClintock (1953) proposed that the combined uncertainty δg of a measured quantity $g(x_i)$ due to independent effects x_i is expressed as

$$\frac{\delta g}{g} = \left\{ \sum_{i=1}^{N} \left(\frac{\partial g}{\partial x_i} \cdot \frac{\delta x_i}{g} \right)^2 \right\}^{1/2} \qquad \text{(A. 1)}$$

Since the calibration and the data reduction errors are the most significant errors involved, the combined uncertainty determined by (A. 1) is mainly contributed from these two uncertainties.

For the measured data in this study, the uncertainty is also dependent on the elevation y* where the data were collected, because different signal-to-noise ratios occur at different elevations. For instance, $\theta_{\tilde{r}_{ij}}$ at $ky^* \simeq 0.6$ usually has very high uncertainties because $\tilde{r}_{ij} \simeq 0$ there. The following list shows the overall uncertanties estimated for the present measured data, but does not represent

the values where the signal is weak in comparison to the noise:

$\tilde{\eta}$	± 3%
$\widetilde{\eta'^2}$	± 3%
U	± 4%
V	± 4%
$\overline{u_i' u_j'}$	± 7%
$\tilde{u}$	± 8%
$\tilde{v}$	± 13%
$\tilde{r}_{ij}$	± 20%
$\lvert\hat{u}\rvert$	± 4%
$\theta_{\tilde{u}}$	± 2°
$\lvert\hat{v}\rvert$	± 5%
$\theta_{\tilde{v}}$	± 3°
$\lvert\hat{r}_{ij}\rvert$	± 8%
$\theta_{\tilde{r}_{ij}}$	± 4°
$\lVert\tilde{u}_a\rVert$	± 4%
$\lVert\tilde{v}_a\rVert$	± 20%
$\lVert\tilde{r}_{ija}\rVert$	± 20%
$\lVert\tilde{u}_s\rVert$	± 30%
$\lVert\tilde{v}_s\rVert$	± 30%

TABLE 5.1

Parameters for Mean Velocity Profiles and Comparisons of the Friction Velocity

Data Used	Profile Parameters (Results of Curve Fitting)						Direct Measurement	Difference
f_a (Hz)	U_∞ (cm/sec)	δ (cm)	W_c	C	δ^+	u_* (cm/sec)	u_* (cm/sec)	$\frac{\Delta u_*}{u_*} \times 100\%$
0. 0.4 0.7	239.4	23.50	0.3240	8.619	1267	8.520	8.561	0.48
1.5	244.0	22.15	0.3050	7.178	1286	9.174	8.630	6.11
Average	240.5	23.16	0.3193	8.259	1272	8.684	8.578	1.23

TABLE 6.1

Energy Balance for Wave Perturbation Field

The short notations used in this table represent quantities described as follows:

$$\text{PROD} = -\overline{\tilde{u}^*\tilde{v}^*}\,\frac{\partial U}{\partial y^*} \qquad \text{PRES} = \overline{\tilde{p}^*\,\frac{\partial \tilde{u}^*}{\partial x^*}}$$

$$\text{DIFU} = \frac{1}{2\text{Re}}\cdot\frac{\partial^2}{\partial y^{*2}}\,\overline{(\tilde{u}^*\tilde{u}^*)} \qquad \text{DIXX} = \frac{1}{\text{Re}}\cdot\overline{\left(\frac{\partial \tilde{u}^*}{\partial x^*}\right)^2}$$

$$\text{DIXY} = \frac{1}{\text{Re}}\cdot\overline{\left(\frac{\partial \tilde{u}^*}{\partial y^*}\right)^2} \qquad \text{DISX} = \text{DIXX} + \text{DIXY}$$

$$\text{DTRU} = \frac{\partial}{\partial y^*}\,\overline{\tilde{r}^*_{12}\tilde{u}^*} \qquad \text{DRAUU} = \overline{\tilde{r}^*_{11}\,\frac{\partial \tilde{u}^*}{\partial x^*}}$$

$$\text{DRAUV} = \overline{\tilde{r}^*_{12}\,\frac{\partial \tilde{u}^*}{\partial y^*}} \qquad \text{DRAX} = \text{DRAUU} + \text{DRAUV}$$

$$\text{DPOW} = -\frac{\partial}{\partial y^*}\,\overline{\tilde{p}^*\tilde{v}^*} \qquad \text{DIFV} = \frac{1}{2\text{Re}}\,\frac{\partial^2}{\partial y^{*2}}\,\overline{(\tilde{v}^*\tilde{v}^*)}$$

$$\text{DIYX} = \frac{1}{\text{Re}}\cdot\overline{\left(\frac{\partial \tilde{v}^*}{\partial x^*}\right)^2} \qquad \text{DIYY} = \frac{1}{\text{Re}}\cdot\overline{\left(\frac{\partial \tilde{v}^*}{\partial y^*}\right)^2}$$

$$\text{DISY} = \text{DIYX} + \text{DIYY} \qquad \text{DTRV} = \frac{\partial}{\partial y^*}\,\overline{\tilde{r}^*_{22}\tilde{v}^*}$$

$$\text{DRAVU} = \overline{\tilde{r}^*_{12}\,\frac{\partial \tilde{v}^*}{\partial x^*}} \qquad \text{DRAVV} = \overline{\tilde{r}^*_{22}\,\frac{\partial \tilde{v}^*}{\partial y^*}}$$

$$\text{DRAY} = \text{DRAVU} + \text{DRAVV} \qquad \text{DIFF} = \text{DIFU} + \text{DIFV}$$

$$\text{DISS} = \text{DISX} + \text{DISY} \qquad \text{DTTR} = \text{DTRU} + \text{DTRV}$$

$$\text{DRAT} = \text{DRAX} + \text{DRAY}$$

All quantities are normalized by $\rho k U_\infty^3 = 6.715\cdot 10^2$ erg/cm^3-sec.

HORIZONTAL DIFFERENTIAL ENERGY BALANCE

Y	PROD	PRES	DIFU	DIXX	DIXY
59.4495	.0000E+00	.1020E-04	-.3307E-07	.1967E-08	.1037E-06
55.0995	.1365E-06	-.4235E-06	-.8559E-08	.3565E-08	.8980E-06
60.7495	.1901E-07	-.3594E-05	-.3550E-06	.4396E-08	.8498E-04
61.0095	.1916E-05	-.8775E-05	-.9266E-06	.4581E-08	.8054E-04
17.8595	.2620E-05	-.1920E-03	-.2166E-07	.5525E-08	.3926E-06
15.5195	-.2910E-05	.2557E-03	-.1198E-07	.3601E-06	.2561E-07
12.7795	-.1425E-04	.1590E-04	.4484E-07	.4345E-06	.1170E-06
10.8745	-.2740E-04	.2693E-04	.1517E-06	.5045E-06	.2330E-06
8.9095	-.3403E-04	.3874E-04	.2942E-06	.5503E-06	.3706E-06
7.6995	-.2919E-04	.3197E-04	.3704E-06	.5090E-06	.5739E-06
6.4295	-.3203E-03	.2189E-05	.1327E-05	.8477E-06	.1020E-05
5.1595	.6303E-04	-.6141E-04	.3342E-05	.1579E-07	.2039E-05
4.1495	.1376E-03	-.1403E-03	.7491E-05	.2746E-07	.4217E-05
3.3815	.2922E-03	-.3146E-03	.1548E-04	.4620E-07	.7958E-05
2.8755	.4560E-03	-.3380E-03	.2907E-04	.7045E-07	.1280E-04
2.3855	.6550E-03	-.4101E-03	.6365E-04	.1106E-06	.2570E-04
1.9045	.8971E-03	-.1365E-02	.1157E-03	.1599E-06	.5080E-04
1.6055	.1302E-02	-.2138E-02	.2524E-03	.2821E-06	.1578E-03

DISX	DIRU	DRAUU	DRAUV	DRAX
.1057E-06	-.5452E-05	-.8563E-06	-.3751E-05	-.4605E-05
.1255E-07	-.1006E-03	.5338E-06	.7805E-06	.1514E-05
.5240E-08	.8665E-06	.2256E-05	.4015E-06	.2657E-05
.5187E-08	.1699E-05	.4924E-05	.2496E-06	.5174E-05
.9252E-08	-.7685E-06	.4725E-05	.1379E-05	.8101E-05
.5121E-07	-.3156E-05	.2202E-05	.1350E-05	.3552E-05
.1214E-06	.3137E-05	-.4287E-06	-.4277E-05	-.4706E-05
.2560E-06	.1965E-04	-.4427E-05	-.1666E-04	-.2128E-04
.3801E-06	.4431E-04	-.1146E-04	-.3667E-04	-.4013E-04
.5790E-06	.6508E-04	-.1584E-04	-.5001E-04	-.6585E-04
.1056E-05	.8062E-04	-.1658E-04	-.6123E-04	-.7961E-04
.2035E-05	.9248E-04	-.2131E-04	-.7486E-04	-.9619E-04
.4244E-05	.9971E-04	-.2746E-04	-.9206E-04	-.1203E-03
.8004E-05	.1390E-03	-.3097E-04	-.9517E-04	-.1241E-03
.1208E-04	.2247E-03	-.3846E-04	-.1004E-03	-.1389E-03
.2581E-04	.4202E-03	-.6549E-04	-.1354E-03	-.2009E-03
.5104E-04	.7173E-03	-.1017E-03	-.1922E-03	-.2959E-03
.1360E-03	.1500E-02	-.2013E-03	-.3364E-03	-.7376E-03

VERTICAL DIFFERENTIAL ENERGY BALANCE

Y	DFDA	DIFV	DIFX	DIFY	DISF
39.4495	.9477E-03	-.8814E-04	.3358E-04	.7096E-06	.7852E-06
33.0995	-.3047E-03	-.1291E-06	.1204E-06	.1794E-06	.2998E-06
26.7495	-.6176E-03	-.9603E-04	.1661E-06	.3462E-04	.2207E-06
21.8695	-.9793E-03	.3964E-10	.2019E-06	.3194E-04	.2358E-06
17.0395	-.3989E-03	.4347E-04	.2127E-06	.8946E-04	.3022E-06
15.3195	.8444E-03	-.2952E-06	.2225E-06	.1342E-06	.3567E-06
12.7795	.1999E-04	-.8388E-06	.2353E-06	.1103E-06	.3720E-06
10.8745	.3107E-04	-.3886E-06	.2596E-06	.2888E-06	.5284E-06
8.9695	.3893E-04	.4071E-06	.2291E-06	.7051E-06	.9342E-06
7.6995	.2753E-04	.1255E-07	.2172E-06	.1151E-07	.1388E-07
6.4295	-.4733E-03	.2284E-07	.2149E-06	.1784E-07	.1978E-07
5.1595	-.8933E-04	.4834E-07	.2235E-06	.2359E-07	.2782E-07
4.1495	-.1447E-03	.8920E-07	.2317E-06	.4523E-07	.4557E-07
3.3815	-.3145E-03	.1708E-06	.2616E-06	.8443E-07	.8705E-07
2.8735	-.3249E-03	.3222E-06	.2888E-06	.1272E-06	.1501E-06
2.3655	-.8861E-03	.7523E-06	.3388E-06	.1714E-06	.1748E-06
1.9345	-.1284E-02	.1350E-05	.3905E-06	.2712E-06	.2731E-06
1.6035	-.1919E-02	.2997E-05	.5113E-06	.6990E-06	.7041E-06

DIRV	DRAVU	DRAVV	DRAY
-.1795E-03	.3905E-07	.2485E-05	.2324E-05
.1072E-03	.3456E-06	.8099E-06	.9555E-06
.2202E-03	.5114E-06	-.2086E-06	.3029E-06
.1250E-03	.4077E-06	-.8571E-06	-.2294E-06
-.1303E-03	.8880E-07	-.7002E-06	-.8314E-06
-.3228E-03	-.3632E-07	-.8165E-06	-.8528E-06
-.4349E-03	.7735E-06	-.5002E-06	.2733E-06
-.2967E-03	.1749E-05	-.9131E-06	.8362E-06
.1450E-03	.2959E-05	-.2596E-05	.3835E-06
.5436E-03	.3619E-05	-.4459E-05	-.8395E-06
.9771E-03	.4132E-05	-.6984E-05	-.2852E-05
.1295E-04	.3970E-05	-.9018E-05	-.5040E-05
.1524E-04	.3452E-05	-.1252E-04	-.8867E-05
.1350E-04	.3346E-05	-.1685E-04	-.1350E-04
.8715E-03	.2920E-05	-.2040E-04	-.1748E-04
-.2033E-04	.1602E-05	-.2580E-04	-.2420E-04
-.6815E-04	.8514E-06	-.3450E-04	-.3395E-04
-.1903E-03	-.1937E-05	-.4290E-04	-.4465E-04

DIFFERENTIAL TOTAL ENERGY BALANCE

Y	DIFF	DISS	DTTR	DKAI
39.4495	-.3595E-07	.1135E-06	-.7247E-05	-.2083E-05
33.0995	-.9850E-08	.1554E-07	.6660E-06	.2270E-05
26.7495	-.4518E-08	.7455E-08	.3149E-05	.2960E-05
21.6695	-.9226E-08	.7525E-08	.2949E-05	.4944E-05
17.8595	-.2122E-07	.1227E-07	-.2073E-05	.5470E-05
15.3195	-.1495E-07	.5478E-07	-.6584E-05	.2900E-05
12.7795	.5643E-07	.1251E-06	-.1212E-05	-.4432E-05
10.8745	.1258E-06	.2413E-06	.1684E-04	-.2045E-04
8.9695	.2991E-06	.3695E-06	.4576E-04	-.4777E-04
7.6995	.5029E-06	.5927E-06	.6852E-04	-.6669E-04
6.4295	.1330E-05	.1056E-05	.9039E-04	-.8266E-04
5.1595	.3508E-05	.2085E-05	.1054E-03	-.1012E-03
4.1455	.7580E-05	.4290E-05	.1130E-03	-.1292E-03
3.5815	.1305E-04	.8091E-05	.1525E-03	-.1576E-03
2.8755	.2940E-04	.1501E-04	.2334E-03	-.1564E-03
2.3055	.6456E-04	.2598E-04	.3999E-03	-.2251E-03
1.9045	.1170E-03	.5152E-04	.6492E-03	-.3278E-03
1.6055	.2554E-03	.1587E-03	.1503E-02	-.7825E-03

TABLE 6.2

Energy Balance for Equation (6.24)

(h = 1.604 cm)

	Transfer Mechanism	Transfer Rate Normalized by $\rho U_\infty^3 = 1.668 \cdot 10^4$ erg/cm^2-sec	
(1)	$\int_h^\infty -\overline{\tilde{u}^*\tilde{v}^*} \frac{\partial U}{\partial y^*} dy^*$	$6.112 \cdot 10^{-5}$	
(2)	Wave-Dissipation*	$-3.357 \cdot 10^{-6}$	$1.692 \cdot 10^{-5}$
(3)	Drain to Turbulence**	$-4.084 \cdot 10^{-5}$	
(4)	$\frac{1}{Re} \cdot \frac{\partial K}{\partial y^*}$	$-5.066 \cdot 10^{-6}$	
(5)	$-\overline{\tilde{r}^*_{12}\tilde{u}^*} - \overline{\tilde{r}^*_{22}\tilde{v}^*}$	$-5.031 \cdot 10^{-5}$	$1.693 \cdot 10^{-5}$
(6)***	$-\overline{\tilde{p}^*\tilde{v}^*}$	$7.231 \cdot 10^{-5}$	

* Wave-dissipation $= -\frac{1}{Re} \int_h^\infty \left[\overline{\left(\frac{\partial \tilde{u}^*}{\partial x^*}\right)^2 + \left(\frac{\partial \tilde{u}^*}{\partial y^*}\right)^2 + \left(\frac{\partial \tilde{v}^*}{\partial x^*}\right)^2 + \left(\frac{\partial \tilde{v}^*}{\partial y^*}\right)^2}\right] dy^*$

** Drain to Turbulence $= \int_h^\infty \left(\overline{\tilde{r}^*_{11}\frac{\partial \tilde{u}^*}{\partial x^*}} + \overline{\tilde{r}^*_{12}\frac{\partial \tilde{u}^*}{\partial y^*}} + \overline{\tilde{r}^*_{12}\frac{\partial \tilde{v}^*}{\partial x^*}} + \overline{\tilde{r}^*_{22}\frac{\partial \tilde{v}^*}{\partial y^*}}\right) dy^*$

*** (6) = (1) + (2) + (3) - (4) - (5)

TABLE 6.3

Energy Transfer from Wind to Water Wave

(Evaluated at $ky^* = 0.0646$)

Transfer Mechanism	Normalized Transfer Rate**
$-\overline{\tilde{p}\tilde{v}}$	$1.603 \cdot 10^{-4}$
$-\overline{\tilde{r}_{12}\tilde{u}}$	$-2.324 \cdot 10^{-5}$
$-\overline{\tilde{r}_{22}\tilde{v}}$	$-3.766 \cdot 10^{-6}$
$\frac{1}{Re}\frac{\partial}{\partial y^*}\left(\frac{1}{2}\overline{\tilde{u}\tilde{u}}\right)$	$2.594 \cdot 10^{-7}$
$\frac{1}{Re}\frac{\partial}{\partial y^*}\left(\frac{1}{2}\overline{\tilde{v}\tilde{v}}\right)$	$-6.993 \cdot 10^{-8}$
E (Total)	$1.335 \cdot 10^{-4}$

**Normalized by $\rho U_\infty^3 = 1.668 \cdot 10^4$ erg/cm^2-sec

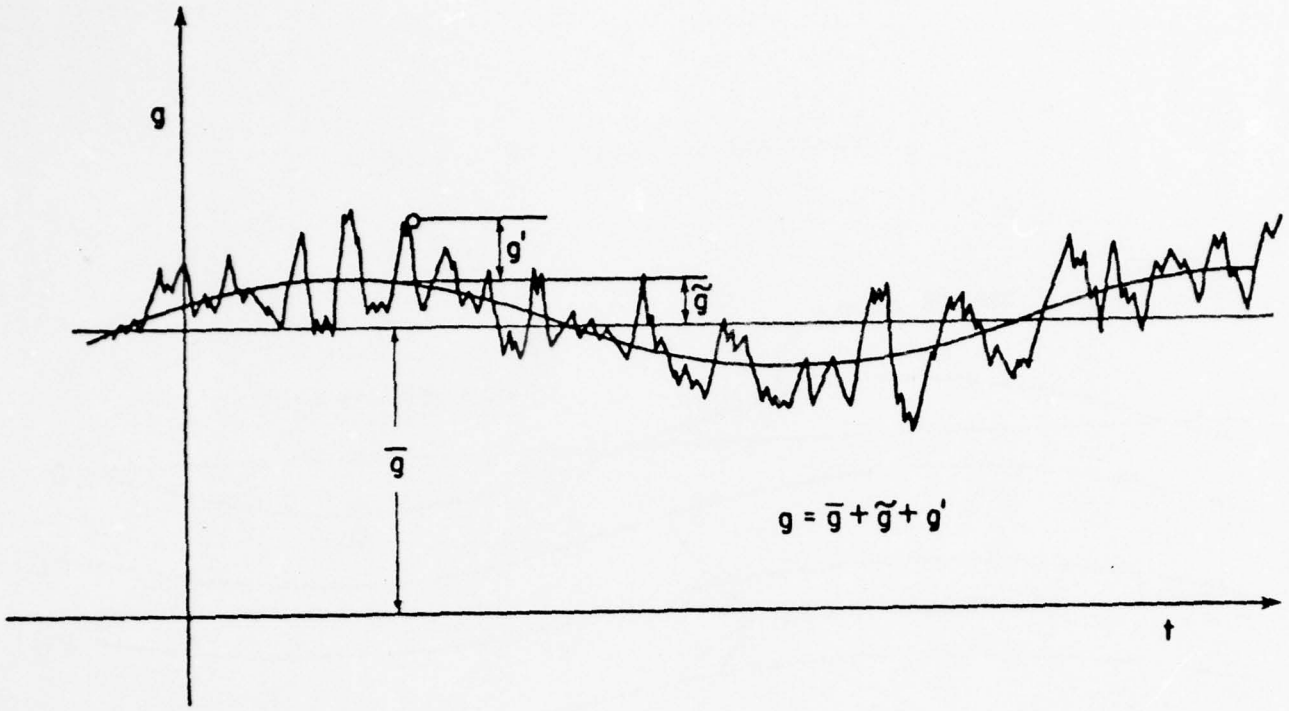

$$\bar{g} = \lim_{N \to \infty} \frac{1}{2N+1} \sum_{n=-N}^{N} g(t + n\Delta t)$$

$$\langle g \rangle = \lim_{N \to \infty} \frac{1}{2N+1} \sum_{n=-N}^{N} g(t + n\tau)$$

Figure 2.1 Schematic of Phase and Time Averages

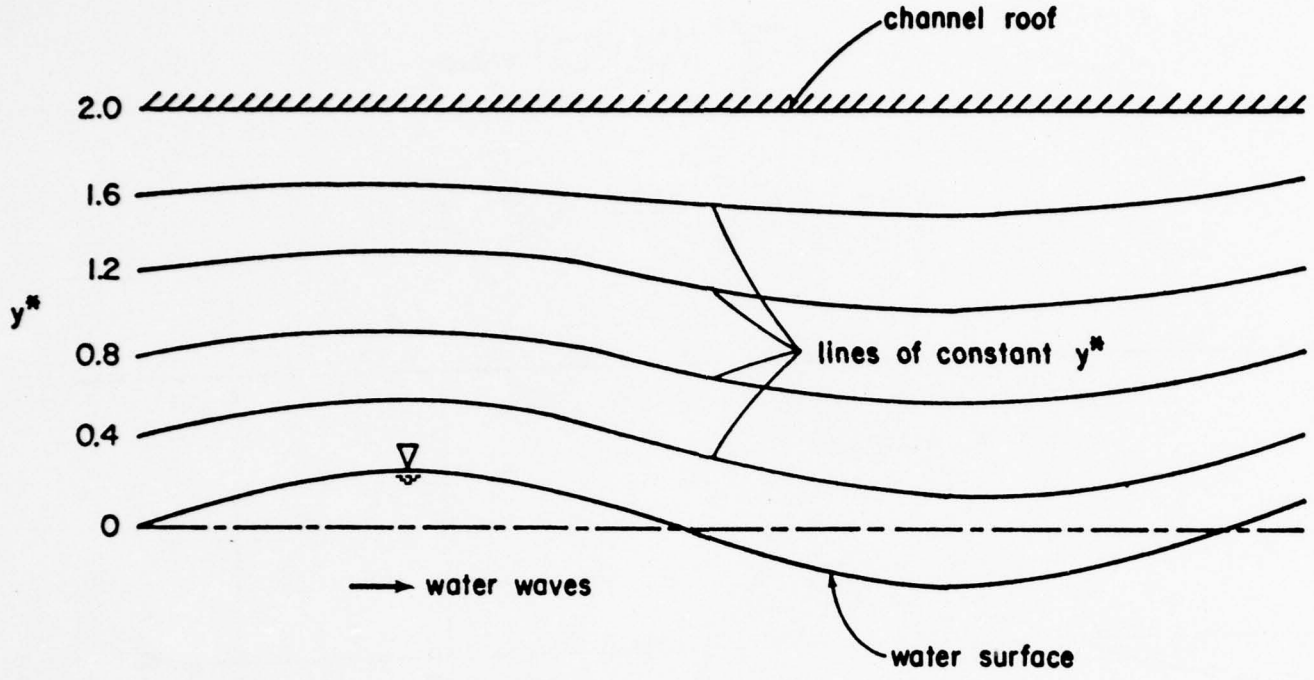

Figure 2.2 Lines of Constant y^*

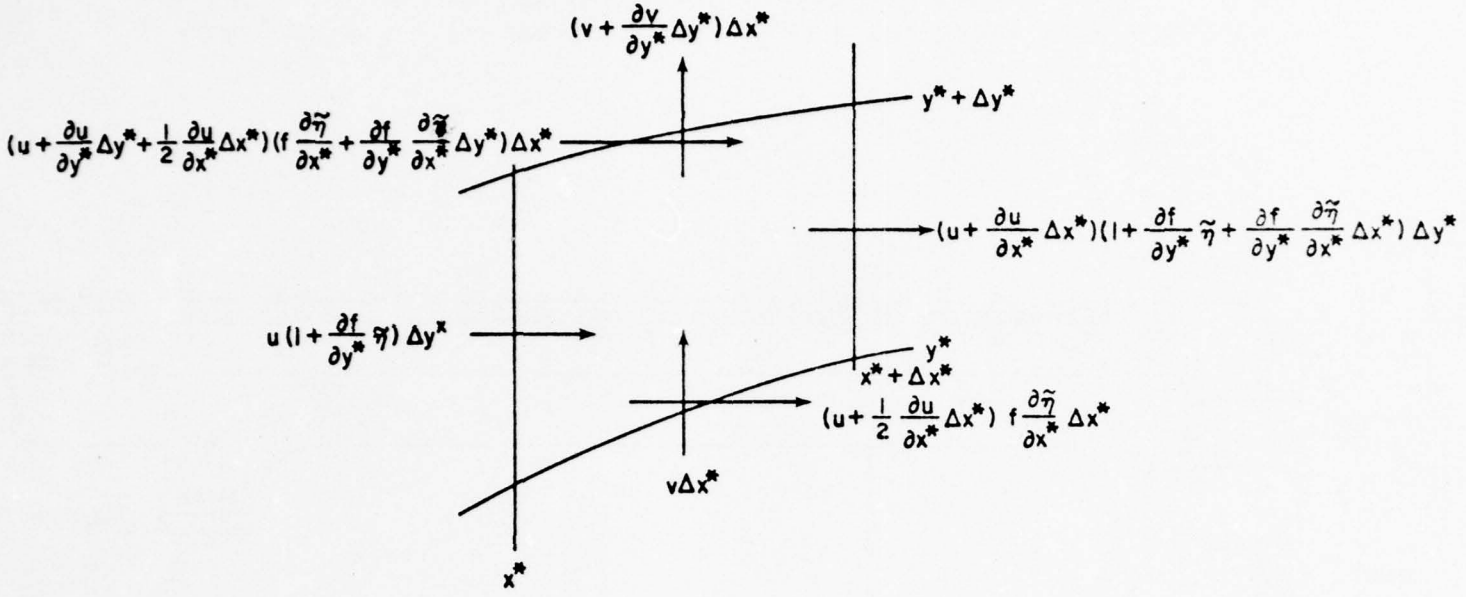

Figure 2.3 Mass Balance in the (x*, y*, t*) Coordinate System

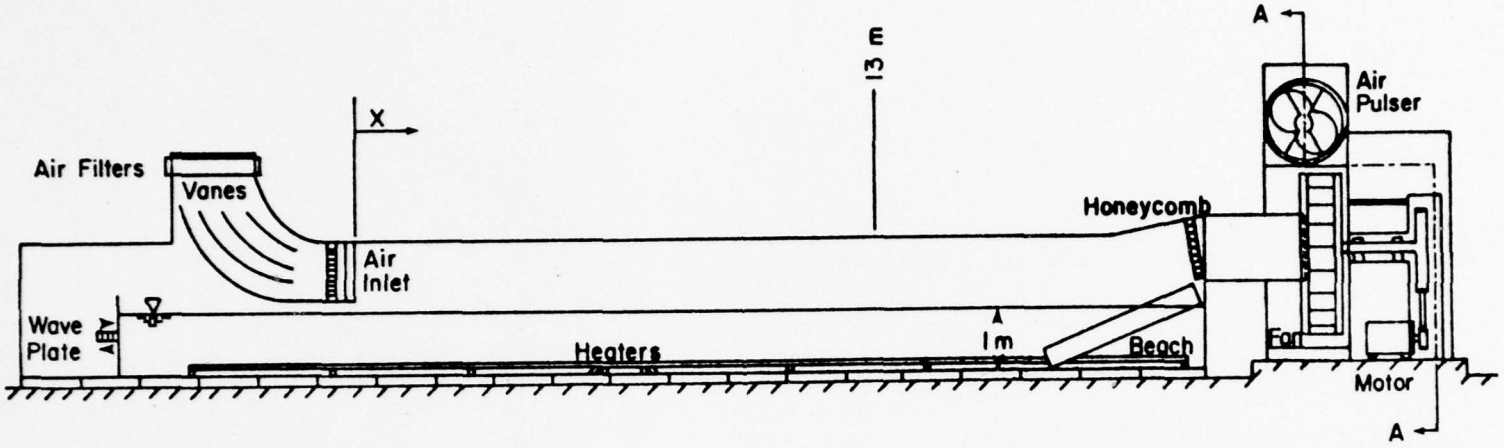

Figure 4.1 Schematic of Stanford Wind, Water Wave Facility (Cross-Section A-A Shown in Figure 4.2)

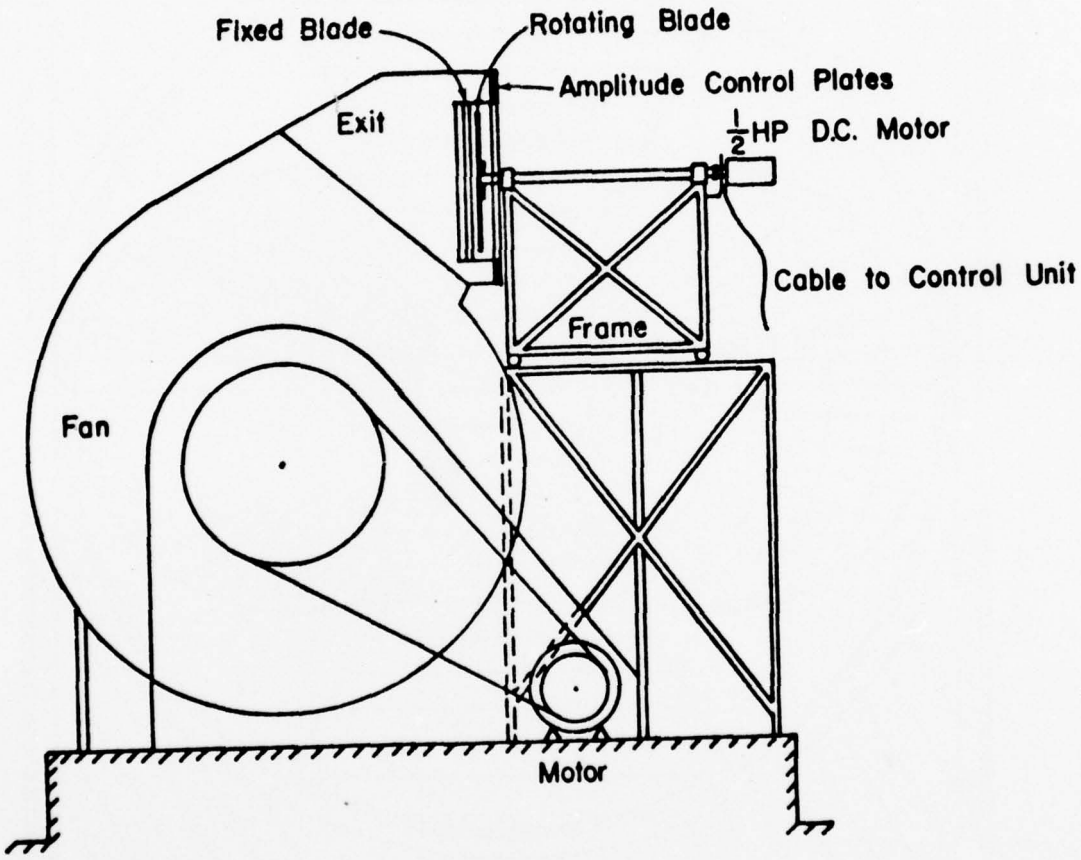

Figure 4.2 Schematic of Air Flow Pulser
(Cross-Section A-A of Figure 4.1)

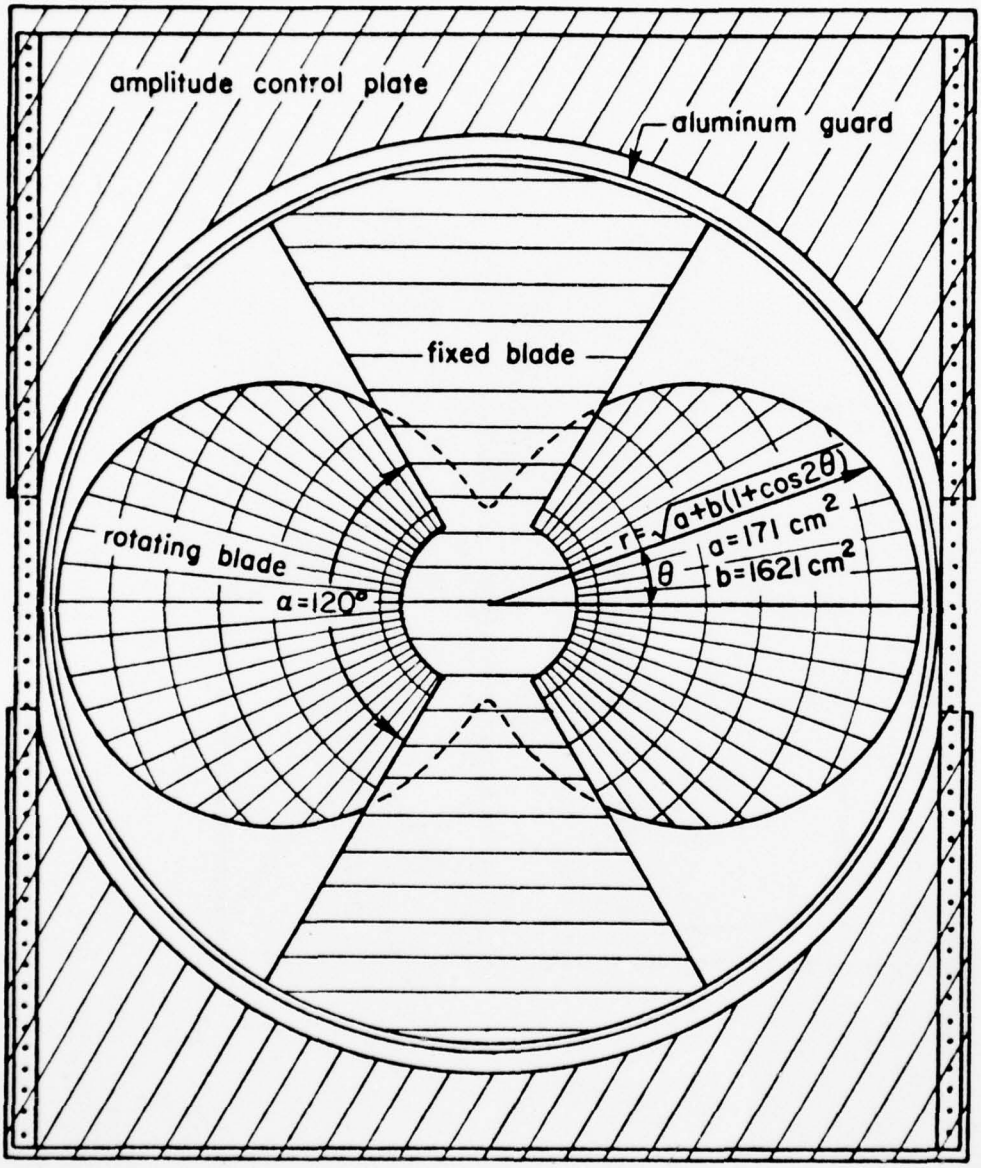

Figure 4.3 Cross-Sectional View of Air Flow Pulser and Amplitude Control Plates

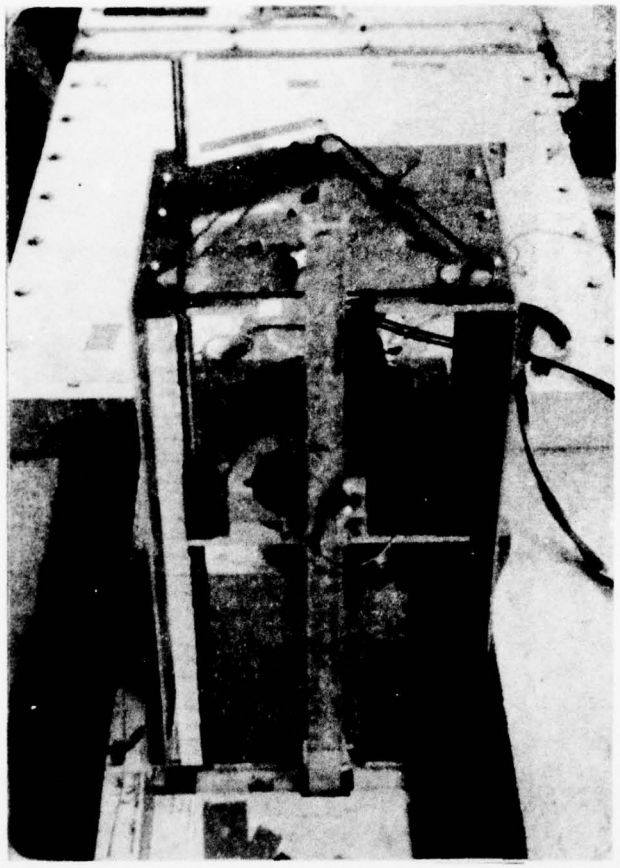

Figure 4.4. Photograph of Wave-Follower System and Wave-Follower Elevator

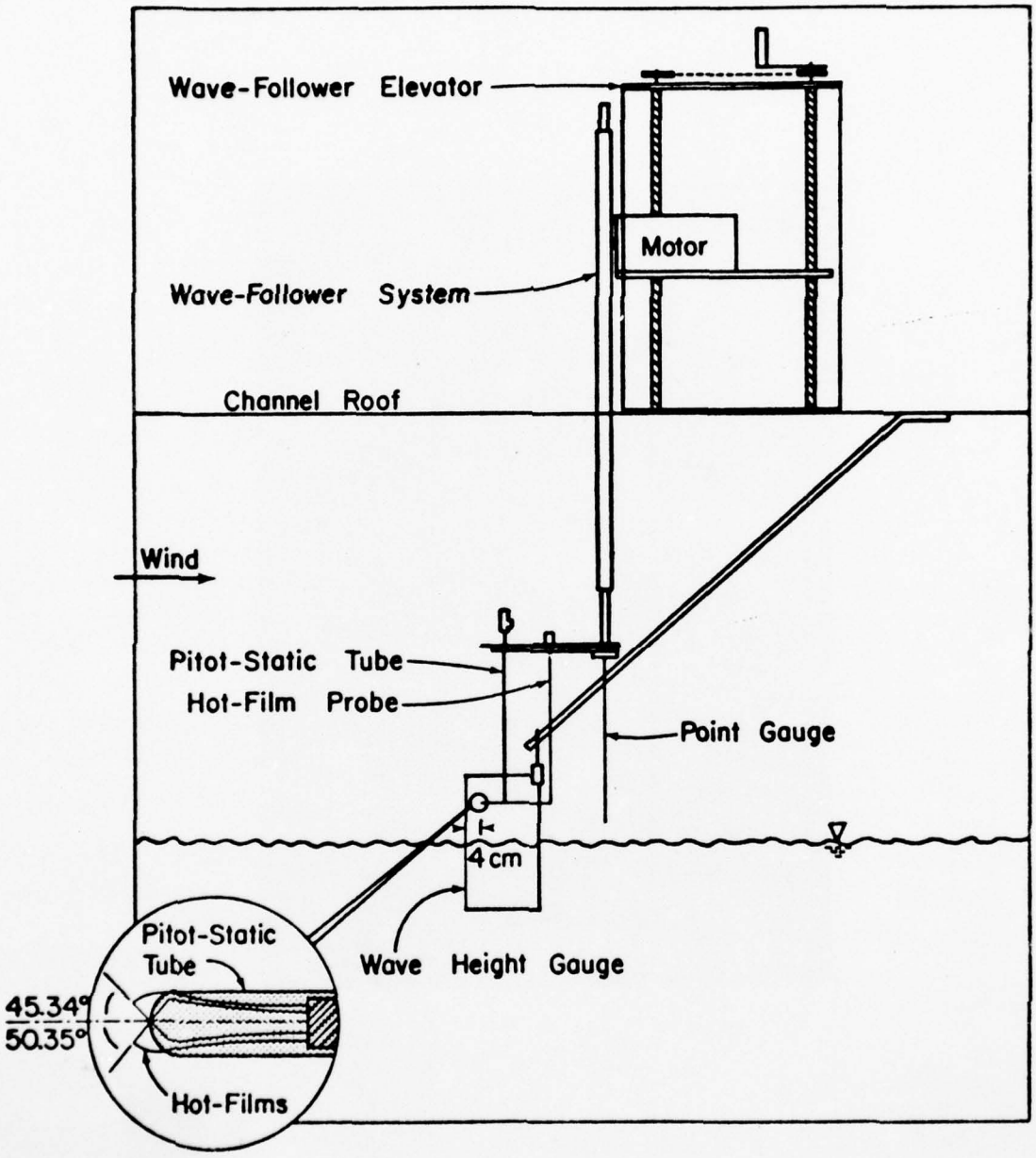

Figure 4.5 Probe Configurations

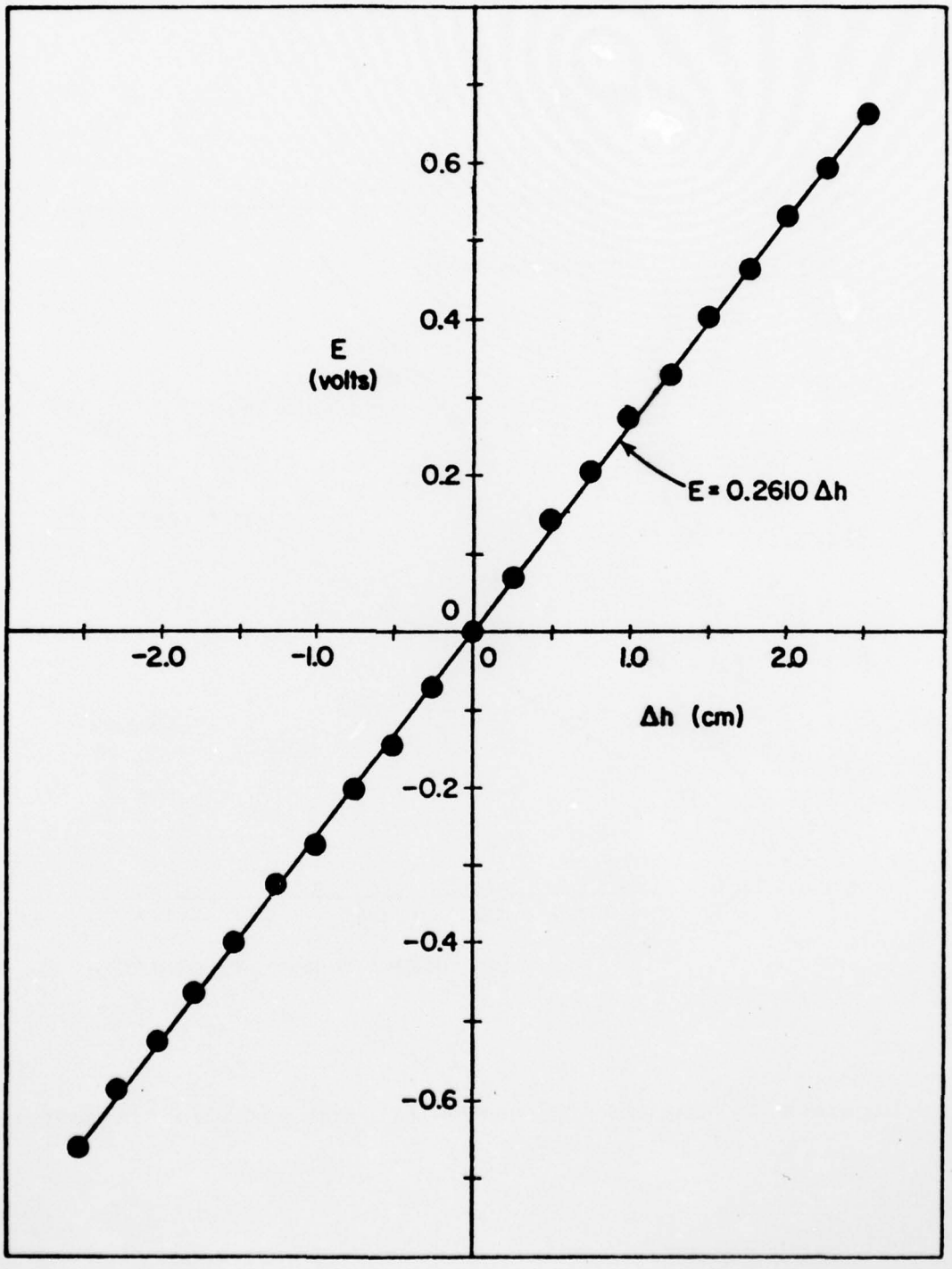

Figure 4.6 Calibration Curve of Wave Height Gauge

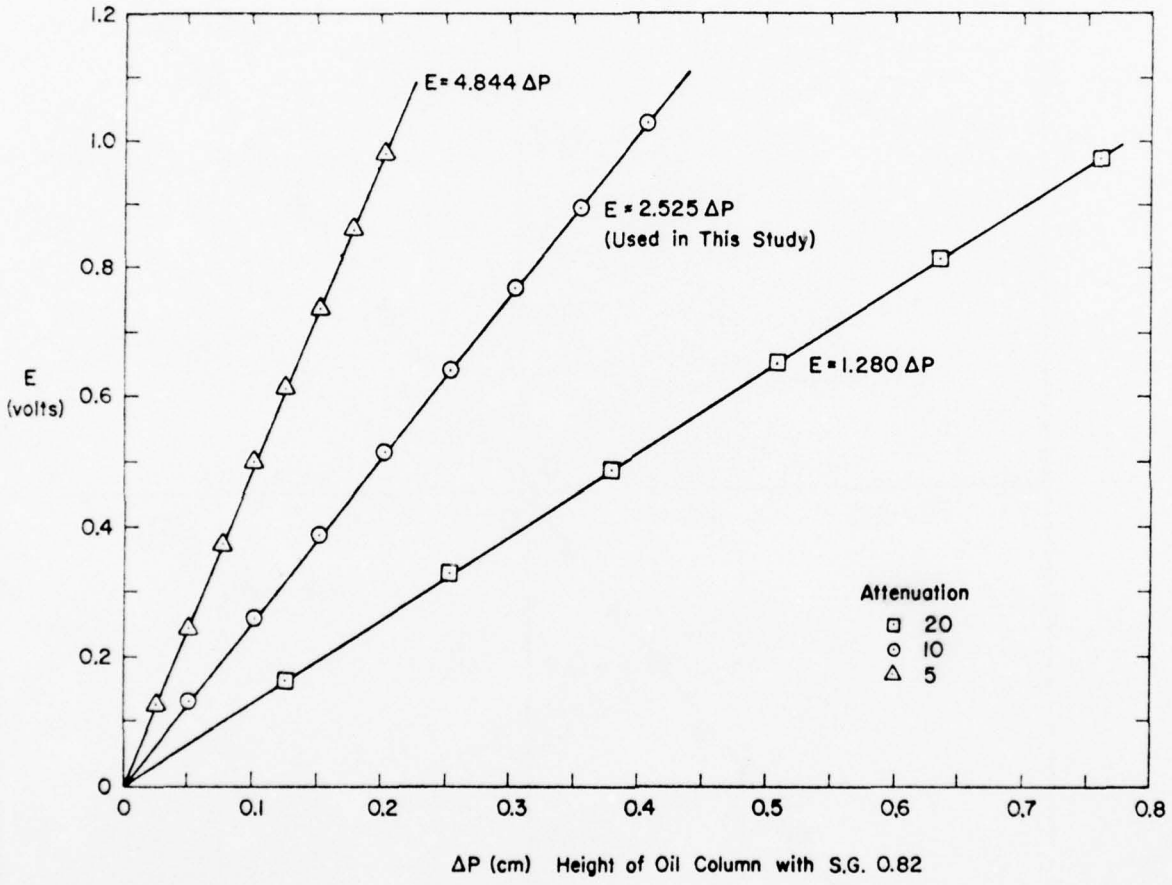

Figure 4.7 Calibration Curves of Pace Pressure Transducer

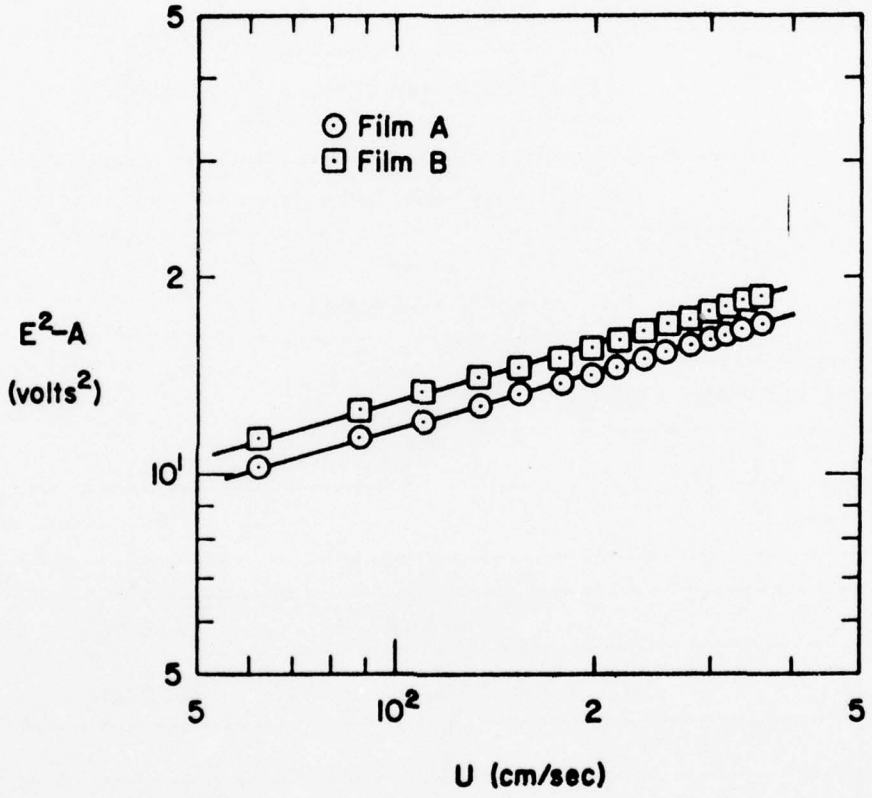

Figure 4.8 Typical Hot-Film Calibration Curves

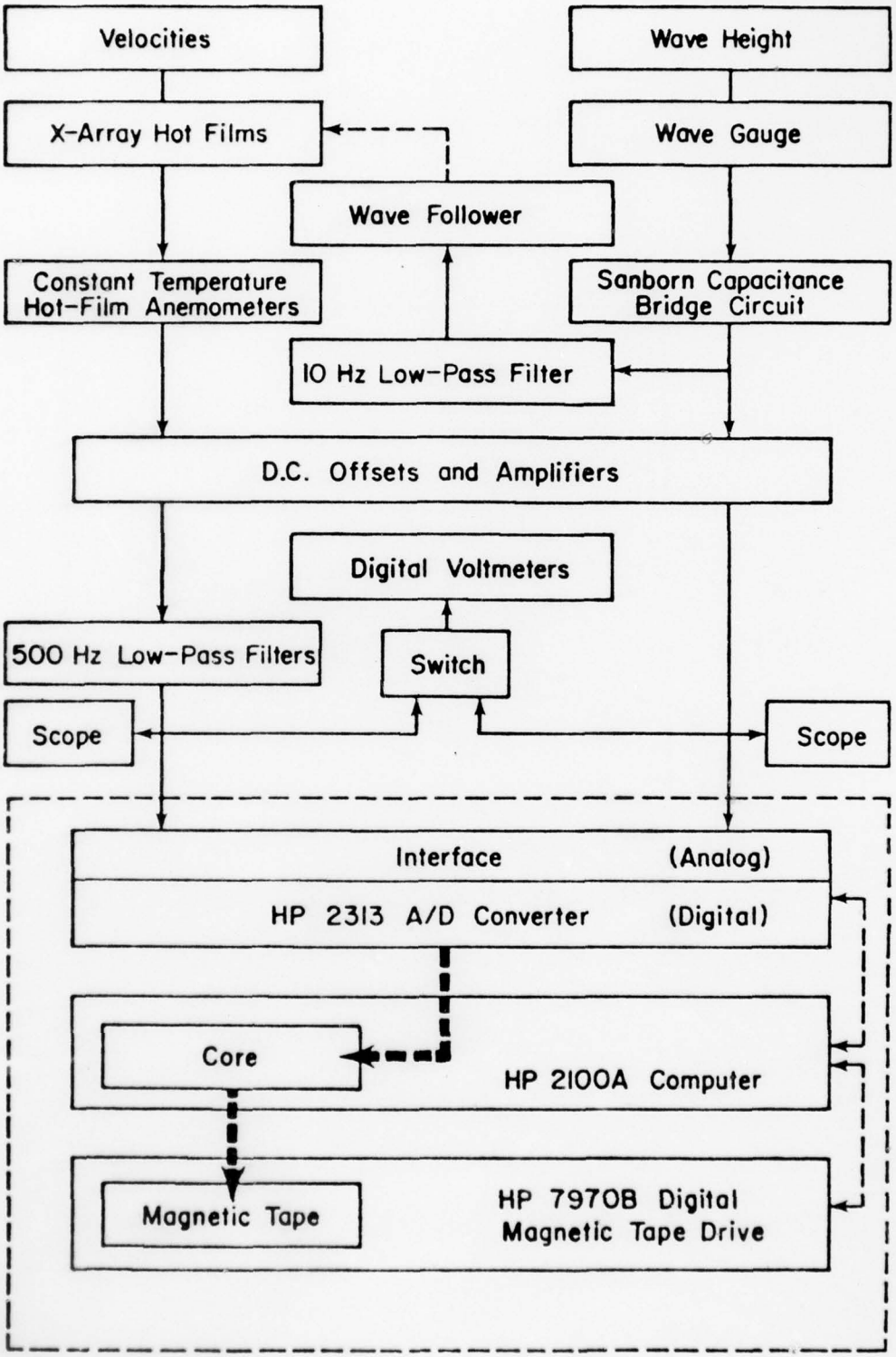

Figure 4.9 Flow Chart of Data Acquisition

AD-A044 743 STANFORD UNIV CALIF DEPT OF CIVIL ENGINEERING F/G 8/3
THE STRUCTURE OF MODULATED TURBULENT FLOW OVER PROGRESSIVE WATE--ETC(U)
AUG 77 C HSU, E Y HSU, R L STREET DAAG29-76-G-0125
UNCLASSIFIED TR-221 NL

3 OF 3
AD
A044743

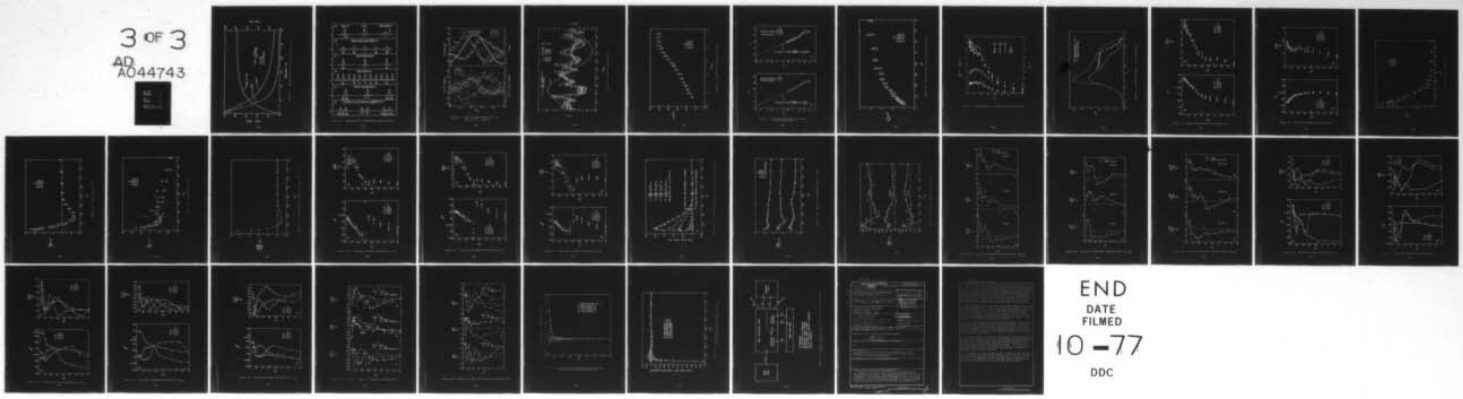

END
DATE
FILMED
10-77
DDC

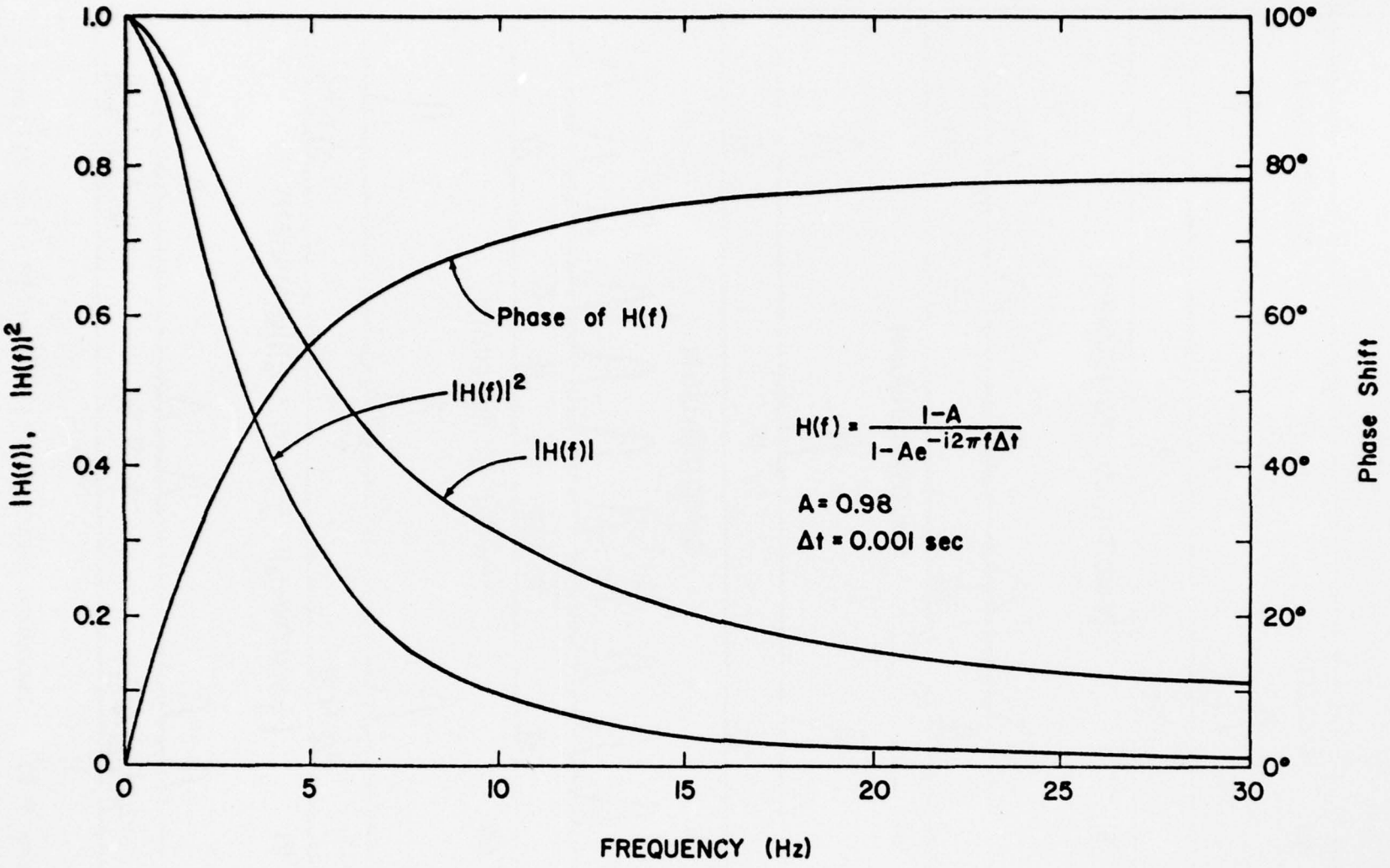

Figure 4.10 Characteristics of Low-Pass Digital Filter

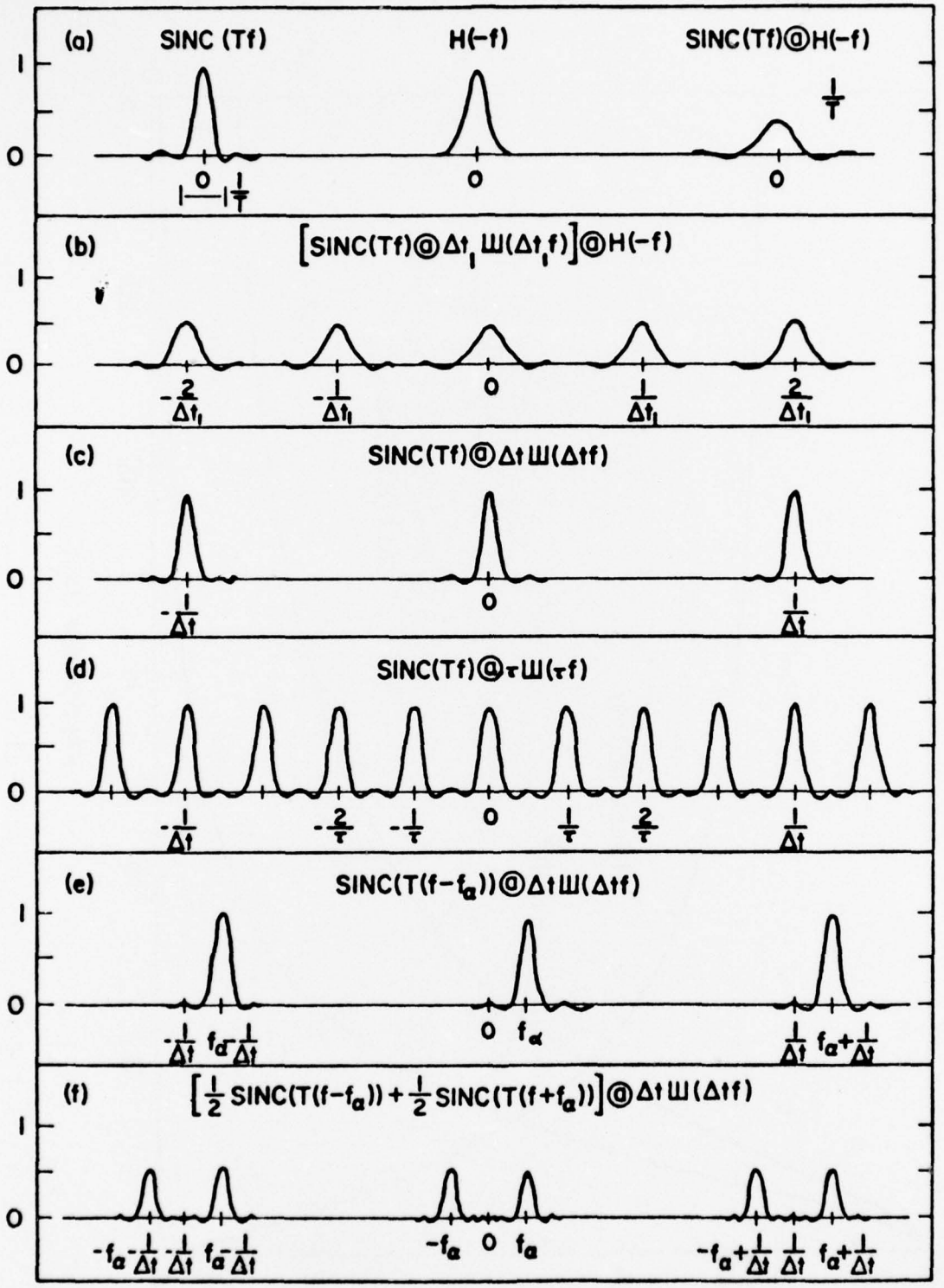

Figure 4.11 Characteristics of Band-Pass Digital Filters

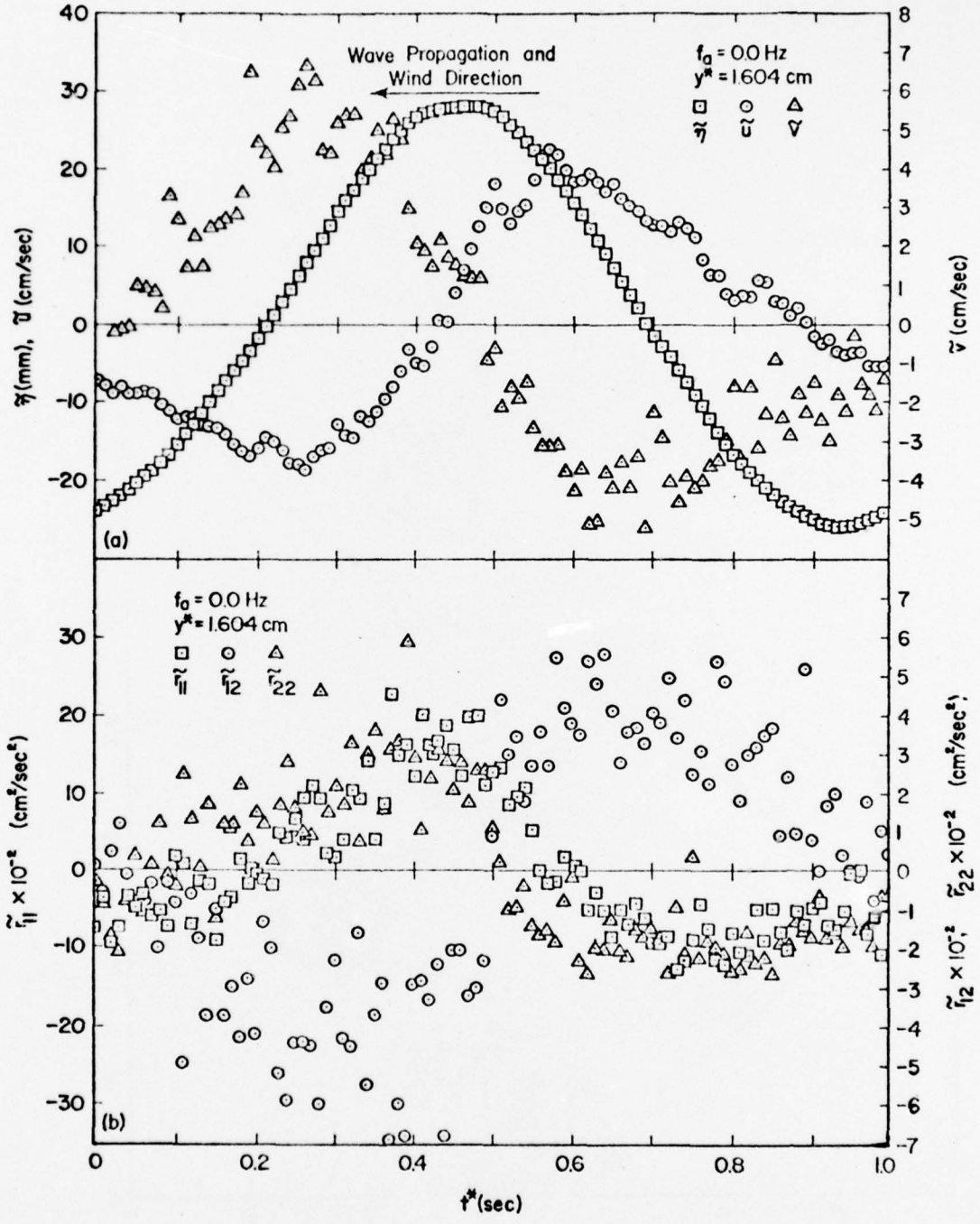

Figure 5.1 Phase Averaged Results for $\tilde{\eta}$, $\tilde{u}_i$ and $\tilde{r}_{ij}$ at y* = 1.604 cm

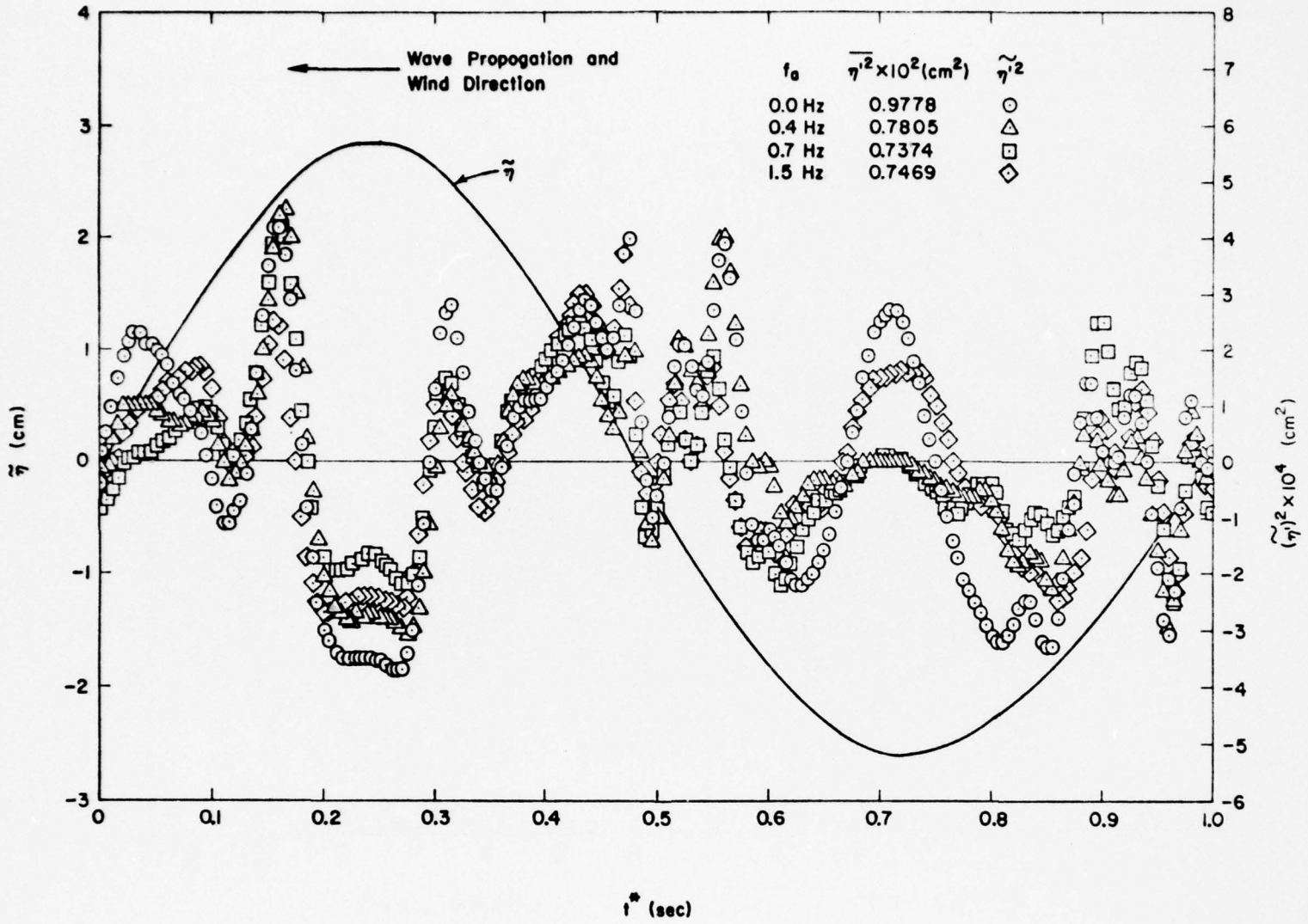

Figure 5.2 Phase Averaged Results of η'^2

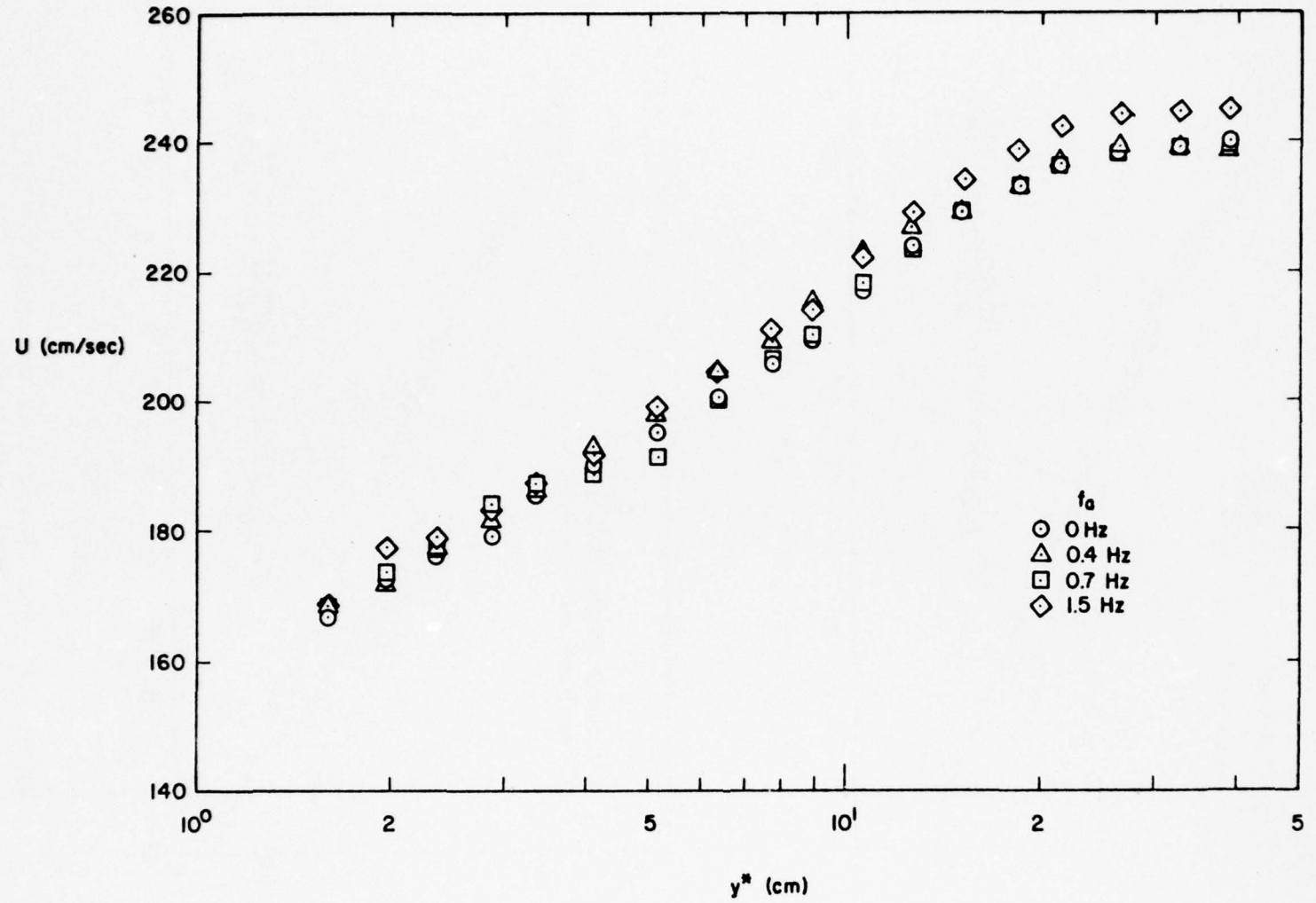

Figure 5.3 Mean Horizontal Velocity Profiles

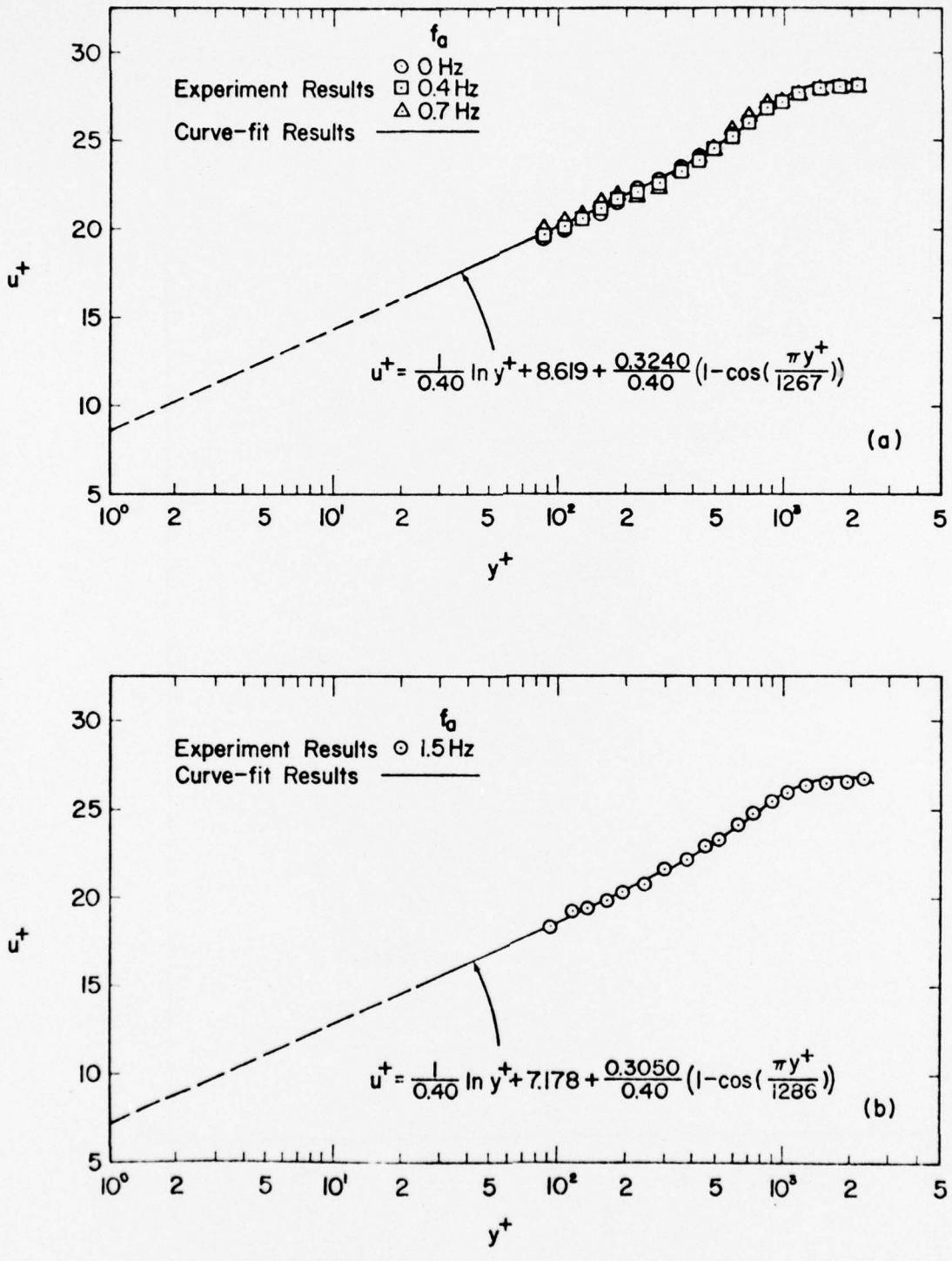

Figure 5.4 Mean Horizontal Velocity Profiles in Wall Coordinates

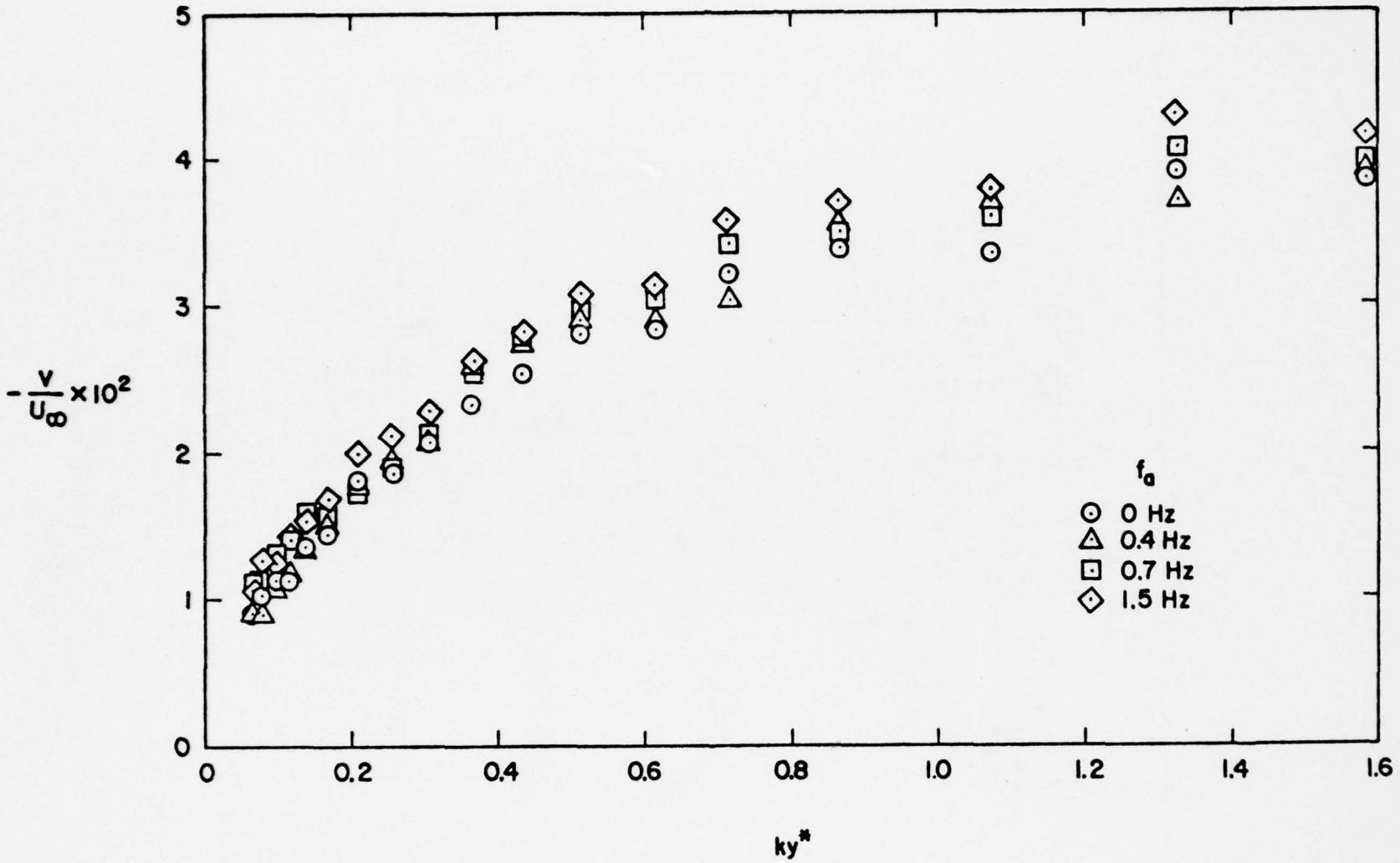

Figure 5.5 Mean Vertical Velocity Profiles versus ky*

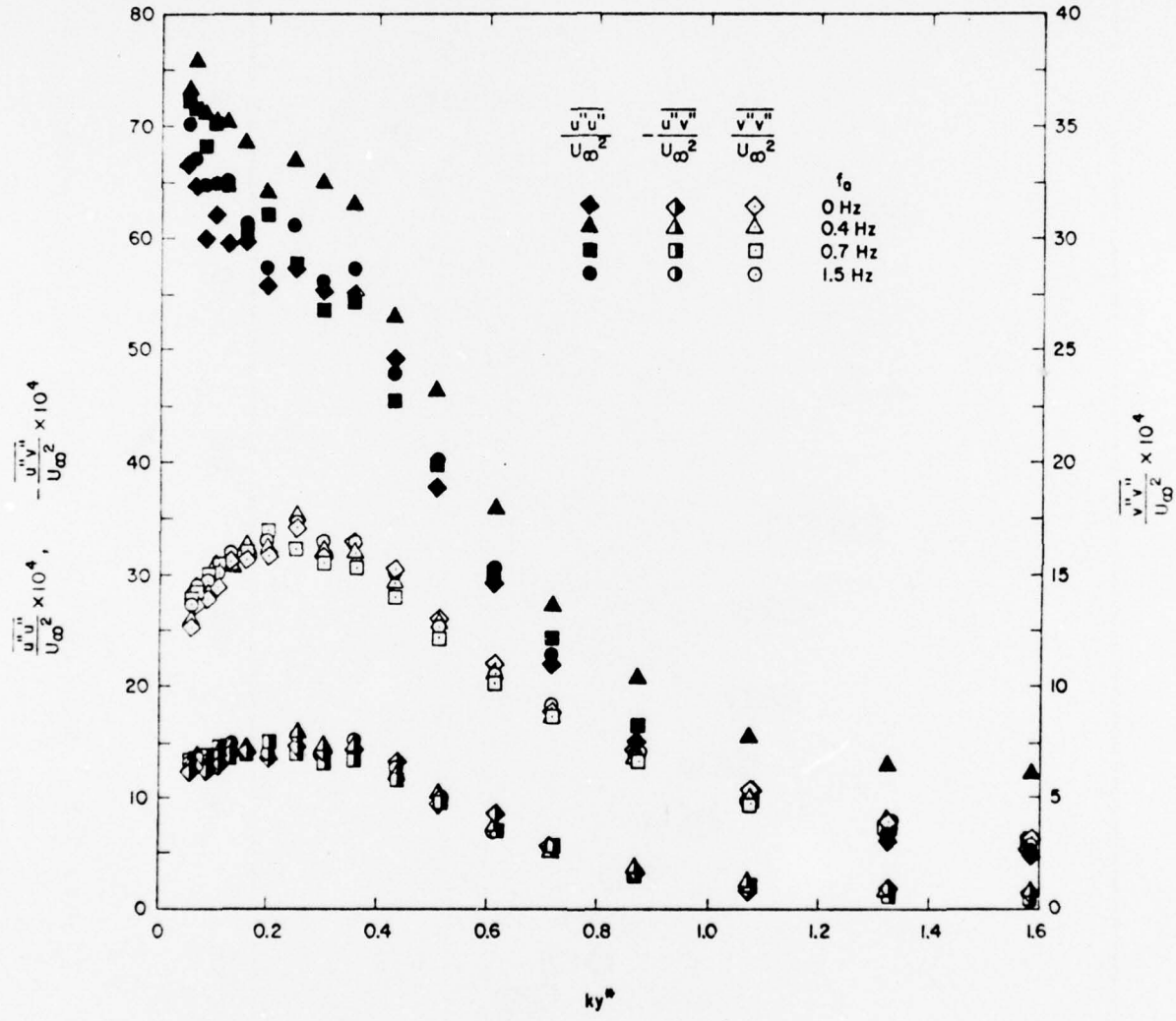

Figure 5.6 Distributions of Turbulent Reynolds Stresses

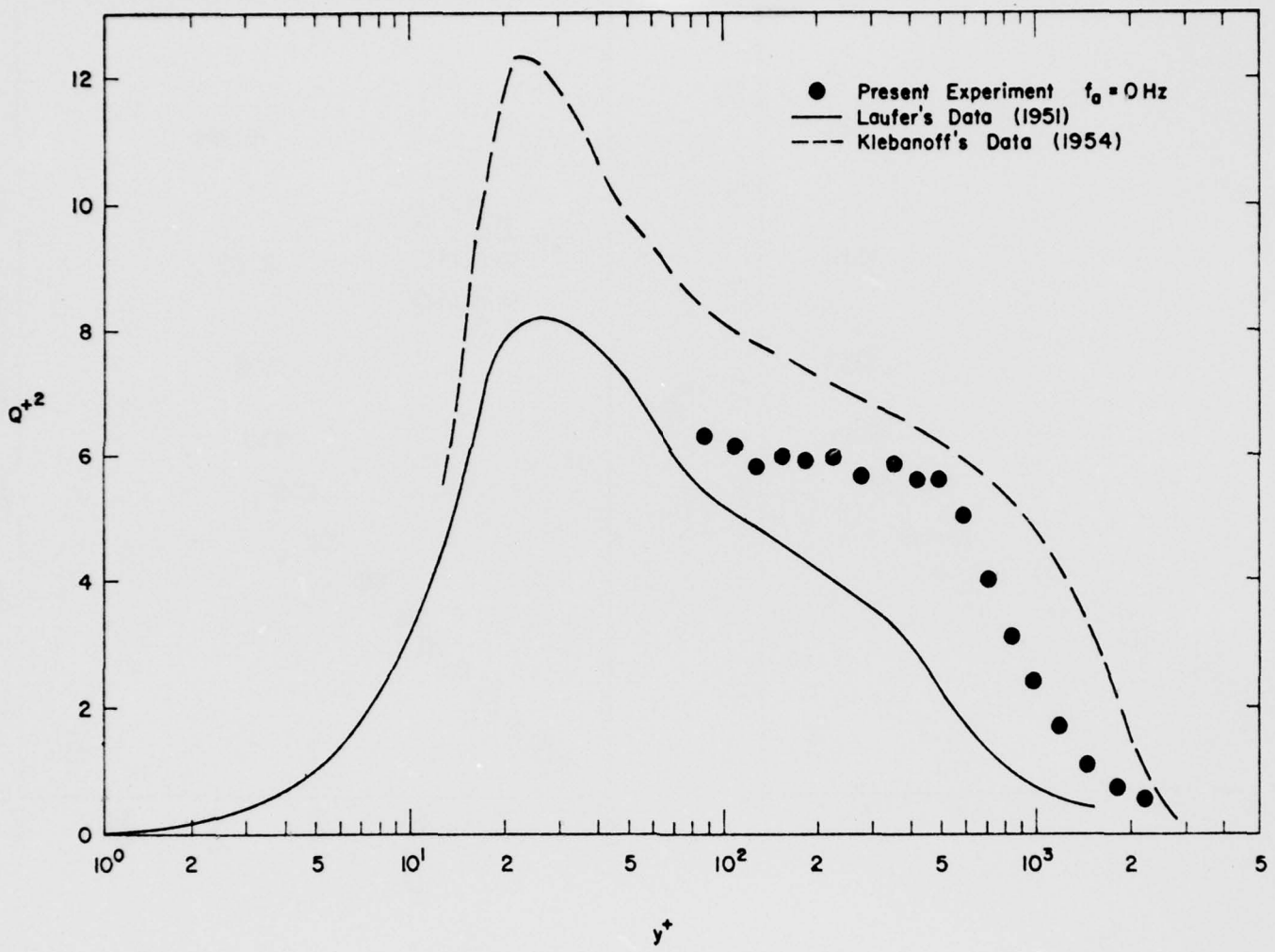

Figure 5.7 Turbulent Intensity in Wall Coordinates

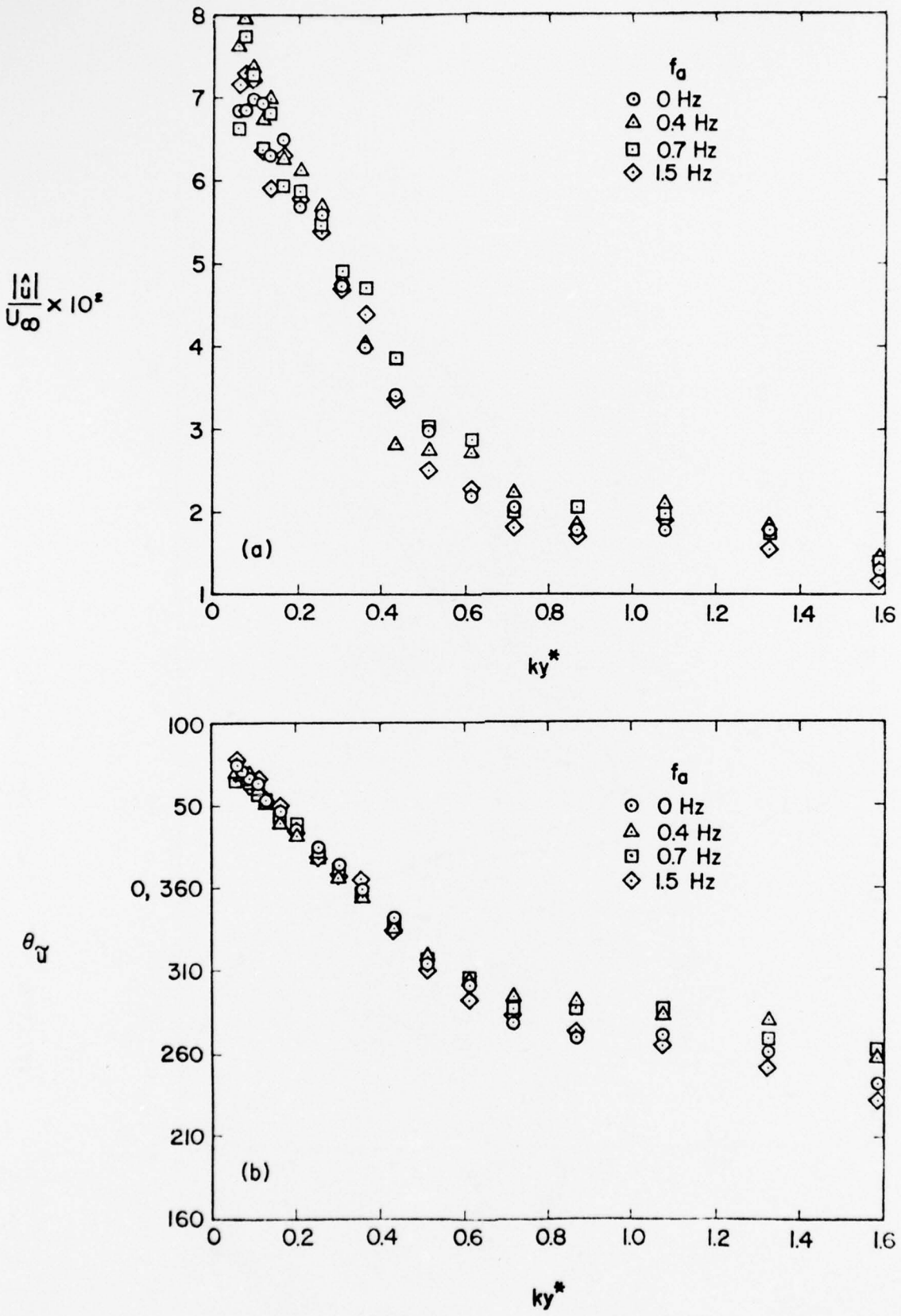

Figure 5.8 Amplitude and Phase Distributions of $\tilde{u}$

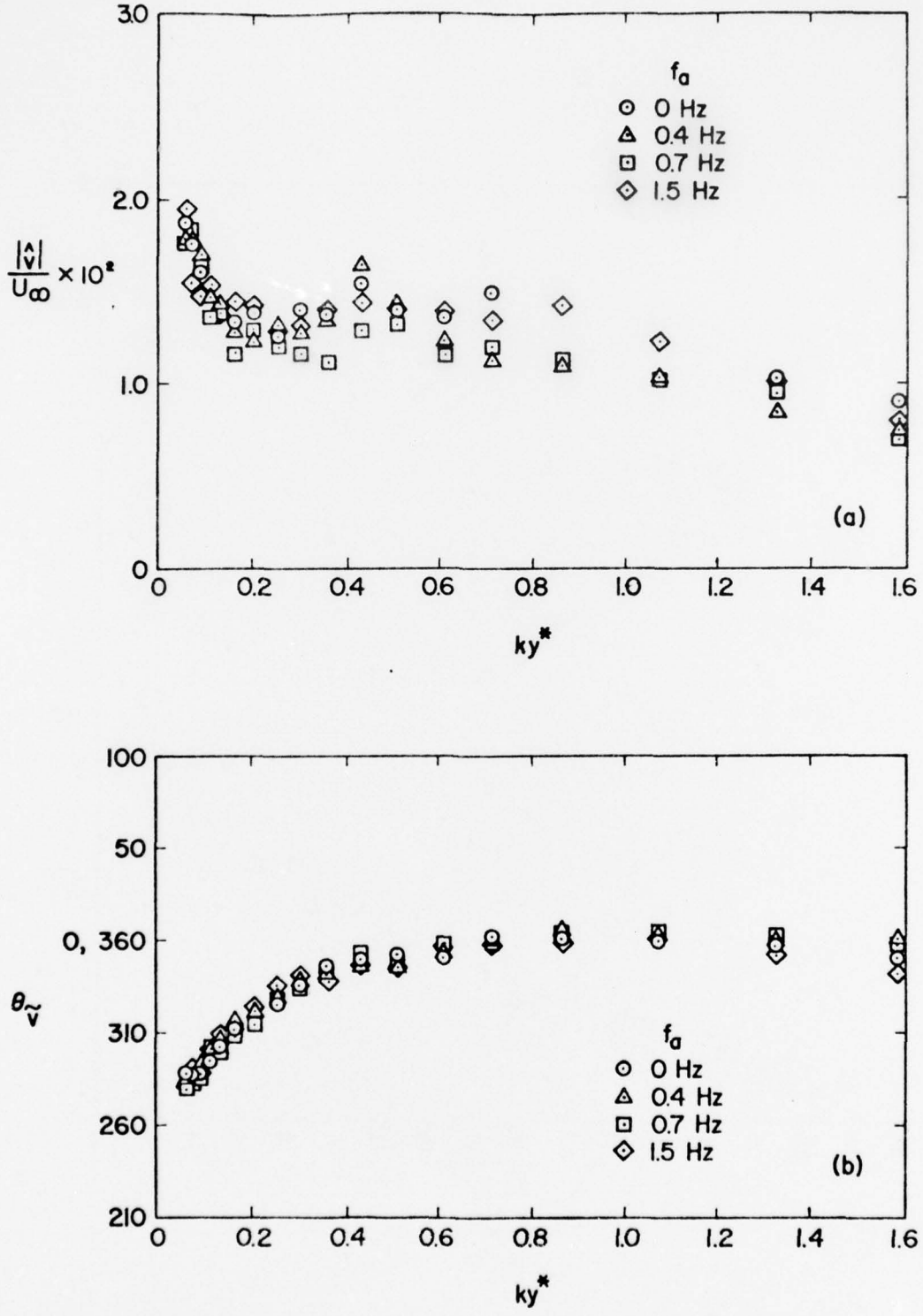

Figure 5.9 Amplitude and Phase Distributions of $\tilde{v}$

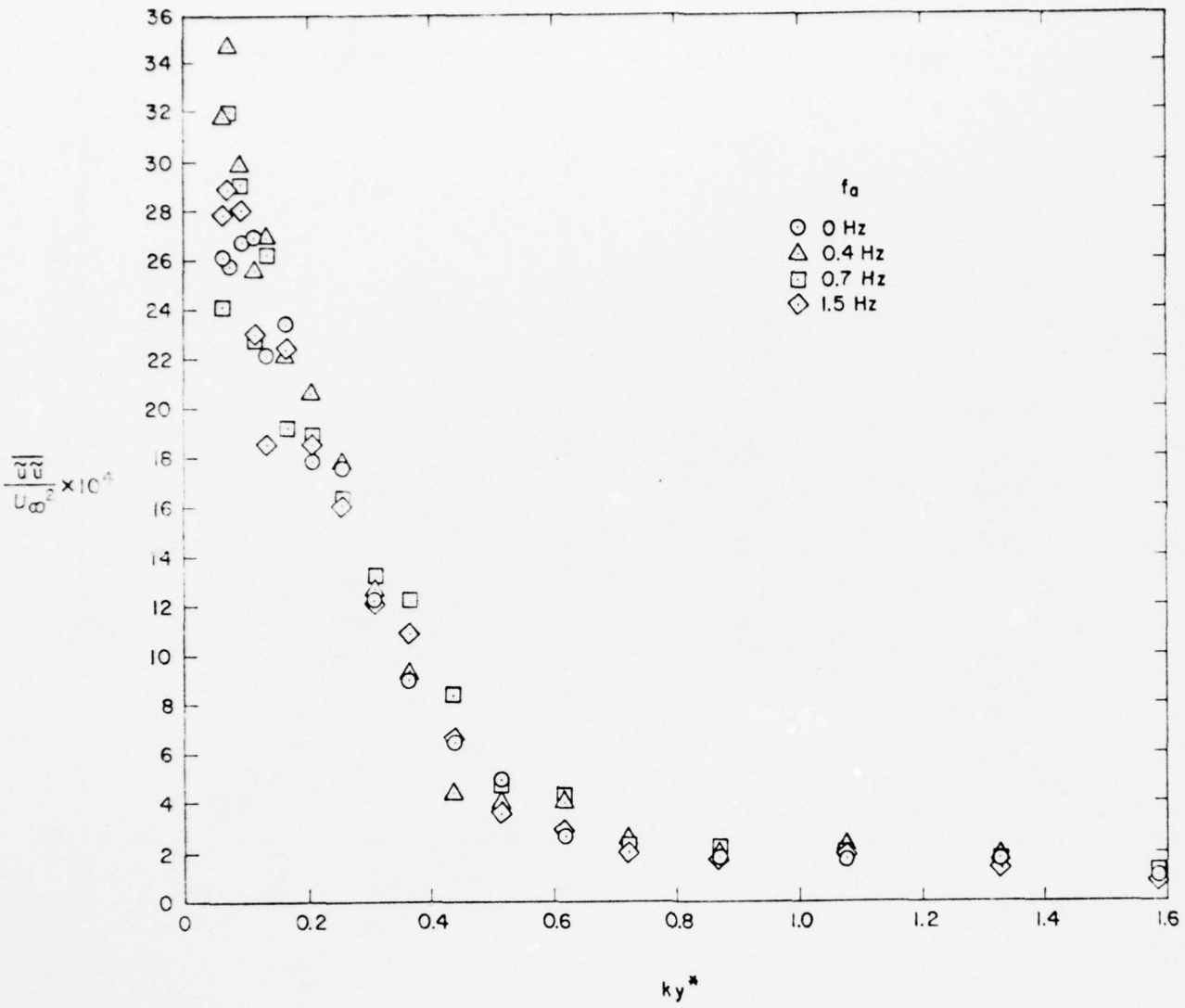

Figure 5.10 Distributions of $\widetilde{u}\widetilde{u}$

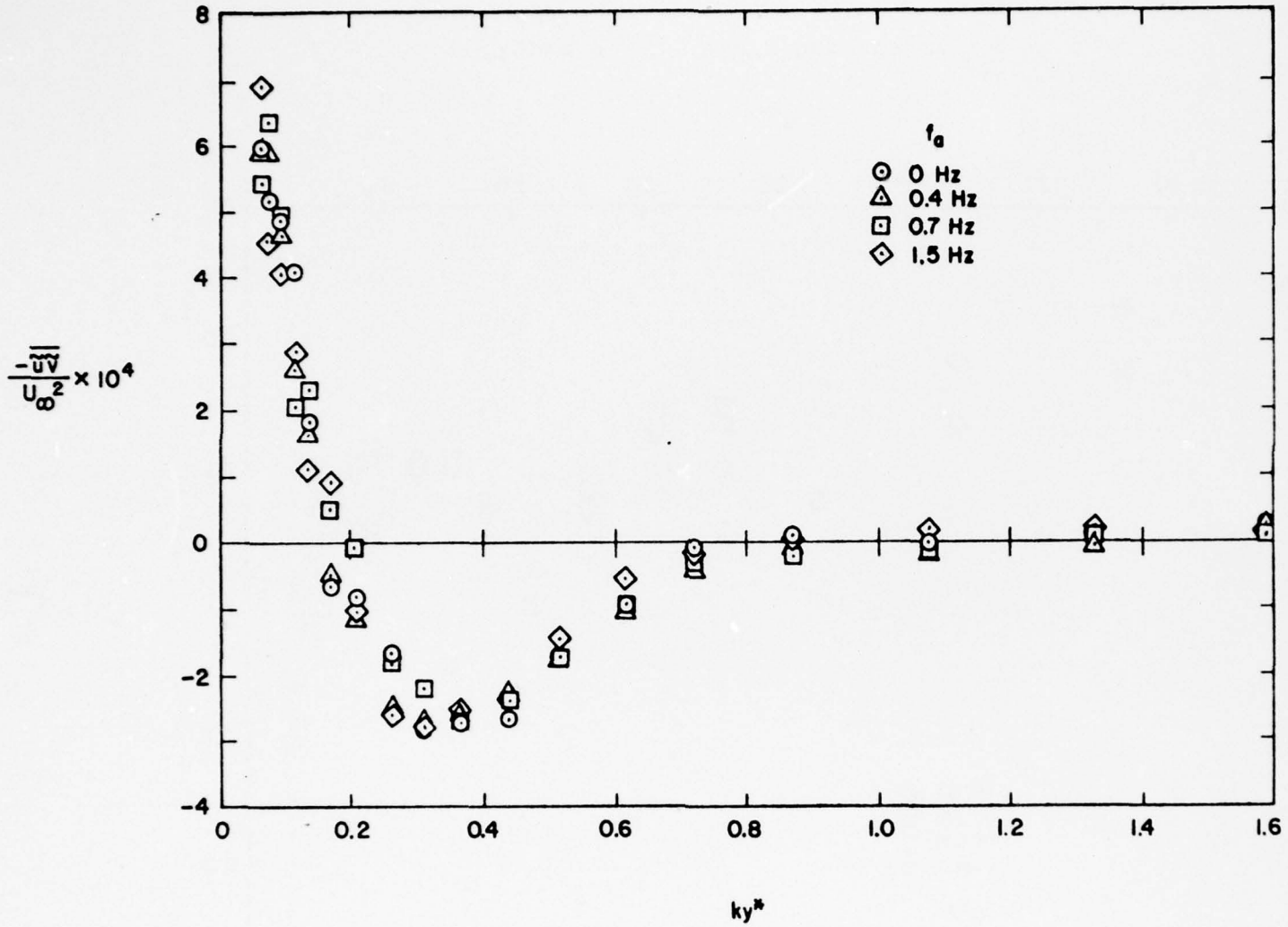

Figure 5.11 Distributions of $-\widetilde{u}\widetilde{v}$

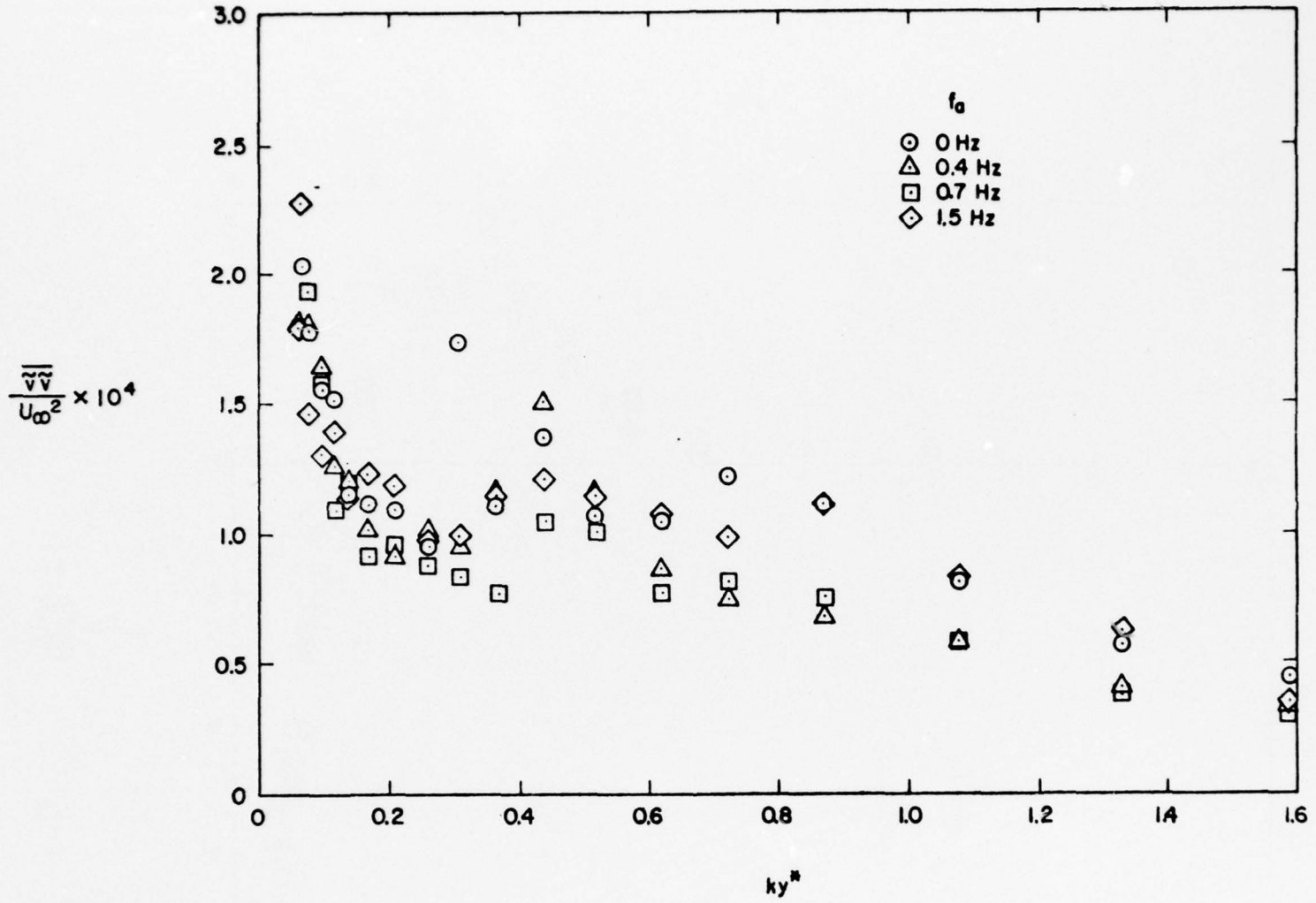

Figure 5.12 Distributions of $\overline{\tilde{v}\tilde{v}}$

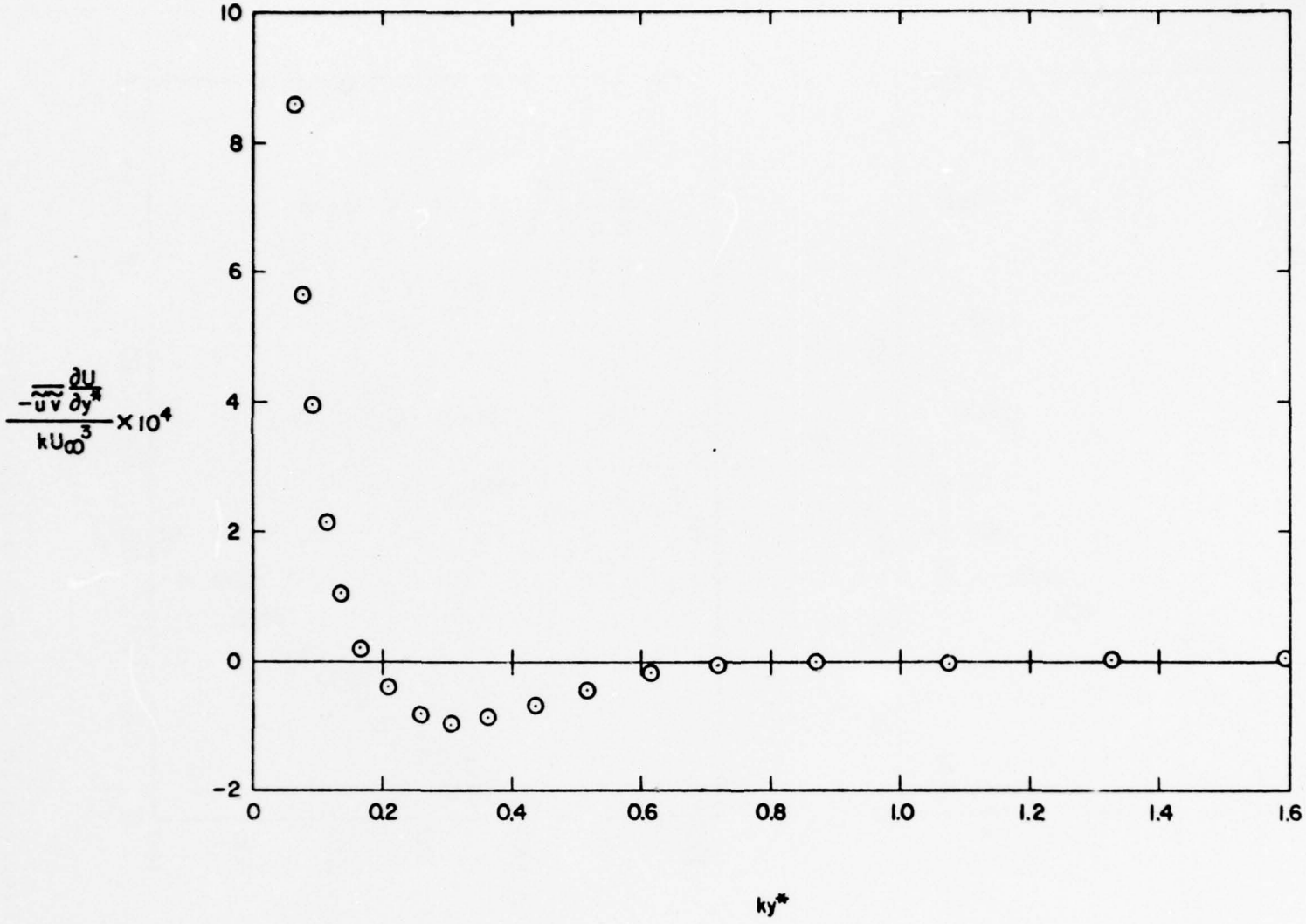

Figure 5.13 Distributions of Energy Production $-\overline{\tilde{u}\tilde{v}} \cdot \partial U/\partial y^*$

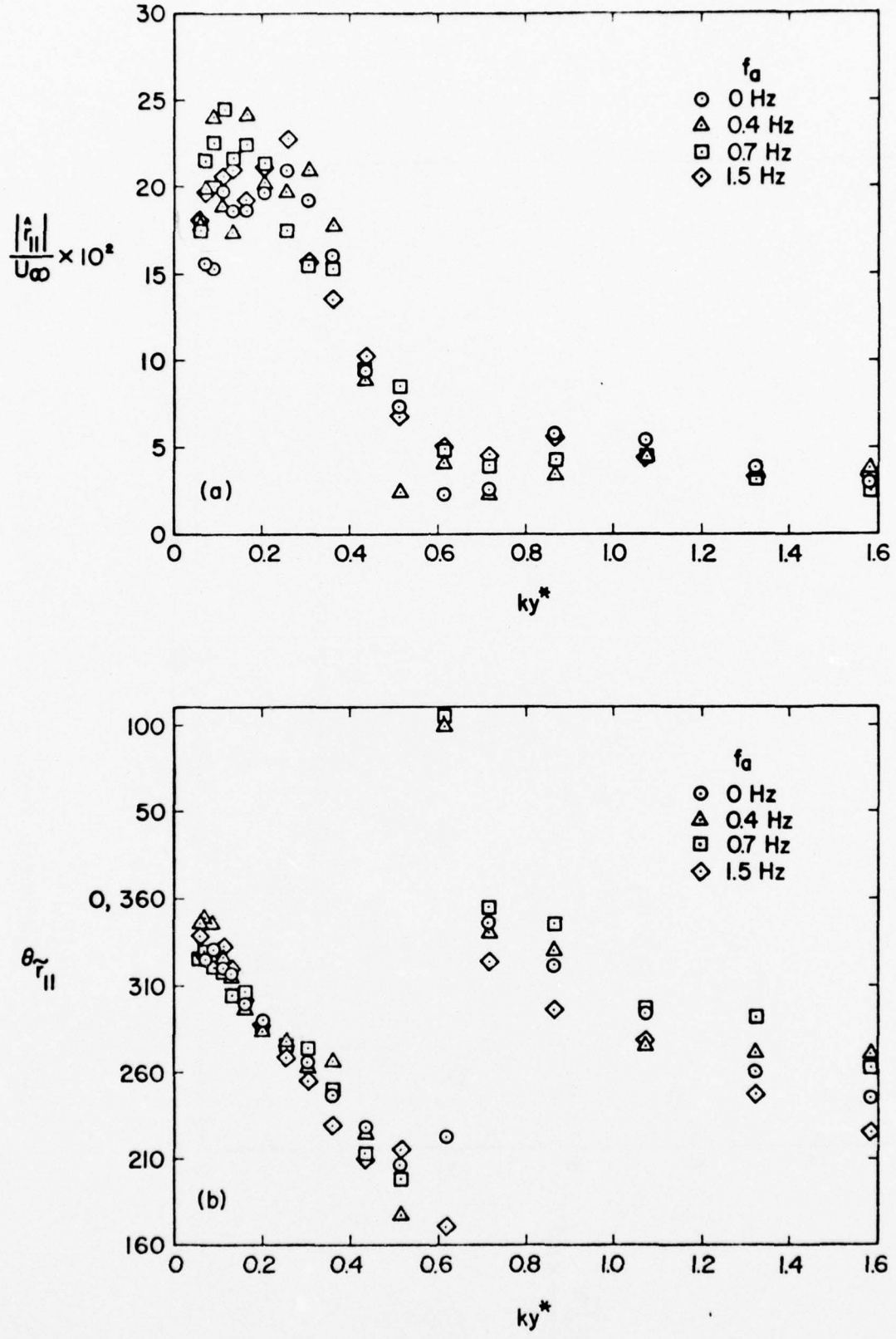

Figure 5.14 Amplitude and Phase Distributions of $\tilde{r}_{11}$

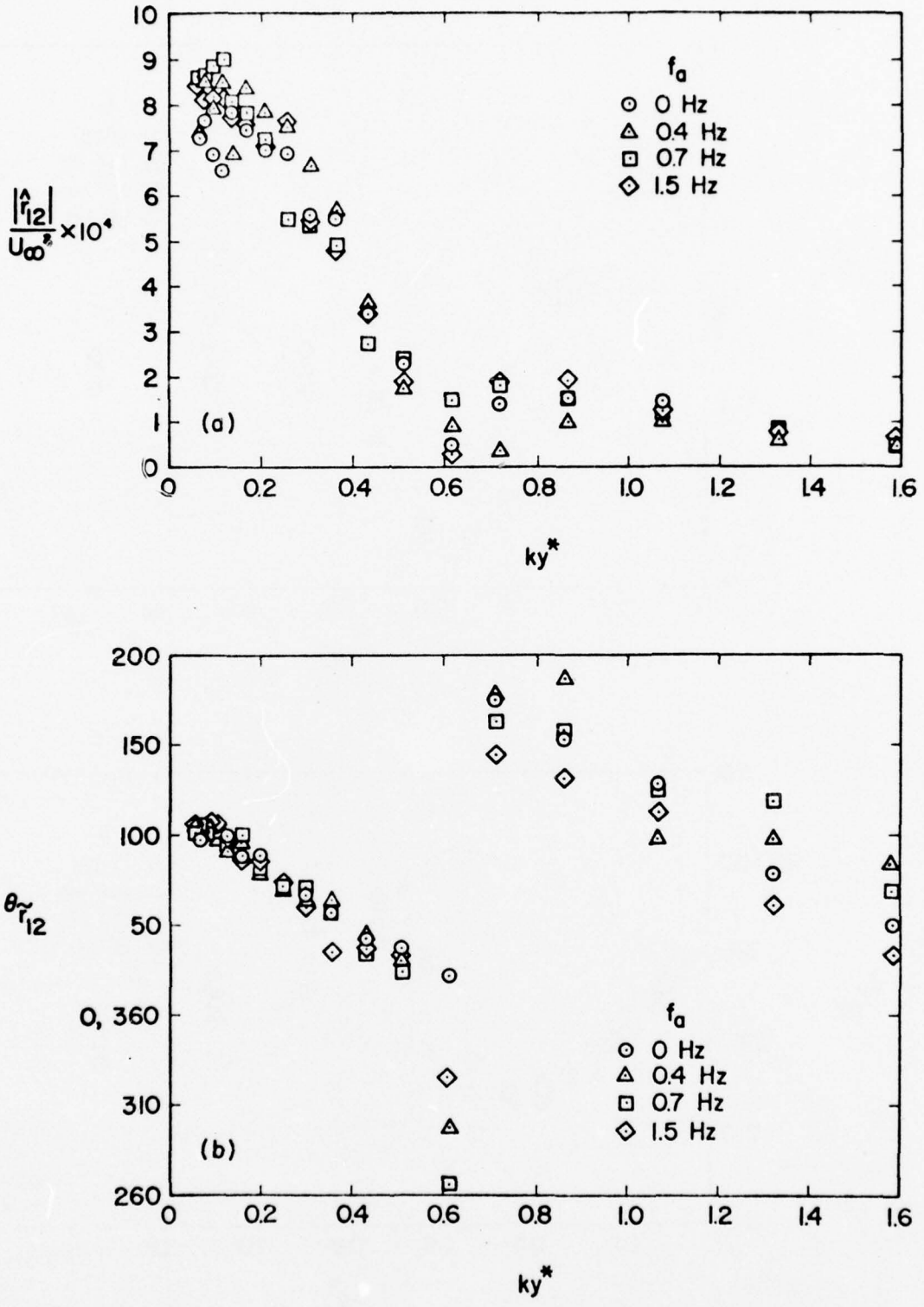

Figure 5.15 Amplitude and Phase Distributions of $\tilde{r}_{12}$

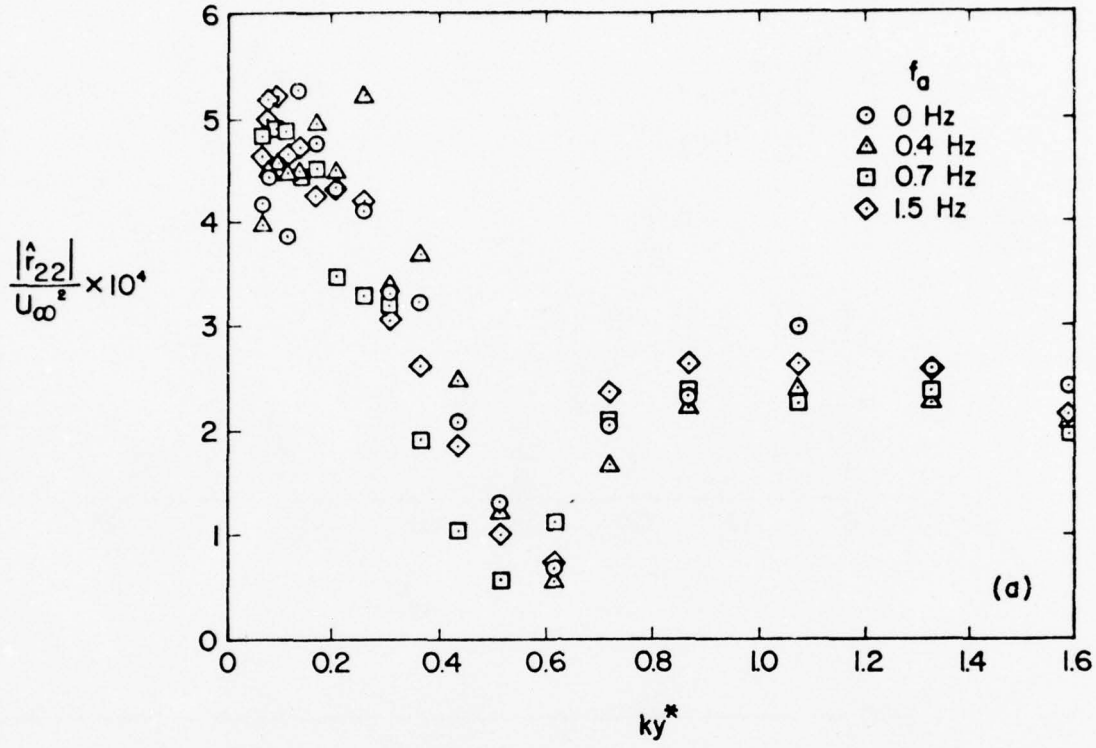

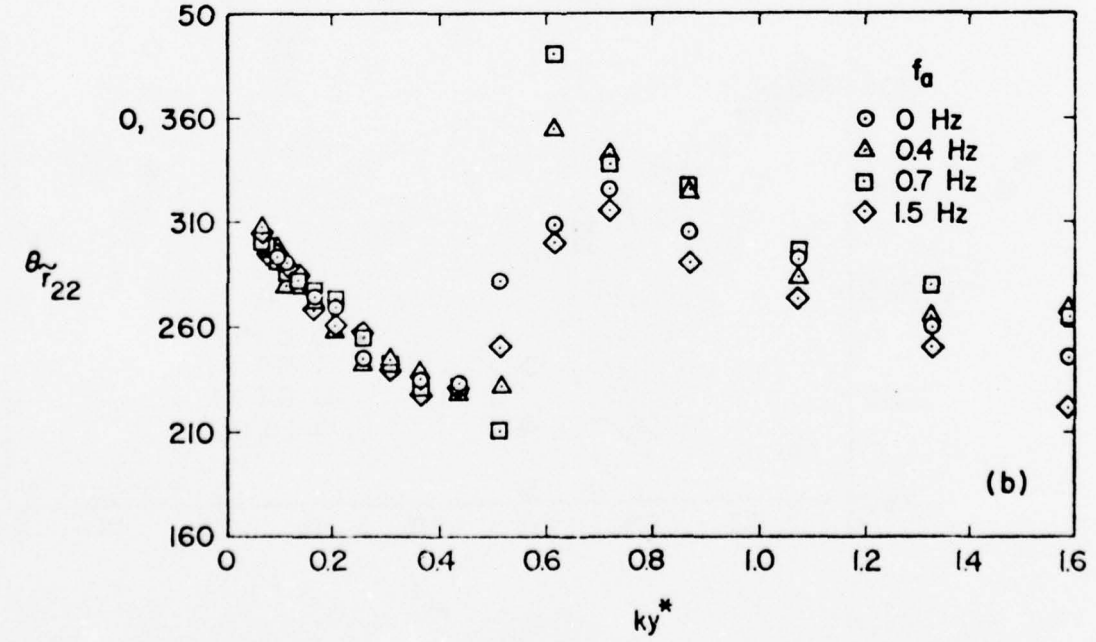

Figure 5.16 Amplitude and Phase Distributions of $\tilde{r}_{22}$

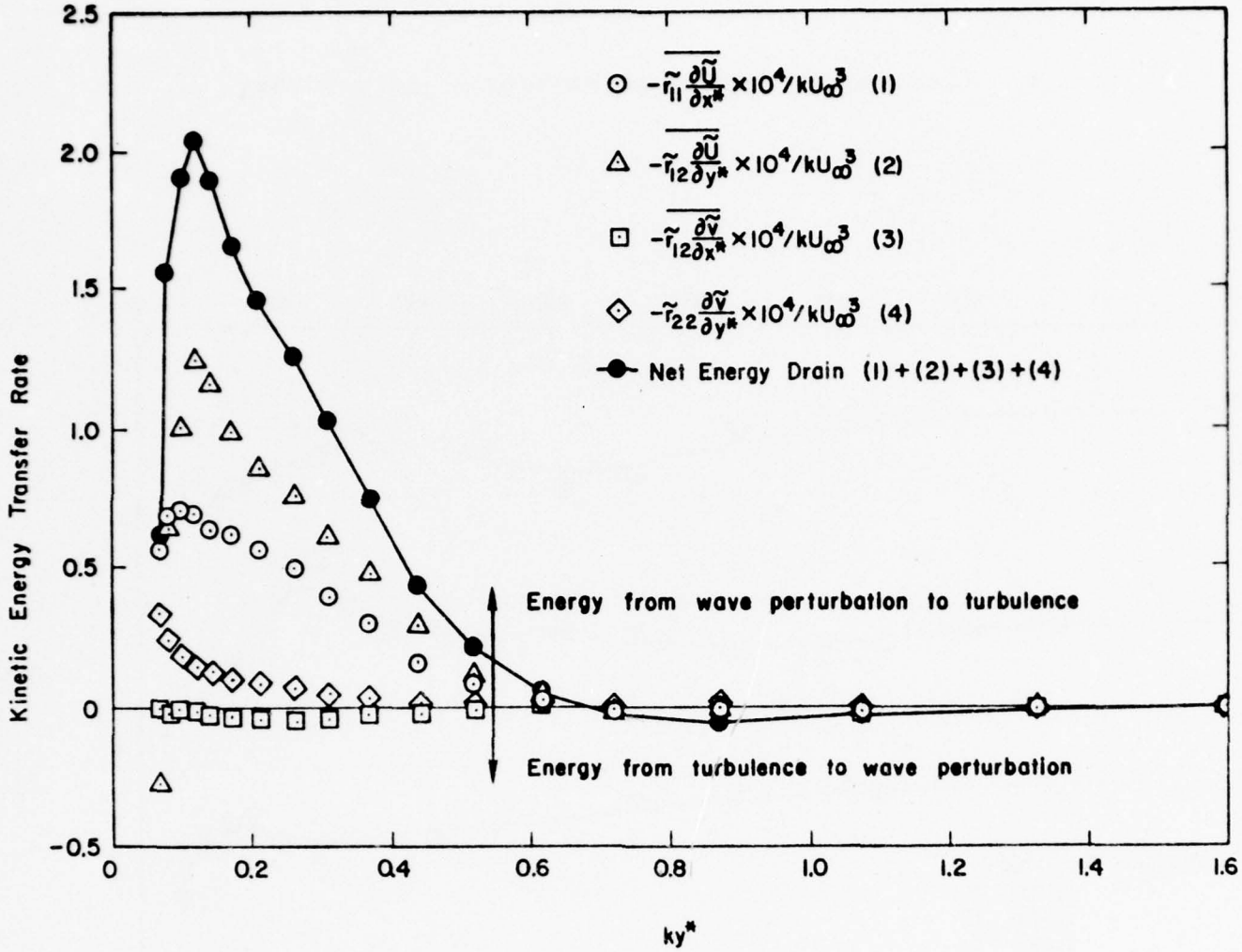

Figure 5.17 Distributions of Energy Drain from Wave to Turbulence

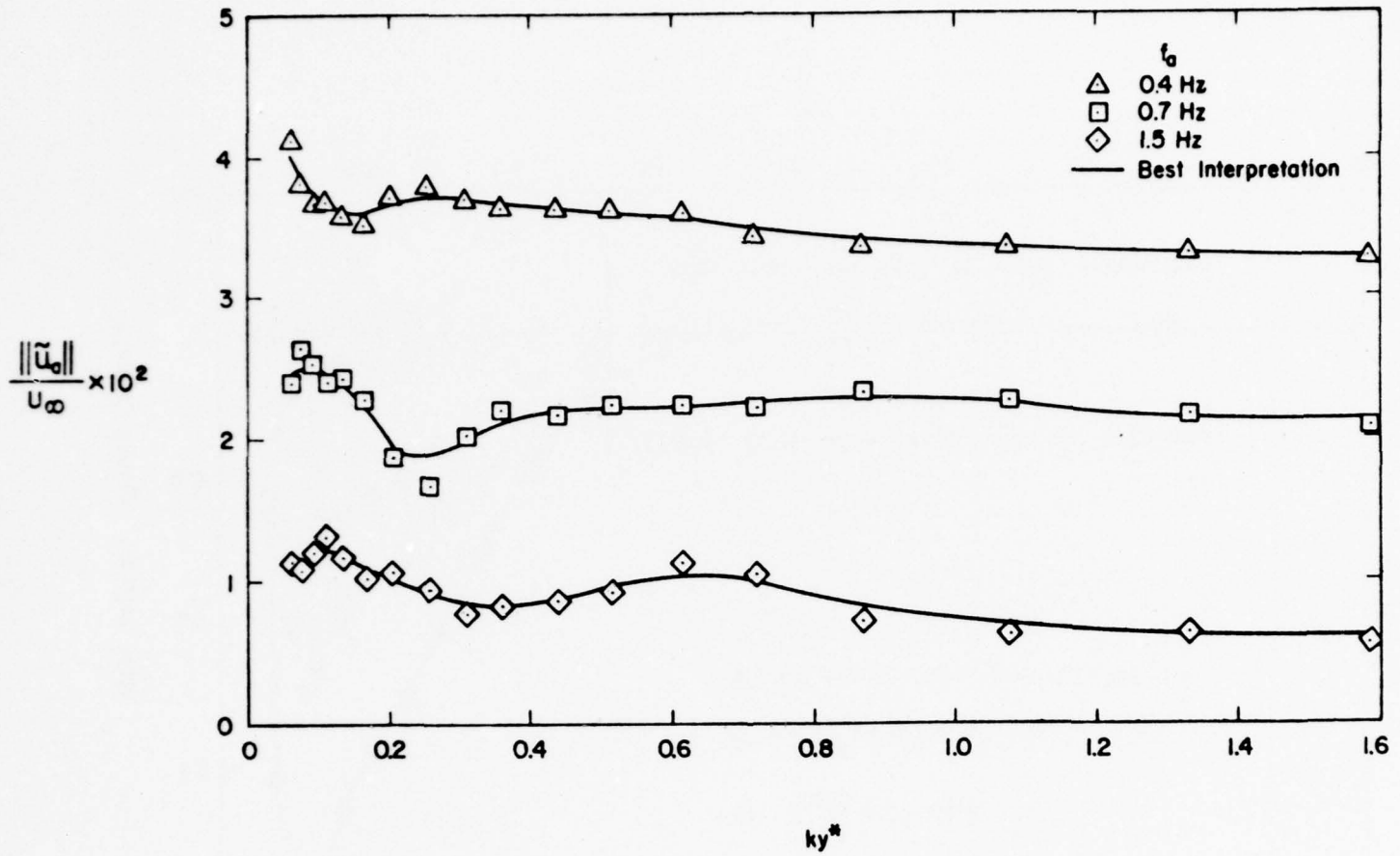

Figure 5.18 Profiles of Modulation Velocity $\|\tilde{u}_a\|$

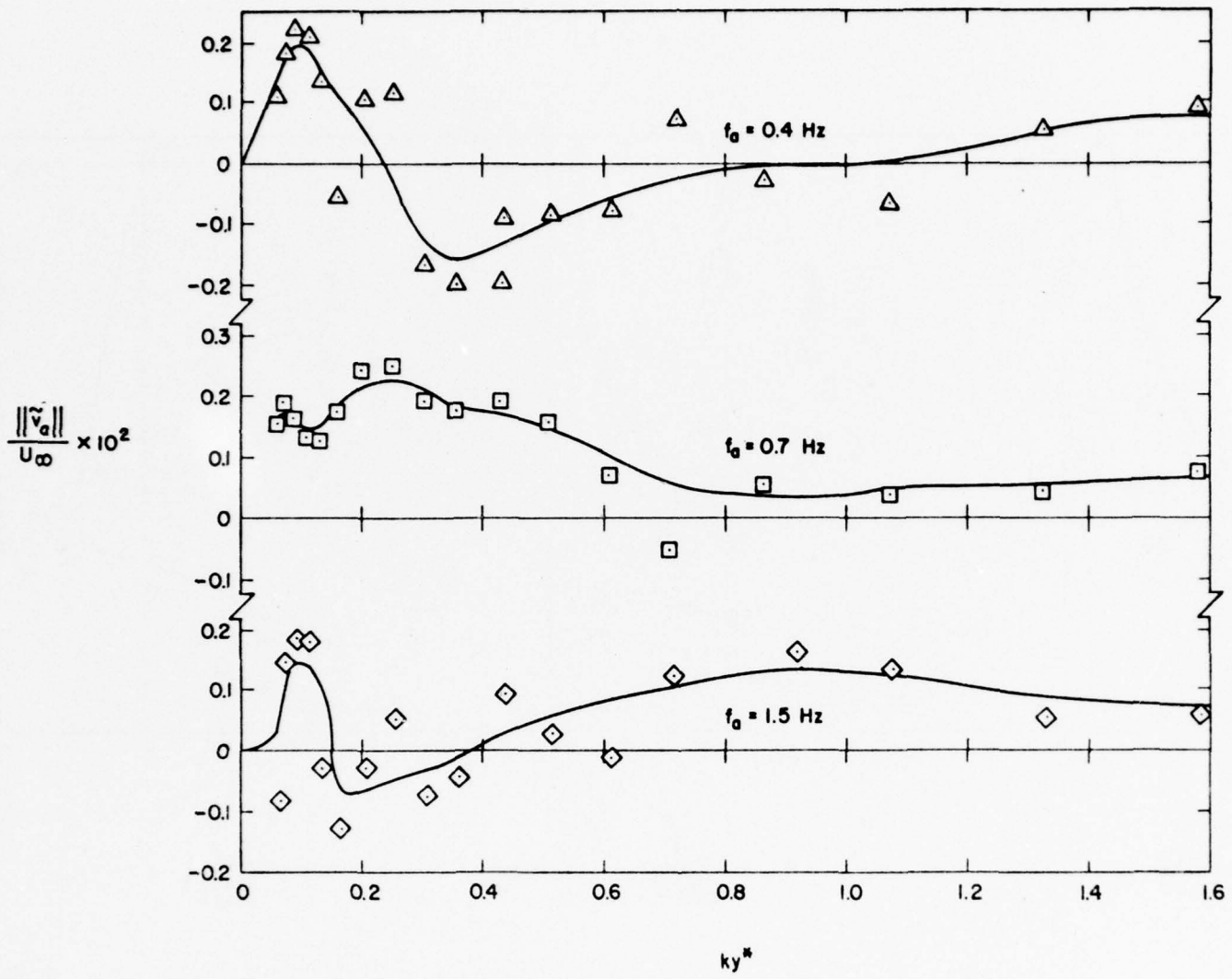

Figure 5.19 Profiles of Modulation Velocity $\|\tilde{v}_a\|$

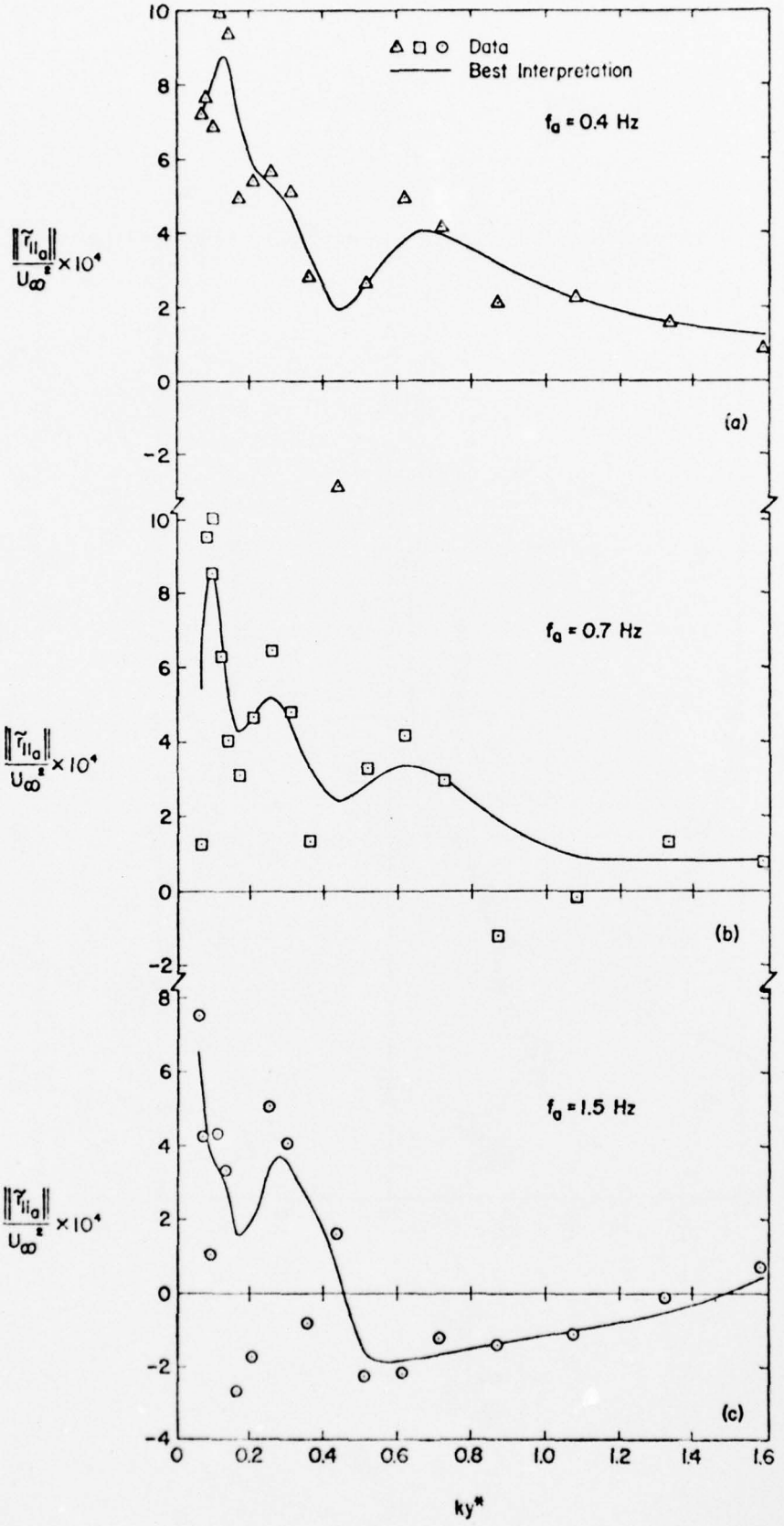

Figure 5.20 Profiles of Modulated Turbulent Stress $\|\tilde{r}_{11a}\|$

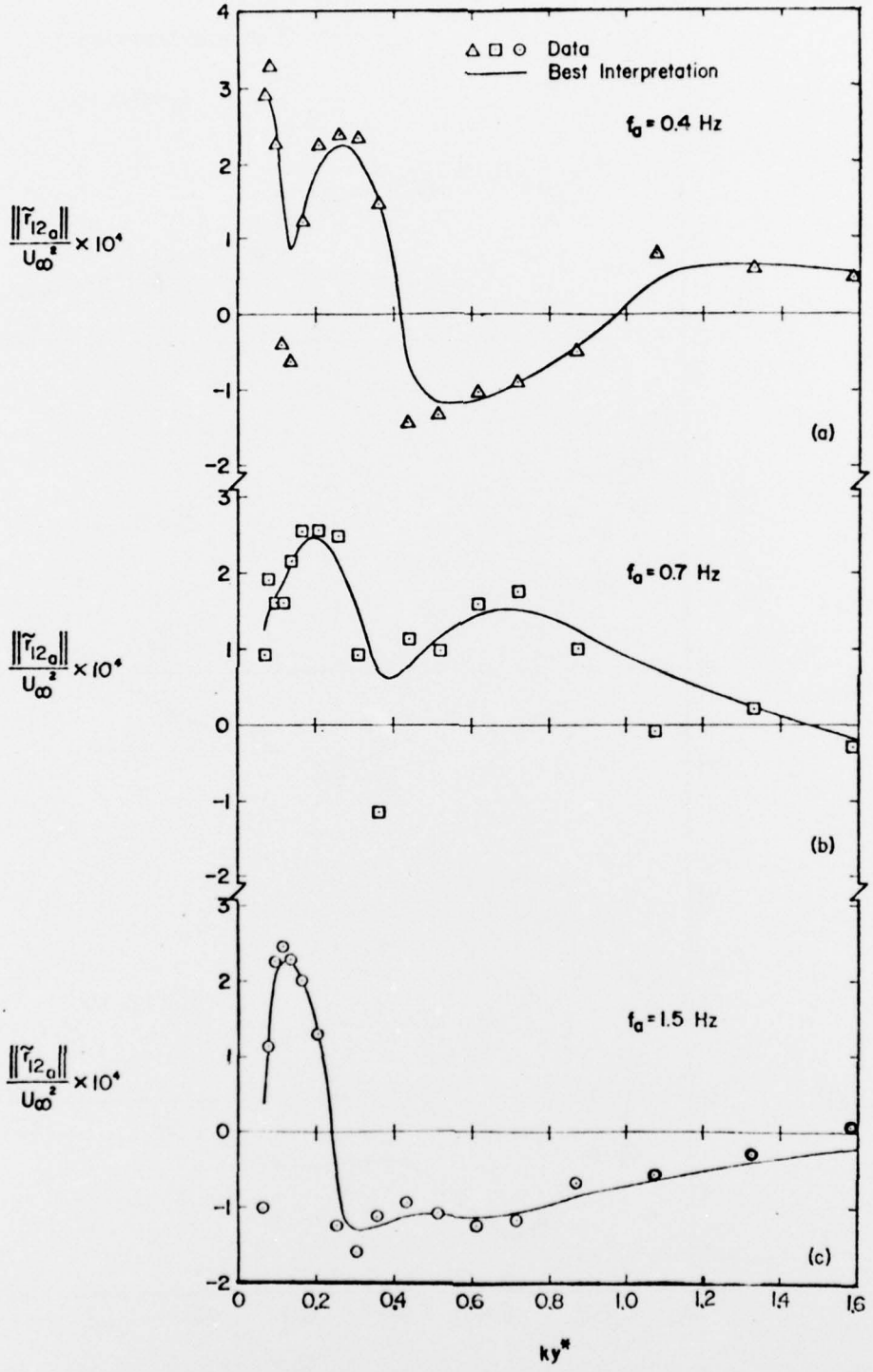

Figure 5.21 Profiles of Modulated Turbulent Stress $\|\tilde{r}_{12a}\|$

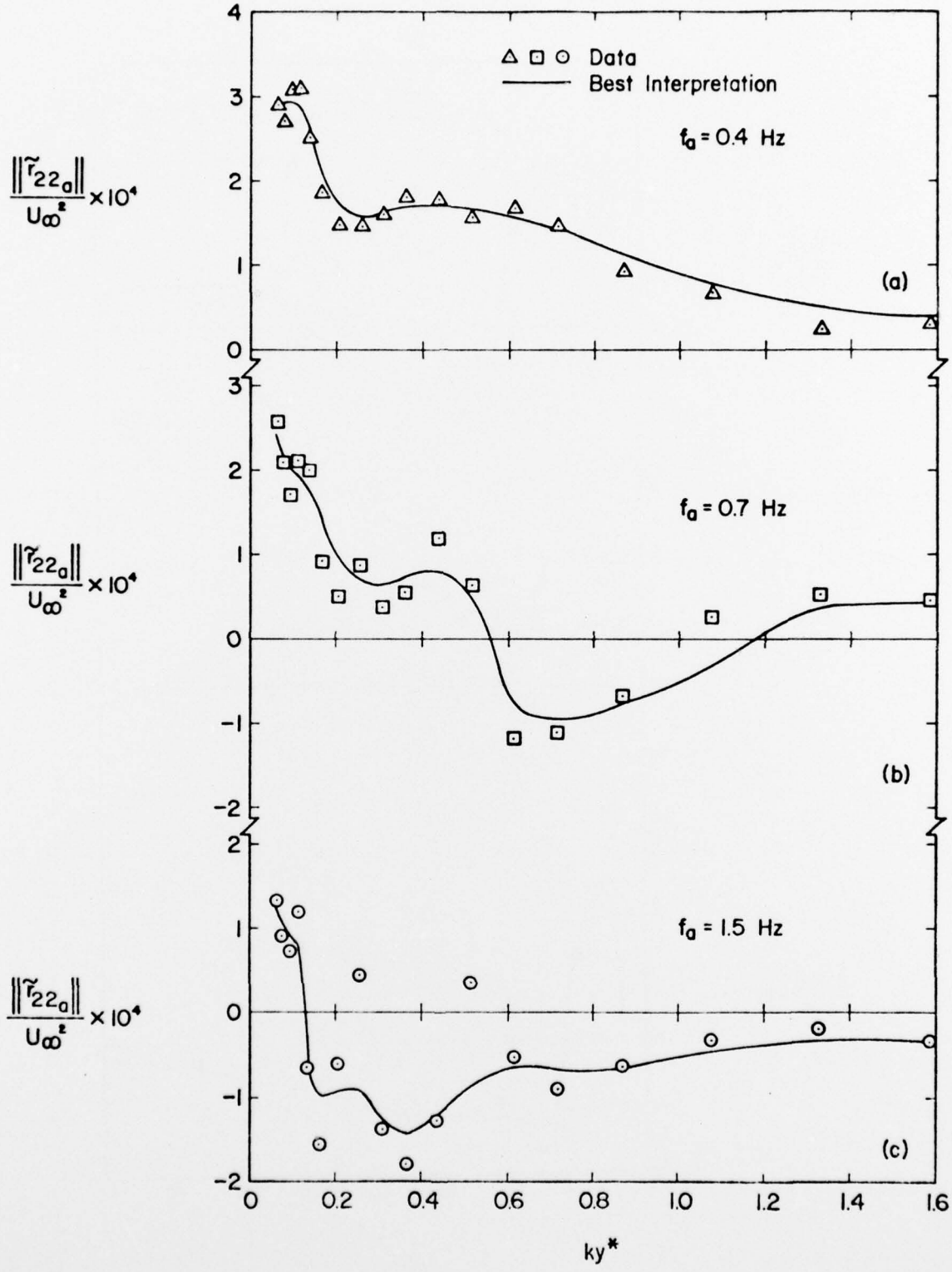

Figure 5.22 Profiles of Modulated Turbulent Stress $\|\tilde{r}_{22a}\|$

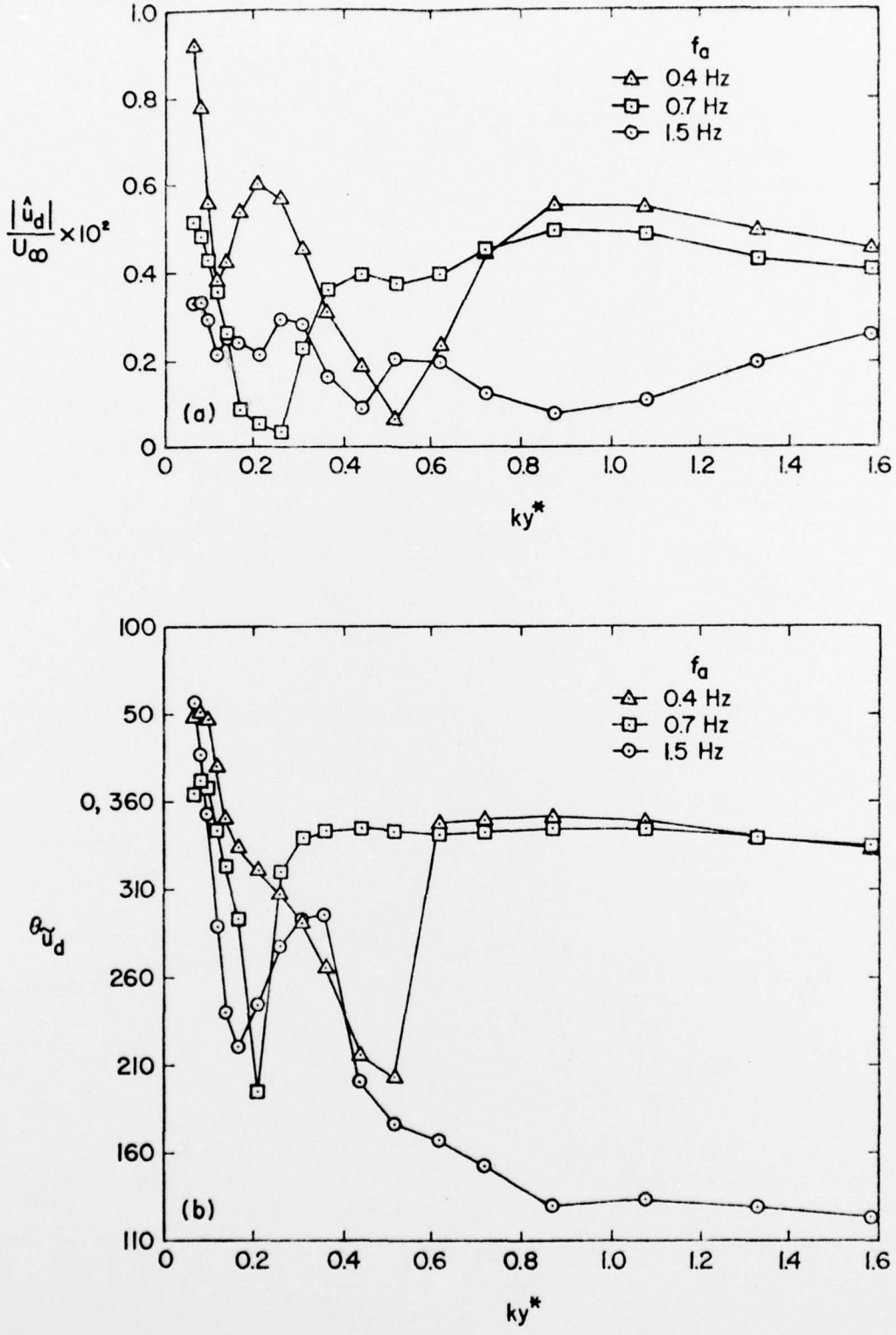

Figure 5.23 Amplitude and Phase Distributions of $\tilde{u}_d$

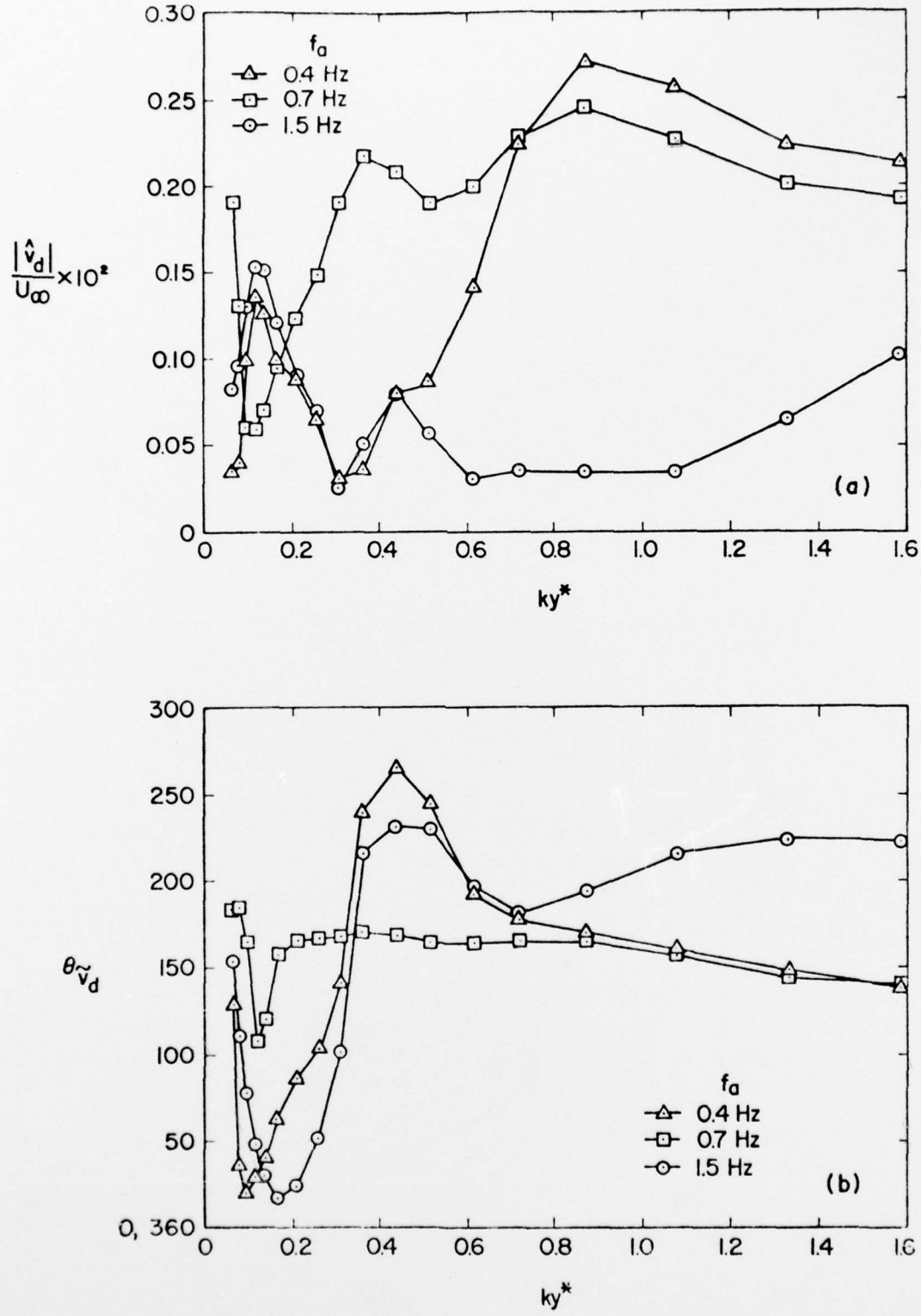

Figure 5.24 Amplitude and Phase Distributions of $\tilde{v}_d$

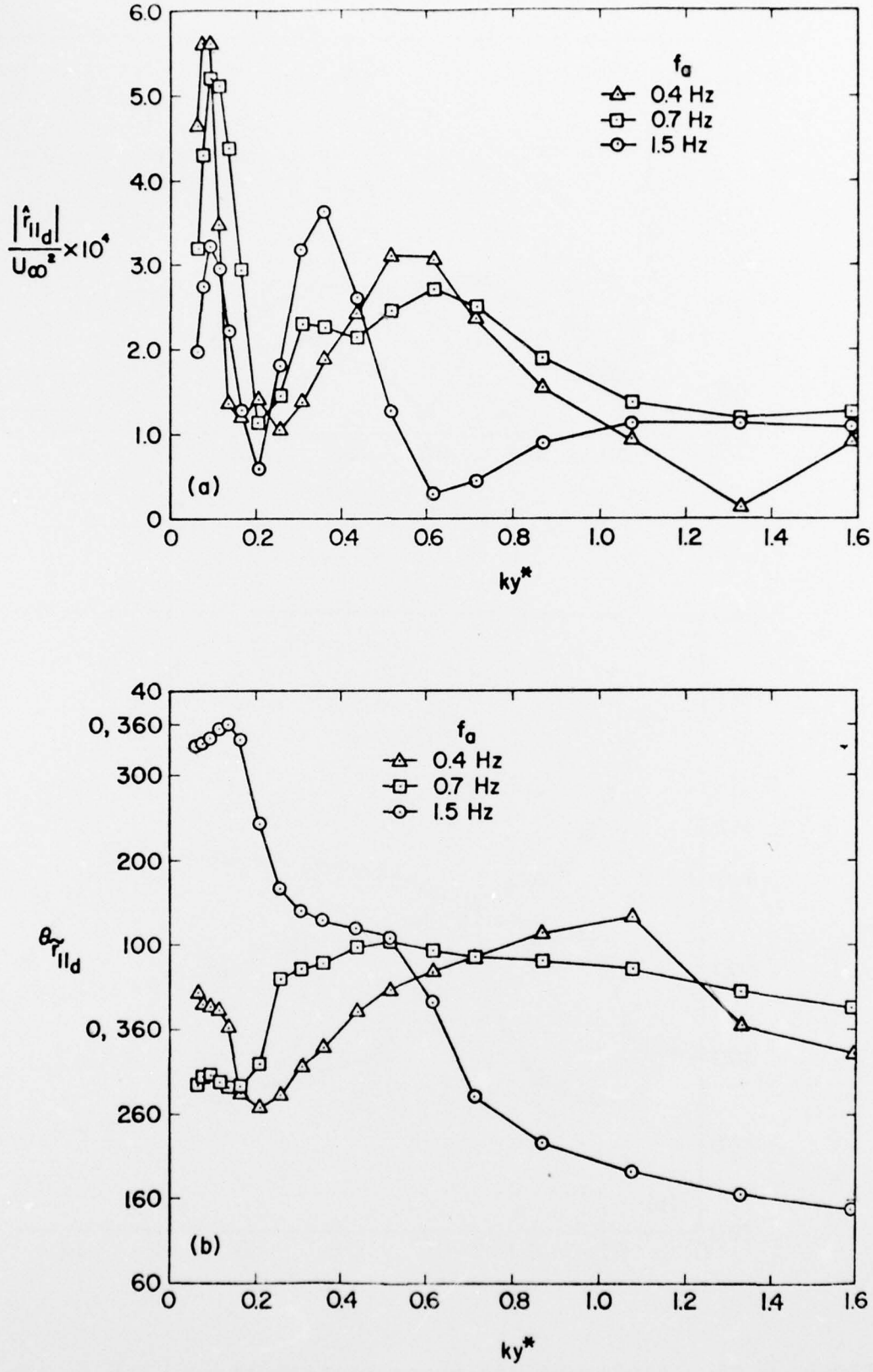

Figure 5.25 Amplitude and Phase Distributions of $\tilde{r}_{11d}$

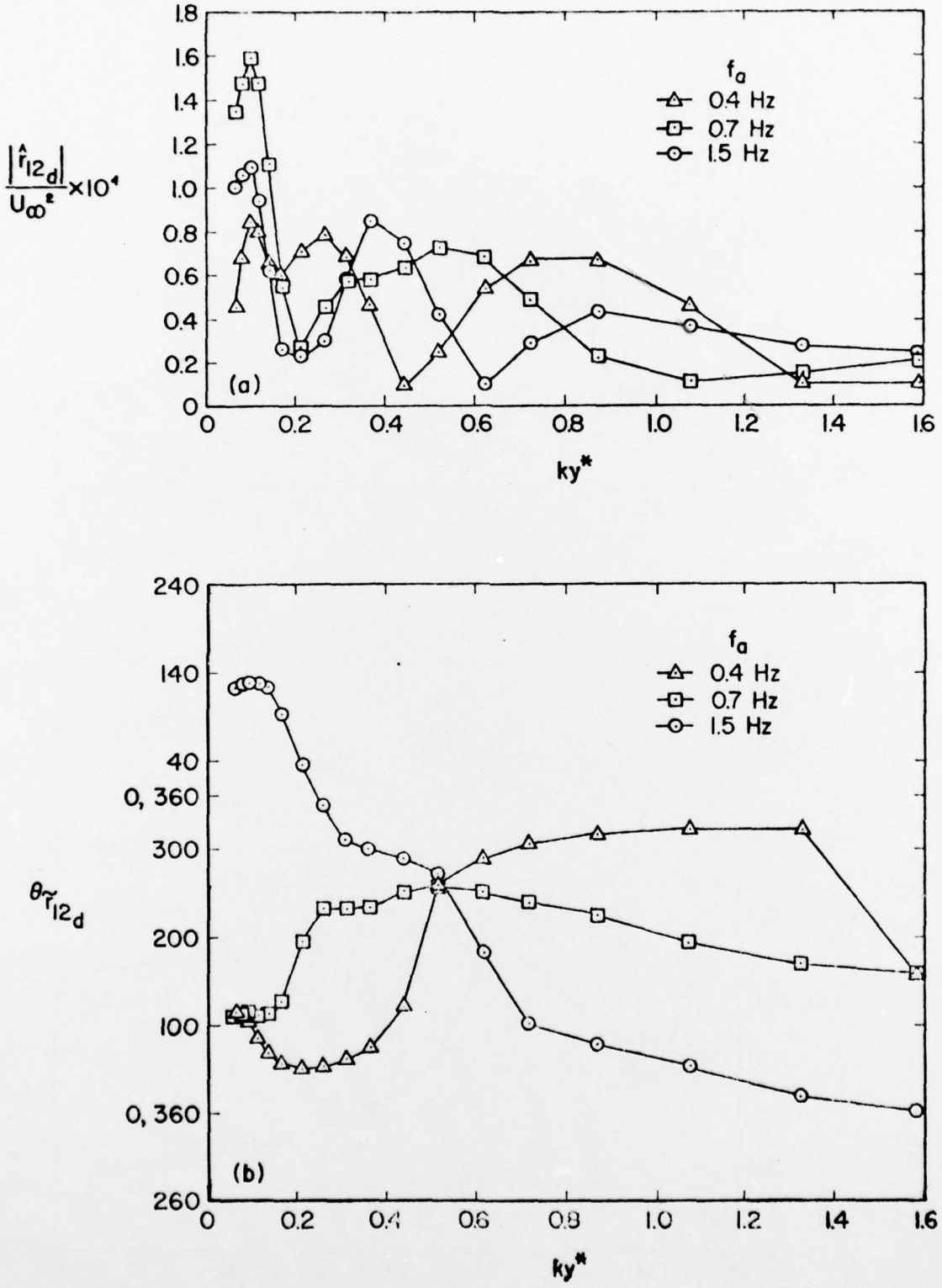

Figure 5.26 Amplitude and Phase Distributions of $\tilde{r}_{12d}$

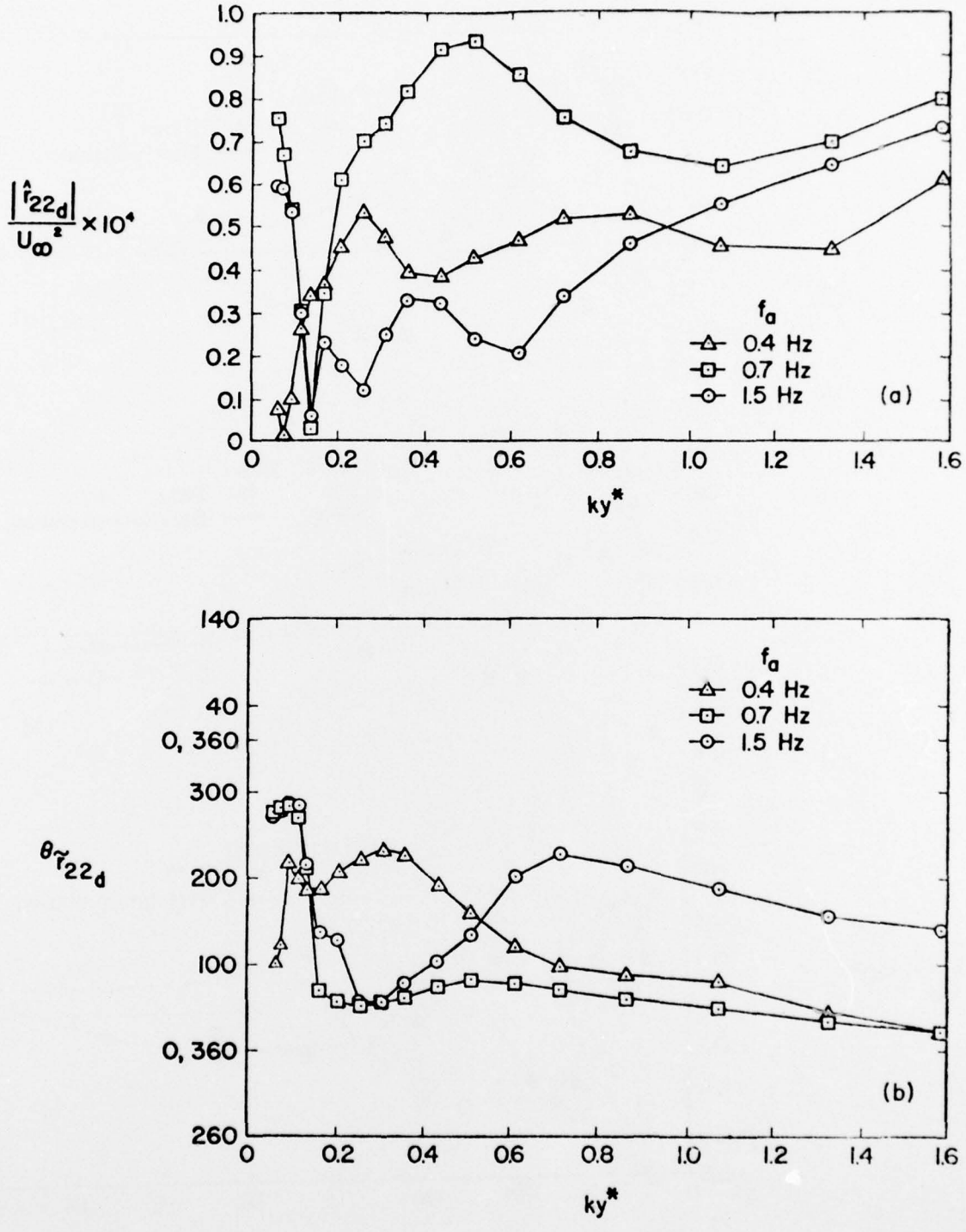

Figure 5.27 Amplitude and Phase Distributions of $\tilde{r}_{22d}$

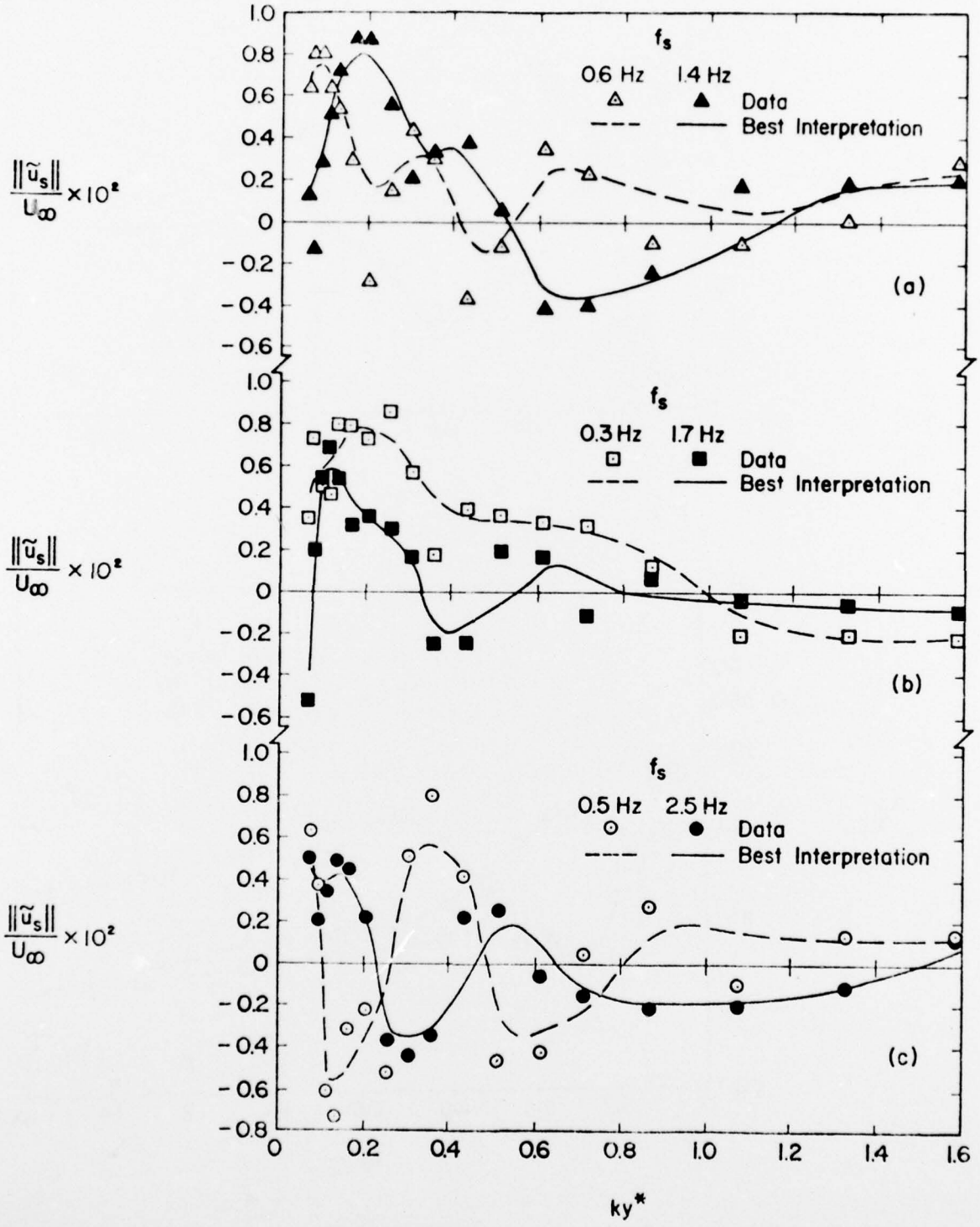

Figure 5.28 Profiles of $\|\tilde{u}_s\|$ for Interaction-Produced Waves

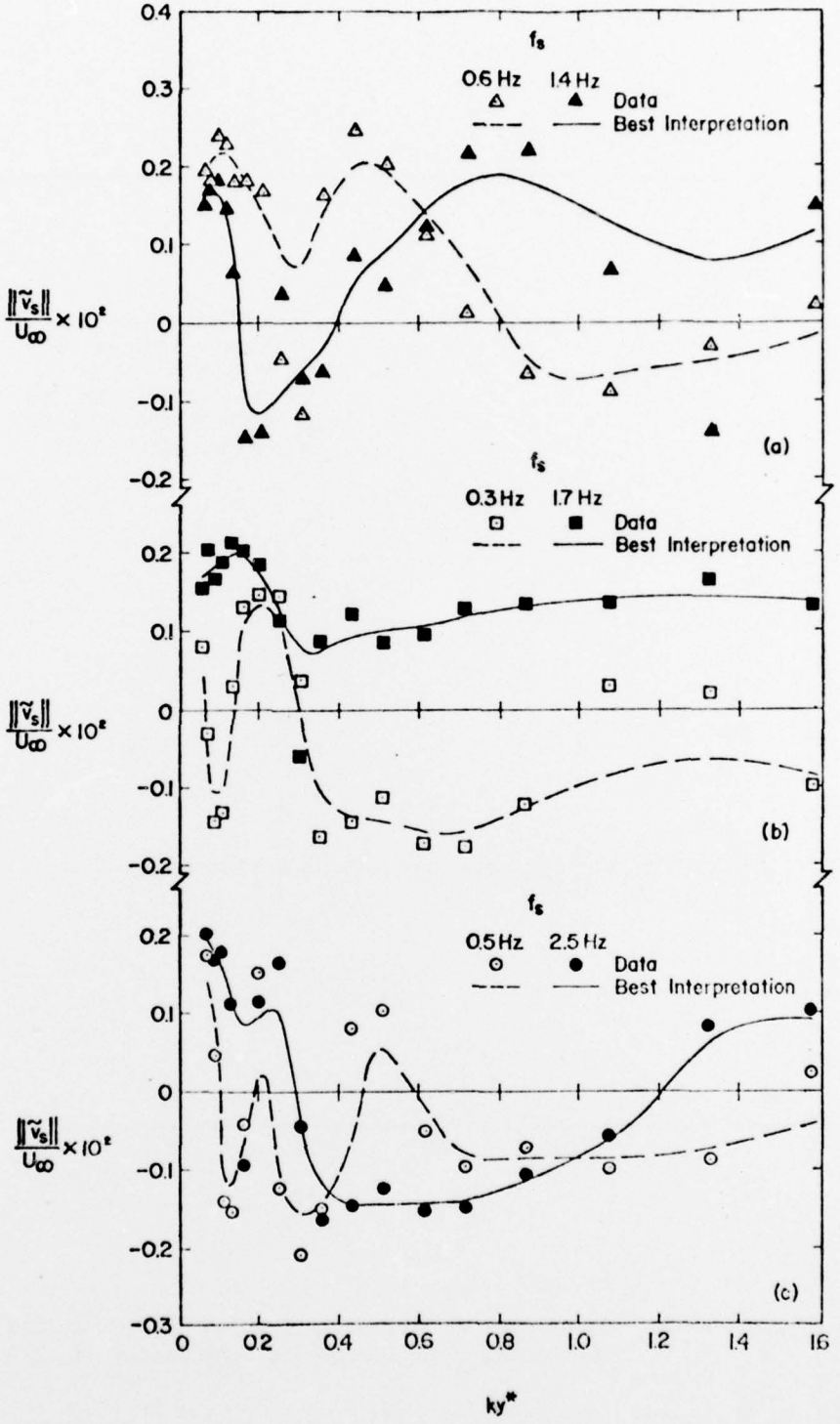

Figure 5.29 Profiles of $\|\tilde{v}_s\|$ for Interaction-Produced Waves

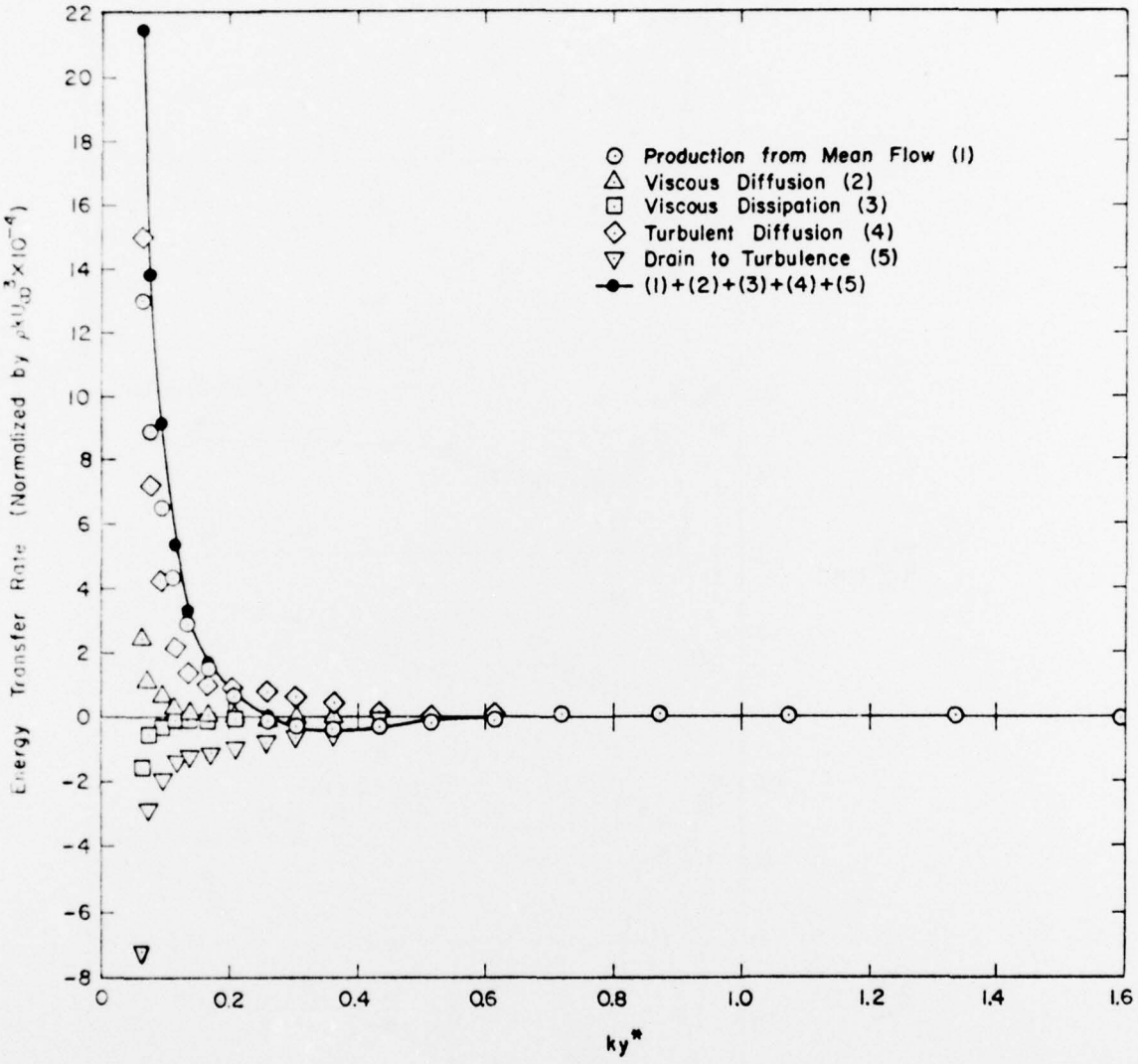

Figure 6.1 Horizontal Kinetic Energy Balance for Wave Perturbation Field by Equation (6.21)

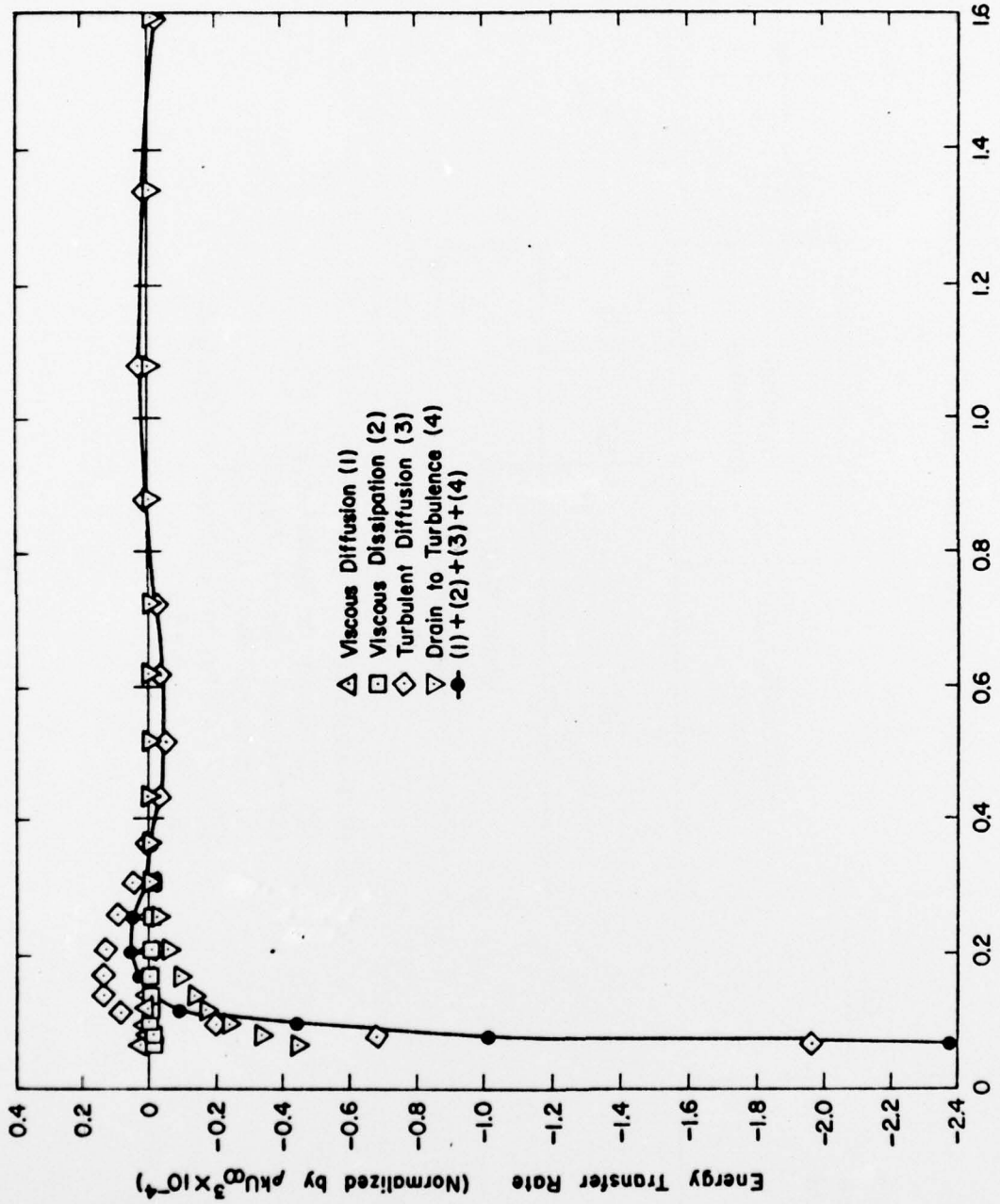

Figure 6.2 Vertical Kinetic Energy Balance for Wave Perturbation Field by Equation (6.22)

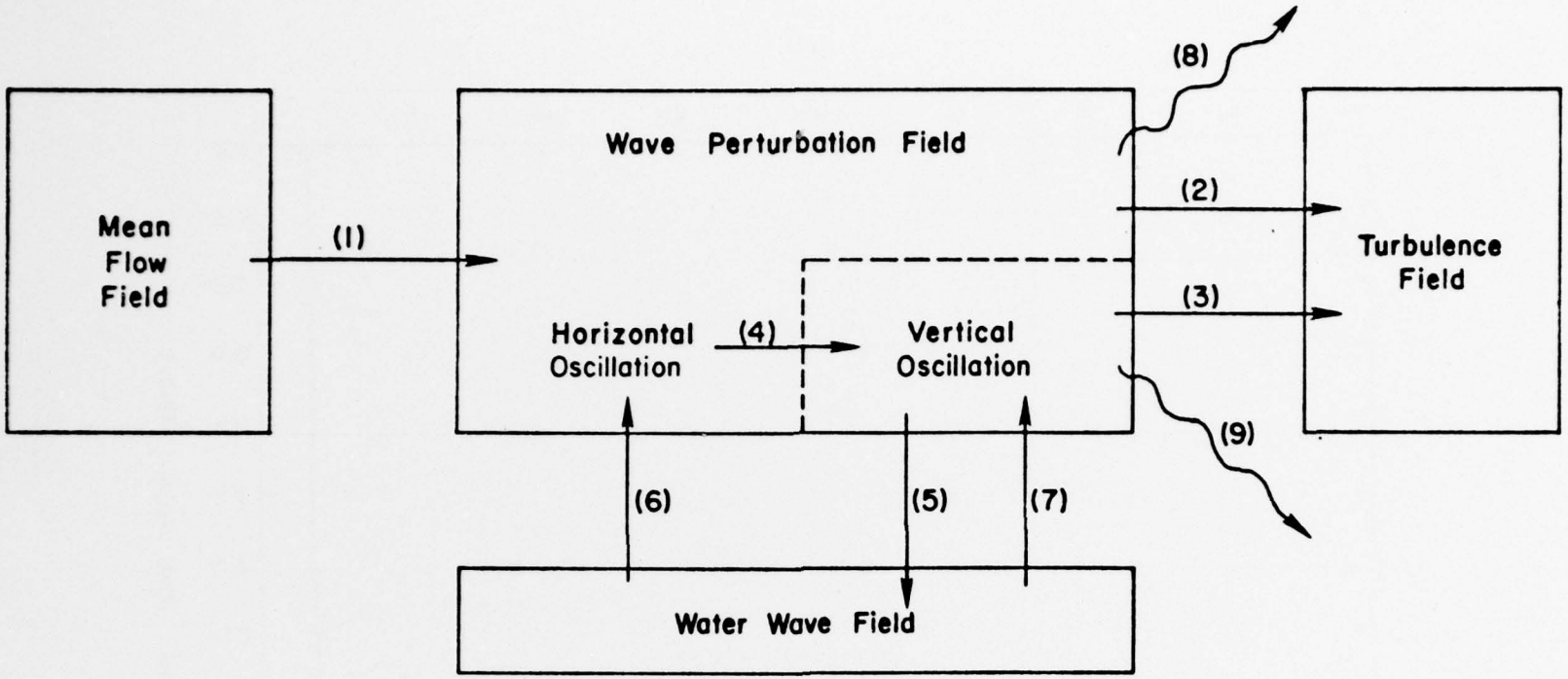

(1) Production
(2), (3) Drain to Turbulence
(4) Pressure Strain Transfer
(5) Pressure Work to Wave
(6), (7) Diffusion (Viscous + Turbulent)
(8), (9) Dissipation

Figure 6.3 Schematic of Energy Flux into and from Wave Perturbation Field of Interface Flow

Unclassified

SECURITY CLASSIFICATION OF THIS PAGE (When Data Entered)

REPORT DOCUMENTATION PAGE

READ INSTRUCTIONS BEFORE COMPLETING FORM

1. REPORT NUMBER: (14) TR- Technical Report No. 221
2. GOVT ACCESSION NO.
3. RECIPIENT'S CATALOG NUMBER

4. TITLE (and Subtitle): (6) THE STRUCTURE OF MODULATED TURBULENT FLOW OVER PROGRESSIVE WATER WAVES

5. TYPE OF REPORT & PERIOD COVERED: (7) Interim Technical Report

6. PERFORMING ORG. REPORT NUMBER

7. AUTHOR(s): (10) Chin-Tsau Hsu, E. Y. Hsu and Robert L. Street

8. CONTRACT OR GRANT NUMBER(s): (15) DAAG29-76-G-0125, N00014-76-C-0155, NSF-ENG 76-15106

9. PERFORMING ORGANIZATION NAME AND ADDRESS
Department of Civil Engineering
Stanford University
Stanford, California 94305

10. PROGRAM ELEMENT, PROJECT, TASK AREA & WORK UNIT NUMBERS

11. CONTROLLING OFFICE NAME AND ADDRESS
U.S. Army Research Office
Post Office Box 12211
Research Triangle Park, NC 27709 and

Office of Naval Research, Code 438
Department of the Navy
Arlington, Virginia 22217

12. REPORT DATE: (11) August 1977

13. NUMBER OF PAGES: 216

14. Monitoring Agency Name & Address --- NA

15. SECURITY CLASS. (of this report): Unclassified

15a. DECLASSIFICATION/DOWNGRADING SCHEDULE: NA

16. DISTRIBUTION STATEMENT (of this Report)

Approved for public release; distribution unlimited.

(12) 228 p.

17. DISTRIBUTION STATEMENT (of the abstract entered in Block 20, if different from Report)

NA

18. SUPPLEMENTARY NOTES

The findings in this report are not to be construed as an official Department of the Army or Department of the Navy position, unless so designated by other authorized documents.

19. KEY WORDS (Continue on reverse side if necessary and identify by block number)

20. ABSTRACT (Continue on reverse side if necessary and identify by block number)

Theoretical predictions of wave growth by closure modelling have been hindered by the ambiguity about the interface conditions and the lack of knowledge of the dynamics of wave-turbulence interaction. The present experimental program was undertaken in an attempt to clarify the interface flow structure, as well as the closure relations, and to study the dynamic response of wave perturbations to the imposition of air modulations.

DD FORM 1 JAN 73 1473 EDITION OF 1 NOV 65 IS OBSOLETE
S/N 0102 LF 014 6601

Unclassified

SECURITY CLASSIFICATION OF THIS PAGE (When Data Entered)

400117

The Stanford wind-wave facility was modified to permit generation of an air modulation with a sinusoidal variation. A wave height gauge and an X-array hot-film probe were used to measure simultaneously the wave height and the wind velocity from a wave-follower operating in a transformed coordinate system. Four runs were made, all with a 2.4 m/sec mean free stream velocity and a 1 Hz mechanically-generated water wave of amplitude 2.67 cm, but with modulating frequencies at 0.0, 0.4, 0.7 and 1.5 Hz respectively. Each velocity profile consists of 18 points ranging in mean elevations from 1.604 cm to 39.45 cm above the interface. Theoretical bases were also formed for a better understanding of the flow characteristics in the transformed coordinate system.

The mean velocity profile was found to be basically log-linear with a wake characteristic near the free stream. The friction velocity computed from the profile method agrees with the result obtained from the measured constant shear stress layer near the interface. The lower portion of the mean profiles follows the wave form but the upper portion of the mean profiles seems to be unaware of the existence of the water wave underneath. Thus, describing the flow in the transformed coordinate system is an appropriate approach. Drift current effects on the mean flow were also discussed.

The wave perturbation motion was found to be irrotational near the free stream and to have a strong shear behavior near the interface. All the phases of the wave-induced turbulent Reynolds stresses have a jump of 180° in the middle of the boundary layer, but such jumps do not occur in the phases of the wave perturbation velocities. The relationships between the observed wave perturbation velocities and the induced turbulent Reynolds stresses are basically of an eddy viscosity type.

The energy balance of the wave perturbation field showed that most of the energy transfer occurs in the vicinity of the interface. Energy was drawn from the mean flow to wave perturbation, and then from the wave perturbation to turbulence and to the water wave. The energy transfer from wind to waves is predominantly caused by the wave perturbation pressure. The measured wave growth rate agrees with that observed by Dobson (1971), and is one order in magnitude greater than Miles' prediction. Wave-turbulence interaction is responsible for this higher growth rate.

The response of the wave perturbation to air modulations when the modulating frequencies are lower than the frequency of the water wave is different from that when the modulating frequency is higher than the frequency of the water wave. Air modulations tend to decrease the ripple formation over the mechanically-generated water wave under the same mean flow condition.